

**THE ROLE OF NANOSTRUCTURAL AND ELECTRICAL SURFACE
PROPERTIES ON THE OSTEOGENIC POTENTIAL OF TITANIUM IMPLANTS**

A Thesis
Presented to
The Academic Faculty

by

Rolando Arturo Gittens Ibacache

In Partial Fulfillment
of the Requirements for the Degree
Doctor of Philosophy in Bioengineering in the
School of Materials Science and Engineering

Georgia Institute of Technology
December 2012

COPYRIGHT © 2012 BY ROLANDO ARTURO GITTENS IBACACHE

**THE ROLE OF NANOSTRUCTURAL AND ELECTRICAL SURFACE
PROPERTIES ON THE OSTEOGENIC POTENTIAL OF TITANIUM IMPLANTS**

Approved by:

Dr. Barbara D. Boyan, Co-Advisor
School of Biomedical Engineering
Georgia Institute of Technology

Dr. Rina Tannenbaum, Co-Advisor
School of Materials Science and
Engineering
Georgia Institute of Technology

Dr. Zvi Schwartz, Co-Advisor
School of Biomedical Engineering
Georgia Institute of Technology

Dr. Kenneth H. Sandhage
School of Materials Science and
Engineering
Georgia Institute of Technology

Dr. Robert Butera
School of Electrical and Computer
Engineering
Georgia Institute of Technology

Date Approved: August 3, 2012

But a statement presented to the mind accompanied by proofs which the senses can perceive to be correct, which the faculty of reason can accept, which is in accord with traditional authority and sanctioned by the promptings of the heart, can be adjudged and relied upon as perfectly correct, for it has been proved and tested by all the standards of judgment and found to be complete.

'Abdu'l-Bahá

Esta tesis va dedicada a las dos rosas de mi vida, que han moldeado mi carácter y han sacado a relucir lo mejor que hay en mí.

ACKNOWLEDGEMENTS

I would like to start by thanking my advisors Dr. Barbara Boyan and Dr. Zvi Schwartz for their mentorship throughout the years in my Ph. D. Although I still consider my arrival to Dr. Boyan's lab somewhat fortuitous, her impact on my scientific career will never be forgotten. Her passion for scientific research was contagious to the point where she trained an engineer to appreciate the intricacies of biology and to ask the right questions. At the same time, her drive to commercialize any good (or bad) idea provided me with invaluable experience that resulted in two patent applications with my research. In addition, Dr. Schwartz's commitment to work was enough motivation to always want to do better. Even from our first meeting, when I still had no idea what an osteoblast was, he held his high standard and only expected the best from me. Such lessons will always make me demand the highest standard as well.

I would also like to thank my first mentor, Dr. Rina Tannenbaum. Her mentorship during my first years in my doctorate degree helped me reaffirm the reasons why I wanted to get a Ph. D. She taught me the right balance can be achieved between family and work, and that the former does not have to be sacrificed to do great research.

The rest of my committee members also deserve high praise for their time and support with my projects, to the point where I can easily consider them as advisors as well. Dr. Ken Sandhage was instrumental for the development of my nanomodification projects, and his expertise always provided much needed insight. Dr. Butera's hands-on approach to solving problems was also very important for my electrical stimulation project. I was extremely happy to have Dr. Butera in my committee, considering that he was one of the first faculty members I met at Georgia Tech, when I was able to visit the campus with the FOCUS program in 2003 with the help of Dr. Arturo Lindsay, my tio and

my father in Atlanta. His influence on me served as great motivation for me to want to pursue a Ph. D., and his efforts are partly responsible for me to have been given an opportunity at GATech. I'm extremely joyful that I got to work on my Ph. D. in Atlanta, where he lives.

From Dr. Tannenbaum's lab, I am grateful to Dr. Larry Pranger for his continuous advice, which he offered until the moment he left. I would also like to mention Dr. Lex Nunnery, Dr. Kasi David, Dr. Jung Hwa Park and Dr. Il Tae Kim for help and support at all times. And I am probably most grateful to Dr. Kit Carson for his contributions to my intellect and my spirituality.

From Dr. Boyan and Dr. Schwartz's lab, I would first like to thank Dr. Rene Olivares-Navarrete for his true mentorship and ability to always find the other side of the story. If I were able to take with me just a quarter of all his recommendations and ideas, I could rest assured to have a very successful research career. I am also extremely grateful to Sharon Hyzy for teaching me how to work in a research lab and for always being open for one more question. Also, I would like to thank everyone that graduated before my time and those that I will leave behind for always being there for me. I have to mention Reyhaan and Khairat, however, for being two of the more generous souls in my path. Of course I have to thank Rosemary Song, my undergrad, for all her help and for being so patient and understanding with me. And last, but not least, I would also like to thank Maribel Baker for helping me conserve my sanity and allowing me to vent in Spanish when I needed to.

Briefly, I also have to thank PANAS for helping me remember why I should be excited to go back to Panama when I finish. I would also like to thank all the faculty members, who through classes or during meetings shared with me their wisdom about research or life, such as Dr. Lisa Rosenstein, Dr. Brent Carter, Dr. Tom Sanders, Dr.

Preet Singh, Dr. Robert Snyder, Dr. Andres Garcia, Dr. Thomas Burkholder, Dr. Valeria Milam, Dr. Julia Babensee, and many others. In addition, I'm very grateful to the administrative staff that has helped me throughout the years, including Ms. Brentis Henderson, Susan Bowman, Teresa Nelson, James Cagle, Chris Ruffin, James Godard, Megan McDevitt, Floyd, Sandra, Janice. And I also have to thank the facilities crew that would allow me to talk to a human being after hours of just staring a computer, including Mildred, Shemika, Sherry, and others.

I would like to thank my friends throughout the years in Atlanta that helped me enjoy life while in my Ph. D., including friends from school and the program like Nathan Hotaling, Lindsey Goodman, Yair Korenblit, Seth Gazes, Prem Midha, Roy Wang, Gregory Philips, Brad White and others. Of my friends from Atlanta, I would like to recognize the unconditional support (and unofficial IP law advise) of Kevin Belote and Rachel Gage, who were instrumental especially when dealing with my thesis and the pregnancy. I also have to mention Wes Baker, Don Lee, Clint Pritchard, Matt Maguire, Erick Carlson, and many others that made my life in Atlanta much more fun. I would also like to thank the Baha'i community of Atlanta for keeping me engaged with society and good causes. The highest praise needs to go to Maureen Mercer, my neighbor, my friend, my mother in Atlanta. Her emotional and culinary support helped me (my lab and my family) go through a lot. Her generosity has no end.

To my best friends from Panama, Jorge, Berno, Galo, Damian, and Manuel, I had what it took to even start a program like this thanks to our philosophical discussions starting in middle school and to us being lifelong "nerds". I also need to recognize the absolute love from my sisters back in Panama, Gaby, Katia and Marisol.

I would not be in this world if it wasn't for my parents, and they are the biggest motivation for me to ever want to get a Ph. D in the United States. Their continuous

support from Panama was very necessary to focus on the goal and finish. But I would not have reached this point, to write this last paragraph on my thesis if it wasn't for the unconditional love of my wife, Kimberly Portmess, who in the good and the bad times always had my back. And I have to include my little king, Bayano Arturo, who was hanging from my shoulder as I wrote the last sentence of my thesis.

This research was partly funded with a scholarship from Panama's Government (IFARHU-SENACYT).

Alláh'u'Abhá!

TABLE OF CONTENTS

	Page
ACKNOWLEDGEMENTS	v
LIST OF TABLES	xiv
LIST OF FIGURES	xv
LIST OF SYMBOLS AND ABBREVIATIONS	xix
SUMMARY	xxi
CHAPTER 1. SPECIFIC AIMS	1
1.1. Specific Aim 1	3
1.2. Specific Aim 2	4
1.3. References	5
PART I: EVALUATION OF MICROROUGHENED AND NANOSTRUCTURED	
SURFACES ON OSTEOBLAST LINEAGE CELL RESPONSES	7
CHAPTER 2. BACKGROUND ON IMPLANT OSSEOINTEGRATION AND THE	
ROLE OF NANOSTRUCTURES	8
2.1. Introduction	8
2.2. Osseointegration: Key Biological Processes	11
2.2.1. Wound Healing and Fibrin Clot Formation	11
2.2.2. Mimicking Bone Structure: Bone Remodeling	13
2.3. Osseointegration and Implant Surface Structure	16
2.3.1. Microroughness Effect <i>In Vivo</i>	17
2.3.2. Microroughness Effect <i>In Vitro</i>	20
2.3.3. Role of Nanostructures <i>In Vivo</i>	22
2.3.4. <i>In vitro</i> response to nanostructures	24
2.4. References	26

CHAPTER 3. THE EFFECTS OF COMBINED MICRO/SUB-MICROSCALE SURFACE ROUGHNESS AND NANOSCALE FEATURES ON CELL PROLIFERATION AND DIFFERENTIATION	33
3.1. Introduction	33
3.2. Materials and Methods	36
3.2.1. Titanium Disks	36
3.2.2. Surface Modification	36
3.2.3. Surface Characterization	37
3.2.4. Cell Culture Model and Assays	39
3.2.5. Statistical Analysis	41
3.3. Results	42
3.4. Discussion	51
3.5. Conclusions	55
3.6. References	56
CHAPTER 4. THE ROLE OF TITANIUM SURFACE MICRO/NANOTOPOGRAPHY AND WETTABILITY ON THE DIFFERENTIAL RESPONSE OF HUMAN OSTEOBLAST LINEAGE CELLS	60
4.1. Introduction	60
4.2. Materials and Methods	64
4.2.1. Titanium Specimens and Surface Modification Treatments	64
4.2.2. Surface Characterization	65
4.2.3. Cell Culture Model	69
4.2.4. Statistical Analysis	70
4.3. Results	70
4.3.1. Characterization of Nanomodified Surfaces	70

4.3.2. Osteoblast Lineage Cell Response to Nanomodified Surfaces	76
4.4. Discussion	79
4.5. Conclusions	84
4.6. References	85
CHAPTER 5. DIFFERENTIAL RESPONSES OF OSTEOLAST LINEAGE CELLS TO NANOTOPOGRAPHICALLY-MODIFIED, MICROROUGHENED TITANIUM- ALUMINUM-VANADIUM ALLOY SURFACES	89
5.1. Introduction	89
5.2. Materials and Methods	91
5.2.1. Titanium Alloy Specimens and Surface Modification Treatments	91
5.2.2. Surface Characterization	92
5.2.3. Cell Culture Model	94
5.2.4. Statistical Analysis	96
5.3. Results	97
5.3.1. Characterization of Nanomodified Surfaces	97
5.3.2. Osteoblast Lineage Cell Response to Nanomodified Surfaces	105
5.4. Discussion	108
5.5. Conclusions	114
5.6. References	115
CHAPTER 6. EFFECTS OF STRUCTURAL PROPERTIES OF ELECTROSPUN TiO ₂ NANOFIBER MESHES ON THEIR OSTEOGENIC POTENTIAL	118
6.1. Introduction	118
6.2. Materials and Methods	120
6.2.1. Preparation and Characterization of TiO ₂ Scaffolds	120
6.2.2. Cell Culture	122

6.2.3. Biochemical Assays	123
6.2.4. Statistical Analysis	124
6.3. Results	124
6.4. Discussion	133
6.5. Conclusion	137
6.6. References	138
PART II: EVALUATION OF ELECTRICAL STIMULATION OF TITANIUM SURFACES ON OSTEOBLAST LINEAGE CELL RESPONSES	142
CHAPTER 7. REVIEW OF BONE ELECTRICAL PROPERTIES AND THE ELECTRICAL IMPLICATIONS OF CORROSION ON OSTEOINTEGRATION OF TITANIUM IMPLANTS	143
7.1. Biopotentials	143
7.2. Electrical Signals in Bone	144
7.3. Electrical Stimulation of Bone	149
7.3.1. Direct Current (DC) Stimulation	150
7.3.2. Capacitive Stimulation	152
7.3.3. Inductive Stimulation	152
7.4. Electrical Implications of Corrosion	155
7.4.1. Basic Electrochemistry	155
7.4.2. Passivity of Titanium	157
7.4.3. Types of Corrosion	158
7.5. Clinical Relevance of Corrosion	160
7.6. References	162
CHAPTER 8. DELIVERY OF FIXED DC POTENTIALS TO TITANIUM SURFACES FOR THE ENHANCEMENT OF OSTEOBLAST DIFFERENTIATION	169

8.1. Introduction	169
8.2. Materials and Methods	171
8.2.1. Titanium Specimens	171
8.2.2. Electrical Stimulation System	171
8.2.3. Electrochemical Measurements	172
8.2.4. Surface Analysis of Ti Specimens	173
8.2.5. Cell Culture Model and Assays	173
8.2.6. Statistical Analysis	176
8.3. Results	177
8.3.1. Characterization of Electrical Stimulation System	177
8.3.2. Cell Assays: Cathodic vs. Anodic Effect	180
8.3.3. Electrically-Isolated Versus Non-Stimulated Controls	180
8.3.4. Voltage-Dependent Effect of Stimulated PT Surfaces on MG63 Response	181
8.4. Discussion	185
8.5. Conclusions	190
8.6. References	190
CHAPTER 9. Conclusions and Future Perspectives	193
APPENDIX A	196
VITA	197

LIST OF TABLES

	Page
Table 3.1. Roughness measurements on titanium specimens.	47
Table 3.2. Surface chemical evaluation of nanomodified Ti specimens.	50
Table 3.3. Mean values of water contact angle \pm one standard deviation (SD) on Ti specimens.	50
Table 6.1. Surface roughness \pm standard deviation (SD) of TiO ₂ meshes measured by LCM.	126
Table 6.2. Elemental composition \pm standard deviation (SD) of TiO ₂ meshes analyzed by EDX.	127
Table 6.3. Surface elemental composition \pm standard deviation (SD) of TiO ₂ meshes analyzed by XPS.	128

LIST OF FIGURES

	Page
Figure 2.1 Schematics of failed or osseointegrated (A-B) dental and (C-E) spine implants.	9
Figure 2.2 Diagram showing the direct and indirect interactions between surface properties and biological events.	11
Figure 2.3. Schematic depicting fibrin clot adhesion to a rough surface and mesenchymal stem cell (MSC) migration through the clot.	13
Figure 2.4. Interactions between bone and the implant surface at different length-scales.	15
Figure 2.5. Schematic and SEM images of various surface modifications.	19
Figure 3.1. Morphological assessment of nanostructure evolution with time. NM-treatment of (A) PT surfaces via oxidation in flowing synthetic air (21 % O ₂ , 79 % N ₂) at 740 °C for times of: (B) 45 minutes; (C) 90 minutes; (D) 180 minutes.	43
Figure 3.2. Thermogravimetric (TG) data showing the mass increase of a Ti substrate exposed to the oxidation-based nanomodification treatment.	44
Figure 3.3. SEM images of microrough and micro/nanostructured titanium specimens.	45
Figure 3.4. SEM images of the surface of titanium specimens.	47
Figure 3.5. Surface characterization data of the NM-treated samples and their controls.	49
Figure 3.6. Effects of nanoscale surface features and microscale surface roughness on osteoblast differentiation.	52
Figure 4.1. Static and dynamic evaluations of surface wettability of Ti specimens.	62
Figure 4.2. Morphological evaluation of micro/nanostructured Ti specimens.	71

Figure 4.3. Mean values of the surface roughness average (Sa) of original and nanomodified surfaces measured by laser confocal microscopy (LCM, black bars) and atomic force microscopy (AFM, grey bars).	72
Figure 4.4. Surface elemental compositions of the SLA and NMSLA specimens measured by XPS.	72
Figure 4.5. Static and dynamic contact angle analyses on SLA and NMSLA specimens.	75
Figure 4.6. Comparison of the contact angles measured by the optical sessile-drop technique in air, ESEM in water vapor, or calculated from the measured F/L values from dynamic analyses of the autoclaved SLA and NMSLA specimens.	76
Figure 4.7. Effects of micro- and nanoscale surface modifications on immature osteoblast-like cells and human MSCs evaluated as treatment over microsmooth controls (dotted line).	78
Figure 5.1. SE images and image analyses of the Ti alloy surfaces used for <i>in vitro</i> cell studies.	98
Figure 5.2. (A) Optical and (B-D) SE images of the surface nanostructural modification applied to clinically relevant Ti alloy spine implants.	99
Figure 5.3. SE images of the original microrough titanium alloy (rTiAlV) surface after different nanomodification times of 45, 90 and 180 minutes.	100
Figure 5.4. Surface characterization of nanomodified Ti alloy specimens.	102
Figure 5.5. Focused ion beam (FIB) milling preparation of a TEM foil from a NMSTiAlV surface.	103
Figure 5.6. Elemental compositions of the sTiAlV, NMSTiAlV, rTiAlV and NMrTiAlV specimens measured by XPS.	104

Figure 5.7. Effects of micro- and nanoscale surface modifications on human primary osteoblasts (A-E) and human MSCs (F-J).	106
Figure 5.7. Continued	107
Figure 6.1. LCM images of TiO ₂ meshes, made with (A, B) 6 % and (C, D) 10 % PVP showing their flat and patterned surfaces.	125
Figure 6.2. SEM images and analysis of the morphology of the electrospun nanofiber TiO ₂ meshes produced with (A, B) 6 % or (C, D) 10 % PVP.	126
Figure 6.3. XRD spectra of 6 % and 10 % TiO ₂ nanofiber meshes.	128
Figure 6.4. SEM images at different magnifications of the morphology of MG63 osteoblast-like cells cultured on the flat side of the nanofiber TiO ₂ meshes.	130
Figure 6.5. SEM images at different magnifications of the morphology of MG63 osteoblast-like cells cultured on the patterned side of the nanofiber TiO ₂ meshes.	131
Figure 6.6. Effects of structural properties of electrospun nanofiber TiO ₂ meshes on osteoblast maturation.	132
Figure 7.1. Schematics of injury potentials.	146
Figure 7.2. Schematics of the relationship between mechanical forces and electrical signals in bone.	148
Figure 7.3. Schematics of different electrical stimulation systems.	151
Figure 7.4. Schematic of possible cell signaling pathways activated by mechanical and electrical stimulation systems.	154
Figure 7.5. Schematic of the initiation and mechanism of corrosion of a dental implant.	156
Figure 8.1. Optical images and schematic of a custom-made electrical stimulation system used to deliver fixed DC potentials to cells growing on Ti substrates.	174

Figure 8.2. Routine characterization of voltage and currents in the electrical stimulation system.	178
Figure 8.3. Cyclic voltammetry curves for PT surfaces in (A) 1 M sulfuric acid or (B) cell culture media.	178
Figure 8.4. SEM images of laser-etched PT surface before and after electrical stimulation.	179
Figure 8.5. Effects of anodically and cathodically polarized surfaces using fixed DC potentials of 100 mV on osteoblast-like MG63 cells.	182
Figure 8.6. Evaluation of different control surfaces on the response of osteoblast-like MG63 cells.	183
Figure 8.7. Voltage-dependent effects of cathodically polarized PT surfaces on osteoblast-like MG63 cells.	184
Video A.1. Representative video of the condensation dynamics of water droplets on microrough Ti (SLA) surfaces	196

LIST OF SYMBOLS AND ABBREVIATIONS

µg	micrograms
µm	micrometers
3D	three dimensional
AFM	atomic force microscopy
ALP	alkaline phosphatase
ASTM	American Society for Testing and Materials
BMP	bone morphogenic proteins
CaP	calcium phosphate
cpTi	commercially pure titanium
CT	computed tomography
CV	cyclic voltammetry
DC	direct current
DCA	dynamic contact angle
DMEM	Dulbecco's modified Eagle medium
DNA	deoxyribonucleic acid
ECM	extracellular matrix
EDX	energy dispersive X-ray spectroscopy
ELISA	enzyme-linked immunosorbent assay
ESEM	environmental scanning electron microscopy
FBS	fetal bovine serum
FEG-TEM	field emission gun transmission electron microscopy
FE-SEM	field emission scanning electron microscope
FGF	fibroblast growth factor
HA	hydroxyapatite
HF	hydrofluoric acid
hOB	human primary osteoblast
kGy	kilo-Gray (unit of adsorbed dose of ionizing radiation)
LCM	laser confocal microscopy
MG63	human osteoblast-like osteosarcoma cell line
mL	milliliters
mm	millimeters
mRNA	messenger ribonucleic acid
MSC	human mesenchymal stem cell
ng	nanograms
nm	nanometers
NM	nanoscale modification
OCN	osteocalcin
P/S	penicillin-streptomycin
pA	pico-amperes
PBS	phosphate buffered saline
PC	polycarbonate

PEEK	polyether ether ketone
PGE	prostaglandin E
PLC	poly(epsilon-caprolactone)
PLGA	poly(lactide-co-glycolide)
PT	pre-treatment titanium surface
Pt	platinum
PVP	poly(vinyl pyrrolidone)
qPCR	quantitative polymerase chain reaction
Ra	surface roughness average (profile)
RANKL	receptor activator for nuclear factor k B ligand
RF	radio-frequency
Runx2	runt-related transcription factor 2
Sa	surface roughness average (area)
SAED	selective area electron diffraction
SD	standard deviation
SE	secondary electron
SLA	sandblasted-large-grit-acid-etched titanium surface
Sz	surface roughness peak-to-valley height (area)
TG	thermogravimetric
TGF- β	transforming growth factor beta
Ti	titanium
Ti6Al4V	titanium-6%aluminum-4%vanadium alloy
TiAlV	titanium-aluminium-vanadium alloy
TiO ₂	titanium dioxide or titania
TiP	titanium isopropoxide
UV	ultra-violet
VEGF	vascular endothelial growth factor
XPS	X-ray photoelectron spectroscopy
XRD	X-ray diffraction
ZrO ₂	zirconium oxide or zirconia

SUMMARY

Dental and orthopaedic implants are currently the solutions of choice for teeth and joint replacements with success rates continually improving, but they still have undesirable failure rates in patients who are compromised by disease or age, and who in many cases are the ones most in need. The success of titanium (Ti) implants depends on their ability to osseointegrate with the surrounding bone and this, in turn, is greatly dependent on the surface characteristics of the device. Advancements in surface analysis and surface modification techniques have improved the biological performance of metallic implants by mimicking the hierarchical structure of bone associated with regular bone remodeling. In this process, damaged bone is resorbed by osteoclasts, which produce resorption lacunae containing high microroughness generated after mineral dissolution under the ruffled border, as well as superimposed nanoscale features created by the collagen fibers left at the surface. Indeed, increasing Ti surface roughness at the micro and sub-microscale level has been shown to increase osteoblast differentiation *in vitro*, increase bone-to-implant contact *in vivo*, and accelerate healing times clinically. Recently, the clinical application of surface nanomodification of implants has been evaluated. Still, most clinically-available devices remain smooth at the nanoscale and fundamental questions remain to be elucidated about the effect of nanoroughness on the initial response of osteoblast lineage cells.

Another property that could be used to control osteoblast development and the process of osseointegration is the electrical surface charge of implants. The presence of endogenous electrical signals in bone has been implicated in the processes of bone remodeling and repair. The existence of these native signals has prompted the use of external electrical stimulation to enhance bone growth in cases of fractures with delayed

union or nonunion, with several *in vitro* and *in vivo* reports confirming its beneficial effects on bone formation. However, the use of electrical stimulation on Ti implants to enhance osseointegration is less understood, in part because of the lack of *in vitro* models that truly represent the *in vivo* environment. In addition, an aspect that has not been thoroughly examined is the electrical implication of implant corrosion and its effect on the surrounding tissue. Implants are exposed to extreme conditions in the body such as high pH during inflammation, and cyclic loads. These circumstances may lead to corrosion events that generate large electrochemical currents and potentials, and may cause abnormal cell and tissue responses that could be partly responsible for complications such as aseptic loosening of implants.

Consequently, Ti implants with tailored surface characteristics such as nanotopography and electrical polarization, could promote bone healing and osseointegration to ensure successful outcomes for patients by mimicking the biological environment of bone without the use of systemic drugs. The **objective** of this thesis is to understand how surface nanostructural and electrical characteristics of Ti and Ti alloy surfaces may affect osteoblast lineage cell response *in vitro* for normal tissue regeneration and repair. Our **central hypothesis** is that combined micro/nanostructured surfaces, as well as direct stimulation of Ti surfaces with fixed direct current (DC) potentials, can enhance osteoblast differentiation.

CHAPTER 1. SPECIFIC AIMS

Dental and orthopaedic implants are currently the solutions of choice for teeth and joint replacements with success rates continually improving, but they still have undesirable failure rates in patients who are compromised by disease or age, and who in many cases are the ones most in need [1, 2]. The success of titanium (Ti) implants depends on their ability to osseointegrate with the surrounding bone and this, in turn, is greatly dependent on the surface characteristics of the device. Advancements in surface analysis and surface modification techniques have improved the biological performance of metallic implants by mimicking the hierarchical structure of bone associated with regular bone remodeling [3, 4]. In this process, damaged bone is resorbed by osteoclasts, which produce resorption lacunae containing high microroughness generated after mineral dissolution under the ruffled border [5], as well as superimposed nanoscale features created by the collagen fibers left at the surface [6]. Indeed, increasing Ti surface roughness at the micro and sub-microscale level has been shown to increase osteoblast differentiation *in vitro* [7, 8], increase bone-to-implant contact *in vivo* [9, 10] and accelerate healing times clinically [11, 12]. Recently, the clinical application of surface nanomodification of implants has been evaluated [13, 14]. Still, most clinically available devices remain smooth at the nanoscale and fundamental questions remains to be elucidated about the effect of nanoroughness on the initial response of osteoblast lineage cells.

Another property that could be used to control osteoblast development and the process of osseointegration is the electrical surface charge of implants. The presence of endogenous electrical signals in bone has been implicated in the processes of bone remodeling and repair [15, 16]. The existence of these native signals has prompted the

use of external electrical stimulation to enhance bone growth in cases of fractures with delayed union or nonunion, with several *in vitro* and *in vivo* reports confirming its beneficial effects on bone formation [17-19]. However, the use of electrical stimulation on Ti implants to enhance osseointegration is less understood, in part because of the lack of *in vitro* models that truly represent the *in vivo* environment. In addition, an aspect that has not been thoroughly examined is the electrical implication of implant corrosion and its effect on the surrounding tissue. Implants are exposed to extreme conditions in the body such as high pH during inflammation, and cyclic loads [20, 21]. These circumstances may lead to corrosion events that generate large electrochemical currents and potentials, and may cause abnormal cell and tissue responses that could be partly responsible for complications such as aseptic loosening of implants [22].

Consequently, tailoring the surface characteristics of Ti implants, such as surface nanostructure and electrical polarization, could promote bone healing and osseointegration to ensure a successful outcome for the patient by mimicking the biological environment of bone without the use of systemic drugs. **The objective of this thesis is to understand how surface nanostructural and electrical characteristics of titanium surfaces may affect osteoblast lineage cell response and normal tissue regeneration and repair.**

Our central hypothesis is that combined micro/nanostructured surfaces, as well as electrical stimulation with fixed direct current (DC) potentials, can enhance the osteoblastic differentiation of osteoblast lineage cells. We have formulated this hypothesis based on the essential role of the hierarchical surface structure left by osteoclasts after bone resorption (*i.e.*, microscale resorption pits, sub-microscale collagen tufts, nanoscale collagen fibers and other molecules) for subsequent bone formation by osteoblasts, and our preliminary results demonstrating significant

enhancements in osteoblast response to nanostructures. The presence and vital importance of endogenous electric fields for normal development of tissues in embryos and adult animals, as well as the negative effects of abnormal electrochemical products from corrosion events serve as additional support of our hypothesis. The *rationale* for this work is that mimicking all hierarchical roughness scales of bone may enhance osteoblast differentiation, and this effect may be further evaluated by challenging cells grown on these surfaces with different electrical potentials. The overall objective will be accomplished by testing our central hypothesis in the following *specific aims*.

1.1. Specific Aim 1

To evaluate the effect of combined microroughened and nanostructured surfaces on osteoblast lineage cell responses.

The *working hypothesis* is that nanostructures superimposed on both microsmooth and microrough Ti surfaces can enhance osteoblast differentiation. A simple and efficient oxidation treatment that uses flowing synthetic air at high temperatures will be applied to microsmooth and microrough commercially pure (cp) Ti and Ti6Al4V specimens for different durations. Several surface analysis techniques will be used to thoroughly characterize each surface and find similarities and differences that may help explain the results of subsequent cell studies with human osteoblast-like MG63 cells, human primary osteoblasts (hOBs), and human mesenchymal stem cells (MSCs). The surfaces will be assayed for cell number and DNA content, as a measure of cell proliferation. Additionally, early and late cell differentiation markers, alkaline phosphatase specific activity and osteocalcin, respectively, as well as the local factors osteoprotegerin, and vascular endothelial growth factor (VEGF) will be measured. The

combined micro/nanostructured surfaces are expected to provide a synergistic enhancement in osteoblastic differentiation and local factor production.

1.2. Specific Aim 2

To determine the effect of fixed DC electric potentials on osteoblast lineage cell response.

The *working hypothesis* is that fixed DC electric potentials applied directly to Ti substrates affect osteoblast differentiation, measured the production of the late differentiation marker osteocalcin, when compared to non-stimulated surfaces. Tissue culture plates that can supply DC stimulation are not commercially available, so we will design custom-made polycarbonate 24-well plates adapted for direct stimulation of the Ti surfaces used to culture the cells. Electrical connections will be established directly underneath the Ti specimens using a metallic screw and a series of springs, and electrical stimulation will be provided with DC power supplies. A range of fixed voltages will be evaluated to identify optimal conditions for enhanced differentiation marker production on MG63s.

The proposed research is *innovative* because it focuses on the development of clinically relevant nanomodification method. Additionally, the development of a new *in vitro* system for the assessment of fixed DC potentials will provide insights into the mechanism of action of electrical signals on cell response. This work is fundamentally different from current surface nano-modification techniques in that it can superimpose nanostructures on existing Ti surfaces of complex designs, without greatly affecting their microroughness. This is a key consideration because of the inability of existing nanomodification techniques to maintain the original surface properties of the device being modified, and because preliminary results show that the combination of

micro/nanostructured surfaces can cause synergistic effects in the maturation of osteoblasts.

This work is expected to yield the following outcomes. First, we will develop a simple, clinically-relevant nanomodification process that does not affect the starting surface roughness of the specimens. This result is critical to decouple the benefits of surface nanoroughness from the well-known effects of surface microroughness on cell behavior and differentiation. Second, we will design a DC electrical stimulation assay using standard tissue culture conditions to evaluate the response of osteoblasts to a wide range of fixed DC potentials. This information will be essential to evaluate the positive and negative effects of electric potentials on cell response and differentiation *in vitro*. Collectively, these studies will provide additional tools for biomimetic approaches of materials engineering, which may have an immediate impact in clinical applications by providing better designs that more closely resemble natural biological environments, in contrast to current techniques that fail to consider key aspects of *in vivo* conditions.

1.3. References

1. Fransson C, Wennstrom J, Berglundh T. Clinical characteristics at implants with a history of progressive bone loss. Clin Oral Implants Res 2008;19(2):142-147.
2. Granstrom G. Osseointegration in irradiated cancer patients: An analysis with respect to implant failures. J Oral Maxillofac Surg 2005;63(5):579-585.
3. Rho JY, Kuhn-Spearing L, Zioupos P. Mechanical properties and the hierarchical structure of bone. Med Eng Phys 1998;20(2):92-102.
4. Kubo K, Tsukimura N, Iwasa F, Ueno T, Saruwatari L, Aita H, et al. Cellular behavior on TiO₂ nanonodular structures in a micro-to-nanoscale hierarchy model. Biomaterials 2009;30(29):5319-5329.
5. Geblinger D, Addadi L, Geiger B. Nano-topography sensing by osteoclasts. J Cell Sci 2010;123(9):1503-1510.
6. Mulari MTK, Qu Q, Harkonen PL, Vaananen HK. Osteoblast-like cells complete osteoclastic bone resorption and form new mineralized bone matrix in vitro. Calcif Tissue Int 2004;75(3):253-261.
7. Kieswetter K, Schwartz Z, Hummert TW, Cochran DL, Simpson J, Dean DD, et al. Surface roughness modulates the local production of growth factors and cytokines by osteoblast-like MG-63 cells. J Biomed Mater Res 1996;32(1):55-63.

8. Raines AL, Olivares-Navarrete R, Wieland M, Cochran DL, Schwartz Z, Boyan BD. Regulation of angiogenesis during osseointegration by titanium surface microstructure and energy. *Biomaterials* 2010;31(18):4909-4917.
9. Buser D, Schenk RK, Steinemann S, Fiorellini JP, Fox CH, Stich H. Influence of surface characteristics on bone integration of titanium implants - A histomorphometric study in miniature pigs. *J Biomed Mater Res* 1991;25(7):889-902.
10. Cochran DL, Schenk RK, Lussi A, Higginbottom FL, Buser D. Bone response to unloaded and loaded titanium implants with a sandblasted and acid-etched surface: A histometric study in the canine mandible. *J Biomed Mater Res* 1998;40(1):1-11.
11. Cochran DL. A comparison of endosseous dental implant surfaces. *J Periodontol* 1999;70(12):1523-1539.
12. Cochran DL, Buser D, ten Bruggenkate CM, Weingart D, Taylor TM, Bernard JP, et al. The use of reduced healing times on ITI (R) implants with a sandblasted and acid-etched (SLA) surface: Early results from clinical trials on ITI (R) SLA implants. *Clin Oral Implants Res* 2002;13(2):144-153.
13. Tsukimura N, Ueno T, Iwasa F, Minamikawa H, Sugita Y, Ishizaki K, et al. Bone integration capability of alkali- and heat-treated nanobimorphic Ti-15Mo-5Zr-3Al. *Acta Biomater* 2011;7(12):4267-4277.
14. Jimbo R, Xue Y, Hayashi M, Schwartz HO, Andersson M, Mustafa K, et al. Genetic Responses to Nanostructured Calcium-phosphate-coated Implants. *J Dent Res* 2011;90(12):1422-1427.
15. Lokietek W, Pawluk RJ, Bassett CAL. Muscle injury potentials - source of voltage in undeformed rabbit tibia. *J Bone Jt Surg (Br)* 1974;B 56(2):361-369.
16. Guzelsu N, Demiray H. Electro-mechanical properties and related models of bone tissues - review. *Int J Eng Sci* 1979;17(7):813-851.
17. Becker RO, Spadaro JA, Marino AA. Clinical experiences with low intensity direct-current stimulation of bone-growth. *Clin Orthop* 1977;124:75-83.
18. Brighton CT, Wang W, Seldes R, Zhang GH, Pollack SR. Signal transduction in electrically stimulated bone cells. *J Bone Jt Surg (Am)* 2001;83A(10):1514-1523.
19. Song JK, Cho TH, Pan H, Song YM, Kim IS, Lee TH, et al. An Electronic Device for Accelerating Bone Formation in Tissues Surrounding a Dental Implant. *Bioelectromagnetics* 2009;30(5):374-384.
20. Lewis AC, Kilburn MR, Papageorgiou I, Allen GC, Case CP. Effect of synovial fluid, phosphate-buffered saline solution, and water on the dissolution and corrosion properties of CoCrMo alloys as used in orthopedic implants. *J Biomed Mater Res A* 2005;73A(4):456-467.
21. Papakyriacou M, Mayer H, Pypen C, Plenk H, Stanzl-Tschegg S. Effects of surface treatments on high cycle corrosion fatigue of metallic implant materials. *Int J Fatigue* 2000;22(10):873-886.
22. Gilbert JL, Zarka L, Chang EB, Thomas CH. The reduction half cell in biomaterials corrosion: Oxygen diffusion profiles near and cell response to polarized titanium surfaces. *J Biomed Mater Res* 1998;42(2):321-330.

**PART I: EVALUATION OF MICROROUGHENED AND NANOSTRUCTURED
SURFACES ON OSTEOLAST LINEAGE CELL RESPONSES**

CHAPTER 2. BACKGROUND ON IMPLANT OSSEOINTEGRATION AND THE ROLE OF NANOSTRUCTURES

In [Gittens RA, Olivares-Navarrete R, Schwartz Z, Boyan BD. Spine fusion: implant osseointegration and the role of nanostructures. Spine J 2012;(In Preparation).]

2.1. Introduction

Musculoskeletal diseases, such as back pain, arthritis and bone fractures, have been recognized as the most reported health conditions in the United States (US), amounting to almost 8% of the US gross domestic product in lost wages and healthcare related costs [1]. In the case of chronic back pain, spinal fusions have become a viable treatment of choice to eliminate pain and restore a patient's quality of life [2-4]. Autologous bone grafts are the gold standard filler for orthopaedic surgeries because of their osteogenic capabilities, but increased complications and morbidity of the donor site have shifted the focus to graft substitutes and spinal implant devices [5, 6]. With an aging population in the US, there is a pressing need for surgical approaches that can capitalize on the intrinsic regenerative capacity of mineralized tissues to provide a more permanent treatment.

The modern use of metallic and polymeric implants for orthopaedic and dental applications has been evolving for the last 60 years, with major advances coming from the dental implant field [7-10]. Originally, endosseous implants were expected to function through a mechanical anchorage with bone. Early efforts had relatively high failure rates, in part due to a layer of fibrous connective tissue that grows between the bone and the implant [11] (Figure 2.1). The formation of the fibrous capsule, thought to be an inevitable consequence of the implantation procedure [12, 13], can start a vicious cycle of micromotion and inflammation around the implant that eventually leads to osteolysis and implant failure [14-16]. However, to achieve long-lasting and successful outcomes, strong and direct interaction between bone and the implant surface is required [7, 17].

Such direct contact between bone and the implant surface defines osseointegration and, nowadays, is the goal of a successful bone implantation procedure.

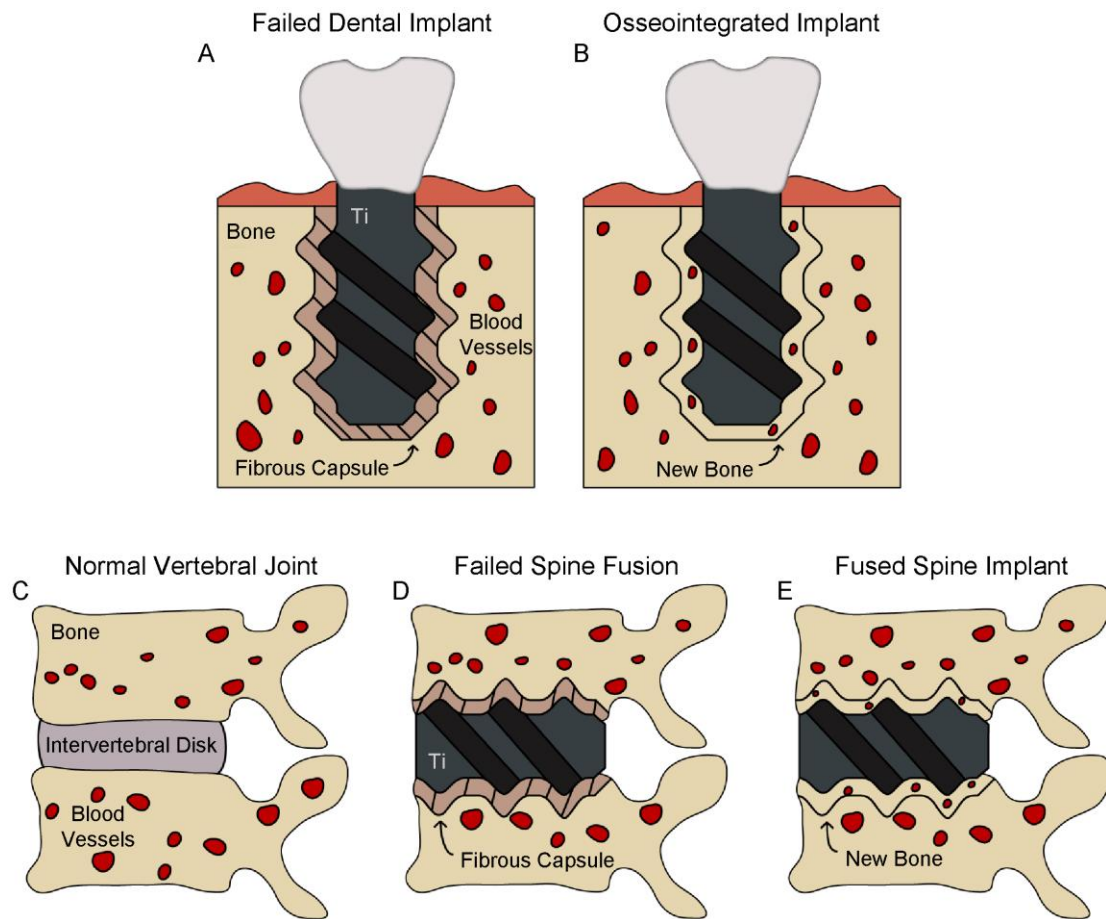


Figure 2.1 Schematics of failed or osseointegrated (A-B) dental and (C-E) spine implants.

In the orthopaedic implant field, several reports have found such fibrous capsules around implants of metallic [18, 19] or polymeric nature [20-22]. This type of failure is commonly attributed to toxic wear debris phagocytosed by macrophages and other cells of the surrounding tissue [23-25]. However, several cases that involve fibrous encapsulation of implants do not present detectable traces of wear debris [26, 27] and still elicit an aseptic inflammatory response that can lead to osteolysis [14]. Most of these cases are associated to implants made from polymers, due to their low bioactivity, or to metallic implants with smooth surfaces. Yet, from experiences in the dental field, it is now well accepted that the presence of a fibrous layer can be avoided by controlling the surface properties of the implant, such as increasing surface roughness, to promote bone apposition directly onto the implant surface [28-31].

The process of osseointegration involves a complex chain of events, from protein adsorption and blood clotting at the implant surface to site infiltration and biological recognition of the surface by mesenchymal stem cells and osteoblasts, finally leading to bone deposition and mineralization by these cells at the interface, thus creating an intimate bond between the bone and implant [30, 32]. All these events are directly and indirectly affected by the surface properties of the device, making these properties the key determinants of the implant's outcome *in vitro*, *in vivo* and clinically [33-35] (Figure 2.2).

This section will cover some of the key biological processes that occur around an implant focusing on the role of surface properties, specifically surface structure, on osseointegration. Other factors that may also have a major impact on the final outcome of the implant, such as surgical technique, patient's record and implant shape have been previously reviewed [36-38].

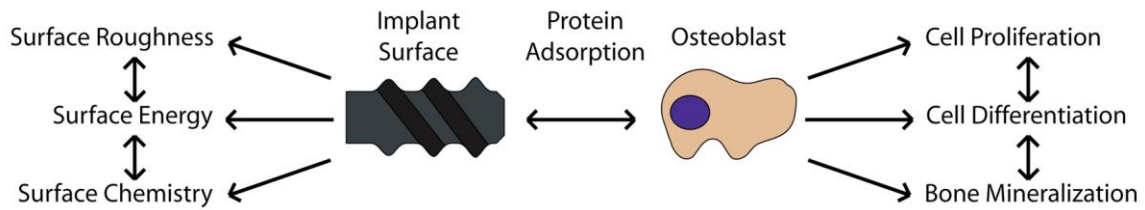


Figure 2.2 Diagram showing the direct and indirect interactions between surface properties and biological events.

2.2. Osseointegration: Key Biological Processes

2.2.1. Wound Healing and Fibrin Clot Formation

The process of osseointegration involves several biological events that determine the mechanical stability, and final outcome of the implant. One of the first events to occur when an implant is placed in the body is the adsorption of water molecules, proteins and lipids from the blood to the surface of the device [39, 40]. The specific protein profile presented on the surface will depend on the surface characteristics of the implant. Many proteins present in blood may interact with the implant's surface, some of which are associated with the host inflammatory response, such as fibrinogen and complement molecules, as well as other proteins involved in cell attachment, such as fibronectin and vitronectin [40-42]. The attachment of blood platelets, and the subsequent release of their inner contents, promotes the formation of fibrin clots that serve as an immature meshwork to fill void spaces and facilitate cell migration towards the surface of the implant [43] (Figure 2.3). The surface coverage and strength of attachment of the fibrin clots to the surface of an implant will depend on its surface properties [44, 45]. One hypothesis is that increasing surface roughness enhances the strength of fibrin clot attachment, which is important because cells moving along the fibrin clot pull on these

fibers to promote wound contraction [46]. Other reports suggest that increasing surface roughness supports higher amounts of fibrin clot extension on the surface, promoting a better wound healing response [44].

Some of the first cells to arrive to the implantation site include neutrophils and macrophages that clean the wound site from possible pathogens and necrotic tissue [47, 48]. Other important cell types to colonize the implantation site include mesenchymal stem cells (MSCs) coming from blood and bone marrow [45, 49]. These cells have the motility and enzymatic activity to travel through dense fibrin clots on their way to the surface of the implant [50], where they will be exposed to inflammatory cytokines and growth factors conducive to wound healing and tissue regeneration [51] (Figure 2.3). MSCs have the potential to differentiate into several cell types, such as osteoblasts, chondrocytes and fibroblasts, depending on the biological environment and the implant surface properties [51, 52]. However, the fate of stem cells around osseous implants seems to be biased towards the formation of bone tissue, with some soft tissue being formed at the interface between bone and the implant depending on the latter's surface properties. Thus, by the time MSCs reach the surface of the implant, they might have already set in motion the differentiation machinery necessary to become pre-osteoblasts and to start forming bone.

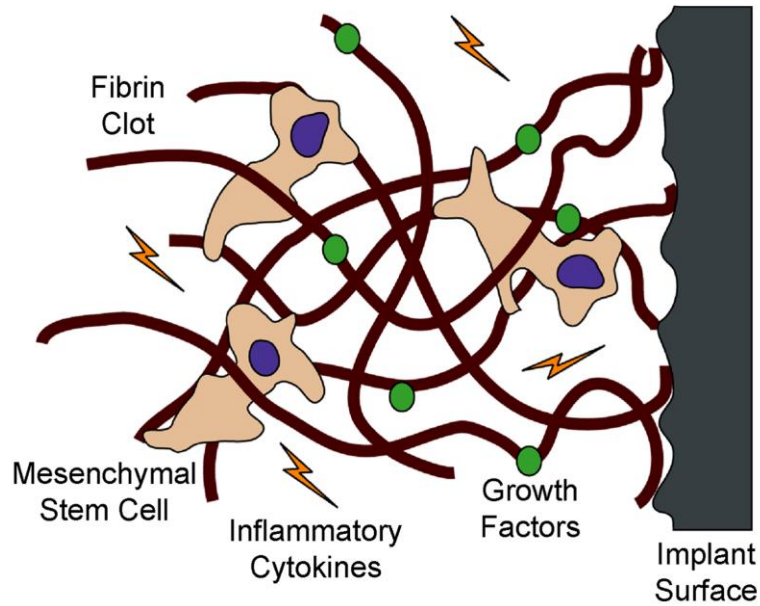


Figure 2.3. Schematic depicting fibrin clot adhesion to a rough surface and mesenchymal stem cell (MSC) migration through the clot. The MSCs pull on the fibrin clot to reach the surface of the implant, and at the same time are exposed to several inflammatory cytokines and growth factors that can influence their differentiation state.

2.2.2. Mimicking Bone Structure: Bone Remodeling

Once the implant has been stably fixed in the bone and the fibrin meshwork firmly established, bone can form on two different fronts: on the surface of the bone surrounding the implant (distance osteogenesis) and directly on the surface of the implant (contact osteogenesis) [46]. Depending on the surface properties, the differentiating osteoblasts reaching any of these two fronts will have to choose between a few options, such as to proliferate for a few cycles or to start laying down a non-collagenous assortment of proteins that initiates mineralization called lamina limitans, or “cement line” [53-55]. The cement line, rich in proteins like osteopontin, bone sialoprotein and proteoglycans [32, 56, 57], further promotes osteoblast recruitment to

the surface and maturation. For successful osseointegration, contact osteogenesis is required and should be promoted by the implant.

The bone remodeling cycle is completed when osteoclasts resorb previously formed bone to resolve microcracks and wear and tear, and prime the surface for new bone formation [58, 59]. Bone resorption by osteoclasts leaves large pits, or resorption lacunae, covered with small tufts of proteins on the surface that give bone a high degree of structural complexity. Osteoclasts acidify the mineralized matrix just underneath their ruffled membranes to dissolve calcium phosphate crystals and create microscale resorption lacunae that are 30 to 100 μm in diameter [60, 61]. Osteoclasts, however, do not produce collagenase, an enzyme required to degrade collagen [58]. Thus, resorption lacunae have various sub-micro and nanoscale features created by the collagen tufts and fibers left by osteoclasts. This nanotopography, with its inherent biochemical information, could be the signal that osteoblasts require when looking for a surface that requires new bone formation. The concept of mimicking the hierarchical structure of bone on implant surfaces by including nanostructures on commercially available devices originates from this observation (Figure 2.4).

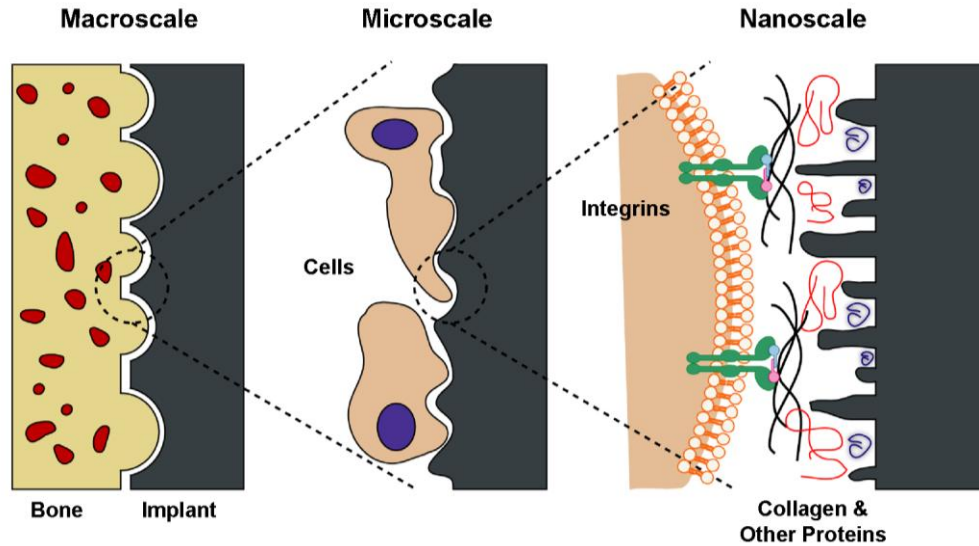


Figure 2.4. Interactions between bone and the implant surface at different length-scales. At the macroscale, the implant should provide good mechanical fixation with bone. Microscale features presented on the surface, of similar size than osteoblasts and mesenchymal stem cells, can physically constrain cell morphology. At the nanoscale, cell membrane receptors, such as integrins, can recognize proteins adsorbed on the surface, which in turn are modulated by the nanostructures on the surface.

If the surface properties of the implant are not selected appropriately, the invading cells can form a layer of fibrous tissue between the implant and the bone that jeopardizes the outcome of the procedure. The lack of bone attachment to such an implant generates a vicious cycle that starts with micromotion and inflammation, and ends up with thickening of the fibrous layer, degradation of the surrounding bone and loosening of the implanted device [14, 26, 27]. Interestingly, tailoring the surface properties of implants can help avoid these failed outcomes.

2.3. Osseointegration and Implant Surface Structure

Although certain patient conditions such as age, bone quality and smoking, can jeopardize the success of the implantation surgery [38], the goal is to design implants in such a way as to minimize the effect of patient variables and improve the success rate. Much attention is usually paid to the shape of an implant to acquire good primary fixation, or to the chemical composition of the implant to ensure the mechanical properties required for the application. Indeed, these macroscale aspects are important, but surface characteristics at the micro, sub-micro, and nanoscale should be addressed at the same time to ensure successful and long-term osseointegration. A loose definition of micro, sub-micro, and nano applies to features having at least one of their dimensions (*i.e.*, height, length, width) smaller than 100 μm , 1 μm or 100 nm, respectively. More stringent evaluations apply the aforementioned thresholds to all dimensions of the feature. Notably, such small surface structures are invisible to the naked eye and require specialized equipment to quantify them, such as electron microscopy [62], laser confocal microscopy [63] or atomic force microscopy [64].

In the dental and orthopaedic fields, implants are commonly made out of metals, with titanium and its alloys being widely used for dental implant applications due to their suitable weight-to-strength ratio and good biological performance. Interestingly, the surface chemistry of an implant can be quite different than its bulk chemistry. Titanium spontaneously forms a thin oxide layer that inhibits further corrosion of the implant. This oxide layer has been suggested as the reason behind titanium's good biological performance by mimicking the ceramic properties of hydroxyapatite in bone [28]. However, the topography of the surface, regardless of the chemistry, still requires attention to enhance the process of osseointegration.

In the case of spinal implants, PEEK has become a popular bulk material for spinal cage manufacturing due to its mechanical properties, which can be tailored to resemble those of bone, and its low radio-opacity when compared to metals [20]. Although attractive, these properties are not required for successful osseointegration. Furthermore, PEEK's low bioactivity with bone promotes the formation of a fibrous layer between bone and the implant [21, 22] that can also be tackled through surface modifications, such as coating the PEEK surface with titanium [65-67].

Reports on surface modification of PEEK are not as readily available in the literature or are still proprietary. In addition, recent efforts have focused on coating PEEK surfaces with bioactive metals [67], thus most of the following evaluation will focus on the vast literature related to surface modification of titanium implants. Our approach will be to describe reports that provide evidence of the favorable effects of surface topography *in vivo*, and then try to explain some of these results through findings *in vitro*.

2.3.1. Microroughness Effect *In Vivo*

Most commercially-available implants in the dental field contain some type of surface modification to increase their surface roughness. This is in part due to the large number of studies showing beneficial results of microroughness *in vitro*, *in vivo* and clinically [10, 29, 34]. Several surface modification techniques exist to increase microroughness such as acid etching, sand blasting, heat treatments, anodic oxidation, as well as the combination of any of these treatments (Figure 2.5). The surface topography created by these different microstructuring treatments will vary greatly and, although seldom compared among each other, they commonly enhance the process of osseointegration when compared to relatively smooth surfaces.

In one study, machined, relatively smooth pedicle screws were compared to grit-blasted, microrough screws, both made out of titanium alloy (Ti6Al4V), in a sheep spine

model after 12 weeks of healing [68]. Implant osseointegration was assessed by micro-CT and histomorphometry. The results from micro-CT showed that both machined and grit-blasted implants were surrounded by bone. However, the resolution of the micro-CT was not sufficient for detailed judgment of the bone-implant interface. Through histomorphometrical analysis, the authors found higher incidence of soft tissue between bone and the machined surface when compared to the grit-blasted surface, and this observation was correlated to a higher bone-to-implant contact percentage for grit-blasted implants ($73.5 \pm 28.5 \%$) versus machined ones ($59.6 \pm 25.8 \%$).

Similar results are abundant in the literature and show enhanced osseointegration on microrough surfaces with very different topography, from simple uniform micropatterns [69] to more complex restructured surfaces [70], compared to machined surfaces as measured by bone-to-implant contact and mechanical testing [71, 72]. However, the type (e.g., sharp peaks, grooves, pores) and degree of microroughness (*i.e.*, as quantified by surface roughness measurements) can affect the early healing and long-term success of the implant [73, 74].

In another study, acid etched titanium surfaces were compared to sand-blasted and acid-etched surfaces in a pig maxilla model after 10 weeks of healing [75]. Both treatments increased surface microroughness, but sand-blasted and acid-etched surfaces had a considerably higher roughness average ($R_a = 1.53 \pm 0.11 \mu\text{m}$) than just acid etched surfaces ($R_a = 0.90 \pm 0.11 \mu\text{m}$). The authors reported that both surfaces had the ability to interlock with bone, but the removal torque force on the sand-blasted and acid-etched implant was significantly higher ($157.29 \pm 38.04 \text{ N}$) than on the acid-etched implants ($105.33 \pm 25.12 \text{ N}$).

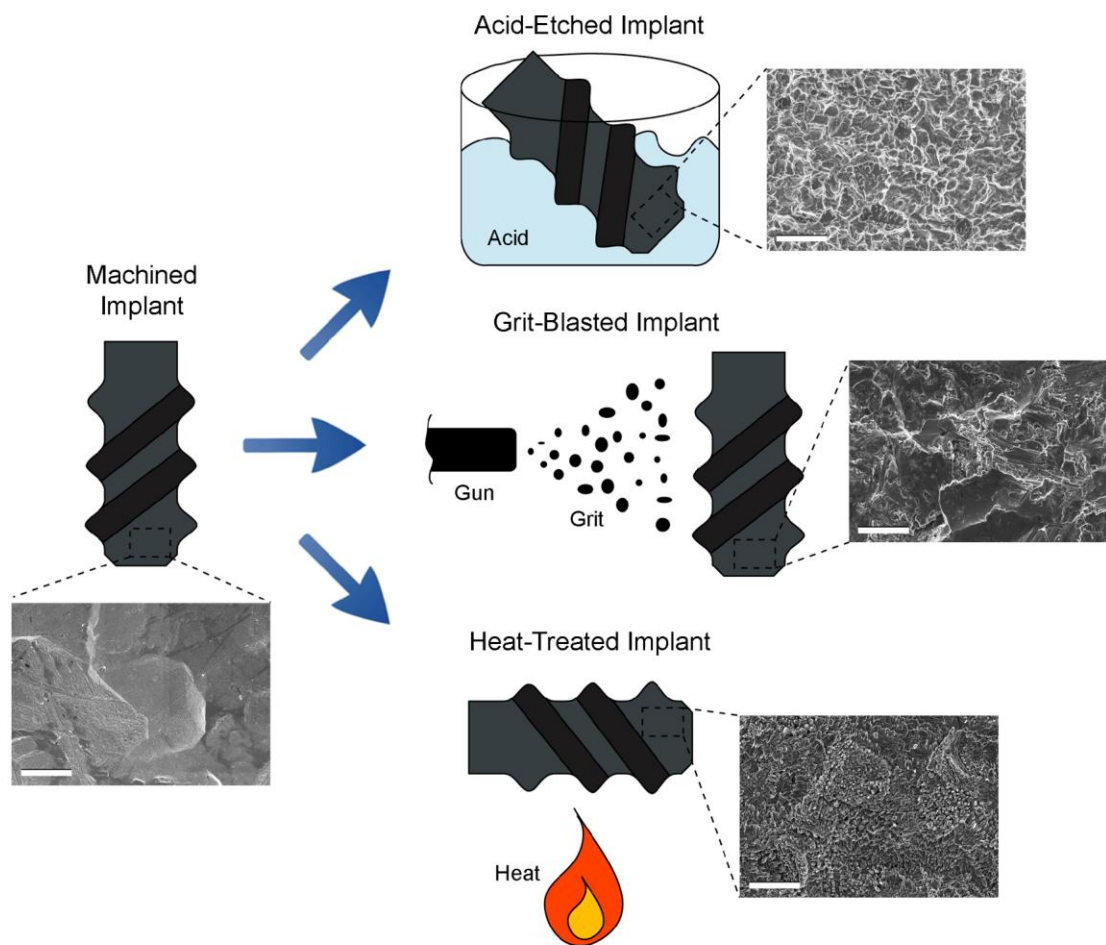


Figure 2.5. Schematic and SEM images of various surface modifications. Modifications applied to machined implants include acid etching, grit blasting and heat treatment. SEM scale bar = 3 μm .

2.3.2. Microroughness Effect *In Vitro*

The favorable response elicited by microrough implants at the *in vivo* level has been attributed to the activation of several important signaling pathways in osteoblasts and mesenchymal stem cells *in vitro*. Once these cells come in contact with a surface, either an osteoclast-primed bone surface or an implant surface, they go through a progression of well-defined phases including proliferation, differentiation and, in some cases, apoptosis. These phases are transcriptionally regulated, meaning that mRNA and protein profiles during each phase are specific and, thus, one cell cannot be simultaneously going through two of these phases [76]. The duration of each phase may be determined by the surface properties of the device.

A key observation *in vitro* has been that osteoblasts and MSCs after 5 to 7 days of culture on microrough surfaces *in vitro* have lower cell numbers and higher levels of differentiation markers, such as alkaline phosphatase and osteocalcin among others, when compared to relatively smooth surfaces [68, 77, 78]. Alkaline phosphatase is an enzyme produced early during osteoblast differentiation and is important for the onset of mineralization; while osteocalcin is a late differentiation marker produced at high levels during the mature state of the osteoblast [79, 80]. The decrease in cell number and increase in differentiation markers agree with the normal progression of osteoblast phenotype, indicating that cells growing on the microrough surfaces exit the proliferation phase earlier to start differentiating and producing the proteins necessary for bone formation.

Osteoblasts do not interact directly with the surface of the implant but can sense the changes in surface properties by identifying the layer of adsorbed proteins from the surrounding environment using cell membrane receptors, such as integrins [81, 82]. Integrins are transmembrane, heterodimeric receptors composed of α and β subunits

that can bind motifs of specific proteins in the extracellular matrix and start signaling cascades within the cell [82]. Microroughness has been shown to influence the expression of integrins, promoting those subunits associated with bone proteins (*i.e.*, α_2 , β_1), but not those subunits associated with soft tissue proteins (*i.e.*, α_5 , α_v) [83]. Thus, microroughness can affect the progression of the osteoblast phenotype by upregulating integrins such as $\alpha_2\beta_1$, which directly regulates osteoblast differentiation and local factor production [83].

Additionally, healthy bone growth and regeneration requires a healthy vasculature that develops in intimate association with osteoblasts to supply oxygen, nutrients and other factors that can enhance bone formation [84, 85]. In turn, osteoblasts can promote the formation of blood vessels through secretion of angiogenic factors, such as vascular endothelial growth factor (VEGF) and fibroblast growth factor 2 (FGF-2), which can be enhanced by an increase in surface microroughness [86]. At the same time, other important factors secreted by osteoblasts during implant osseointegration that can be enhanced by adjusting surface microroughness include BMPs [87], which are a group of proteins that have a direct role in skeletal development, and Wnts [88], whose signaling is required for embryonic bone development.

Unfortunately, even with an increase in surface microroughness, implant failure still occurs in challenging cases such as those with patients compromised by disease or age. Thus, other key characteristics such as surface energy and surface nanotopography may be manipulated and when combined with surface microroughness can synergistically promote bone formation in direct contact with the implant, especially in cases of patients with compromised bone [29, 89].

2.3.3. Role of Nanostructures *In Vivo*

In recent years, a few studies have been published that report the beneficial effects of adding nanostructures to implants *in vivo* [90-92]. However, most surface nanostructural modifications introduce changes to other implant characteristics, such as surface chemistry and surface energy, thus complicating the evaluation of the influence of these nanostructures on cell response [93, 94]. Regardless, we will focus on the outcomes of reports suggesting that nanostructures can be attractive features to incorporate into clinical implants, highlighting these limitations when necessary.

Machined, relatively smooth titanium surfaces have been compared to nanostructured surfaces in a rat tibial model for up to 56 days [91]. The nanomodification process used for this study involved depositing oxide nanoparticles on the surface of the implant through a sol-gel technique without affecting the overall microroughness. The oxide nanoparticles used for the coating included different crystalline phases of TiO₂ (*i.e.*, anatase, rutile), as well as zirconia (ZrO₂), introducing changes to either crystal structure or chemistry, respectively, when compared to the machined control. No differences were found between the nanostructured implants compared to the machined control when evaluating removal torque forces up to 56 days after implantation. However, the bone-to-implant contact for all nanomodified implants was higher than the machined control. These results were correlated to quantitative polymerase chain reaction (qPCR) data that showed higher mRNA levels of osteogenic differentiation markers, such as osteocalcin and osteopontin, in the bone surrounding the nanostructured implants.

Nanomodified implants have also been compared to microrough implants as a positive control. Nanomodified coin-shaped implants were assessed against grit-blasted implants in a rabbit tibial model after 4 weeks [90]. Electrochemical anodization in

hydrofluoric acid (HF) and annealing (550 °C) was used to create well-defined, anatase nanotubes on the surface of the test implants. The nanomodification altered the crystal structure, as reported, and possibly the surface chemistry by incorporating F traces from the anodization treatment, but the latter was not evaluated. Biomechanical testing revealed that the pull-out force for nanotube implants was 9-fold higher (10.8 ± 3.1 N) than for grit-blasted controls (1.2 ± 2.7 N), and these results were corroborated by histological sections that showed increased bone-to-implant contact percentage on nanotube surfaces (78.3 ± 33.3 %) when compared to controls (21.7 ± 24.7 %). Chemical mapping of the pulled-out surfaces by energy dispersive x-ray (EDX) spectroscopy also provided confirmation of higher percentages of calcium phosphate, as a marker of remnant bone, on the nanomodified surfaces (41.7 %) compared to grit-blasted controls (8.3 %).

The ultimate goal in implant design is to mimic bone hierarchical structure at all different length scales (*i.e.*, macro, micro and nano) and this has also been assessed by adding nanostructure to already microrough implants. The performance of sand-blasted Ti alloy (Ti-15Mo-5Zr-3Al) implants was compared to that of sandblasted and nanomodified implants in a rat femoral model for up to 8 weeks [92]. In this particular case, the nanomodification was termed nanobimorphic for the presence of what the authors called nanotrabeular and nanotuft-like structures on the surface, created by alkali (*i.e.*, NaOH) and heat (600 °C) treatments. The modification introduced surface chemical changes by increasing the oxygen content and the O/Ti ratio. Biomechanical evaluation found that push-in forces for the sand-blasted, alkali and heat-treated implants were significantly higher after 1, 2, 4 and 8 weeks when compared to sand-blasted-only implants. These results were also confirmed by greater CaP content and by

histomorphometrical analysis showing more bone-to-implant contact after 4 weeks of implantation, on the surface of the extracted nanomodified implants.

These different studies taken together support the concept of adding nanostructures to both microsmooth and microrough implants to improve the early healing and long-term osseointegration of implants for bone applications.

2.3.4. *In vitro* response to nanostructures

The phenomena seen *in vivo* of more bone-to-implant contact and higher forces during biomechanical testing on nanostructured implants have been attributed to enhanced activity at the cellular level by osteoblasts and mesenchymal stem cells. Although few studies have been published questioning the influence of nanostructures on cell behavior [95], many other reports have shown that osteoblasts are indeed sensitive to these small features and can respond strongly to them. Morphological evaluations of cells growing on nanomodified substrates compared to nanosmooth controls show more filopodia extensions and actin cytoskeletal alignment [96, 97], as well as enhanced cell adhesion [98]. This response can be associated with the fact that the spacing of adhesion sites on a surface can regulate integrin binding to the ECM, with a spacing of less than 54 nm promoting the formation of focal adhesion complexes important for cell signaling and recognition of the ECM [99].

Cell spreading and attachment assays by themselves, however, are not sufficient to establish the beneficial role of nanostructures. Studies looking at the differentiation state of osteoblasts growing on nanostructured surfaces have found higher mRNA production of osteoblast markers, such as osterix, alkaline phosphatase and osteocalcin [100]. The final protein levels of these markers have also been shown to increase on nanomodified surfaces when compared to nanosmooth surfaces, confirming the influence of nanostructures on osteoblast phenotype [101].

For clinical applications, the addition of nanostructures to microrough implants is the most attractive option for surface modifications to take advantage of the already demonstrated enhancements of microroughness and to couple them to the improvements generated by nanostructures. Yet, cellular response is rarely linear, thus requiring assessment of the effects of such a combination of microroughness and nanostructures at the cellular level. Indeed, reports show synergistic effects in terms of enhanced osteoblast interactions with the surface, as well as higher mRNA and protein production of markers for osteoblast differentiation on the combined microrough and nanostructured surfaces when compared to just microrough surfaces [102-105].

Osteoblasts have been consistently shown to respond to nanostructures by increasing production of differentiation markers and other local factors [105]. Mesenchymal stem cells (MSCs), usually isolated from bone marrow and treated with osteogenic media to drive them into osteoblastic differentiation, have also been assessed and confirmed to be sensitive to nanostructures [103]. In addition, MSCs have been shown to be sensitive to microstructures even when not exposed to osteogenic media or other inducible factors in the environment [52]. Interestingly, when MSCs are cultured without osteogenic media on nanostructured surfaces, their fate seems to depend on the order (or randomness) of the nanostructures being presented [106]. Namely, randomly displaced patterns of nanostructures, without the use of soluble factors, can direct MSCs to produce osteogenic markers to similar levels as those treated with osteogenic media on flat substrates. Furthermore, highly ordered patterns may prevent spontaneous MSC osteoblastic differentiation and promote the maintenance of MSC stemness. The concept of maintaining MSC stemness can be extensively exploited in the field of tissue regeneration and the manipulation of stem cells. However, these results also indicate that many questions remain to be answered

in the quest to incorporate nanostructures in clinical implants. The positive *in vivo* results can be considered a good first step to bring these surface modifications closer to the clinics, but not until long-term clinical studies are performed will the full implications of these different surface features on the performance of implants for bone applications be completely understood.

2.4. References

1. Jacobs JJ, Andersson GBJ, Bell JE, Weinstein SL, Dormans JP, Gnat SM, et al. United States Bone and Joint Decade: The burden of musculoskeletal diseases in the United States. 1st ed. Rosemont: AAOS; 2008.
2. Hanley EN. The indications for lumbar spinal fusion with and without instrumentation. *Spine* 1995;20(24):S143-S153.
3. Hacker RJ, Cauthen JC, Gilbert TJ, Griffith SL. A prospective randomized multicenter clinical evaluation of an anterior cervical fusion cage. *Spine* 2000;25(20):2646-2654.
4. Zdeblick TA, Phillips FM. Interbody cage devices. *Spine* 2003;28(15):S2-S7.
5. Agrawal CM, Attawia M, Borden MD, Boyan BD, Bruder SP, Bucholz RW, et al. Bone graft substitutes. 1st ed. West Conshohocken: ASTM International / AAOS; 2003.
6. Ray CD. Threaded fusion cages for lumbar interbody fusions - An economic comparison with 360 degrees fusions. *Spine* 1997;22(6):681-685.
7. Branemark PI, Hansson BO, Adell R, Breine U, Lindstrom J, Hallen O, et al. Osseointegrated implants in the treatment of the edentulous jaw. Experience from a 10-year period. *Scand J Plast Reconstr Surg Suppl* 1977;16:1-132.
8. Bobbio A. The first endosseous alloplastic implant in the history of man. *Bull Hist Dent* 1972;20(1):1-6.
9. Lang BR, Chiappa AA. Mandibular Implants - a New Method of Attachment. *J Prosthet Dent* 1969;22(2):261-267.
10. Sykaras N, Iacopino AM, Marker VA, Triplett RG, Woody RD. Implant materials, designs, and surface topographies: their effect on osseointegration. A literature review. *Int J Oral Maxillofac Implants* 2000;15(5):675-690.
11. Beck PM. Endosseous implants: a review of current advances and a case report. *Oral Health* 1970;60(4):19-21.
12. Southam JC, Selwyn P. Structural changes around screws used in the treatment of fractured human mandibles. *Br J Oral Surg* 1971;8(3):211-221.
13. Picton DC, Johns RB, Wills DJ, Davies WI. The relationship between the mechanisms of tooth and implant support. *Oral Sci Rev* 1974;5(0):3-22.
14. Athanasou NA, Quinn J, Bulstrode CJ. Resorption of bone by inflammatory cells derived from the joint capsule of hip arthroplasties. *J Bone Joint Surg Br* 1992;74(1):57-62.
15. Lassus J, Salo J, Jiranek WA, Santavirta S, Nevalainen J, Matucci-Cerinic M, et al. Macrophage activation results in bone resorption. *Clin Orthop Relat Res* 1998(352):7-15.

16. Szmukler-Moncler S, Salama H, Reingewirtz Y, Dubruille JH. Timing of loading and effect of micromotion on bone-dental implant interface: Review of experimental literature. *J Biomed Mater Res* 1998;43(2):192-203.
17. Cook HP. Immediate reconstruction of the mandible by metallic implant following resection for neoplasm. *Ann R Coll Surg Engl* 1968;42(4):233-259.
18. Thomas KA, Kay JF, Cook SD, Jarcho M. The Effect of Surface Macrotecture and Hydroxylapatite Coating on the Mechanical Strengths and Histologic Profiles of Titanium Implant Materials. *J Biomed Mater Res* 1987;21(12):1395-1414.
19. Hallab NJ, Cunningham BW, Jacobs JJ. Spinal implant debris-induced osteolysis. *Spine (Phila Pa 1976)* 2003;28(20):S125-138.
20. Kurtz SM, Devine JN. PEEK biomaterials in trauma, orthopedic, and spinal implants. *Biomaterials* 2007;28(32):4845-4869.
21. Santos ER, Goss DG, Morcom RK, Fraser RD. Radiologic assessment of interbody fusion using carbon fiber cages. *Spine (Phila Pa 1976)* 2003;28(10):997-1001.
22. Anjarwalla NK, Morcom RK, Fraser RD. Supplementary stabilization with anterior lumbar intervertebral fusion - A radiologic review. *Spine* 2006;31(11):1281-1287.
23. Cunningham BW, Orbegoso CM, Dmitriev AE, Hallab NJ, Seftor JC, Asdourian P, et al. The effect of spinal instrumentation particulate wear debris. an in vivo rabbit model and applied clinical study of retrieved instrumentation cases. *Spine J* 2003;3(1):19-32.
24. Lohmann CH, Schwartz Z, Koster G, Jahn U, Buchhorn GH, MacDougall MJ, et al. Phagocytosis of wear debris by osteoblasts affects differentiation and local factor production in a manner dependent on particle composition. *Biomaterials* 2000;21(6):551-561.
25. Pioletti DP, Takei H, Kwon SY, Wood D, Sung KLP. The cytotoxic effect of titanium particles phagocytosed by osteoblasts. *J Biomed Mater Res* 1999;46(3):399-407.
26. Maniopoulos C, Pilliar RM, Smith DC. Threaded versus porous-surfaced designs for implant stabilization in bone-endodontic implant model. *J Biomed Mater Res* 1986;20(9):1309-1333.
27. Piattelli A, Scarano A, Favero L, Iezzi G, Petrone G, Favero GA. Clinical and histologic aspects of dental implants removed due to mobility. *J Periodontol* 2003;74(3):385-390.
28. Sul YT, Johansson C, Wennerberg P, Cho LR, Chang BS, Albrektsson P. Optimum surface properties of oxidized implants for reinforcement of osseointegration: Surface chemistry, oxide thickness, porosity, roughness, and crystal structure. *Int J Oral Maxillofac Implants* 2005;20(3):349-359.
29. Schwarz F, Wieland M, Schwartz Z, Zhao G, Rupp F, Geis-Gerstorfer J, et al. Potential of chemically modified hydrophilic surface characteristics to support tissue integration of titanium dental implants. *J Biomed Mater Res B Appl Biomater* 2009;88B(2):544-557.
30. Puleo DA, Nanci A. Understanding and controlling the bone-implant interface. *Biomaterials* 1999;20(23-24):2311-2321.
31. Kokubo T, Kim HM, Kawashita M, Nakamura T. Bioactive metals: preparation and properties. *J Mater Sci Mater Med* 2004;15(2):99-107.
32. Davies JE. Bone bonding at natural and biomaterial surfaces. *Biomaterials* 2007;28(34):5058-5067.
33. Albrektsson T, Wennerberg A. Oral implant surfaces: Part 1--review focusing on topographic and chemical properties of different surfaces and in vivo responses to them. *Int J Prosthodont* 2004;17(5):536-543.

34. Wennerberg A, Albrektsson T. Effects of titanium surface topography on bone integration: a systematic review. *Clin Oral Implants Res* 2009;20:172-184.
35. Mendonca G, Mendonca DBS, Aragao FJL, Cooper LF. Advancing dental implant surface technology - From micron- to nanotopography. *Biomaterials* 2008;29(28):3822-3835.
36. Regan JJ, Yuan H, McAfee PC. Laparoscopic fusion of the lumbar spine: minimally invasive spine surgery. A prospective multicenter study evaluating open and laparoscopic lumbar fusion. *Spine (Phila Pa 1976)* 1999;24(4):402-411.
37. McAfee PC. Interbody fusion cages in reconstructive operations on the spine. *J Bone Joint Surg Am* 1999;81(6):859-880.
38. Baelum V, Ellegaard B. Implant survival in periodontally compromised patients. *J Periodontol* 2004;75(10):1404-1412.
39. Andrade JD, Hlady V. Protein adsorption and materials biocompatibility - A tutorial review and suggested hypotheses. *Adv Polym Sci* 1986;79:1-63.
40. Wilson CJ, Clegg RE, Leavesley DI, Percy MJ. Mediation of biomaterial-cell interactions by adsorbed proteins: A review. *Tissue Eng* 2005;11(1-2):1-18.
41. Jansson E, Tengvall P. In vitro preparation and ellipsometric characterization of thin blood plasma clot films on silicon. *Biomaterials* 2001;22(13):1803-1808.
42. Keselowsky BG, Collard DM, Garcia AJ. Surface chemistry modulates fibronectin conformation and directs integrin binding and specificity to control cell adhesion. *Journal of Biomedical Materials Research Part A* 2003;66A(2):247-259.
43. Marx RE. Platelet-rich plasma: Evidence to support its use. *J Oral Maxillofac Surg* 2004;62(4):489-496.
44. Di Iorio D, Traini T, Degidi M, Caputi S, Neugebauer J, Piattelli A. Quantitative evaluation of the fibrin clot extension on different implant surfaces: An in vitro study. *J Biomed Mater Res B Appl Biomater* 2005;74B(1):636-642.
45. Davies JE. Understanding peri-implant endosseous healing. *J Dent Educ* 2003;67(8):932-949.
46. Davies JE. Mechanisms of endosseous integration. *Int J Prosthodont* 1998;11(5):391-401.
47. Babensee JE, Anderson JM, McIntire LV, Mikos AG. Host response to tissue engineered devices. *Adv Drug Del Rev* 1998;33(1-2):111-139.
48. Schindeler A, McDonald MM, Bokko P, Little DG. Bone remodeling during fracture repair: The cellular picture. *Semin Cell Dev Biol* 2008;19(5):459-466.
49. Caplan AI, Dennis JE. Mesenchymal stem cells as trophic mediators. *J Cell Biochem* 2006;98(5):1076-1084.
50. Neuss S, Schneider RK, Tietze L, Knuchel R, Jahnen-Dechent W. Secretion of fibrinolytic enzymes facilitates human mesenchymal stem cell invasion into fibrin clots. *Cells Tissues Organs* 2010;191(1):36-46.
51. Bruder SP, Fink DJ, Caplan AI. Mesenchymal stem cells in bone development, bone repair, and skeletal regeneration therapy. *J Cell Biochem* 1994;56(3):283-294.
52. Olivares-Navarrete R, Hyzy SL, Hutton DL, Erdman CP, Wieland M, Boyan BD, et al. Direct and indirect effects of microstructured titanium substrates on the induction of mesenchymal stem cell differentiation towards the osteoblast lineage. *Biomaterials* 2010;31(10):2728-2735.
53. Saruwatari L, Aita H, Butz F, Nakamura HK, Ouyang J, Yang Y, et al. Osteoblasts generate harder, stiffer, and more delamination-resistant mineralized tissue on titanium than on polystyrene, associated with distinct tissue micro- and ultrastructure. *J Bone Miner Res* 2005;20(11):2002-2016.

54. Owen TA, Aronow M, Shalhoub V, Barone LM, Wilming L, Tassinari MS, et al. Progressive development of the rat osteoblast phenotype invitro - Reciprocal relationships in expression of genes associated with osteoblast proliferation and differentiation during formation of the bone extracellular-matrix. *J Cell Physiol* 1990;143(3):420-430.
55. Davies JE, Baldan N. Scanning electron microscopy of the bone bioactive implant interface. *J Biomed Mater Res* 1997;36(4):429-440.
56. McKee MD, Nanci A. Osteopontin at mineralized tissue interfaces in bone, teeth, and osseointegrated implants: Ultrastructural distribution and implications for mineralized tissue formation, turnover, and repair. *Microsc Res Tech* 1996;33(2):141-164.
57. Thurner PJ, Lam S, Weaver JC, Morse DE, Hansma PK. Localization of Phosphorylated Serine, Osteopontin, and Bone Sialoprotein on Bone Fracture Surfaces. *J Adhes* 2009;85(8):526-545.
58. Mulari MTK, Qu Q, Harkonen PL, Vaananen HK. Osteoblast-like cells complete osteoclastic bone resorption and form new mineralized bone matrix in vitro. *Calcif Tissue Int* 2004;75(3):253-261.
59. Teitelbaum SL, Ross FP. Genetic regulation of osteoclast development and function. *Nat Rev Genet* 2003;4(8):638-649.
60. Teitelbaum SL. Bone resorption by osteoclasts. *Science* 2000;289(5484):1504-1508.
61. Chambers TJ, Revell PA, Fuller K, Athanasou NA. Resorption of bone by isolated rabbit osteoclasts. *J Cell Sci* 1984;66(MAR):383-399.
62. Svanborg LM, Andersson M, Wennerberg A. Surface characterization of commercial oral implants on the nanometer level. *J Biomed Mater Res B Appl Biomater* 2010;92(2):462-469.
63. Wennerberg A, Ohlsson R, Rosen BG, Andersson B. Characterizing three-dimensional topography of engineering and biomaterial surfaces by confocal laser scanning and stylus techniques. *Med Eng Phys* 1996;18(7):548-556.
64. Wieland M, Textor M, Spencer ND, Brunette DM. Wavelength-dependent roughness: A quantitative approach to characterizing the topography of rough titanium surfaces. *Int J Oral Maxillofac Implants* 2001;16(2):163-181.
65. Wang H, Xu M, Zhang W, Kwok DT, Jiang J, Wu Z, et al. Mechanical and biological characteristics of diamond-like carbon coated poly aryl-ether-ether-ketone. *Biomaterials* 2010;31(32):8181-8187.
66. Sagomonyants KB, Jarman-Smith ML, Devine JN, Aronow MS, Gronowicz GA. The in vitro response of human osteoblasts to polyetheretherketone (PEEK) substrates compared to commercially pure titanium. *Biomaterials* 2008;29(11):1563-1572.
67. Dennes TJ, Schwartz J. A Nanoscale Adhesion Layer to Promote Cell Attachment on PEEK. *JACS* 2009;131(10):3456-3457.
68. Schwartz Z, Raz P, Zhao G, Barak Y, Tauber M, Yao H, et al. Effect of Micrometer-Scale Roughness of the Surface of Ti6Al4V Pedicle Screws in Vitro and in Vivo. *J Bone Jt Surg (Am)* 2008;90A(11):2485-2498.
69. Hallgren C, Reimers H, Chakarov D, Gold J, Wennerberg A. An in vivo study of bone response to implants topographically modified by laser micromachining. *Biomaterials* 2003;24(5):701-710.
70. Giavaresi G, Fini M, Chiesa R, Giordano C, Sandrini E, Bianchi AE, et al. A novel multiphase anodic spark deposition coating for the improvement of orthopedic implant osseointegration: an experimental study in cortical bone of sheep. *J Biomed Mater Res A* 2008;85(4):1022-1031.

71. Simmons CA, Valiquette N, Pilliar RM. Osseointegration of sintered porous-surfaced and plasma spray-coated implants: An animal model study of early postimplantation healing response and mechanical stability. *J Biomed Mater Res* 1999;47(2):127-138.
72. Buser D, Nydegger T, Hirt HP, Cochran DL, Nolte LP. Removal torque values of titanium implants in the maxilla of miniature pigs. *Int J Oral Maxillofac Implants* 1998;13(5):611-619.
73. Buser D, Broggini N, Wieland M, Schenk RK, Denzer AJ, Cochran DL, et al. Enhanced bone apposition to a chemically modified SLA titanium surface. *J Dent Res* 2004;83(7):529-533.
74. He FM, Yang GL, Li YN, Wang XX, Zhao SF. Early bone response to sandblasted, dual acid-etched and H₂O₂/HCl treated titanium implants: an experimental study in the rabbit. *Int J Oral Maxillofac Surg* 2009;38(6):677-681.
75. Szmukler-Moncler S, Perrin D, Ahossi V, Magnin G, Bernard JP. Biological properties of acid etched titanium implants: Effect of sandblasting on bone anchorage. *J Biomed Mater Res B Appl Biomater* 2004;68B(2):149-159.
76. Stein GS, Lian JB. Molecular mechanisms mediating proliferation/differentiation interrelationships during progressive development of the osteoblast phenotype. *Endocr Rev* 1993;14(4):424-442.
77. Zhao G, Zinger O, Schwartz Z, Wieland M, Landolt D, Boyan BD. Osteoblast-like cells are sensitive to submicron-scale surface structure. *Clin Oral Implants Res* 2006;17(3):258-264.
78. Kim MJ, Kim CW, Lim YJ, Heo SJ. Microrough titanium surface affects biologic response in MG63 osteoblast-like cells. *J Biomed Mater Res A* 2006;79(4):1023-1032.
79. Boyan BD, Schwartz Z, Bonewald LF, Swain LD. Localization of 1,25-(OH)₂D₃-responsive alkaline-phosphatase in osteoblast-like cells (Ros 17/2.8, Mg-63, and Mc-3t3) and growth cartilage cells in culture. *J Biol Chem* 1989;264(20):11879-11886.
80. Hauschka PV, Lian JB, Cole DEC, Gundberg CM. Osteocalcin and matrix gla protein - Vitamin K-dependent proteins in bone. *Physiol Rev* 1989;69(3):990-1047.
81. Petrie TA, Reyes CD, Burns KL, Garcia AJ. Simple application of fibronectin-mimetic coating enhances osseointegration of titanium implants. *J Cell Mol Med* 2009;13(8B):2602-2612.
82. van der Flier A, Sonnenberg A. Function and interactions of integrins. *Cell Tissue Res* 2001;305(3):285-298.
83. Olivares-Navarrete R, Raz P, Zhao G, Chen J, Wieland M, Cochran DL, et al. Integrin alpha 2 beta 1 plays a critical role in osteoblast response to micron-scale surface structure and surface energy of titanium substrates. *Proc Natl Acad Sci U S A* 2008;105(41):15767-15772.
84. Villanueva JE, Nimni ME. Promotion of Calvarial Cell Osteogenesis by Endothelial-Cells. *J Bone Miner Res* 1990;5(7):733-739.
85. Maes C, Kobayashi T, Selig MK, Torrekens S, Roth SI, Mackem S, et al. Osteoblast precursors, but not mature osteoblasts, move into developing and fractured bones along with invading blood vessels. *Dev Cell* 2010;19(2):329-344.
86. Raines AL, Olivares-Navarrete R, Wieland M, Cochran DL, Schwartz Z, Boyan BD. Regulation of angiogenesis during osseointegration by titanium surface microstructure and energy. *Biomaterials* 2010;31(18):4909-4917.
87. Balloni S, Calvi EM, Damiani F, Bistoni G, Calvitti M, Locci P, et al. Effects of Titanium Surface Roughness on Mesenchymal Stem Cell Commitment and Differentiation Signaling. *Int J Oral Maxillofac Implants* 2009;24(4):627-635.

88. Olivares-Navarrete R, Hyzy S, Wieland M, Boyan BD, Schwartz Z. The roles of Wnt signaling modulators Dickkopf-1 (Dkk1) and Dickkopf-2 (Dkk2) and cell maturation state in osteogenesis on microstructured titanium surfaces. *Biomaterials* 2010;31(8):2015-2024.
89. Elias CN, Meirelles L. Improving osseointegration of dental implants. *Expert Rev Med Devices* 2010;7(2):241-256.
90. Bjursten LM, Rasmusson L, Oh S, Smith GC, Brammer KS, Jin S. Titanium dioxide nanotubes enhance bone bonding in vivo. *J Biomed Mater Res A* 2010;92(3):1218-1224.
91. Mendonca G, Mendonca DBS, Simoes LGP, Araujo AL, Leite ER, Golin AL, et al. Nanostructured implant surface effect on osteoblast gene expression and bone-to-implant contact in vivo. *Mater Sci Eng C Mater Biol Appl* 2011;31(8):1809-1818.
92. Tsukimura N, Ueno T, Iwasa F, Minamikawa H, Sugita Y, Ishizaki K, et al. Bone integration capability of alkali- and heat-treated nanobimorphic Ti-15Mo-5Zr-3Al. *Acta Biomater* 2011;7(12):4267-4277.
93. Jimbo R, Xue Y, Hayashi M, Schwartz HO, Andersson M, Mustafa K, et al. Genetic Responses to Nanostructured Calcium-phosphate-coated Implants. *J Dent Res* 2011;90(12):1422-1427.
94. Mendonca G, Mendonca DBS, Simoes LGP, Araujo AL, Leite ER, Duarte WR, et al. Nanostructured alumina-coated implant surface: Effect on osteoblast-related gene expression and bone-to-implant contact in vivo. *Int J Oral Maxillofac Implants* 2009;24(2):205-215.
95. Cai KY, Bossert J, Jandt KD. Does the nanometre scale topography of titanium influence protein adsorption and cell proliferation? *Colloids Surf B Biointerfaces* 2006;49(2):136-144.
96. Webster TJ, Eijofor JU. Increased osteoblast adhesion on nanophase metals: Ti, Ti6Al4V, and CoCrMo. *Biomaterials* 2004;25(19):4731-4739.
97. Biggs MJP, Richards RG, Gadegaard N, Wilkinson CDW, Dalby MJ. The effects of nanoscale pits on primary human osteoblast adhesion formation and cellular spreading. *J Mater Sci Mater Med* 2007;18(2):399-404.
98. Khang D, Lu J, Yao C, Haberstroh KM, Webster TJ. The role of nanometer and sub-micron surface features on vascular and bone cell adhesion on titanium. *Biomaterials* 2008;29(8):970-983.
99. Arnold M, Cavalcanti-Adam EA, Glass R, Blummel J, Eck W, Kantlehner M, et al. Activation of integrin function by nanopatterned adhesive interfaces. *Chemphyschem* 2004;5(3):383-388.
100. Mendonca G, Mendonca DBS, Simoes LGP, Araujo AL, Leite ER, Duarte WR, et al. The effects of implant surface nanoscale features on osteoblast-specific gene expression. *Biomaterials* 2009;30(25):4053-4062.
101. de Oliveira PT, Nanci A. Nanotexturing of titanium-based surfaces upregulates expression of bone sialoprotein and osteopontin by cultured osteogenic cells. *Biomaterials* 2004;25(3):403-413.
102. Kubo K, Tsukimura N, Iwasa F, Ueno T, Saruwatari L, Aita H, et al. Cellular behavior on TiO₂ nanonodular structures in a micro-to-nanoscale hierarchy model. *Biomaterials* 2009;30(29):5319-5329.
103. Mendonca G, Mendonca DBS, Aragao FJL, Cooper LF. The combination of micron and nanotopography by H₂SO₄/H₂O₂ treatment and its effects on osteoblast-specific gene expression of hMSCs. *J Biomed Mater Res A* 2010;94A(1):169-179.

104. Wilkinson A, Hewitt RN, McNamara LE, McCloy D, Dominic Meek RM, Dalby MJ. Biomimetic microtopography to enhance osteogenesis in vitro. *Acta Biomater* 2011;7(7):2919-2925.
105. Gittens RA, McLachlan T, Olivares-Navarrete R, Cai Y, Berner S, Tannenbaum R, et al. The effects of combined micron-/submicron-scale surface roughness and nanoscale features on cell proliferation and differentiation. *Biomaterials* 2011;32(13):3395-3403.
106. McMurray RJ, Gadegaard N, Tsimbouri PM, Burgess KV, McNamara LE, Tare R, et al. Nanoscale surfaces for the long-term maintenance of mesenchymal stem cell phenotype and multipotency. *Nat Mater* 2011;10(8):637-644.

CHAPTER 3. THE EFFECTS OF COMBINED MICRO/SUB-MICROSCALE SURFACE ROUGHNESS AND NANOSCALE FEATURES ON CELL PROLIFERATION AND DIFFERENTIATION

In [Gittens RA, McLachlan T, Olivares-Navarrete R, Cai Y, Berner S, Tannenbaum R, Schwartz Z, Sandhage KH, Boyan BD. The effects of combined micron-/submicron-scale surface roughness and nanoscale features on cell proliferation and differentiation. *Biomaterials* 2011;32(13):3395-3403.]

3.1. Introduction

Integration of titanium (Ti) implants with the surrounding bone is critical for successful bone regeneration and healing in dental and orthopedic applications. The desire to accelerate and improve osseointegration drives many implantology research and development efforts, particularly for patients whose bones have been compromised by disease or age. Previous work has shown that the surface characteristics of implants have a direct influence on tissue response by affecting protein adsorption and by modulating cell proliferation and differentiation [1-2]. Surface characteristics such as roughness [3-4], chemistry [5-7] and surface energy [8-9] have been reported to significantly influence cell differentiation, local factor production and, consequently, bone growth and osseointegration [10-11].

Surface modification strategies for metallic implants to improve osseointegration have attempted to mimic the characteristics of bone [12-15]. During bone remodeling, previously-formed bone is resorbed by osteoclasts, in part to remove microcracks before new bone is formed in these primed regions [16-17]. Resorption lacunae left by osteoclasts, created through acidification and proteinase activity [18], have a distinct hierarchical structural complexity [19-20]. Resorption lacunae consist of microscale pits (up to 100 μm in diameter and 50 μm in depth [21-23]) with sub-microscale roughness formed by the irregular acid etching at the ruffled border of the osteoclast [18-19] and nanoscale features created by the collagen fibers left on the surface [20, 22].

Several studies have shown that increases in surface micro- and sub-microscale roughness, with feature sizes comparable to those of resorption pits and cell dimensions, lead to enhanced osteoblast differentiation and local factor production *in vitro* [24-25], increased bone-to-implant contact *in vivo* [26-27] and improved clinical rates of wound healing [28-29]. Surface nanoscale roughness, which directly corresponds to the sizes of proteins and cell membrane receptors, could also play an important role in osteoblast differentiation and tissue regeneration (Figure 2.4).

The effect of nanoscale surface roughness on osteoblast response has drawn the attention of several research groups over the last decade [30-33]. The literature on this topic is dominated by studies on the initial interactions between osteoblasts and nanomodified polymeric substrates, and such work has indicated that nanoscale roughness can significantly affect cell adhesion [34], proliferation [35], and spreading [36]. Similar results have been found for ceramic [37] and metallic [38] substrates. However, other studies report either a decrease in osteoblast proliferation with an increase in nanoscale roughness [39], or no effect of nanoscale roughness on proliferation [40] in the absence of microscale surface roughness [12, 41].

Relatively few studies have examined the effects of nanostructured surfaces on osteoblast differentiation [12, 36-37, 42-43]. Some reports have indicated that increased osteoblast proliferation on nanostructured surfaces coincided with an increase in alkaline phosphatase synthesis, increased Ca-containing mineral deposition [37], and higher immunostaining of osteocalcin and osteopontin [36]. Gene expression studies have shown an increase in the expression of Runx2, osterix, and bone sialoprotein in osteoblasts grown on nanoroughened surfaces [42-43]. Two studies [12, 41] examined the protein levels of different differentiation markers and local factors, and both of these studies reported an increase in differentiation, and an increase in factors PGE2 and

active TGF- β 1, when sub-micro- to nanoscale roughness was introduced to microrough substrates.

More recent studies have focused on the hierarchical combination of both micro- and nanoscale roughness to promote osseointegration on clinically-relevant surfaces [12-14, 44-45]. Although some of these studies have reported promising results of increased osteoblast proliferation and differentiation, it has been challenging to create a tailored hierarchical surface without altering other underlying characteristics of the substrate (particularly the microscale roughness and surface chemistry) [13-14, 45]. For this reason, it has been difficult to decouple the effects of nanoscale features from those of other surface features, such as surface microroughness, surface chemistry, and/or surface energy. Additionally, the simultaneous increase in osteoblast proliferation and differentiation caused by nanoscale roughness remains controversial due to some contradictory results [39-40, 44], which may have been influenced by differences in the types of cells and in the types of nanoscale surface modifications used in these experiments.

The objectives of the present study were twofold. First, we aimed to develop a simple and scalable oxidation-induced surface modification process of clinical relevance in order to alter the nanoscale topography of Ti substrates without greatly affecting surface chemistry or the starting micro/sub-microscale roughness. Second, we aimed to evaluate the influence of such modified nanoscale surface topography, with and without additional micro/sub-microscale roughness, *in vitro* on the differentiation and local factor production of human osteoblast-like MG63 cells.

3.2. Materials and Methods

3.2.1. Titanium Disks

Ti disks with a diameter of 15 mm were punched from 1 mm thick sheets of grade 2 unalloyed Ti (ASTM F67 unalloyed Ti for surgical implant applications) and supplied by Institut Straumann AG (Basel, Switzerland). After degreasing the disks in acetone, the disks were exposed at 55 °C for 30 seconds to an aqueous solution consisting of 2 % ammonium fluoride, 2 % hydrofluoric acid and 10 % nitric acid to generate “pre-treatment” (PT) Ti disks. The PT disks were further sandblasted with corundum grit (0.25 to 0.50 μm) at 5 bar, followed by etching in a solution of hydrochloric and sulfuric acids heated above 100 °C for several minutes (proprietary process of Institut Straumann AG) to produce “sandblasted-large-grit-acid-etched” (SLA) disks. The samples were then rinsed with water and sterilized by gamma irradiation at 25 kGy overnight (≥ 12 h).

3.2.2. Surface Modification

A simple and scalable process for achieving a homogenous and relatively high surface density of nanoscale structures on titanium metal surfaces, referred to herein as “nanoscale modification” (NM), was developed [46]. An additional attribute of the surface modification process is that it does not require a straight line path to modify or superimpose the nanoscale structures on the surface (non-line-of-sight). All PT and SLA disks were cleaned and sterilized before and after the NM treatment process. Prior to NM treatment, samples were cleaned using a protocol that involved two 15 minute sonication cycles each in detergent, ultra-pure water, acetone, isopropanol, ethanol, and then three 10 minute sonication cycles each in ultra-pure water, followed by plasma cleaning for 2 minutes at a maximum oxygen pressure of 0.27 mbar and at an RF power of 6.8 W (PDC-32G plasma cleaner, Harrick Plasma, Ithaca, NY). The NM treatments

consisted of exposure of the cleaned specimens at 740 °C to flowing (0.85 standard liters per minute) synthetic air (21 % O₂, 79 % N₂) at 1 atm for varied times. To evaluate the change in surface topography with exposure time, PT samples were treated for 45 minutes (NMPT45), 90 minutes (NMPT90), and 180 minutes (NMPT180). The development of nanoscale features on specimen surfaces was evaluated using scanning electron microscopy (SEM). The mass increase of the samples during such NM treatment was monitored via thermogravimetric (TG) analysis (Q50, TA Instruments, New Castle, DE). After optimization of the NM treatment using PT samples, this treatment was applied to SLA samples. Prior to use in cell experiments, the NM-treated PT (NMPT) and NM-treated SLA (NMSLA) samples, and their respective unmodified controls, were cleaned by sonication in detergent and ultra-pure water and autoclave sterilized.

3.2.3. Surface Characterization

The NMPT and NMSLA specimens were examined after sterilization by a variety of surface-sensitive techniques as described below.

3.2.3.1. *Scanning Electron Microscopy (SEM):*

The specimen surface topography was qualitatively evaluated using a field-emission-gun scanning electron microscope (Ultra 60 FEG-SEM, Carl Zeiss SMT Ltd., Cambridge, UK). Images were recorded using a 5 kV accelerating voltage and 30 µm aperture. Image analysis software (ImageJ, NIH software) was used to evaluate the dimensions of nanoscale structural features generated by the NM treatment.

3.2.3.2. *Transmission Electron Microscopy (TEM):*

The thickness and crystal structure of the oxide layer formed upon NM treatment was evaluated using a field-emission-gun transmission electron microscope (HF-2000 FEG-TEM, Hitachi High Technologies America, Inc., Pleasanton, CA). The NMPT90

sample was embedded in epoxy, cross-sectioned, and then ground, polished, dimpled, and ion-milled to perforation. TEM characterization was then performed using an accelerating voltage of 200 KV.

3.2.3.3. Atomic Force Microscopy (AFM):

Surface measurements at the nanoscale were evaluated using atomic force microscopy (Nano-R AFM, Pacific Nanotechnology, Santa Clara, CA) in close-contact mode. AFM analyses were conducted using silicon probes (P-MAN-SICC-O, Agilent Technologies, Santa Clara, CA) with dimensions of $1.14 \times 0.25 \text{ cm}^2$, a nominal force constant of 40 N/m, a nominal resonance frequency of 300 kHz, and tip radii of up to 10 nm. Each AFM analysis was performed over a 730 nm x 730 nm area. Two samples of every group were scanned three times each, under ambient atmosphere. The original data was plane-leveled to remove tilt by applying a numerical second-order correction, and mean values of surface roughness (S_a) and peak-to-valley height (S_z) were determined using the NanoRule+ software (Pacific Nanotechnology).

3.2.3.4. Laser Confocal Microscopy (LCM):

Surface roughness at the macro and microscale was evaluated using a laser confocal microscope (Lext, Olympus, Center Valley, PA). Each LCM analysis was performed over a $644 \mu\text{m} \times 644 \mu\text{m}$ area using a scan height step of 50 nm, a 20X objective, and a cutoff wavelength of $100 \mu\text{m}$. Two samples of every group were scanned three times each, under ambient atmosphere. Mean values of surface roughness (S_a) and peak-to-valley height (S_z) were determined.

3.2.3.5. X-Ray Photoelectron Spectroscopy (XPS):

Atomic concentration and chemical bonding information were obtained from the specimen surfaces by X-ray photoelectron spectroscopy (Thermo K-Alpha XPS, Thermo Fisher Scientific, West Palm Beach, FL). The instrument was equipped with a

monochromatic Al-K α X-ray source ($h\nu = 1468.6$ eV). The XPS analysis chamber was evacuated to a pressure of 5×10^{-8} mbar or lower before collecting XPS spectra. Spectra were collected using an X-ray spot size of 400 μm and pass energy of 100 eV, with 1 eV increments, at a 55 ° takeoff angle. Two samples of every group were scanned two times each.

3.2.3.6. *Contact Angle Measurements:*

Contact angle measurements were obtained using a goniometer (CAM 100; KSV, Helsinki, Finland) equipped with a digital camera and image analysis software. Ultra-pure water was used as the wetting liquid with a drop size of 5 μL . Sessile drop contact angles of the air-water-substrate interface were measured four times in two samples of every group.

3.2.3.7. *X-ray diffraction (XRD):*

X-ray diffraction analyses were conducted using 1.8 kW Cu K α radiation, a 1 ° parallel plate collimator, a 1/4 divergence slit, and a 0.04 rad soller slit (X'Pert PRO Alpha-1 diffractometer, PANalytical, Almelo, The Netherlands). Both Bragg-Brentano and θ – 2θ para-focusing setups were used for regular and grazing-angle (*i.e.*, 4 ° take-off angle) analyses, respectively. Two samples of every group were scanned two times each, under ambient atmosphere.

3.2.4. Cell Culture Model and Assays

MG63 cells were obtained from the American Type Culture Collection (Rockville, MD) and were cultured in Dulbecco's modified Eagle medium, containing 10 % fetal bovine serum (FBS) and 1 % penicillin and streptomycin, at 37 °C in an atmosphere of 5 % CO₂ and 100 % humidity. Cells were grown on tissue culture polystyrene (TCPS) or on one of the four types of specimens (PT, NMPT, SLA, NMSLA) at a density of 10,000 cells/cm². MG63 cells were fed 24 hours after they were plated on the different surfaces

and every 48 hours until confluent, as evaluated on the TCPS substrate. At confluence, cells were treated with fresh media for 24 hours and harvested for assays. At harvest, conditioned media were collected and cell layers were washed twice with serum-free media to remove any non-adherent cells, followed by two sequential incubations in 500 μ L of 0.25 % trypsin for 10 minutes at 37 °C to release the cells from their substrate. The trypsin reaction was terminated by adding FBS-containing media to the tubes and cells were then centrifuged at 2000 rpm for 15 minutes. The supernatant was decanted, and the cell pellets were resuspended by vortexing in 500 μ L of 0.05 % Triton-X-100. The cells were then lysed to release cell contents.

Cell proliferation was evaluated by measuring DNA content with a commercially-available kit (Quant-iT™ PicoGreen® dsDNA assay, Invitrogen, Carlsbad, CA). Cells were harvested as described above and 50 μ L of lysed cell content were diluted with 50 μ L of 0.05 % Triton-X-100. Fluorescence measurements were obtained using a fluorescent multimode detector (DTX880, Beckman Coulter, Brea, CA) with reference to a standard.

Cell differentiation was evaluated using two markers of osteoblast differentiation: cellular alkaline phosphatase-specific activity [orthophosphoric monoester phosphohydrolase, alkaline; E.C. 3.1.3.1] as an early differentiation marker; and osteocalcin content in the conditioned media as a late differentiation marker. Alkaline phosphatase activity was assayed from the release of *p*-nitrophenol from *p*-nitrophenylphosphate at pH 10.2 as previously described [47]. Activity values were normalized to the protein content, which was detected as colorimetric cuprous cations in biuret reaction (BCA Protein Assay Kit, Pierce Biotechnology Inc., Rockford, IL, USA) at 570 nm (Microplate reader, BioRad Laboratories Inc., Hercules, CA, USA). Osteocalcin levels in the conditioned media were measured using a commercially available

radioimmunoassay kit (Human Osteocalcin RIA Kit, Biomedical Technologies, Stoughton, MA), as described previously [48]. Briefly, 50 μ L of conditioned media were mixed with [125 I] osteocalcin tracer and human osteocalcin anti-serum (100 μ L each), and incubated at 37 °C for 2.5 hours. Goat anti-rabbit IgG, polyethylene glycol (100 μ L each), and 1 mL of PBS were then added, followed by centrifugation at a minimum of 1500x g for 15 minutes at 4 °C. The supernatant was decanted and the pellets were counted for 1 minute in a LS1500 gamma counter (Perkin Elmer, Waltham, CA).

The conditioned media were also assayed for protein levels of growth factors and cytokines. Osteoprotegerin (OPG), a cytokine that works as a decoy receptor for “receptor activator for nuclear factor κ B ligand” (RANKL) to inhibit osteoclastogenesis, was measured using enzyme-linked immunosorbent assay (ELISA) kits (DY805 Osteoprotegerin DuoSet, R&D Systems, Minneapolis, MN). Vascular endothelial growth factor (VEGF), a potent growth factor involved in vasculogenesis and angiogenesis, was also measured using an enzyme-linked immunosorbent assay (ELISA) kit (DY293B VEGF DuoSet, R&D Systems).

3.2.5. Statistical Analysis

Data from experiments characterizing the surface properties of the substrates are presented as the mean \pm one standard deviation (SD) of all the measurements performed on different samples. Data from experiments examining cell response are presented as mean \pm standard error for six independent cultures. All experiments were repeated at least twice to ensure validity of the observations and results from individual experiments are shown. Data were evaluated by analysis of variance, and significant differences between groups were determined using Bonferroni's modification of Student's t-test. A p value below 0.05 was considered to indicate a statistically-significant difference.

3.3. Results

Scanning electron microscopy (Figures 3.1, 3.3, 3.4) confirmed that an oxidation treatment at a modest temperature could be used to introduce nanoscale structural features to the Ti surfaces. In this study, the oxidation temperature (*i.e.*, 740 °C) and gaseous environment (*i.e.*, synthetic air) were fixed while the duration of the process was varied. The surfaces of the starting PT samples were relatively smooth on the microscale (LCM $S_a = 0.43 \pm 0.02 \mu\text{m}$), although surface pits, presumably resulting from the PT acid pickling process, were detected (Figure 3.1A). After 45 minutes of controlled oxidation (NMPT45), a low density of nanoscale protuberances was observed to have formed on the specimen surfaces (Figure 3.1B), with protuberance sizes ranging from about 40 to 200 nm in diameter (Figure 3.1E) and about 10 to 150 nm in height. After 90 minutes of modification (NMPT90), the entire surface was homogeneously covered with a relatively high density of nanoscale structures (Figure 3.1C), which ranged in size from about 40 to 360 nm in diameter (Figure 3.1F) and about 60 to 350 nm in height. Following 180 minutes of modification (NMPT180), the nanostructures coalesced into coarser structures (Figure 3.1D) that spanned about 500 to 1000 nm in diameter and about 80 to 500 nm in height. The mass increase of the oxidized samples was also monitored by TG analyses and correlated to changes in surface topography (Figure 3.2). Indeed, by coupling weight gain measurements to the resulting surface topography, TG analyses may be used to monitor the time required for the generation of a high surface density of nanoscale structures on titanium implants of various geometries.

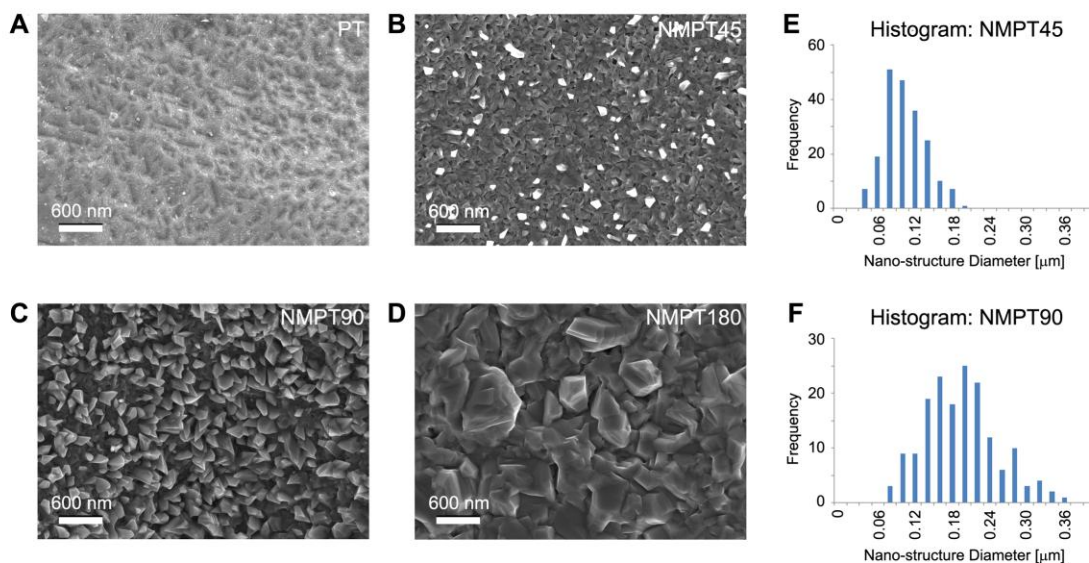


Figure 3.1. Morphological assessment of nanostructure evolution with time. NM-treatment of (A) PT surfaces via oxidation in flowing synthetic air (21 % O₂, 79 % N₂) at 740 °C for times of: (B) 45 minutes; (C) 90 minutes; (D) 180 minutes. The modification process introduced: (B) nanoscale protuberances with low surface coverage after 45 minutes; (C) a relatively high density of nanostructures after 90 minutes; and (D) coarse structures after 180 minutes. These SEM images are representative of the entire PT Ti disk surfaces. (E, F) Image analyses of SEM images revealing the distribution of diameters of the nanoscale structures formed after 45 minutes and 90 minutes, respectively.

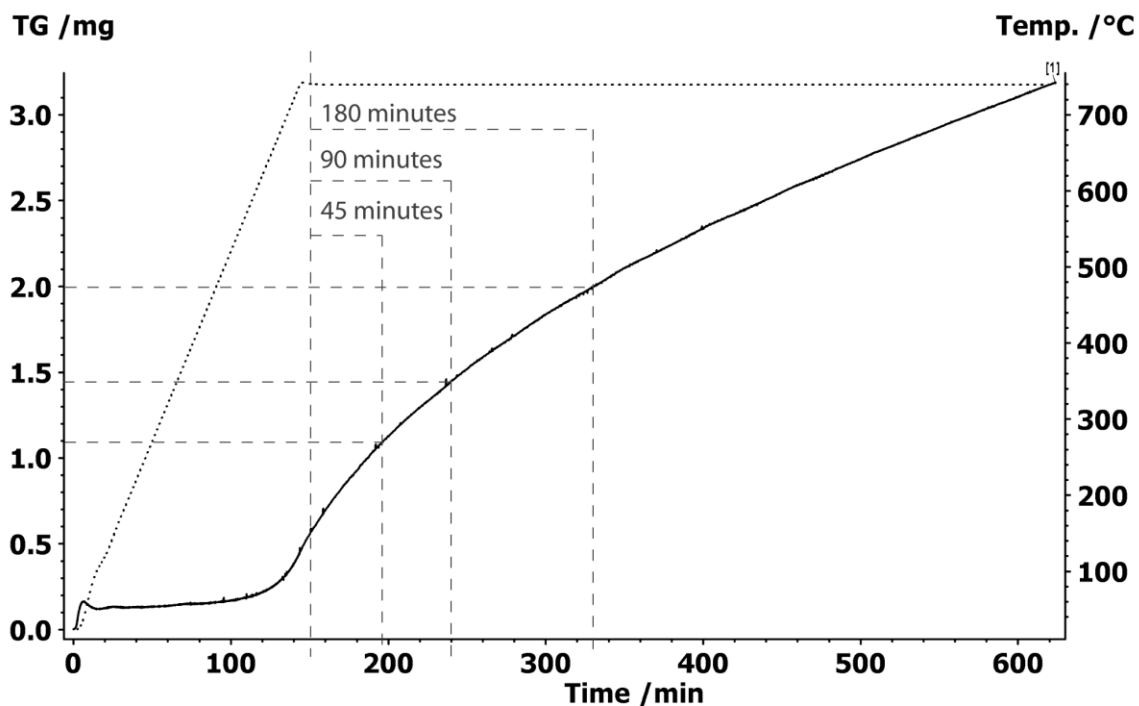


Figure 3.2. Thermogravimetric (TG) data showing the mass increase of a PT substrate exposed to the oxidation-based nanomodification treatment at 740 °C for 8 h. Discrete weight gain increments could be observed for the different modification times chosen for this study (45, 90 and 180 minutes).

The NM treatment was also applied to SLA substrates that possessed a greater degree of microscale roughness (LCM $S_a = 3.29 \pm 0.18 \mu\text{m}$) than for the PT specimens. NMSLA samples were generated using the same oxidation conditions as for the NMPT90 samples (*i.e.*, 740 °C, 90 min, synthetic flowing air). At low magnifications (Figures 3.3A, B), SEM analyses revealed a similar microscale topography for the SLA and NMSLA samples. However, at intermediate (Figures 3.3C, D) and higher magnifications (Figures 3.3E, F), NMSLA surfaces were observed to possess a relatively high and uniform density of nanoscale structures.

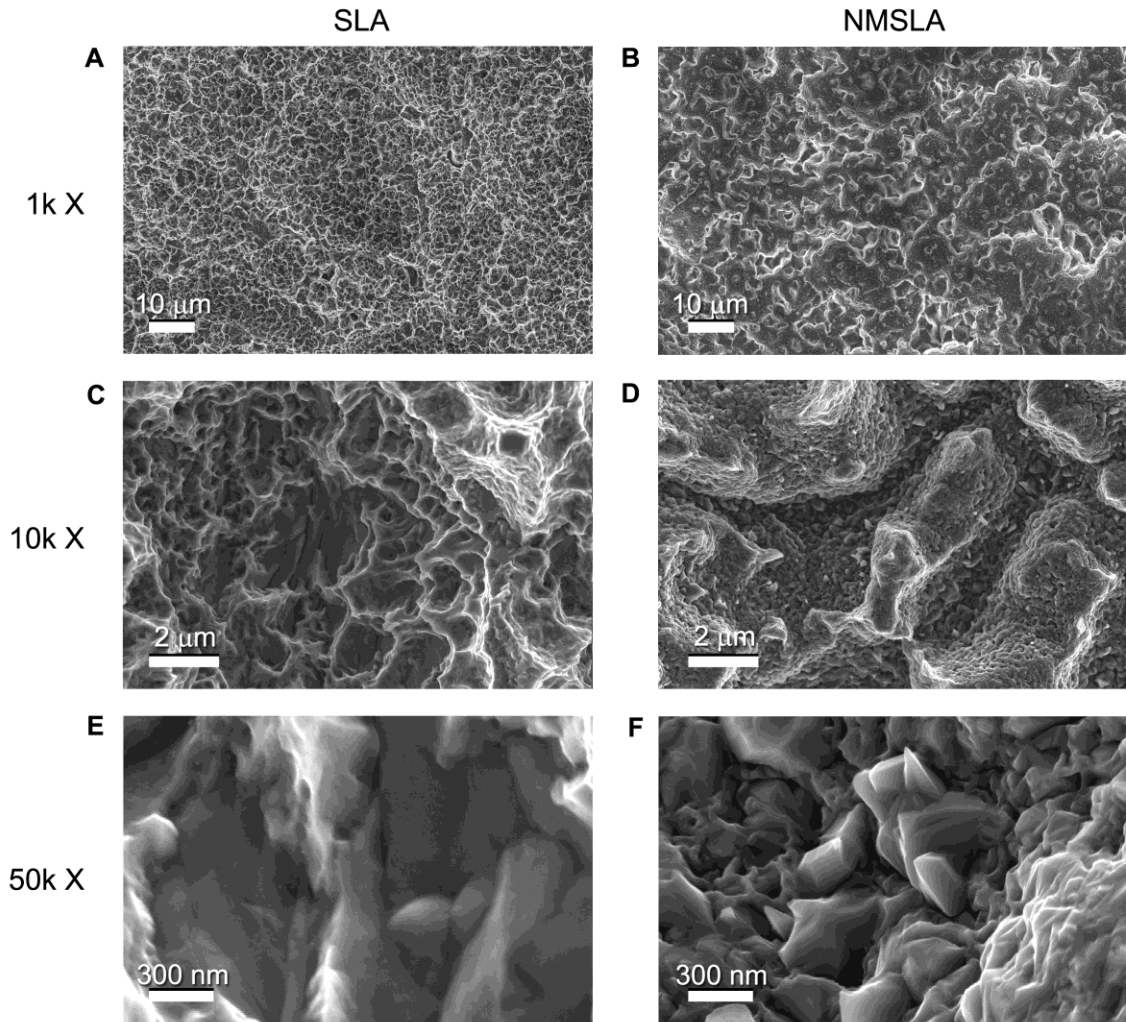


Figure 3.3. SEM images of microrough and micro/nanostructured titanium specimens. Secondary electron images of starting SLA samples (A, C, E), and of NMSLA samples (B, D, F) generated via oxidation in flowing synthetic air at 740 °C for 90 minutes show that the NM process yielded a relatively high density of nanoscale structures over the entire specimen surface and did not appreciably affect the overall microscale roughness of the SLA surface.

After verifying that a NM treatment (740 °C, 90 min., synthetic flowing air) could be used to introduce a relatively high density of nanoscale structural features to Ti surfaces that were relatively smooth or rough at the microscale, this treatment was applied to Ti specimens for further surface characterization and for use in cell experiments. Cell interactions with four types of specimens were examined: PT (Figure 3.4A), NMPT (Figure 3.4B), SLA (Figure 3.4C) and NMSLA (Figure 3.4D). The microscale and nanoscale topography of these samples was measured quantitatively using LCM and AFM, respectively (Table 3.1). As expected, the mean values of microscale (LCM-derived) roughness average and peak-to-valley height obtained for the PT and NMPT specimens were lower than for the SLA and NMSLA samples. Additionally, the mean values of the microscale (LCM-derived) roughness parameters S_a and S_z of the nanomodified samples, NMPT and NMSLA, were slightly lower than for the respective controls. The mean nanoscale (AFM-derived) roughness average of the NMPT specimens was considerably higher than for the PT controls (Table 3.1), although little statistical difference in the mean nanoscale roughness could be discerned between the SLA and NMSLA specimens. However, the NMPT and NMSLA surfaces shared noticeably higher (and similar) mean values of nanoscale peak-to-valley height relative to the PT and SLA surfaces. The combined LCM and AFM analyses were consistent with the presence of a relatively high density of nanoscale features on the NMPT and NMSLA specimens with little change in the microscale topography.

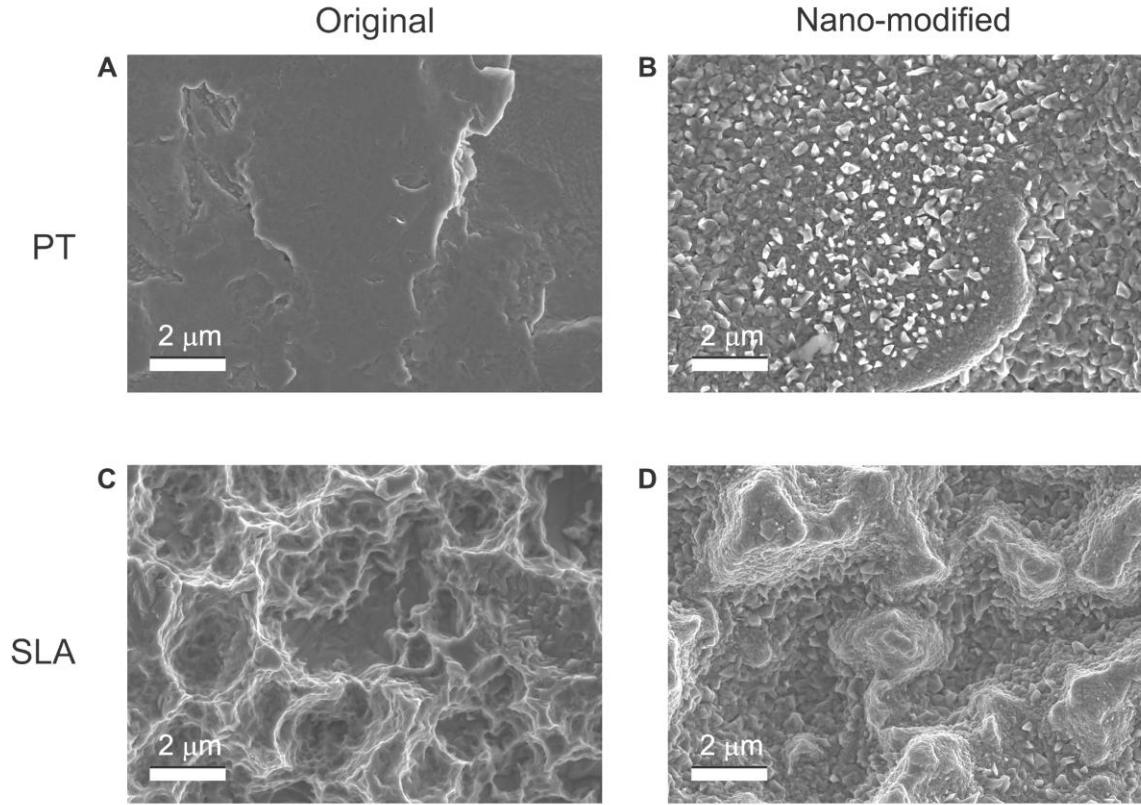


Figure 3.4. SEM images of the surface of titanium specimens. (A) PT, (B) NMPT, (C) SLA, and (D) NMSLA samples were used for surface characterization and cell experiments. The NM treatment consisted of oxidation in flowing synthetic air for 90 min at 740 °C.

Table 3.1. Roughness measurements on titanium specimens. Mean \pm one standard deviation (SD) values of average roughness (S_a) and peak-to-valley height (S_z) of the different titanium surfaces examined using atomic force microscopy (AFM) and laser confocal microscopy (LCM).

Sample	AFM Mean Roughness (S_a) \pm 1 SD [nm]	AFM Peak-to- Valley Height (S_z) \pm 1 SD [nm]	LCM Mean Roughness (S_a) \pm 1 SD [μ m]	LCM Peak-to- Valley Height (S_z) \pm 1 SD [μ m]
PT	6 \pm 3	58 \pm 41	0.43 \pm 0.02	7.99 \pm 1.67
NMPT	16 \pm 8	142 \pm 69	0.37 \pm 0.01	5.58 \pm 0.35
SLA	14 \pm 6	50 \pm 22	3.29 \pm 0.18	42.01 \pm 4.02
NMSLA	18 \pm 3	141 \pm 80	2.80 \pm 0.06	36.57 \pm 2.00

Static water contact angle measurements in air indicated that all of the samples exhibited relatively hydrophobic behavior (Figure 3.5, Table 3.2). The contact angles measured for the SLA and NMSLA samples were significantly larger than for the PT and NMPT samples (Figure 3.5, Table 3.2), which was consistent with the enhanced mean values of microscale roughness (LCM -derived S_a values) and microscale peak-to-valley height (LCM -derived S_z values) for the SLA and NMSLA samples (Table 3.1).

General surveys of the surface chemistry of the different specimens by XPS analyses revealed the presence of appreciable oxygen and titanium. Within statistical error, the concentrations of oxygen and titanium on the PT and NMPT surfaces, and of oxygen and titanium on the SLA and NMSLA surfaces, were similar (Table 3.3). However, a detectable change in the phase content on the Ti surfaces after the NM treatment was revealed by XRD and TEM analyses (Figure 3.5). XRD analyses of the surfaces of the PT and SLA samples yielded major diffraction peaks for α -Ti (ICDD 01-089-3073) and did not yield detectable diffraction peaks for crystalline oxides of titanium (Figure 3.5E). The SLA samples also exhibited additional diffraction peaks of modest intensity that were attributed to titanium hydride (TiH_2 , ICDD 04-008-1386). Both NMPT and NMSLA specimens exhibited relatively intense diffraction peaks for the rutile polymorph of TiO_2 (ICDD 01-071-6411). The α -Ti diffraction peaks in the NM-treated samples also appeared to shift to lower two-theta values. TEM analysis of an ion-milled cross-section of the NMPT sample (Figure 3.5F) revealed the presence of a compact and conformal oxide layer on the Ti surface. The average thickness of this oxide layer, generated within 90 min at 740°C in air, was about 1.2 μm . Selected area electron diffraction (SAED) analysis (Figure 3.5G) of this oxide scale yielded a diffraction pattern that was consistent with the presence of only the rutile polymorph of TiO_2 (as had also been revealed by the XRD analyses of NM-treated specimens).

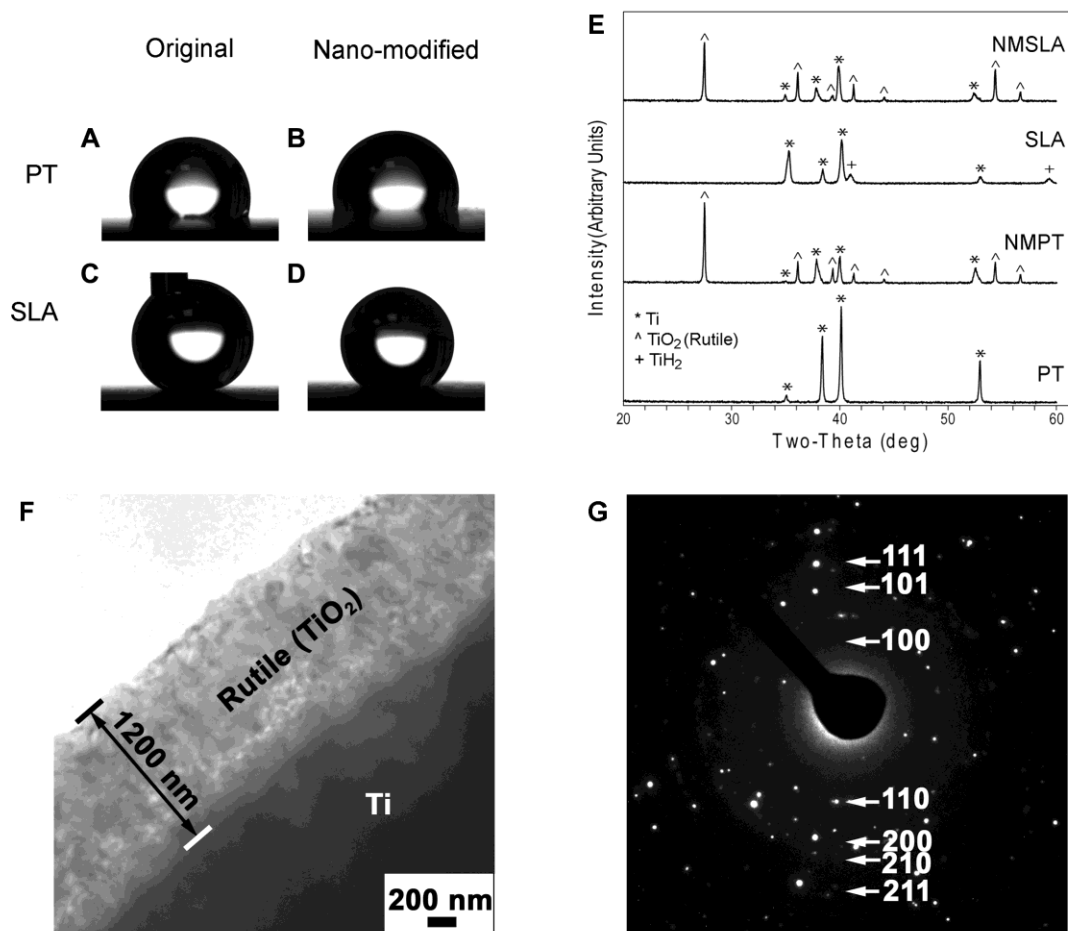


Figure 3.5. Surface characterization data of the NM-treated samples and their controls. (A-D) Optical images of water contact angles on PT, SLA, NMPT, and NMSLA surfaces. The contact angles measured for PT and NMPT samples were similar and smaller than for the SLA and NMSLA samples. (E) X-ray diffraction (XRD) patterns obtained from PT, SLA, NMPT, and NMSLA samples. (F) TEM image of an ion-milled cross-section of a NMPT specimen revealing the compact and conformal oxide layer formed after NM treatment. The average thickness of this oxide scale was 1.2 μm . (G) Selective area electron diffraction pattern obtained from the oxide scale, which was consistent with pure rutile TiO₂.

Table 3.2. Surface chemical evaluation of nanomodified Ti specimens. Mean values of NMPT/PT and NMSLA/SLA O and Ti concentration ratios \pm one standard deviation (SD) as determined by x-ray photoelectron spectroscopy (XPS).

Sample	Mean Ratios of Elemental Concentrations \pm 1 SD	
	O	Ti
NMPT/PT	0.97 \pm 0.23	0.89 \pm 0.20
NMSLA/SLA	1.24 \pm 0.07	1.29 \pm 0.13

Table 3.3. Mean values of water contact angle \pm one standard deviation (SD) on Ti specimens.

Sample	Contact Angle [$^{\circ}$ \pm SD]
PT	92 \pm 1
NMPT	101 \pm 0
SLA	157 \pm 3
NMSLA	142 \pm 1

Osteoblasts were sensitive to the surface modifications. The number of MG63 osteoblast cells, as deduced from DNA measurements (Figure 3.6A), and alkaline phosphatase specific activity (Figure 3.6B) for the NMPT, SLA, and NMSLA samples were statistically lower than for the PT specimens. This reduction in cell content and ALP activity paralleled an increase in mean nanoscale roughness (NMPT vs. PT) and the microscale roughness (SLA and NMSLA vs. PT). While the levels of osteocalcin, osteoprotegerin, and vascular endothelial growth factor (Figures 3.6C-E) measured for the PT and NMPT samples were not noticeably different, statistically-significant increases in the levels of these markers were observed for the SLA specimens, which paralleled the increase in microscale roughness for the SLA specimens relative to the PT and NMPT samples (Table 3.1). Further statistically significant increases in the osteocalcin, osteoprotegerin, and VEGF levels over the SLA specimens were observed for the NMSLA specimens.

3.4. Discussion

In the present study, a simple, readily-scalable (non-line-of-sight) oxidation-based surface modification process was developed that resulted in the superimposition of a high density of nanoscale structures on Ti substrates (as revealed by SEM and AFM analyses) in the absence or presence of appreciable microscale roughness. This nanoscale modification (NM) treatment did not appreciably affect surface chemistry (as revealed by XPS measurements) or wettability (as revealed by static water contact angle measurements), and did change surface crystal structure (as revealed by XRD and TEM analyses). Moreover, osteoblast behavior was sensitive to the modified surfaces.

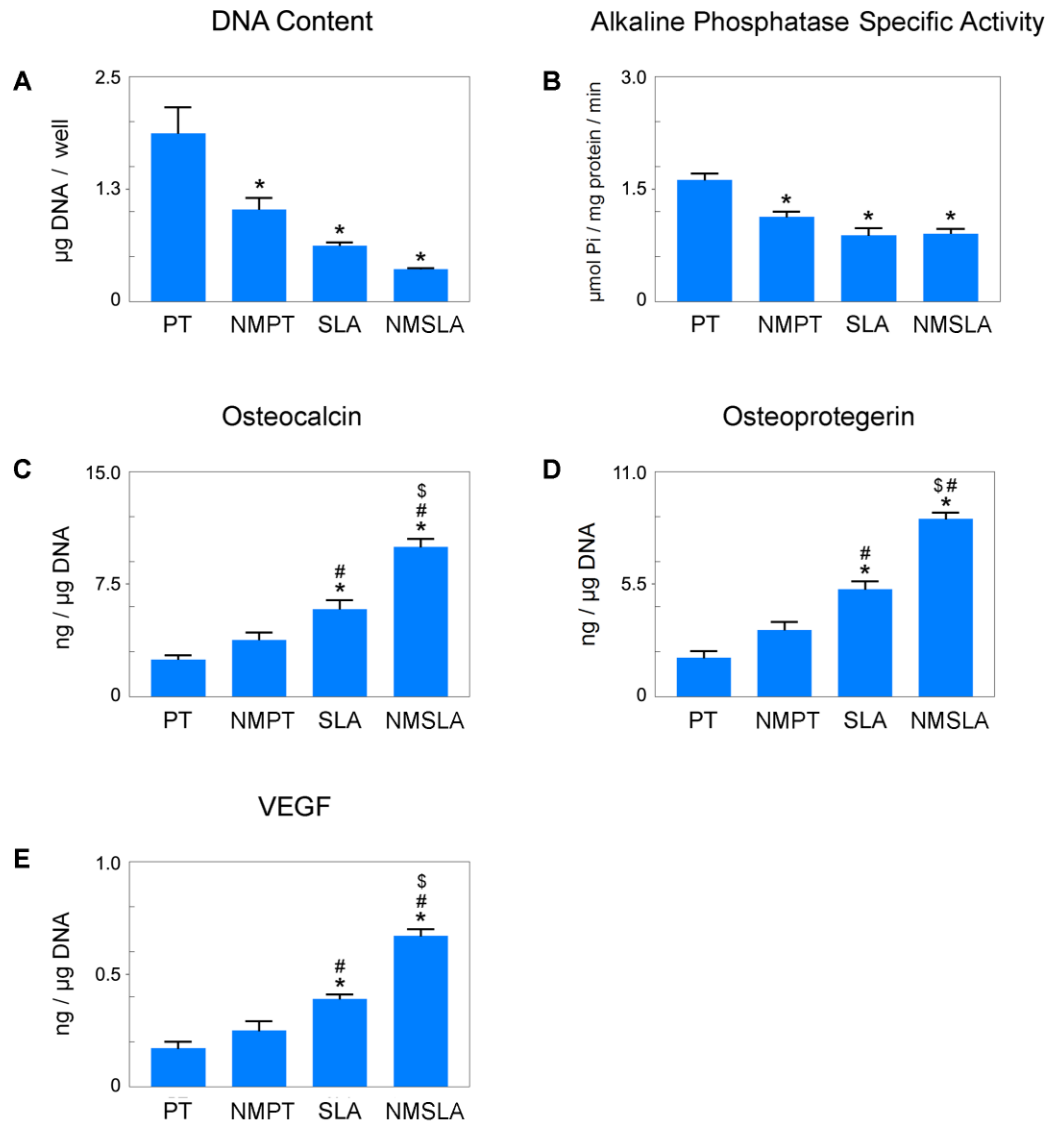


Figure 3.6. Effects of nanoscale surface features and microscale surface roughness on osteoblast differentiation. MG63 cells were plated on PT, NMPT, SLA, and NMSLA surfaces and grown to confluence. The NM treatment consisted of oxidation in flowing synthetic air for 90 min at 740 °C. At confluence, (A) DNA content, (B) ALP specific activity, (C) OCN, (D) OPG, and (E) VEGF levels were measured. Data represented are the mean \pm standard error of six independent samples. * refers to a statistically-significant p value below 0.05 vs. PT; # refers to a statistically-significant p value below 0.05 vs. NMPT; \$ refers to a statistically-significant p value below 0.05 vs. SLA.

The development of this oxidation-based modification process involved correlation of the changes in surface topography and weight of Ti disks with the duration of oxidation in synthetic air at 740 °C. Two types of Ti specimens were examined: pretreated specimens, and large-grit sandblasted and acid-etched specimens. As expected, laser confocal microscopy measurements indicated that the microscale surface roughness of the SLA specimens was significantly enhanced relative to the PT specimens. SEM analyses revealed the formation of nanoscale structures on the specimen surfaces upon oxidation at 740 °C for times between 45 and 180 min. With an increase in oxidation time, the surface density and average sizes of nanoscale structures formed on this scale increased. After 90 min, a relatively high density of such structures was observed to have formed uniformly over the specimen surfaces, with the SEM-derived diameters and heights ranging from about 40 to 360 nm and about 60 to 350 nm respectively. It is interesting to note that the nanostructures formed by the present oxidation-based process are not unlike the nanostructures associated with collagen fibrils left by osteoclasts after bone resorption [20, 22]. The average values of the LCM - derived microscale roughness (S_a) and the peak-to-valley height (S_z) for the nanomodified samples were slightly lower than for the respective controls. At least one contribution to such modest reductions in the average S_a and S_z values was likely to have been the formation of the 1.2 μm -thick oxide scale. AFM measurements revealed a significant increase in the mean nanoscale surface roughness, and mean peak-to-valley height, after exposure of PT samples to this 740 °C/90 min oxidation treatment. While a statistically-significant increase in the nanoscale roughness average could not be detected after exposure of SLA specimens to this 740 °C/90 min treatment, a significant increase in the mean peak-to-valley height was detected.

XPS analyses indicated that exposure of the PT and SLA specimens to the 740 °C/90 min treatment did not greatly affect the concentration of titanium and oxygen on the outer surfaces of these specimens, which was not surprising due to the presence of a thin native titanium oxide layer on both original and modified samples. The static water contact angles on the PT and SLA samples also did not appreciably change after the 740 °C/90 min oxidation treatment. However, XRD and TEM analyses revealed that this treatment resulted in the formation of a compact and conformal rutile TiO₂ scale of about 1.2 µm thickness. Noticeable shifts in the two-theta positions of α-Ti diffraction peaks were also detected in the modified samples, which was consistent with an expansion of the α-Ti lattice associated with the incorporation of oxygen [49-50] (note: the solubility of oxygen in α-Ti at 740 °C is 33.3 at % [49]).

A high density of nanoscale structures, as well as the presence of appreciable microscale roughness, affected the proliferation of MG63 cells. The number of MG63 osteoblast cells detected on the nanomodified PT (NMPT) samples was lower than for the starting PT specimens. Similarly, cell numbers on SLA and nanomodified SLA (NMSLA) samples were lower than on the PT specimens. In previous studies, cell proliferation on combined micro/nanostructured surfaces has been reported to increase when compared to microrough surfaces [13, 44]. However, in some of these studies, cell proliferation was evaluated at very early time points (*i.e.*, two days or less), using assays that tested for cell metabolic activity rather than for proliferation [13]. Although simultaneous and enhanced cell proliferation and differentiation would provide an ideal situation for bone growth and repair, studies have shown that the development of the osteoblast phenotype requires a regulated interrelation between proliferation and differentiation with transcriptionally restricted transitions that mark the end point of proliferation and the onset of differentiation [51-53].

Osteoblast differentiation was greatly enhanced on surfaces that possessed both microscale roughness and a high density of nanoscale features. These results are in agreement with previous studies [12, 41], which have indicated that a combination of nanoscale features and microscale roughness are required to achieve an additive, if not synergistic increase, in osteoblast differentiation. In our study, ALP activity was reduced and osteocalcin production was increased in a surface microroughness and nanostructure density dependent manner. Other studies reported larger ALP stained areas [13] and higher ALP activity as well as higher osteocalcin gene expression [14] for osteoblasts grown on micro/nanostructured surfaces. Differences in ALP activity between the present results and those of other studies could be due to the biphasic nature of ALP, which has been shown to increase at the early stages of osteoblast differentiation followed by a decrease in activity when more mature osteoblasts start producing osteocalcin just before mineralization [54].

The cells growing on the NMSLA surfaces also produced significantly higher levels of the local factor osteoprotegerin, which inhibits osteoclastogenesis, and VEGF, which is a potent angiogenic factor. Taken together with the DNA, ALP, and osteocalcin measurements, these results suggest that the combined superimposition of a high density of nanoscale structures with a surface possessing appreciable micro/sub-microscale roughness may promote bone formation directly in contact with the surface as well as in the surrounding tissue, thereby improving implant osseointegration.

3.5. Conclusions

A simple and readily-scalable (non-line-of-sight) oxidation-based surface modification process has been developed that superimposes a high density of nanoscale structures on the surfaces of Ti samples without greatly affecting other surface

properties (e.g., microscale roughness, hydrophobicity). The nanoscale structures are not unlike the nanoscale topography associated with collagen fibrils left by the osteoclasts after bone resorption. The results suggest that, while the nanostructures alone may regulate osteoblast proliferation, osteoblast differentiation is not appreciably affected in the absence of microscale surface roughness. However, the combination of micro/sub-microscale surface roughness with a high density of nanoscale structures resulted in an additive, if not synergistic effect, on cell differentiation and local factor production. These results suggest a potential opportunity for faster healing times and improved *in vivo* implant osseointegration through mimicry of bone hierarchical complexity via the combined tailoring of nanoscale and microscale surface features.

3.6. References

1. Kieswetter K, Schwartz Z, Dean DD, Boyan BD. The role of implant surface characteristics in the healing of bone. *Crit Rev Oral Biol Medicine* 1996;7(4):329-345.
2. Schwartz Z, Boyan BD. Underlying mechanisms at the bone-biomaterial interface. *J Cell Biochem* 1994;56:340-347.
3. Martin JY, Schwartz Z, Hummert TW, Schraub DM, Simpson J, Lankford J, et al. Effect of titanium surface-roughness on proliferation, differentiation, and protein-synthesis of human osteoblast-like cells (mg63). *J Biomed Mater Res* 1995;29(3):389-401.
4. Boyan BD, Bonewald LF, Paschalis EP, Lohmann CH, Rosser J, Cochran DL, et al. Osteoblast-mediated mineral deposition in culture is dependent on surface microtopography. *Calcif Tissue Int* 2002;71(6):519-529.
5. Sul YT, Johansson C, Wennerberg P, Cho LR, Chang BS, Albrektsson P. Optimum surface properties of oxidized implants for reinforcement of osseointegration: Surface chemistry, oxide thickness, porosity, roughness, and crystal structure. *Int J Oral Maxillofac Implants* 2005;20(3):349-359.
6. Buser D, Broggini N, Wieland M, Schenk RK, Denzer AJ, Cochran DL, et al. Enhanced bone apposition to a chemically modified sla titanium surface. *J Dent Res* 2004;83(7):529-533.
7. Liu X, Lim JY, Donahue HJ, Dhurjati R, Mastro AM, Vogler EA. Influence of substratum surface chemistry/energy and topography on the human fetal osteoblastic cell line hFOB 1.19: Phenotypic and genotypic responses observed in vitro. *Biomaterials* 2007;28(31):4535-4550.
8. Rupp F, Scheideler L, Olshanska N, deWild M, Wieland M, Geis-Gerstorfer J. Enhancing surface free energy and hydrophilicity through chemical modification of microstructured titanium implant surfaces. *J Biomed Mater Res* 2006;76A:323-334.

9. Zhao G, Schwartz Z, Wieland M, Rupp F, Geis-Gerstorfer J, Cochran DL, et al. High surface energy enhances cell response to titanium substrate microstructure. *J Biomed Mater Res* 2005;74A:49-58.
10. Schwartz Z, Raz P, Zhao G, Barak Y, Tauber M, Yao H, et al. Effect of micrometer-scale roughness of the surface of ti6al4v pedicle screws in vitro and in vivo. *J Bone Joint Surg Am* 2008;90A(11):2485-2498.
11. Att W, Tsukimura N, Suzuki T, Ogawa T. Effect of supramicron roughness characteristics produced by 1-and 2-step acid etching on the osseointegration capability of titanium. *Int J Oral Maxillofac Implants* 2007;22(5):719-728.
12. Zhao G, Zinger O, Schwartz Z, Wieland M, Landolt D, Boyan BD. Osteoblast-like cells are sensitive to submicron-scale surface structure. *Clin Oral Implants Res* 2006;17(3):258-264.
13. Kubo K, Tsukimura N, Iwasa F, Ueno T, Saruwatari L, Aita H, et al. Cellular behavior on tio2 nanonodular structures in a micro-to-nanoscale hierarchy model. *Biomaterials* 2009;30(29):5319-5329.
14. Mendonca G, Mendonca DBS, Aragao FJL, Cooper LF. The combination of micron and nanotopography by h2so4/h2o2 treatment and its effects on osteoblast-specific gene expression of hmscs. *J Biomed Mater Res* 2010;94A(1):169-179.
15. Schwartz Z, Lohmann CH, Wieland M, Cochran DL, Dean DD, Textor M, et al. Osteoblast proliferation and differentiation on dentin slices are modulated by pretreatment of the surface with tetracycline or osteoclasts. *J Periodontol* 2000;71(4):586-597.
16. Mulari MTK, Qu Q, Harkonen PL, Vaananen HK. Osteoblast-like cells complete osteoclastic bone resorption and form new mineralized bone matrix in vitro. *Calcif Tissue Int* 2004;75(3):253-261.
17. Mori S, Burr DB. Increased intracortical remodeling following fatigue damage. *Bone* 1993;14(2):103-109.
18. Baron R, Neff L, Louvard D, Courtoy PJ. Cell-mediated extracellular acidification and bone-resorption - evidence for a low ph in resorbing lacunae and localization of a 100-kd lysosomal membrane-protein at the osteoclast ruffled border. *J Cell Biol* 1985;101(6):2210-2222.
19. Chambers TJ, Revell PA, Fuller K, Athanasou NA. Resorption of bone by isolated rabbit osteoclasts. *J Cell Sci* 1984;66(MAR):383-399.
20. Rho JY, Kuhn-Spearing L, Zioupos P. Mechanical properties and the hierarchical structure of bone. *Med Eng Phys* 1998;20(2):92-102.
21. Boyde A, Ali NN, Jones SJ. Optical and scanning electron-microscopy in the single osteoclast resorption assay. *Scan Electron Microsc* 1985:1259-1271.
22. Boyan BD, Schwartz Z, Lohmann CH, Sylvia VL, Cochran DL, Dean DD, et al. Pretreatment of bone with osteoclasts affects phenotypic expression of osteoblast-like cells. *J Orthop Res* 2003;21(4):638-647.
23. Teitelbaum SL, Ross FP. Genetic regulation of osteoclast development and function. *Nat Rev Genet* 2003;4(8):638-649.
24. Kieswetter K, Schwartz Z, Hummert TW, Cochran DL, Simpson J, Dean DD, et al. Surface roughness modulates the local production of growth factors and cytokines by osteoblast-like mg-63 cells. *J Biomed Mater Res* 1996;32(1):55-63.
25. Raines AL, Olivares-Navarrete R, Wieland M, Cochran DL, Schwartz Z, Boyan BD. Regulation of angiogenesis during osseointegration by titanium surface microstructure and energy. *Biomaterials* 2010;31(18):4909-4917.

26. Buser D, Schenk RK, Steinemann S, Fiorellini JP, Fox CH, Stich H. Influence of surface characteristics on bone integration of titanium implants - a histomorphometric study in miniature pigs. *J Biomed Mater Res* 1991;25(7):889-902.
27. Cochran DL, Schenk RK, Lussi A, Higginbottom FL, Buser D. Bone response to unloaded and loaded titanium implants with a sandblasted and acid-etched surface: A histometric study in the canine mandible. *J Biomed Mater Res* 1998;40(1):1-11.
28. Cochran DL. A comparison of endosseous dental implant surfaces. *J Periodontol* 1999;70(12):1523-1539.
29. Cochran DL, Buser D, ten Bruggenkate CM, Weingart D, Taylor TM, Bernard JP, et al. The use of reduced healing times on iti (r) implants with a sandblasted and acid-etched (sla) surface: Early results from clinical trials on iti (r) sla implants. *Clin Oral Implants Res* 2002;13(2):144-153.
30. Lipski AM, Pino CJ, Haselton FR, Chen IW, Shastri VP. The effect of silica nanoparticle-modified surfaces on cell morphology, cytoskeletal organization and function. *Biomaterials* 2008;29(28):3836-3846.
31. Curtis ASG, Gadegaard N, Dalby MJ, Riehle MO, Wilkinson CDW, Aitchison G. Cells react to nanoscale order and symmetry in their surroundings. *IEEE Trans Nanobioscience* 2004;3(1):61-65.
32. Riehle MO, Dalby MJ, Johnstone H, MacIntosh A, Affrossman S. Cell behaviour of rat calvaria bone cells on surfaces with random nanometric features. *Mater Sci Eng C Biomimetic Supramol Syst* 2003;23(3):337-340.
33. Ward BC, Webster TJ. Increased functions of osteoblasts on nanophase metals. *Mater Sci Eng C Biomimetic Supramol Syst* 2007;27(3):575-578.
34. Biggs MJP, Richards RG, Gadegaard N, McMurray RJ, Affrossman S, Wilkinson CDW, et al. Interactions with nanoscale topography: Adhesion quantification and signal transduction in cells of osteogenic and multipotent lineage. *Journal of Biomedical Materials Research Part A* 2009;91A(1):195-208.
35. Palin E, Liu HN, Webster TJ. Mimicking the nanofeatures of bone increases bone-forming cell adhesion and proliferation. *Nanotechnology* 2005;16(9):1828-1835.
36. Dalby MJ, McCloy D, Robertson M, Wilkinson CDW, Oreffo ROC. Osteoprogenitor response to defined topographies with nanoscale depths. *Biomaterials* 2006;27(8):1306-1315.
37. Webster TJ, Ergun C, Doremus RH, Siegel RW, Bizios R. Enhanced functions of osteoblasts on nanophase ceramics. *Biomaterials* 2000;21(17):1803-1810.
38. Webster TJ, Eijffinger JU. Increased osteoblast adhesion on nanophase metals: Ti, ti6al4v, and cocrmo. *Biomaterials* 2004;25(19):4731-4739.
39. Washburn NR, Yamada KM, Simon CG, Kennedy SB, Amis EJ. High-throughput investigation of osteoblast response to polymer crystallinity: Influence of nanometer-scale roughness on proliferation. *Biomaterials* 2004;25(7-8):1215-1224.
40. Cai KY, Bossert J, Jandt KD. Does the nanometre scale topography of titanium influence protein adsorption and cell proliferation? *Colloids Surf B Biointerfaces* 2006;49(2):136-144.
41. Zinger O, Zhao G, Schwartz Z, Simpson J, Wieland M, Landolt D, et al. Differential regulation of osteoblasts by substrate microstructural features. *Biomaterials* 2005;26(14):1837-1847.
42. Guo J, Padilla RJ, Ambrose W, De Kok IJ, Cooper LF. The effect of hydrofluoric acid treatment of tio2 grit blasted titanium implants on adherent osteoblast gene expression in vitro and in vivo. *Biomaterials* 2007;28(36):5418-5425.

43. Mendonca G, Mendonca DBS, Simoes LGP, Araujo AL, Leite ER, Duarte WR, et al. The effects of implant surface nanoscale features on osteoblast-specific gene expression. *Biomaterials* 2009;30(25):4053-4062.
44. Zhao L, Mei S, Chu PK, Zhang Y, Wu Z. The influence of hierarchical hybrid micro/nano-textured titanium surface with titania nanotubes on osteoblast functions. *Biomaterials* 2010;31(19):5072-5082.
45. Mendes VC, Moineddin R, Davies JE. The effect of discrete calcium phosphate nanocrystals on bone-bonding to titanium surfaces. *Biomaterials* 2007;28(32):4748-4755.
46. Gittens RA, Sandhage KH, Schwartz Z, Tannenbaum R, Boyan BD. Surface modification under controlled oxidative environment. U.S. Patent Application No. 61/299,433, 2010.
47. Bretaudiere JP, and Spillman, T. Alkaline phosphatases. *Methods of Enzymatic Analysis*, Verlag Chemica 1984;75-92.
48. Boyan BD, Batzer R, Kieswetter K, Liu Y, Cochran DL, Szmuckler-Moncler S, et al. Titanium surface roughness alters responsiveness of mg63 osteoblast-like cells to 1 alpha,25-(oh)(2)d-3. *J Biomed Mater Res* 1998;39(1):77-85.
49. Murray JL, Wriedt HA. Phase diagrams of binary titanium alloys. Metals Park, OH: ASM International, 1987.
50. Unnam J, Clark RK. Oxidation of commercial purity titanium. *Oxid Met* 1986;26(3-4):231-252.
51. Lian JB, Stein GS, Bortell R, Owen TA. Phenotype suppression - a postulated molecular mechanism for mediating the relationship of proliferation and differentiation by fos/jun interactions at ap-1 sites in steroid responsive promoter elements of tissue-specific genes. *J Cell Biochem* 1991;45(1):9-14.
52. Stein GS, Lian JB. Molecular mechanisms mediating proliferation/differentiation interrelationships during progressive development of the osteoblast phenotype. *Endocr Rev* 1993;14(4):424-442.
53. Stein GS, Lian JB, Stein JL, VanWijnen AJ, Montecino M. Transcriptional control of osteoblast growth and differentiation. *Physiol Rev* 1996;76(2):593-629.
54. Lian JB, Stein GS. Concepts of osteoblast growth and differentiation - basis for modulation of bone cell-development and tissue formation. *Crit Rev Oral Biol Medicine* 1992;3(3):269-305.

CHAPTER 4. THE ROLE OF TITANIUM SURFACE MICRO/NANOTOPOGRAPHY AND WETTABILITY ON THE DIFFERENTIAL RESPONSE OF HUMAN OSTEOBLAST LINEAGE CELLS

In [Gittens RA, Olivares-Navarrete R, Cheng A, Anderson DM, McLachlan T, Stephan I, Geis-Gerstorf J, Sandhage KH, Fedorov AG, Rupp F, Boyan BD, Tannenbaum R, Schwartz Z. The roles of titanium surface micro/nanotopography and wettability on the differential response of human osteoblast lineage cells. *Acta Biomater* 2012;(Submitted).]

4.1. Introduction

While implants can provide important solutions to dental and orthopaedic problems, they still have undesirable failure rates in patients who are compromised by disease or age [1, 2]. Titanium (Ti) is widely used for implant applications due to its favorable weight-to-strength ratio and good biological performance in bone, which is intimately dependent on surface characteristics such as surface roughness, chemistry and wettability. Surface topographical modifications at the micrometer scale, such as are induced by acid etching and sandblasting, have been used effectively to enhance osteoblastic lineage cell differentiation *in vitro* [3, 4], and osseointegration *in vivo* [5] and clinically [6] compared to smoother surfaces. Recently, the addition of nanostructures to the surface of implants, to better mimic the hierarchical structure of bone, has also shown promising results *in vitro* [7], *in vivo* [8] and in the clinic [9, 10], which validates the biological relevance of nanotopography for bone formation.

Surface wettability can also influence implant osseointegration, with hydrophilic surfaces promoting an environment conducive to bone formation, as evidenced by enhanced osteoblast maturation *in vitro* [11, 12] and improved clinical success rates [13]. Certain surface treatments on clinically-available implants, such as microroughening and sterilization, can render surfaces hydrophobic due to adsorption of hydrocarbons and other contaminants [14, 15]. This can delay the initial interactions

between the implant and the biological milieu, thereby impacting the subsequent cellular responses [16, 17].

The most common techniques to measure surface wettability (*i.e.*, optical sessile-drop contact angle measurements) were devised for smooth samples and only provide a static and approximate evaluation for microrough, clinically-relevant surfaces [18, 19] (Figure 4.1A). Other factors that complicate the sessile-drop technique include variability in the chemistry of the wetting liquid and in the drop volume and size, as well as changes in vapor pressure and evaporation with temperature and time [18, 20]. Advancing and receding angles can be obtained with goniometers used for sessile-drop analyses; however, the dynamic information that can be extracted from the tilting of the stage is rather limited.

Other contact angle analyses have been developed to obtain a better representation of the true nature of the wettability of surfaces with complex topography. The environmental scanning electron microscope (ESEM) provides enhanced spatial resolution and an environment with controlled pressure, temperature and humidity for microscale assessment of contact angle during nucleation, growth and coalescence of condensed droplets. ESEM imaging of water condensation can help minimize confounding results by avoiding air entrapment between microscale surface roughness features, which may make the surface appear more hydrophobic [21, 22] (Figure 4.1B). Dynamic contact angle analysis using the Wilhelmy plate technique, in which a specimen is immersed into a known liquid using a tensiometer to measure the balancing forces, can also be used for the comprehensive assessment of surface wettability on non-ideal surfaces [23, 24] (Figures 4.1C, D).

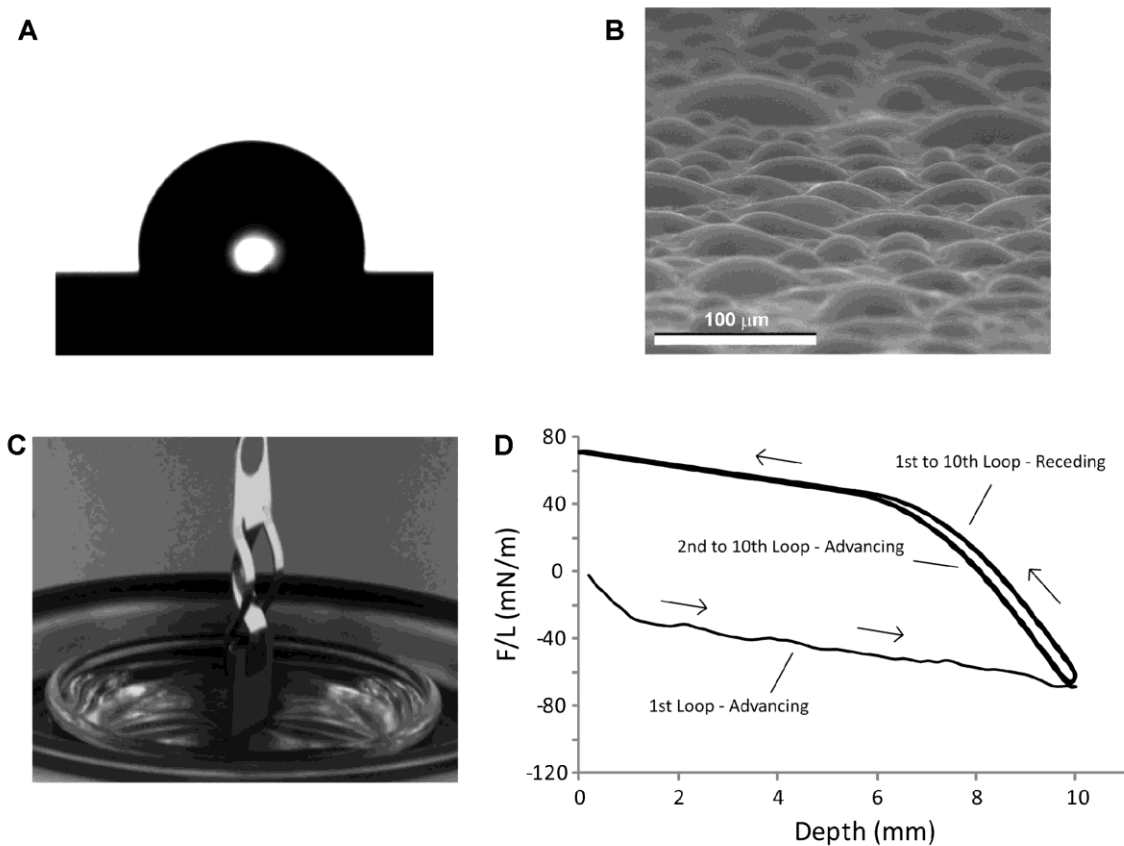


Figure 4.1. Static and dynamic evaluations of surface wettability of Ti specimens. (A) Micrograph from a goniometer used to measure contact angles using the sessile-drop technique. (B) ESEM image of the condensation of water on the surface of Ti specimens for contact angle assessment. (C) Photograph of the Wilhelmy plate setup revealing the use of a tensiometer to suspend a rectangular Ti specimen that is immersed in a water reservoir. (D) Example of a typical DCA 10-loop cycle, showing the advancing and receding curves.

A recent study by our lab demonstrated that osteoblast-like MG63 cell maturation and local factor production was synergistically enhanced when exposed to oxidation-induced nanostructures superimposed on the surface of microrough Ti specimens [25]. Surface characterization of the nanomodified specimens revealed that other surface properties, such as microroughness and wettability, as evaluated by the sessile-drop technique, were not affected by the oxidation treatment, leading to the conclusion that the addition of nanostructures was mainly responsible for the enhanced osteoblast response. However, experimental observations during the preparation of the specimens for contact angle analyses suggested that the dynamic behavior of the wettability of original and nanomodified specimens might be different (*i.e.*, water droplets would easily roll off microrough surfaces, while the droplets had to be removed with compressed nitrogen from the surface of micro/nanostructured specimens), which could have an influence on the observed osteoblast response.

Mesenchymal stem cells (MSCs) and osteoprogenitor cells operate *in vivo* as initial colonizers of an implant surface due to their ability to migrate on osteoconductive surfaces of titanium implants [26], but comparatively little is known concerning their osteoblastic differentiation in response to implant surface properties, including nanotopography and wettability [27]. Few studies have evaluated MSC osteoblastic differentiation on nanomodified surfaces, and most have used exogenous factors such as β -glycerophosphate, dexamethasone, and bone morphogenetic protein-2 (BMP-2) to force osteoblastic differentiation [28-30], which could obscure the real effects of the surface nanotopography [31]. We have recently demonstrated that human MSCs can differentiate into osteoblasts when cultured on Ti surfaces possessing microscale roughness, even in the absence of these media supplements [32]. In the same study, it was found that MSCs could react synergistically to surface hydrophilicity when cultured

on microrough surfaces. However, it is not known if osteoblastic differentiation of MSCs is a general response to microrough surfaces or if it can be affected by the superposition of nanoscale features, nor is it clear that surface wettability is involved in this response.

The goal of the present study was to test the hypothesis that nanostructural features on implant surfaces can affect the dynamic wettability of microrough Ti specimens, and that such surface property changes can, in turn, modulate the osteoblastic differentiation of osteoblast lineage cells in the absence of any exogenous soluble factors. To test this hypothesis, we superimposed nanostructures on clinically-relevant, microrough Ti surfaces and examined the responses of osteoblast-like MG63 cells and human MSCs without the addition of exogenous soluble osteogenic factors.

4.2. Materials and Methods

4.2.1. Titanium Specimens and Surface Modification Treatments

Commercially pure Ti specimens (ASTM F67 unalloyed Ti grade 2 for surgical implant applications, sheet stock) with a cylindrical (15 mm in diameter, 1 mm thick) or rectangular (20 x 10 x 1 mm³) shape were treated as described previously [11], to produce machined and pickled “pre-treatment” disks that were relatively smooth (referred to herein as PT specimens), and microrough “sandblasted-large-grit-acid-etched” disks (referred to herein as SLA specimens). All specimens were supplied by Institut Straumann AG (Basel, Switzerland).

Some of the microsmooth (PT) and microrough (SLA) specimens were further processed using a simple oxidation treatment to superimpose nanostructures on the surface, as described previously [25], to yield nanomodified, microsmooth (NMPT) or nanomodified, microrough (NMSLA) specimens. This oxidation treatment consisted of exposing the samples to flowing (0.85 standard liters per minute) synthetic air (21 % O₂,

79 % N₂) at 1 atm and 740 °C for 90 minutes [25]. All modified and unmodified disks were ultrasonically cleaned in detergent (Micro-90; International Products Corporation, Burlington, NJ) and ultrapure water (Advantage A10; Millipore, Billerica, MA), followed by autoclave sterilization (Model 2540E; Tuttnauer, Hauppauge, NY) for 20 minutes at 121 °C and 15 PSI before use. Surface characterization and cell culture studies, described below, focused on clinically-relevant, microrough specimens SLA and NMSLA, while microsmooth specimens (PT, NMPT) were used only as reference surfaces for topographical studies of the nanomodification and cell studies.

4.2.2. Surface Characterization

4.2.2.1. *Electron Microscopy*

Surface topography was qualitatively evaluated using a field-emission-gun scanning electron microscope (Ultra 60 FEG-SEM; Carl Zeiss SMT Ltd., Cambridge, UK). Secondary electron (SE) images were recorded using a 5 kV accelerating voltage and 30 µm aperture.

4.2.2.2. *Atomic Force Microscopy (AFM)*

Surface measurements at the nanoscale were evaluated using AFM (Nano-R AFM; Pacific Nanotechnology, Santa Clara, CA) in close-contact mode. Analyses were conducted using silicon probes (P-MAN-SICC-O, Agilent Technologies, Santa Clara, CA) with dimensions of 1.14 cm x 0.25 cm² and tip radii of up to 10 nm, a nominal force constant of 40 N/m, and a nominal resonance frequency of 300 kHz. Microsmooth specimens were used for AFM analyses due to a z-height limit of 5 µm for the AFM, which was less than the feature size of the microrough surfaces. Each AFM analysis was performed over a 730 nm x 730 nm specimen area. Two samples of each type of microsmooth specimen were scanned three times each, under ambient atmosphere. The raw data were plane-leveled to remove tilt by applying a numerical second-order

correction, and mean values of surface roughness (S_a) were determined using NanoRule+ software (Pacific Nanotechnology).

4.2.2.3. Laser Confocal Microscopy (LCM)

Surface roughness at the microscale was evaluated using a laser confocal microscope (Lext LCM; Olympus, Center Valley, PA). Each LCM analysis was performed over a 644 μm x 644 μm area using a scan height step of 100 nm, a 20X objective, and a cutoff wavelength of 100 μm . Two samples of every specimen type were scanned three times each under ambient atmosphere. Mean values of surface roughness average (S_a) were determined.

4.2.2.4. X-ray Photoelectron Spectroscopy (XPS)

Relative atomic concentration and chemical bonding information were obtained from the specimen surfaces by XPS analyses (Thermo K-Alpha XPS; Thermo Fisher Scientific, West Palm Beach, FL). The XPS instrument was equipped with a monochromatic Al-K α X-ray source ($h\nu = 1468.6$ eV). The XPS analysis chamber was evacuated to a pressure of 5×10^{-8} mbar or lower before collecting XPS spectra. Spectra were collected using an X-ray spot size of 400 μm and pass energy of 100 eV, with 1 eV increments, at a 55 ° takeoff angle. Two specimens of the SLA and NMSLA groups were scanned three times each and all values were averaged.

4.2.2.5. Sessile-Drop Contact Angle Measurements

Contact angle measurements were obtained using a drop shape analysis system (DSA 10-MK 2; Krüss, Hamburg, Germany) equipped with an automated stage and droplet dispenser, a digital camera, and image analysis software. Ultra-pure water (Simplicity 185 UV; Millipore, Billerica, MA), with water resistivity of 18.2 M Ω ·cm at 25 °C, was used as the wetting liquid with a drop size of 5 μL (Figure 4.1A). Sessile drop contact

angles of the air-water-substrate interface were measured three times each on two samples from each specimen type.

4.2.2.6. Environmental Scanning Electron Microscope (ESEM) Contact Angle Analyses

Contact angle measurements at the micrometer level were assessed with an ESEM system (Quanta 200; FEI, Hillsboro, OR). Samples were placed directly onto a Peltier cooler (C2-08-0401; Tellurex, Traverse City, MI) in the ESEM chamber using a thin layer of thermal grease to ensure good thermal contact. The samples were oriented vertically, such that the electron beam was incident almost parallel to the surface, providing a side view of a droplet to assess contact angle. Imaged droplets were kept small relative to the capillary length of water ($\ll 2$ mm) such that surface tension forces were dominant over gravitational forces. The chamber was evacuated and then backfilled with pure deionized water vapor to a pressure of 773 Pa. To generate condensed water droplets on the surface, power was supplied to the Peltier cooler to cool the surface temperature below the saturation temperature of 4 °C at 773 Pa (Figure 4.1B). The condensation of droplets on the surface was recorded and contact angles of the right-side interface of at least 10 droplets per image were calculated using image analysis software (ImageJ; NIH Software).

4.2.2.7. Dynamic Contact Angle (DCA) Analyses

Wettability and contact angle hysteresis were tensiometrically examined by the Wilhelmy method using an electrobalance (Sigma 70; Attension/KSV Instruments, Ltd., Espoo, Finland), as described previously [33]. Briefly, this technique uses a tensiometer to measure small changes in the forces (*i.e.* weight, buoyancy, and surface tension forces) exerted on a specimen of known size that is immersed in a reservoir of controlled liquid (Figure 4.1C). The force balance equation is as follows:

$$F = M \cdot g - \rho \cdot g \cdot t \cdot H \cdot d + L \cdot \gamma_L \cdot \cos\theta \quad (1)$$

where F is the total force exerted on the sample, M is the mass of the plate, g is the gravitational acceleration, ρ is the liquid density, t is the thickness of the plate, H is the width of the plate, d is the immersion-emersion depth, L is the plate perimeter [$L = 2(t+H)$], γ_L is the liquid surface tension, and θ is the contact angle at the liquid-solid-vapor interface. By setting the balance (*i.e.*, weight of the specimen) to zero before each run and using a linear regression to zero for the immersion-emersion depth, the first two terms of equation (1) are cancelled and the contact angle can be calculated directly from the force measured by the tensiometer.

Ultra-pure water was selected as the liquid phase for the experiments, and the specimens were immersed and then emerged at a speed of 10 mm/min for a depth of 10 mm for 10 cycles using a motorized water reservoir (Figures 4.1C, D). Once the meniscus had formed, the contact angle was assumed to remain constant throughout the immersion-emersion loop. Contact angle calculations were performed ignoring the initial 6 mm of immersion or emersion from each loop. All measurements were performed at room temperature in an environment with controlled temperature (23 °C) and relative humidity (35 %). Two samples of each specimen group were analyzed. For one of the studies, the autoclave-sterilized SLA specimens that had been analyzed by DCA were subsequently cleaned using ultrasonication in ultra-pure water for 15 minutes and dried for 2 hours under vacuum using a vacuum pump (Trivac D4B; Oerlikon Leybold Vacuum GmbH, Koeln, Germany). These specimens were used again for DCA analyses to determine whether the surface response to the immersion-emersion loops was permanent or dependent on physisorbed molecules.

4.2.3. Cell Culture Model

Human osteoblast-like MG63 cells and human mesenchymal stem cells (MSCs) were used for this study. MG63 cells were obtained from the American Type Culture Collection (Rockville, MD) and were cultured in Dulbecco's modified Eagle medium (DMEM cellgro®; Mediatech, Inc., VA) containing 10 % fetal bovine serum (FBS; Gibco, Carlsbad, CA) and 1 % penicillin-streptomycin. Human MSCs were purchased from a commercial vendor (Lonza, Walkersville, MD) and grown in MSC Growth Medium (MSCGM; Lonza). All cells were cultured at 37 °C with 5 % CO₂ and 100 % humidity. MG63s and MSCs were cultured on tissue culture polystyrene (TCPS) to check for confluence, on PT surfaces as a control, or on the different microrough, clinically-relevant surfaces (SLA, NMSLA) at a seeding density of 10,000 cells/cm². Cells were fed 24 hours after plating, and then every 48 hours until confluence, as evaluated on the TCPS substrates. At confluence, cells were incubated with fresh medium for 24 hours and harvested for assays. Conditioned media were collected and stored at -80 °C until assayed. Cell layers were washed twice with serum-free medium and released from their substrate by two sequential incubations in 500 µL 0.25 % trypsin for 10 minutes at 37 °C. Cells were resuspended in 500 µL 0.05 % Triton-X-100® and lysed by sonication. MG63 cell number was evaluated by measuring DNA content with a commercially-available kit (Quant-iT™ PicoGreen® dsDNA assay; Invitrogen, Carlsbad, CA) and a fluorescent multimode detector (DTX880; Beckman Coulter, Brea, CA) with reference to a standard. MSCs were counted, before cell lysis, with a Z1 Coulter particle counter (Beckman Coulter, Brea, CA).

Osteoblastic differentiation was evaluated by measuring the osteocalcin content in the conditioned media as a late differentiation marker. Osteocalcin was measured using a commercially-available radioimmunoassay kit (Human Osteocalcin RIA Kit;

Biomedical Technologies, Stoughton, MA) as described previously [34], using a LS1500 gamma counter (Perkin Elmer, Waltham, CA). The conditioned media were also assayed for protein levels of local factors important for bone development. Osteoprotegerin (OPG), a cytokine that works as a decoy receptor for “receptor activator for nuclear factor κ B ligand” (RANKL) to inhibit osteoclastogenesis, was measured using enzyme-linked immunosorbent assay (ELISA) kits (DY805 Osteoprotegerin DuoSet; R&D Systems, Minneapolis, MN). Vascular endothelial growth factor (VEGF), a growth factor involved in vasculogenesis and angiogenesis, was also measured using an ELISA kit (DY293B VEGF DuoSet; R&D Systems).

4.2.4. Statistical Analysis

Data from experiments evaluating the surface characteristics of the substrates are presented as the mean \pm one standard deviation (SD) of all the measurements performed on different samples of the same specimen type. Data from experiments examining cell response are presented as the mean \pm standard error of the treatment (SLA, NMSLA) over control (PT) for two experiments with six independent cultures per variable. All experiments were repeated at least twice to ensure reproducibility. Data were evaluated by analysis of variance, and significant differences between groups were determined using Student's t-test. A p value below 0.05 was considered to indicate a statistically-significant difference.

4.3. Results

4.3.1. Characterization of Nanomodified Surfaces

Secondary electron images of the original SLA surfaces revealed peaks and valleys on the order of tens of micrometers as a result of the sandblasting process, with additional sharp sub-microscale features left from the acid-etch treatment (Figure 4.2A).

The surface of the microrough specimens that had received the 740 °C oxidation treatment for 90 minutes (NMSLA) possessed high and homogeneous concentrations of nanostructures (Figure 4.2B). The qualitative increase in the nanoscale roughness of the Ti surfaces detected by electron microscopy after the oxidation treatment was confirmed by AFM analyses (Figure 4.3), which revealed significant enhancements in the values of the mean nanoscale roughness average. As expected, roughness average measured by laser confocal microscopic analyses revealed that the microroughness of the SLA and NMSLA specimens was significantly higher than for the pre-treatment specimens (PT and NMPT) (Figure 4.3). In addition, surface microroughness, as determined by average roughness (S_a), was not noticeably affected by the superposition of surface nanostructures during the subsequent oxidation treatment.

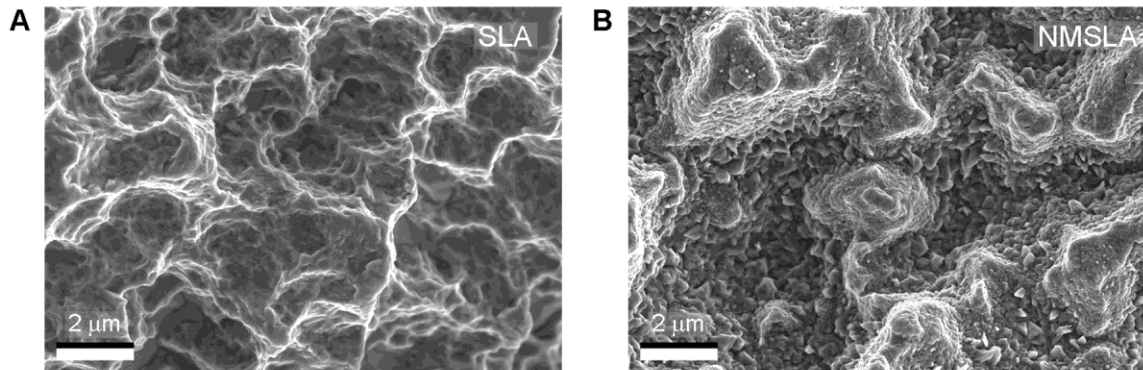


Figure 4.2. Morphological evaluation of micro/nanostructured Ti specimens. SE images of (A) microrough Ti specimens (SLA) and (B) microrough specimens that were subsequently heat-treated to superimpose oxidation-induced nanostructures on the surface (NMSLA). SLA surfaces possessed large peaks and valleys in the order of tens of micrometers as a result of the sandblasting process, with some sharp sub-microscale features left from the acid-etch treatment. After the nanomodification oxidation treatment for 90 minutes at 740 °C in flowing synthetic air, the NMSLA surfaces possessed high and homogeneous surface area concentrations of nanostructures.

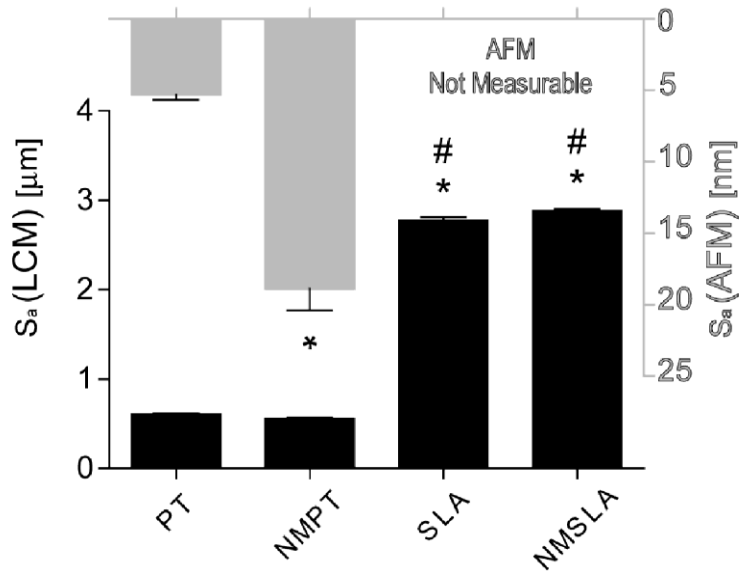


Figure 4.3. Mean values of the surface roughness average (S_a) of original and nanomodified surfaces measured by laser confocal microscopy (LCM, black bars) and atomic force microscopy (AFM, grey bars). AFM scans were not possible on microrough SLA and NMSLA specimens due to z-height tool limitations. * refers to a statistically-significant p value below 0.05 vs. PT; # refers to a statistically-significant p value below 0.05 vs. NMPT.

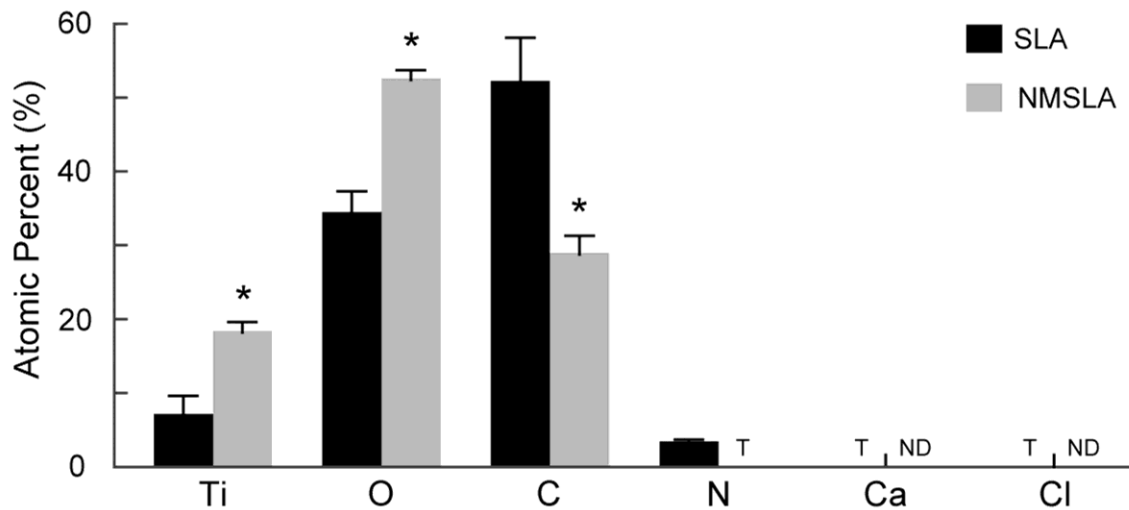


Figure 4.4. Surface elemental compositions of the SLA and NMSLA specimens measured by XPS. All surfaces were mainly composed of Ti, O and C. N was also present at low levels on the SLA surfaces, while NMSLA surfaces only had traces (T) of N. Traces of other contaminants such as Ca and Cl were found on the surface of SLA specimens, but these were not detectable (ND) on the SLA surfaces. * refers to a statistically-significant p value below 0.05 vs. SLA.

The addition of nanoscale features to microrough SLA surfaces by oxidation heat treatment altered the surface chemistry of the specimens (Figure 4.4). The elemental compositions of both the original SLA and nanomodified NMSLA surfaces after autoclave sterilization included the same elements, Ti, atomic oxygen (O) and carbon (C), as the major components. However, the oxidation treatment altered the concentrations of these elements on the surface, with a significant reduction in C and significantly higher concentrations of Ti and O on the oxidized surfaces than for the microrough specimens. Small concentrations of nitrogen (N) were also present on the original SLA surfaces, while only traces were found on the NMSLA surfaces. In addition, traces of impurities such as calcium (Ca) and chlorine (Cl) were found on the SLA specimens, which were not detectable on NMSLA specimens.

Values obtained for the water contact angles for microrough and nanomodified Ti specimens were dependent on the measurement method. Optical sessile-drop contact angle analysis conducted in air, a technique commonly used to indirectly assess the relative surface energy of biomaterials, showed that autoclave-sterilized SLA and NMSLA specimens exhibited strong hydrophobic responses to water (Figure 4.5A). However, in some cases the water droplet could not be dispensed on the surface of SLA specimens or would easily roll off, which was not observed for the NMSLA specimens. ESEM imaging in a pure water vapor atmosphere was used to evaluate the wetting behavior of condensed water droplets on the surfaces of the specimens at the micro scale. ESEM images revealed that the SLA and NMSLA specimens exhibited hydrophilic behavior with droplets having contact angles close to 50 °, whereas droplets that nucleated at length scales smaller than the roughness features exhibited complete wetting of the surface (Figure 4.5B, Video A.1). There was no significant difference in wettability of the SLA and NMSLA surfaces as observed from ESEM analyses.

Dynamic contact angle analyses of the SLA and NMSLA surfaces using the Wilhelmy balance technique provided a quantitative assessment of wettability that differed from the sessile drop measurements. Force graphs of 10-loop Wilhelmy experiments showed extremely negative F/L values for the initial advancing loop of SLA (Figure 4.5C) and NMSLA (Figure 4.5D) specimens. Subsequent immersion-emersion loops on the SLA specimens continued to show negative values with hysteresis, and the sample did not reach equilibrium even after the 10th loop. In contrast, NMSLA specimens presented more positive F/L values for all following loops without evidence of appreciable hysteresis. The sterilized SLA specimens that were ultrasonically cleaned and dried under vacuum after DCA and reanalyzed showed an initial loop with a slightly negative F/L value and more positive values for the subsequent loops with no appreciable hysteresis (Figure 4.5E). Contact angles calculated from the measured F/L values (Figure 4.6) indicated that the initial advancing angles of the autoclaved SLA and NMSLA specimens were hydrophobic and similar to the sessile-drop contact angle values. However, the second to tenth loops on the SLA specimens showed decreasing advancing angles that remained above 100 ° and receding angles that averaged around 70 °. In the case of NMSLA specimens, the second to tenth loops resulted in superhydrophilic advancing and receding contact angles of less than 10 °.

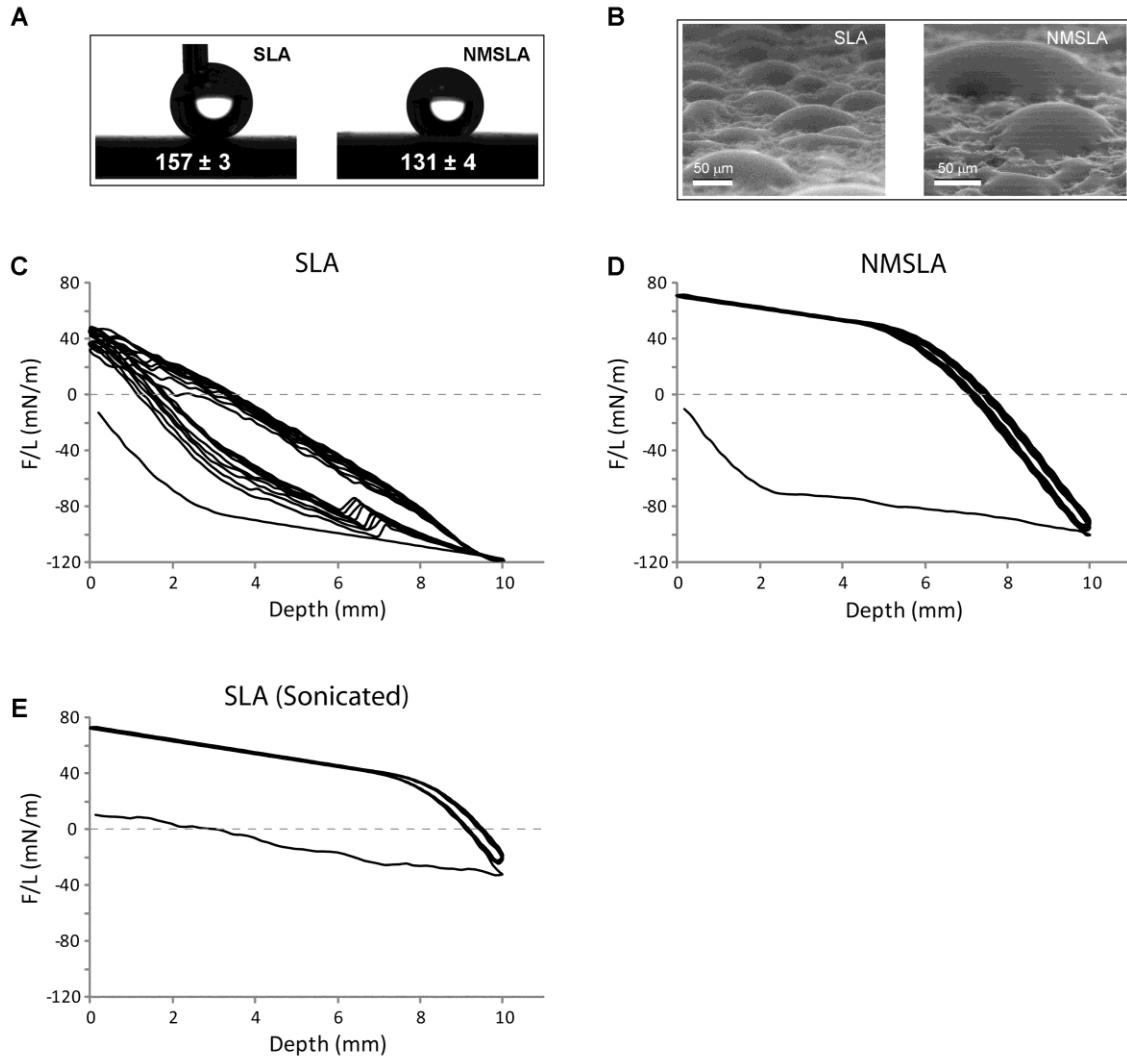


Figure 4.5. Static and dynamic contact angle analyses on SLA and NMSLA specimens. (A) Optical sessile-drop water contact angles on the surfaces of SLA and NMSLA specimens showed hydrophobic static responses. (B) ESEM image showing condensed water droplets on the surface of SLA and NMSLA specimens for contact angle evaluations. Some of the smaller droplets on the NMSLA surface exhibited complete wetting of the surface. (C-E) Force graphs of 10-loop Wilhelmy experiments showed extremely negative F/L values for the initial advancing loop of (C) SLA and (D) NMSLA specimens. Subsequent immersion-emersion loops on the SLA specimens continued to show negative values without reaching equilibrium. In contrast, NMSLA specimens presented positive F/L values for all following loops without evidence of appreciable hysteresis. (E) Sterilized SLA specimens used for dynamic contact angle analyses were ultrasonically cleaned in water and reanalyzed, showing a slightly negative F/L value for the initial loop and positive values for the subsequent loops with no appreciable hysteresis.

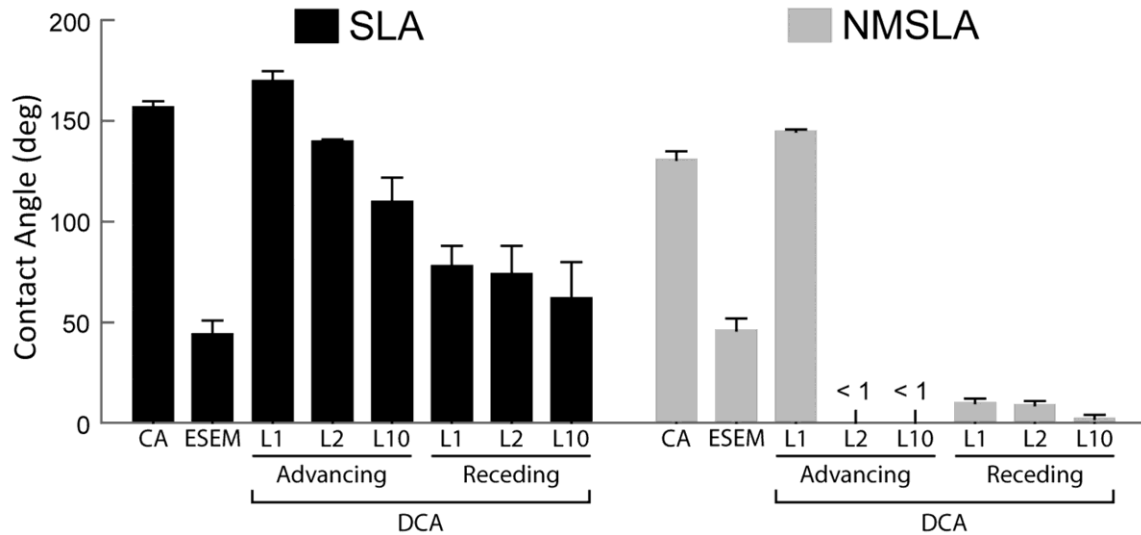


Figure 4.6. Comparison of the contact angles measured by the optical sessile-drop technique in air, ESEM in water vapor, or calculated from the measured F/L values from dynamic analyses of the autoclaved SLA and NMSLA specimens.

4.3.2. Osteoblast Lineage Cell Response to Nanomodified Surfaces

MG63 osteoblastic maturation was synergistically enhanced by the nanostructures superimposed onto microrough Ti surfaces, while MSC osteoblastic differentiation was suppressed by the same micro/nanostructured surfaces. Cell number (Figure 4.7A), which decreases as cells transition from a proliferative to a more mature state, was lower for MG63s on the microrough surfaces compared to the microsmooth control, with the lowest levels on the combined microrough and nanostructured NMSLA surfaces. MSCs on microrough SLA surfaces also had lower numbers than controls, similar to MG63s on SLA, but the numbers were back to control levels on the NMSLA surfaces. At the same time, the production of the late osteoblastic differentiation marker osteocalcin (Figure 4.7B) was higher for MG63s on the SLA group compared to controls

and significantly higher on NMSLA surfaces. MSCs on SLA surfaces also had higher levels of osteocalcin compared to controls, with an increase in production similar to that of MG63s on SLA. Osteocalcin production by MSCs on SLA surfaces was also significantly higher than on NMSLA surfaces, with the latter being no different than controls.

Levels of the anti-osteoclastogenesis factor osteoprotegerin (Figure 4.7C) and the angiogenic factor VEGF (Figure 4.7D) were also evaluated in association to the differentiation of the cells. MG63s produced higher levels of osteoprotegerin and VEGF on both microrough groups compared to microsmooth controls, with the highest levels found on the combined micro/nanostructured NMSLA surfaces. Conversely, MSCs produced slightly lower levels of osteoprotegerin on the different microrough groups compared to controls, with the lowest levels found on the NMSLA specimens. Additionally, MSCs produced higher levels of VEGF on SLA surfaces compared controls, while the levels on NMSLA specimens were slightly lower than controls.

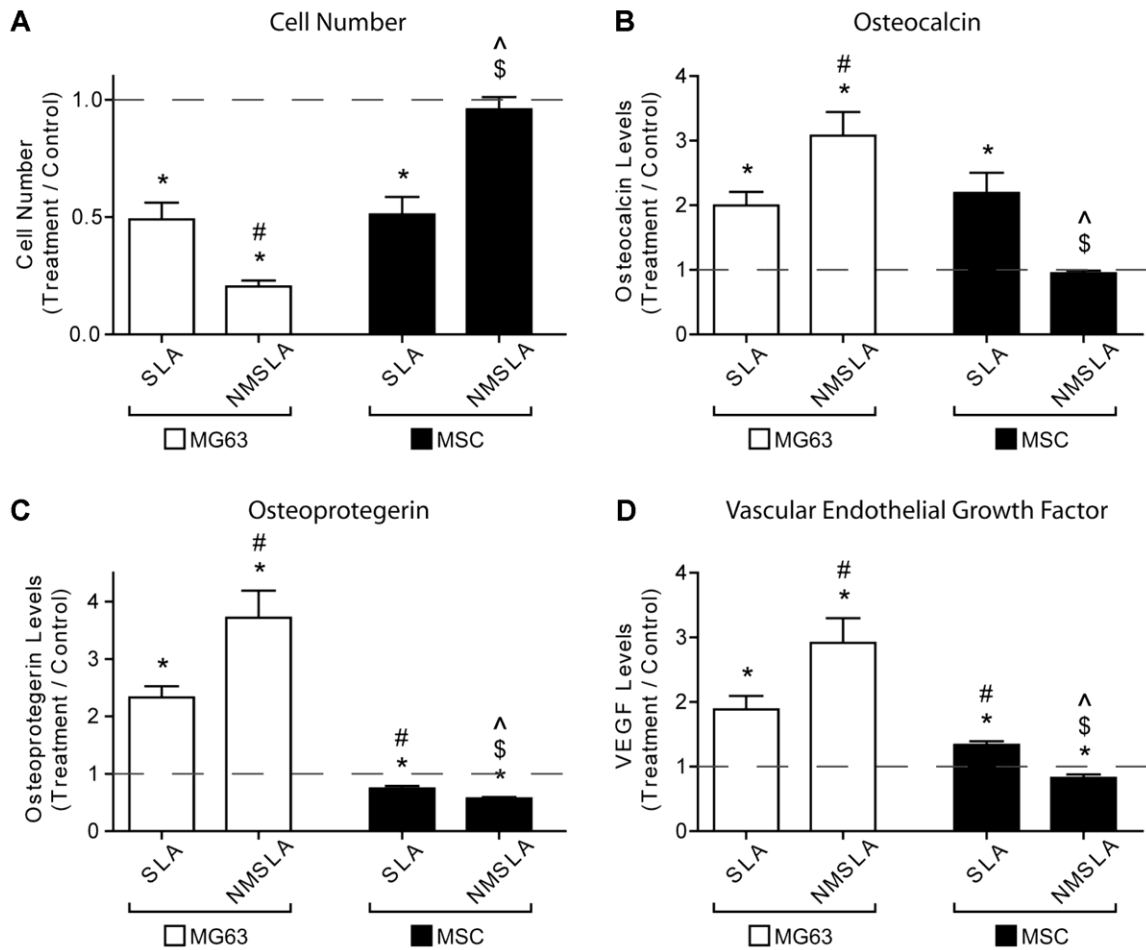


Figure 4.7. Effects of micro- and nanoscale surface modifications on immature osteoblast-like cells and human MSCs evaluated as treatment over microsmooth controls (dotted line). Osteoblasts and MSCs were plated on PT controls, SLA and NMSLA surfaces and grown to confluence. The nanomodification involves surface oxidation in flowing synthetic air for 90 minutes at 740 °C. At confluence, (A) cell number, (B) osteocalcin, (C) osteoprotegerin, and (D) VEGF levels were measured. Data represented are the mean \pm standard error of six independent samples. * refers to a statistically-significant p value below 0.05 vs. PT; # refers to a statistically-significant p value below 0.05 vs. SLA-MG63; \$ refers to a statistically-significant p value below 0.05 vs. NMSLA-MG63; ^ refers to a statistically-significant p value below 0.05 vs. SLA-MSC.

4.4. Discussion

In this study, the cellular responses of progenitor cells and cells representative of an immature osteoblastic phenotype have been compared on clinically-relevant, microrough titanium (Ti) specimens before and after surface superposition of oxidation-induced nanostructures. Osteoblast maturation, as evaluated by the production of osteoblast differentiation markers and local factors that promote osteogenesis, was significantly enhanced by the addition of nanostructures to microrough surfaces. In contrast, our results suggest that MSC osteoblastic differentiation and local osteogenic factor production were suppressed on the combined micro/nanostructured surfaces, whereas MSC cell numbers were increased. These results indicate that osteoblast-lineage cell response to nanostructures presented on the surface of microrough surfaces is dependent on their current differentiation state. Additionally, changes in surface wettability caused by the nanomodification may also be partly responsible for the cellular responses reported. These observations are discussed in detail below.

A surface nanomodification process recently developed by our group [25], which consists of a simple heat treatment to generate a homogeneous coverage of oxidation-induced nanostructures, was used to modify clinically-relevant, microrough Ti specimens. The treatment yielded a high density of nanostructural features on microrough surfaces, covering areas that would have been difficult to modify by line-of-sight sandblasting-based treatments (*i.e.*, standard treatments used for dental implant surfaces). Another attractive attribute of the oxidation-based treatment for the generation of nanostructures on Ti was that other surface characteristics, such as surface microroughness, remained constant, which allowed for reduced ambiguity in assessing the effect of the nanostructures on cell response.

Surface roughness evaluations at the nanoscale, as measured by AFM, quantitatively confirmed the presence of the nanostructures, while assessment by LCM showed no significant degradation in microroughness by the oxidation process, in agreement with our previous study [25]. The major elemental constituents on the surfaces were Ti, O, and C before and after the oxidation treatment. However, the concentrations of these elements were altered, with higher levels of Ti and O, and lower levels of C, on the nanomodified specimens. The surface concentrations of other impurities such as N, Ca, and Cl were also lower or nonexistent on the oxidized specimens. High levels of C on the surface of Ti specimens have been linked to hydrocarbon contamination during autoclave sterilization, which can also be responsible for the addition of other impurities such as N and Cl on the surfaces of Ti implants [15]. Most commercially-available dental implants are currently sterilized by gamma irradiation; however, autoclave sterilization is still widely used for orthopaedic implants. The effect of these impurities on cell response remains unclear, but our results indicate that the oxidation-based generation of surface nanostructures on microrough Ti specimens acted to reduce the presence of hydrocarbons and other impurities.

Static assessment of the wettability of microrough and combined micro/nanostructured surfaces indicated that both groups had strong hydrophobic responses, as shown previously on these same specimens [25]. ESEM measurements can provide insights about the wettability responses of surfaces at the microscale, but still depend on the assessment of single droplets [22]. Microrough and micro/nanostructured specimens exhibited more hydrophilic contact angles when evaluated by ESEM analyses in pure water vapor, compared to optical sessile-drop analyses conducted in ambient air, which suggested that the hydrophobic effect observed by the latter technique could have been due to air trapped underneath the

deposited droplet and that the Ti/TiO₂ surface possessed a hydrophilic nature in the absence of environmental contamination. Regardless, contact angle values obtained by each type of measurement were similar for the SLA and NMSLA specimens.

In contrast to static contact angle analyses, the dynamic behavior of the water/substrate interfaces revealed significant differences between the two types of samples. After sterilization, the microrough specimens exhibited a strong hydrophobic response that did not reach equilibrium even after 10 immersion-emersion loops. The receding angles, which were lower than 90 ° and thus hydrophilic, were still relatively high. Interestingly, the unstable hydrophobic response of the sterilized microrough specimens could be eliminated by cleaning them in ultra-pure water, suggesting that the sustained hydrophobic response was due to physisorbed contaminants on the surface. After the initial hydrophobic loop for all of the autoclaved micro/nanostructured specimens, subsequent advancing and receding loops showed complete wettability. Previous studies on microrough-only specimens without autoclave sterilization showed an initial hydrophobic advancing loop, with subsequent advancing and receding angles reaching an extremely hydrophilic equilibrium [23]. The latter results are unlike what was observed in the present study for the sterilized microrough specimens, but are in agreement with our results on the cleaned, microrough specimens as well as on the micro/nanostructured specimens. Observations of droplets that rolled off easily from SLA specimens, but not from NMSLA specimens, were consistent with the very low receding angles on the NMSLA specimens which were apparently due to a strong surface/water interaction with NMSLA specimens during dewetting (recession). The present data suggest that autoclave sterilization can degrade the dynamic surface wettability response of microrough specimens, possibly due to physisorption of surface contaminants as detected by XPS. The oxidation-based nanomodification process can

help maintain the hydrophilic dynamic behavior of the specimens, which may have an impact on cell response.

Osteoblasts responded synergistically to the combined micro/nanostructured surfaces in terms of maturation and local factor production, as reported in our previous study [25]. Lower osteoblast cell numbers were found on the microrough surfaces, with the lowest levels found on the combined microrough and nanostructured surfaces. In addition, synergistically higher production of the late differentiation marker osteocalcin was reported for the micro/nanostructured surfaces compared to controls and microrough specimens, indicating enhanced osteoblast maturation on these surfaces when taken together with the cell number results. Low cell number in combination with increased production of osteoblastic differentiation markers has been used previously to determine osteoblast maturation *in vitro* [35], in part due to a transcriptionally-restricted regulation between osteoblasts' proliferative and differentiating state [36]. Such osteoblast response is characteristic of microrough surfaces *in vitro* [37] and has been correlated to the successes of microrough surfaces relative to smoother surfaces *in vivo* [38] and in the clinic [39, 40]. Superposition of nanostructures on microrough surfaces also synergistically promoted the production of the anti-osteoclastogenic factor osteoprotegerin and the pro-angiogenic factor VEGF, as reported in our previous study using the same types of specimens [25]. Enhanced differentiation and higher production of local factors by osteoblasts have been reported for microrough surfaces with hydrophilic surfaces [16, 41], suggesting that the dynamic hydrophilic behavior of the micro/nanostructured specimens could be playing a role in the enhanced cell response.

MSC osteoblastic differentiation responded to microroughness, as seen previously [32], but did not react to nanostructures superimposed onto microrough Ti specimens. MSC numbers decreased on the microrough surfaces compared to the

microsmooth controls, to similar levels seen in osteoblasts on these same surfaces. Furthermore, the production of osteocalcin was enhanced on the microrough specimens relative to controls, again to similar levels observed in osteoblasts on these microrough surfaces, confirming the influence of microroughness on the enhanced differentiation of MSCs [3, 32]. Conversely, MSC numbers and osteocalcin production on the micro/nanostructured surfaces were similar to control levels, suggesting that the differentiation of MSCs was suppressed by the superposition of nanostructures. Additionally, compared to the microrough-only surfaces, the nanomodified microrough surfaces generated lower production of local factors associated with bone formation, osteoprotegerin and VEGF.

Our results fall in line with a recent study showing that polycaprolactone (PCL) surfaces with certain symmetric nanostructural features could promote MSC stemness *in vitro* without the use of any exogenous factors, as confirmed by lower production of the osteoblast markers osteocalcin and osteopontin as well as higher levels of the skeletal stem cell markers STRO-1 and ALCAM [42]. Although differences in the substrate characteristics between the studies does not allow for a direct comparison, the superposition of nanostructures on microrough Ti substrates still appeared to interfere with the osteoblastic differentiation of MSCs. MSCs are multipotent, thus it is possible that the nanotopography and wettability of the NMSLA surface elicited alternative lineage commitments. The fact that the cells were able to proliferate to the same extent as cells cultured on microsmooth control surfaces argues against quiescence being induced in the entire MSC population, although it is possible that the stemness property of a subset of cells was retained.

Other groups have reported enhanced osteoblastic differentiation of MSCs growing on micro/nanostructured surfaces [7, 43]. Nonetheless, the majority of these

studies used exogenous factors that can promote osteogenic differentiation of the stem cells, such as dexamethasone and β -glycerophosphate, effectively committing their MSCs to the osteoblast lineage. We observed that MG63 cells, which are immature osteoblasts, responded synergistically to the nanostructures on microrough Ti specimens with increased production of osteocalcin and other osteogenic proteins and this occurred even without the use of these soluble factors. This suggests that the state of maturation within the osteoblast lineage may determine that nature of the response to the material surface.

While surface micro/nanotopography is clearly a critical variable, variations in surface physicochemical properties are also important modulators of cell response. A previous study by our group showed enhanced osteoblastic differentiation by MSCs when grown on hydrophilic microrough Ti surfaces compared to hydrophobic specimens with the same topography [32], suggesting that the effect of superimposed nanostructures may play a more dominant role than wettability in the suppression of MSC osteoblastic differentiation found in the current study. The present results support recent observations using Ti6Al4V surfaces showing that recognition of surface nanostructures, and subsequent cell response, is dependent on the differentiation state of osteoblast lineage cells [44].

4.5. Conclusions

Our results demonstrate that osteoblastic lineage cell fate can be modulated by controlling surface characteristics, such as nanotopography and wettability, without the use of exogenous soluble factors, and the corresponding response is dependent on the differentiation state of the cells. These findings support the conclusion that the successful osseointegration of an implant depends on different contributions from

osteoblast lineage cells at different stages of osteoblast commitment. Nanostructures superimposed by oxidation onto microrough Ti surfaces, in the absence of any exogenous soluble factors, strongly enhanced the maturation of immature osteoblast-like cells, whereas the same surfaces suppressed MSC osteoblastic differentiation and osteogenic local factor production while supporting proliferation. Differences in the surface wettability introduced by the surface nanomodification may be partly responsible for the responses of osteoblast lineage cells.

4.6. References

1. Fransson C, Wennstrom J, Berglundh T. Clinical characteristics at implants with a history of progressive bone loss. *Clin Oral Implants Res* 2008;19(2):142-147.
2. Granstrom G. Osseointegration in irradiated cancer patients: An analysis with respect to implant failures. *J Oral Maxillofac Surg* 2005;63(5):579-585.
3. Wall I, Donos N, Carlqvist K, Jones F, Brett P. Modified titanium surfaces promote accelerated osteogenic differentiation of mesenchymal stromal cells in vitro. *Bone* 2009;45(1):17-26.
4. Kim MJ, Kim CW, Lim YJ, Heo SJ. Microrough titanium surface affects biologic response in MG63 osteoblast-like cells. *J Biomed Mater Res A* 2006;79(4):1023-1032.
5. Buser D, Schenk RK, Steinemann S, Fiorellini JP, Fox CH, Stich H. Influence of surface characteristics on bone integration of titanium implants - A histomorphometric study in miniature pigs. *J Biomed Mater Res* 1991;25(7):889-902.
6. Cochran DL, Jackson JM, Bernard JP, ten Bruggenkate CM, Buser D, Taylor TD, et al. A 5-year prospective multicenter study of early loaded titanium implants with a sandblasted and acid-etched surface. *Int J Oral Maxillofac Implants* 2011;26(6):1324-1332.
7. Mendonca G, Mendonca DBS, Aragao FJL, Cooper LF. The combination of micron and nanotopography by H₂SO₄/H₂O₂ treatment and its effects on osteoblast-specific gene expression of hMSCs. *J Biomed Mater Res A* 2010;94A(1):169-179.
8. Tsukimura N, Ueno T, Iwasa F, Minamikawa H, Sugita Y, Ishizaki K, et al. Bone integration capability of alkali- and heat-treated nanobimorphic Ti-15Mo-5Zr-3Al. *Acta Biomater* 2011;7(12):4267-4277.
9. Orsini G, Piattelli M, Scarano A, Petrone G, Kenealy J, Piattelli A, et al. Randomized, controlled histologic and histomorphometric evaluation of implants with nanometer-scale calcium phosphate added to the dual acid-etched surface in the human posterior maxilla. *J Periodontol* 2007;78(2):209-218.
10. Collaert B, Wijnen L, De Bruyn H. A 2-year prospective study on immediate loading with fluoride-modified implants in the edentulous mandible. *Clin Oral Implants Res* 2011;22(10):1111-1116.
11. Zhao G, Schwartz Z, Wieland M, Rupp F, Geis-Gerstorfer J, Cochran DL, et al. High surface energy enhances cell response to titanium substrate microstructure. *J Biomed Mater Res* 2005;74A:49-58.

12. Park JH, Wasilewski CE, Almodovar N, Olivares-Navarrete R, Boyan BD, Tannenbaum R, et al. The responses to surface wettability gradients induced by chitosan nanofilms on microtextured titanium mediated by specific integrin receptors. *Biomaterials* 2012; doi: 10.1016/j.biomaterials.2012.06.066.
13. Bornstein MM, Wittneben JG, Bragger U, Buser D. Early loading at 21 days of non-submerged titanium implants with a chemically modified sandblasted and acid-etched surface: 3-year results of a prospective study in the posterior mandible. *J Periodontol* 2010;81(6):809-818.
14. Park JH, Olivares-Navarrete R, Baier RE, Meyer AE, Tannenbaum R, Boyan BD, et al. Effect of cleaning and sterilization on titanium implant surface properties and cellular response. *Acta Biomater* 2012;8(5):1966-1975.
15. Lausmaa J. Surface spectroscopic characterization of titanium implant materials. *J Electron Spectrosc Relat Phenom* 1996;81(3):343-361.
16. Park JH, Olivares-Navarrete R, Wasilewski CE, Boyan BD, Tannenbaum R, Schwartz Z. Use of polyelectrolyte thin films to modulate Osteoblast response to microstructured titanium surfaces. *Biomaterials* 2012;33(21):5267-5277.
17. Ferguson SJ, Brogini N, Wieland M, de Wild M, Rupp F, Geis-Gerstorfer J, et al. Biomechanical evaluation of the interfacial strength of a chemically modified sandblasted and acid-etched titanium surface. *J Biomed Mater Res A* 2006;78A(2):291-297.
18. Good RJ. Contact-angle, wetting, and adhesion - a critical-review. *J Adhes Sci Technol* 1992;6(12):1269-1302.
19. Watanabe T. Wettability of ceramic surfaces -A wide range control of surface wettability from super hydrophilicity to super hydrophobicity, from static wettability to dynamic wettability. *J Ceram Soc Jpn* 2009;117(1372):1285-1292.
20. Drelich J, Miller JD, Good RJ. The effect of drop (bubble) size on advancing and receding contact angles for heterogeneous and rough solid surfaces as observed with sessile-drop and captive-bubble techniques. *J Colloid Interf Sci* 1996;179(1):37-50.
21. Rykaczewski K, Scott JHJ, Fedorov AG. Electron beam heating effects during environmental scanning electron microscopy imaging of water condensation on superhydrophobic surfaces. *Appl Phys Lett* 2011;98(9):0931061-0931063.
22. Liukkonen A. Contact angle of water on paper components: Sessile drops versus environmental scanning electron microscope measurements. *Scanning* 1997;19(6):411-415.
23. Rupp F, Scheideler L, Olshanska N, deWild M, Wieland M, Geis-Gerstorfer J. Enhancing surface free energy and hydrophilicity through chemical modification of microstructured titanium implant surfaces. *J Biomed Mater Res A* 2006;76A:323-334.
24. Rupp F, Scheideler L, Eichler M, Geis-Gerstorfer J. Wetting Behavior of Dental Implants. *Int J Oral Maxillofac Implants* 2011;26(6):1256-1266.
25. Gittens RA, McLachlan T, Olivares-Navarrete R, Cai Y, Berner S, Tannenbaum R, et al. The effects of combined micron-/submicron-scale surface roughness and nanoscale features on cell proliferation and differentiation. *Biomaterials* 2011;32(13):3395-3403.
26. Davies JE. In vitro modeling of the bone/implant interface. *Anat Rec* 1996;245(2):426-445.
27. McNamara LE, Sjostrom T, Burgess KEV, Kim JJW, Liu E, Gordonov S, et al. Skeletal stem cell physiology on functionally distinct titania nanotopographies. *Biomaterials* 2011;32(30):7403-7410.
28. Mendonca DBS, Miguez PA, Mendonca G, Yamauchi M, Aragao FJL, Cooper LF. Titanium surface topography affects collagen biosynthesis of adherent cells. *Bone* 2011;49(3):463-472.

29. You MH, Kwak MK, Kim DH, Kim K, Levchenko A, Kim DY, et al. Synergistically Enhanced Osteogenic Differentiation of Human Mesenchymal Stem Cells by Culture on Nanostructured Surfaces with Induction Media. *Biomacromolecules* 2010;11(7):1856-1862.
30. Kubo K, Tsukimura N, Iwasa F, Ueno T, Saruwatari L, Aita H, et al. Cellular behavior on TiO₂ nanonodular structures in a micro-to-nanoscale hierarchy model. *Biomaterials* 2009;30(29):5319-5329.
31. Boyan BD, Bonewald LF, Paschalis EP, Lohmann CH, Rosser J, Cochran DL, et al. Osteoblast-mediated mineral deposition in culture is dependent on surface microtopography. *Calcif Tissue Int* 2002;71(6):519-529.
32. Olivares-Navarrete R, Hyzy SL, Hutton DL, Erdman CP, Wieland M, Boyan BD, et al. Direct and indirect effects of microstructured titanium substrates on the induction of mesenchymal stem cell differentiation towards the osteoblast lineage. *Biomaterials* 2010;31(10):2728-2735.
33. Rupp F, Axmann D, Ziegler C, Geis-Gerstorfer J. Adsorption/desorption phenomena on pure and Teflon((R)) AF-coated titania surfaces studied by dynamic contact angle analysis. *J Biomed Mater Res* 2002;62(4):567-578.
34. Boyan BD, Batzer R, Kieswetter K, Liu Y, Cochran DL, Szmuckler-Moncler S, et al. Titanium surface roughness alters responsiveness of MG63 osteoblast-like cells to 1 α ,25-(OH)(2)D-3. *J Biomed Mater Res* 1998;39(1):77-85.
35. Lincks J, Boyan BD, Blanchard CR, Lohmann CH, Liu Y, Cochran DL, et al. Response of MG63 osteoblast-like cells to titanium and titanium alloy is dependent on surface roughness and composition. *Biomaterials* 1998;19(23):2219-2232.
36. Stein GS, Lian JB, Stein JL, VanWijnen AJ, Montecino M. Transcriptional control of osteoblast growth and differentiation. *Physiol Rev* 1996;76(2):593-629.
37. Zinger O, Zhao G, Schwartz Z, Simpson J, Wieland M, Landolt D, et al. Differential regulation of osteoblasts by substrate microstructural features. *Biomaterials* 2005;26(14):1837-1847.
38. Buser D, Nydegger T, Oxland T, Cochran DL, Schenk RK, Hirt HP, et al. Interface shear strength of titanium implants with a sandblasted and acid-etched surface: a biomechanical study in the maxilla of miniature pigs. *J Biomed Mater Res* 1999;45(2):75-83.
39. Bornstein MM, Schmid B, Belser UC, Lussi A, Buser D. Early loading of non-submerged titanium implants with a sandblasted and acid-etched surface. 5-year results of a prospective study in partially edentulous patients. *Clin Oral Implants Res* 2005;16(6):631-638.
40. Cochran DL, Buser D, ten Bruggenkate CM, Weingart D, Taylor TM, Bernard JP, et al. The use of reduced healing times on ITI (R) implants with a sandblasted and acid-etched (SLA) surface: Early results from clinical trials on ITI (R) SLA implants. *Clin Oral Implants Res* 2002;13(2):144-153.
41. Zhao G, Raines AL, Wieland M, Schwartz Z, Boyan BD. Requirement for both micron- and submicron scale structure for synergistic responses of osteoblasts to substrate surface energy and topography. *Biomaterials* 2007;28(18):2821-2829.
42. McMurray RJ, Gadegaard N, Tsimbouri PM, Burgess KV, McNamara LE, Tare R, et al. Nanoscale surfaces for the long-term maintenance of mesenchymal stem cell phenotype and multipotency. *Nat Mater* 2011;10(8):637-644.
43. Khang D, Choi J, Im YM, Kim YJ, Jang JH, Kang SS, et al. Role of subnano-, nano- and submicron-surface features on osteoblast differentiation of bone marrow mesenchymal stem cells. *Biomaterials* 2012;33(26):5997-6007.

44. Gittens RA, Olivares-Navarrete R, McLachlan T, Cai Y, Hyzy SL, Schneider JM, et al. Differential Responses of Osteoblast Lineage Cells to Nanotopographically-Modified, Microroughened Titanium-Aluminum-Vanadium Alloy Surfaces. 2012; (Submitted).

CHAPTER 5. DIFFERENTIAL RESPONSES OF OSTEOBLAST LINEAGE CELLS TO NANOTOPOGRAPHICALLY-MODIFIED, MICROROUGHENED TITANIUM- ALUMINUM-VANADIUM ALLOY SURFACES

In [Gittens RA, Olivares-Navarrete R, McLachlan T, Cai Y, Hyzy SL, Schneider JM, Tannenbaum R, Schwartz Z, Sandhage KH, Boyan BD. Differential responses of osteoblast lineage cells to nanotopographically-modified, microroughened titanium-aluminum-vanadium alloy surfaces. Biomaterials 2012;(Accepted).]

5.1. Introduction

Bone and joint injuries are among the most reported health problems in the United States [1]. Although orthopaedic implants provide a good option for joint replacements, with success rates continually improving, they still have undesirable failure rates in patients who are compromised by disease or age (*i.e.*, patients who are often the ones most in need) [2, 3].

Surface topographical modifications at the micrometer and nanometer scales have driven improved success rates for dental implants by mimicking the hierarchical structure of bone associated with regular bone remodeling [4, 5]. In this process, damaged bone is resorbed by osteoclasts, which produce resorption lacunae containing high microroughness generated after mineral dissolution under the ruffled border [6], as well as superimposed nanoscale features created by the collagen fibers exposed at the surface [7]. New bone formation by osteoblasts is coupled with these primed surfaces, possibly after recognition of structural and chemical cues [8, 9]. Thus, surface topographical modifications have been exploited for implant design in order to achieve direct and intimate contact between the bone and the surface of the implant (osseointegration). Indeed, the beneficial effects of microroughness for bone formation have been well established in the literature [10], and the addition of nanostructures to the implant surface (to mimic more closely the natural structure of bone) has shown

promising results *in vitro* [11], *in vivo* [12] and clinically [13, 14], validating the biological relevance of nanotopography for bone formation.

Titanium (Ti) and its alloys are widely-used metals for dental and orthopaedic implant applications due to their favorable weight-to-strength ratio and good biological performance in bone. Implant surface modifications at the microscale involve adding to, removing from, or deforming material on the bulk metallic substrate (*e.g.*, acid etching, sandblasting) to generate features that are comparable in size or larger than cells [15, 16]. More recently, surface nanomodifications have been developed to directly restructure the oxide layer formed on the implant surface using different techniques, such as coatings [17], hydrothermal reactions [18], and surface oxidation [19, 20]. The generated oxide nanostructures can then interact with proteins and other small molecules that will eventually influence early cell behavior and long-term osseointegration [21].

The differentiation state required to respond to the surface topographical cues by the initial osteoblast lineage cells (to populate the surface of an implant) remains to be elucidated, with bone marrow mesenchymal stem cells (MSCs) or immature osteoblasts as possible candidates. Several recent studies using MSCs *in vitro* consider these cells as initial colonizers of the implant surface due to their higher mobility and ability to differentiate into osteoblasts and other cell types [22, 23]. Many of these studies culture the MSCs using exogenous factors, such as β -glycerophosphate, dexamethasone, and bone morphogenetic protein-2 (BMP-2) [24, 25], to force their differentiation into osteoblasts, which could be obscuring the real effects of the surface nanotopography [26]. We have recently demonstrated that human MSCs can differentiate into osteoblasts when cultured on Ti surfaces possessing microscale roughness, even in the absence of these media supplements [27]. However, it is not known if osteogenic differentiation of

MSCs is a general response to microrough metal surfaces, including Ti alloys, or if it is specific to commercially pure Ti. How the addition of nanoscale features to a microrough surface will affect such differentiation is also unclear.

The goal of the present study has been to test the hypothesis that nanostructural features on implant surfaces can enhance the osteogenic differentiation of osteoblast-lineage cells in the absence of any exogenous soluble factors. To test this hypothesis, we have superimposed nanostructures on microrough Ti6Al4V surfaces and examined the responses of human MSCs and primary human osteoblasts without the addition of exogenous soluble factors.

5.2. Materials and Methods

5.2.1. Titanium Alloy Specimens and Surface Modification Treatments

Titanium alloy rods (ASTM F136 wrought Ti6Al4V ELI alloy for surgical implant applications) 15 mm in diameter were cut into 1.5 mm thick disks and either machined to create a relatively smooth surface (control specimens referred to herein as “sTiAlV” specimens), or double-acid-etched with a proprietary process (Titan Spine LLC, Mequon, WI) to produce a microrough surface (specimens referred to herein as “rTiAlV” specimens). These disk specimens were provided by Titan Spine LLC. Some of the microsmooth (sTiAlV) and microrough (rTiAlV) specimens were further processed using a simple oxidation treatment to superimpose nanostructures on the surface, as described previously [11], to yield nanomodified, microsmooth (NM sTiAlV) or nanomodified, microrough (NM rTiAlV) specimens. This simple oxidation treatment consisted of exposing the samples to flowing (0.85 standard liters per minute) synthetic air (21 % O₂, 79 % N₂) at 1 atm and 740 °C for relatively short durations. The oxidation treatment was conducted for durations of 45, 90 and

180 minutes on all of the specimens and, based on qualitative evaluations of secondary electron (SE) images (as discussed below), disks modified for 45 minutes were chosen for use in cell experiments. All modified and unmodified disks were ultrasonically cleaned in detergent (Micro-90; International Products Corporation, Burlington, NJ) and ultrapure water (Advantage A10; Millipore, Billerica, MA), followed by autoclave sterilization (Model 2540E; Tuttnauer, Hauppauge, NY) for 20 minutes at 121 °C and 15 PSI before surface characterization and use in cell culture studies.

To confirm the “non-line-of-sight” nature of the nanomodification induced by the oxidation treatment, clinically-available Ti6Al4V spine implants of complex shape that had been exposed to the double acid etch surface modification treatment (Endoskeleton® TT implants; Titan Spine, LLC) were oxidized as described above, and the nanostructures generated on the internal walls of this specimen were compared to those generated on the external surfaces of the disk-shaped NMrTiAlV specimens.

5.2.2. Surface Characterization

5.2.2.1. Electron Microscopy

Surface topography was qualitatively evaluated using a field-emission-gun scanning electron microscope (Ultra 60 FEG-SEM; Carl Zeiss SMT Ltd., Cambridge, UK). Secondary electron (SE) images were recorded using a 5 kV accelerating voltage and 30 µm aperture. Histograms of the diameters of nanoscale protuberances (i.e., the major axis of the nanostructure as determined from top-down views) were generated with image analysis software (ImageJ; NIH Software) using three fields of view from two different samples per specimen type, with at least 150 nanoscale protuberances evaluated per

specimen type. In addition, the thickness of the oxide layer formed upon the nano-modification oxidation treatment was evaluated using a transmission electron microscope (TEM, JEM 4000 EX, JEOL, Tokyo, Japan) with an accelerating voltage of 400 KV. Electron transparent cross-sections obtained from the surface regions of the NMsTiAlV specimens were prepared using a focused ion beam system (FEI Nova Nanolab 200 FIB/SEM; FEI, Hillsboro, OR).

5.2.2.2. Atomic Force Microscopy (AFM)

Surface measurements at the nanoscale were evaluated using AFM (Nano-R AFM; Pacific Nanotechnology, Santa Clara, CA) in close-contact mode. Analyses were conducted using silicon probes (P-MAN-SICC-O, Agilent Technologies, Santa Clara, CA) with dimensions of 1.14 cm x 0.25 cm² and tip radii of up to 10 nm, a nominal force constant of 40 N/m, and a nominal resonance frequency of 300 kHz. Each AFM analysis was performed over a 730 nm x 730 nm specimen area. Two samples of the sTiAlV and NMsTiAlV specimens were scanned three times each, under ambient atmosphere. (Note: because the z-height limit of the AFM was 5 µm, the microrough surfaces could not be analyzed by AFM.) The raw data were plane-leveled to remove tilt by applying a numerical second-order correction, and mean values of surface roughness average (S_a) were determined using NanoRule+ software (Pacific Nanotechnology).

5.2.2.3. Laser Confocal Microscopy (LCM)

Surface roughness at the microscale was evaluated using a laser confocal microscope (Lext LCM; Olympus, Center Valley, PA). Each LCM analysis was performed over a 644 µm x 644 µm area using a scan height step of 100 nm, a 20X objective, and a cutoff wavelength of 100 µm. Two samples of every specimen type were scanned three times each under ambient atmosphere. Mean values of surface roughness average (S_a) were determined.

5.2.2.4. X-ray Photoelectron Spectroscopy (XPS)

Relative atomic concentration and chemical bonding information were obtained from the specimen surfaces by XPS analyses (Thermo K-Alpha XPS; Thermo Fisher Scientific, West Palm Beach, FL). The XPS instrument was equipped with a monochromatic Al-K α X-ray source ($h\nu = 1468.6$ eV). The XPS analysis chamber was evacuated to a pressure of 5×10^{-8} mbar or lower before collecting XPS spectra. Spectra were collected using an X-ray spot size of 400 μm and pass energy of 100 eV, with 1 eV increments, at a 55 ° takeoff angle. Two samples of every specimen type were scanned three times each and all values were averaged.

5.2.2.5. Contact Angle Measurements

Contact angle measurements were obtained using a goniometer (CAM 100; KSV, Helsinki, Finland) equipped with a digital camera and image analysis software. Ultra-pure water was used as the wetting liquid with a drop size of 4 μL . Sessile drop contact angles of the air-water-substrate interface were measured four times over a period of 20 seconds, on five different spots in two samples from each specimen type.

5.2.2.6. X-ray Diffraction (XRD) Analyses

XRD analyses were conducted using 1.8 kW Cu K α radiation, a 1 ° parallel plate collimator, and a $\frac{1}{2}$ divergence slit on an X'Pert PRO Alpha-1 diffractometer (PANalytical, Almelo, The Netherlands). A θ – 2θ parafocusing setup was used for grazing-angle (*i.e.*, 2 ° take-off angle) analyses. All samples were analyzed under ambient atmosphere.

5.2.3. Cell Culture Model

Primary human osteoblasts (HOBs) and human mesenchymal stem cells (MSCs) were used for this study. Osteoblasts were isolated from vertebral bone of a 17-year old male that was collected under Institutional Review Board approval from Children's Healthcare of Atlanta and Georgia Institute of Technology, as described previously [28].

Briefly, periosteum and soft tissues were removed from the bone. Bone fragments were washed three times in Hank's balanced salt solution (HBSS; Invitrogen, Carlsbad, CA) containing 1 % penicillin-streptomycin (Invitrogen), and digested for 15 minutes at 37 °C with 0.25 % trypsin-ethylenediaminetetraacetic acid (EDTA) (Invitrogen). The digest was discarded to avoid fibroblast contamination. The bone was minced into 1 to 2 mm² pieces and bone chips were placed in a 100 × 20 mm² Petri dish (BD, Franklin Lakes, NJ) and cultured in Dulbecco's modified Eagle medium (DMEM; cellgro®, Mediatech, Inc., VA) containing 10 % fetal bovine serum (Gibco, Carlsbad, CA) and 1 % penicillin-streptomycin. At confluence, the cells were further passaged for experiments and were cultured in medium as described above. Human MSCs were purchased from a commercial vendor (Lonza, Walkersville, MD) and grown in MSC Growth Medium (MSCGM, Lonza). All cells were cultured at 37 °C with 5 % CO₂ and 100 % humidity, and cells from the sixth passage or lower were used. Osteoblasts and MSCs were cultured on tissue culture polystyrene (TCPS) or on the different Ti alloy surfaces (sTiAIV, NM sTiAIV, rTiAIV, NM rTiAIV) at a seeding density of 10,000 cells/cm². Cells were fed 24 hours after plating and then every 48 hours until confluence, as evaluated on the TCPS substrates. At confluence, cells were incubated with fresh medium for 24 hours and harvested for assays. Conditioned media were collected, and stored at -80 °C until assayed. Cell layers were washed twice with serum-free medium, released from their substrate by two sequential incubations in 500 µL 0.25 % trypsin for 10 minutes at 37 °C, and counted with a Z1 Coulter particle counter (Beckman Coulter, Brea, CA). Cells were resuspended in 500 µL 0.05 % Triton-X-100® and lysed by sonication.

Two different osteoblast differentiation markers were evaluated: alkaline phosphatase-specific activity [orthophosphoric monoester phosphohydrolase, alkaline; E.C. 3.1.3.1], which serves as an early differentiation marker; and osteocalcin content in

the conditioned medium as a late differentiation marker. Cellular alkaline phosphatase activity was assayed in the cell lysate as the release of *p*-nitrophenol from *p*-nitrophenylphosphate at pH 10.2, and normalized to total protein content (BCA Protein Assay Kit; Pierce Biotechnology Inc., Rockford, IL) as previously described [29]. Osteocalcin levels in the conditioned media were measured using a commercially-available radioimmunoassay kit (Human Osteocalcin RIA Kit, Biomedical Technologies, Stoughton, MA) as described previously [30] using a LS1500 gamma counter (Perkin Elmer, Waltham, CA).

The conditioned media were also assayed for protein levels of local factors important for bone development. Osteoprotegerin (OPG), a cytokine that works as a decoy receptor for “receptor activator for nuclear factor κ B ligand” (RANKL) to inhibit osteoclastogenesis, was measured using enzyme-linked immunosorbent assay (ELISA) kits (DY805 Osteoprotegerin DuoSet, R&D Systems, Minneapolis, MN). Vascular endothelial growth factor (VEGF), a growth factor involved in vasculogenesis and angiogenesis, was also measured using an ELISA kit (DY293B VEGF DuoSet, R&D Systems).

5.2.4. Statistical Analysis

Data from experiments evaluating the surface characteristics of the substrates are presented as the mean \pm one standard deviation (SD) of all the measurements performed on different samples of the same specimen type. Data from experiments examining cell response are presented as mean \pm standard error for six independent cultures per variable. All experiments were repeated at least twice to ensure the validity of the observations, and the results from individual experiments are presented. Data were evaluated by analysis of variance, and significant differences between groups were determined using Tukey's modification

of Student's t-test. A p value below 0.05 was considered to indicate a statistically-significant difference.

5.3. Results

5.3.1. Characterization of Nanomodified Surfaces

SE images of the original sTiAlV and rTiAlV surfaces revealed that both were relatively smooth at the nanoscale, with some sub-microscale features left from the machining or double-acid-etch treatment (Figures 5.1A, B). However, the surfaces of the titanium alloy specimens that had received the 740 °C oxidation treatment for 45 minutes (specimens NM sTiAlV and NM rTiAlV) possessed high and homogeneous coverage of nanoscale protuberances (referred to herein simply as nanostructures) with diameters that ranged between 20 and 180 nm (Figures 5.1C, D). Statistical image analyses (histograms are shown in Figures 5.1E, F) indicated that the average diameters of the nanostructures on the NM sTiAlV and NM rTiAlV surfaces were 73 nm and 61 nm, respectively. SE images from oxidized spine implants that had received the same oxidation treatment revealed that similar nanostructural features were generated on the internal walls as well as external surfaces, confirming the “non-line-of-sight” nature of this surface modification treatment (Figure 5.2).

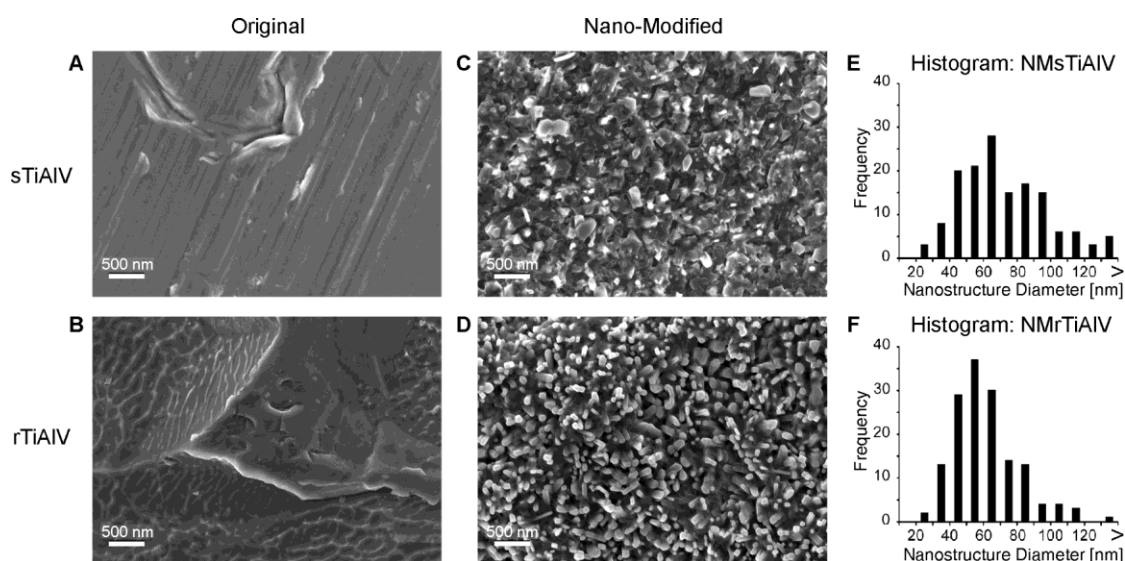


Figure 5.1. SE images and image analyses of the Ti alloy surfaces used for *in vitro* cell studies. (A) Microsmooth (sTiAlV) and (B) microrough (rTiAlV) surfaces were relatively smooth at the nanoscale, with some sub-microscale features. After the nanomodification oxidation treatment for 45 minutes, (C) NMSTiAlV and (D) NMrTiAlV surfaces possessed high and homogeneous surface area coverage of nanostructures. Image analyses of the (E) NMSTiAlV and (F) NMrTiAlV surfaces revealed that the nanostructure diameter (when viewed from above by SEM analyses) ranged between 20 and 180 nm, with average values of 73 nm and 61 nm, respectively.

SEM analyses of Ti alloy surfaces exposed to the same oxidation temperature and atmosphere (740 °C, 21 % O₂/79 % N₂, 1 atm) but for longer times of 90 or 180 minutes revealed the presence of similar nanostructures (Figure 5.3), although some coalescence of the nanostructures and a few visible regions of spallation were occasionally observed. Thus, 45 minutes was selected as the preferred oxidation time for subsequent characterization and cell experiments involving the titanium alloy specimens.

The apparent increase in the nanoscale roughness of the titanium alloy surfaces detected by electron microscopy after the oxidation treatment was confirmed by AFM analyses (Figure 5.4A), which revealed significant enhancements in the values of the

average nanoscale roughness ($6.1 \pm 4.3 \mu\text{m}$ on sTiAlV surfaces compared to $17.0 \pm 4.5 \mu\text{m}$ on NM sTiAlV surfaces). As expected, laser confocal microscopic analyses (Figure 5.4A) also revealed that the microroughness of the rTiAlV and NM rTiAlV specimens (as indicated by the microscale surface roughness average, S_a) was significantly higher than for the specimens that had not been acid etched (sTiAlV and NM sTiAlV). However, such surface microroughness did not appear to significantly inhibit the generation of surface nanostructures during the subsequent oxidation treatment (Figure 5.1). The oxidation treatment used to enhance the nanoscale roughness also did not significantly affect the microscale roughness of the rTiAlV specimens.

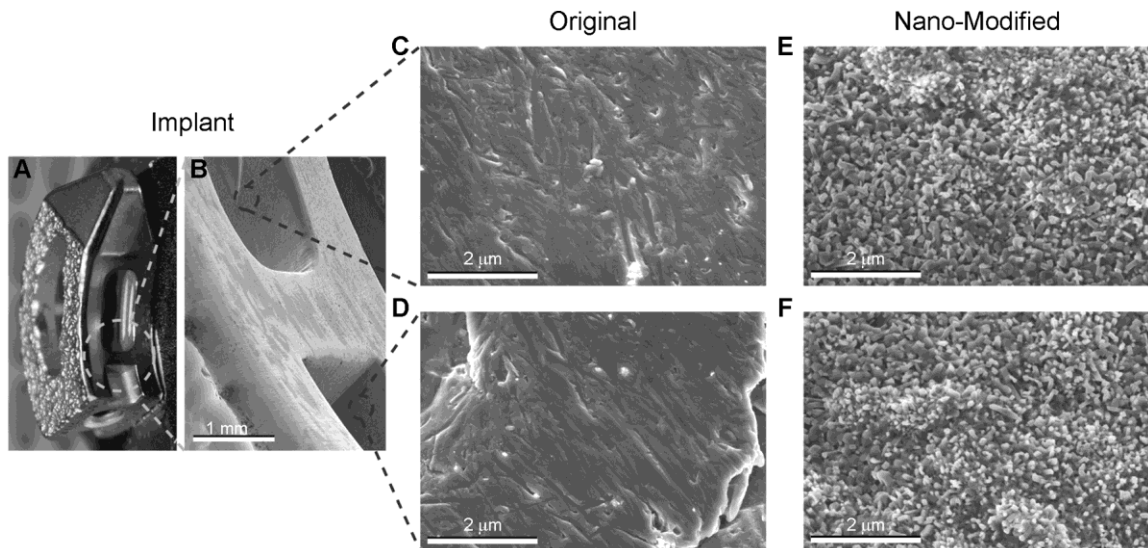


Figure 5.2. (A) Optical and (B-D) SE images of the surface nanostructural modification applied to clinically relevant Ti alloy spine implants. (A, B) Low magnification images show the complex design of the device. (C, D) High magnification images of the unmodified implant reveal that the surface was relatively smooth at the micro and nanoscales. Conversely, (E, F) high magnification images of the nanomodified implant surface display homogeneous coverage of nanostructures throughout exposed and non-line-of-sight areas.

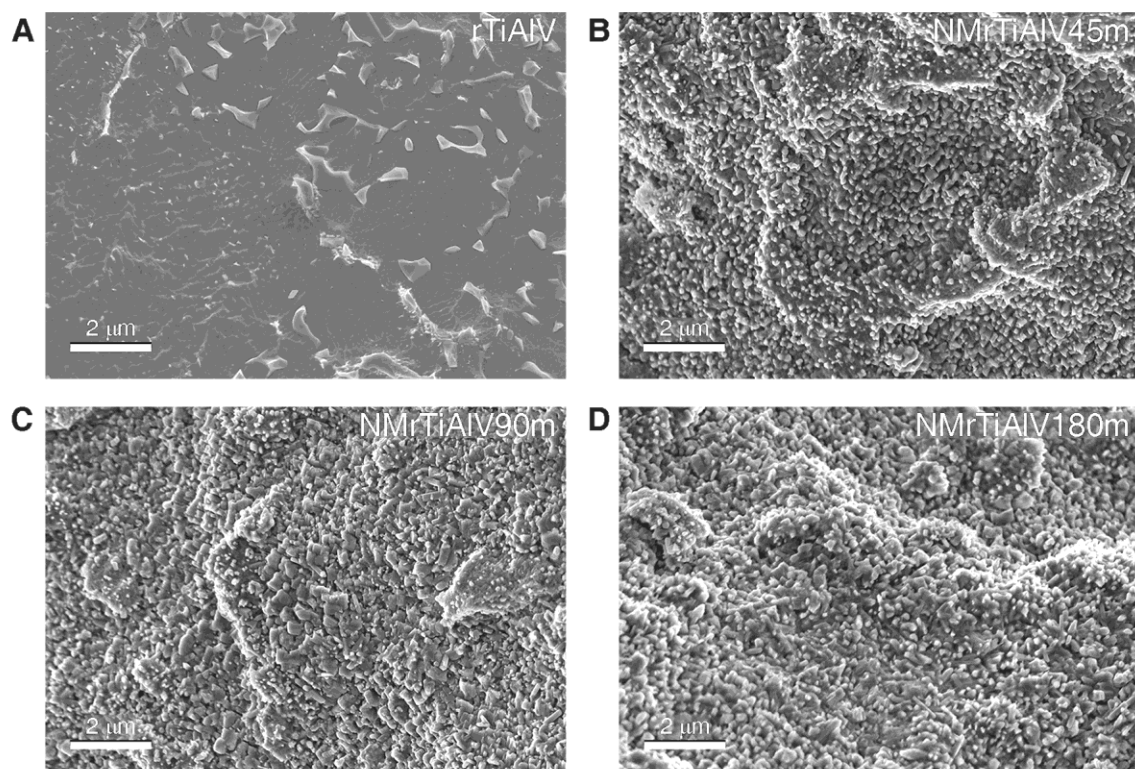


Figure 5.3. SE images of the original microrough titanium alloy (rTiAlV) surface after different nanomodification times of 45, 90 and 180 minutes. (A) The original surface shows some micro- and sub-microscale features left from the double acid etch treatment. (B) After heat treatment for 45 minutes, the entire surface was homogeneously covered by nanostructures superimposed over the preexisting microscale features. Continued modification for durations of (C) 90 minutes and (D) 180 minutes yielded nanostructures similar to those on the surface of specimens modified for 45 minutes, except for some coalescence at the surface that rendered slightly larger nanostructures.

The nanostructural modification of the surface occurred via oxidation of the Ti alloy specimens. TEM evaluation (Figure 5.4B) of the NMSTiAlV sample revealed a conformal, but porous oxide layer that was up to 1600 nm thick. (Note: sample processing during preparation of the FIB cross-sections for TEM evaluation removed nanostructural features found on the top-down SE images, as shown in Figure 5.5). Grazing-angle XRD analysis (Figure 5.4C) of this oxidized alloy specimen revealed the presence of polycrystalline TiO_2 , with rutile (powder diffraction card No. 21-1276) as the predominant polymorph and some anatase (powder diffraction card No. 21-1272) along with polycrystalline α -Ti (powder diffraction card No. 44-1294) from the underlying alloy. Diffraction peaks for the latter phase and β -Ti (powder diffraction card No. 44-1288) were also detected in the unoxidized sTiAlV specimen. Distinct diffraction peaks for the most stable aluminum oxide polymorph, corundum or α -alumina, were not detected. The oxidation treatment did not result in a dramatic change in the wettability of the surface by water, as measured by sessile-drop contact angle (Figure 5.4D).

Nanoscale modification of Ti alloy surfaces by the oxidation heat treatment affected the surface chemistry of the specimens (Figure 5.6). The elemental compositions of the original sTiAlV and rTiAlV surfaces were similar, with Ti, O and C as the main components, and only small amounts of Al and no detectable V present at the surface. However, the surface chemical compositions of the NMSTiAlV and NMRTiAlV specimens were altered after the oxidation treatment, with lower concentrations of Ti and C, and significantly higher concentrations of Al, on the oxidized surfaces, respectively, than for the starting alloy specimens. A larger decrease in Ti concentration and increase in Al concentration were observed after oxidation of the rTiAlV specimen than after oxidation of the sTiAlV specimen.

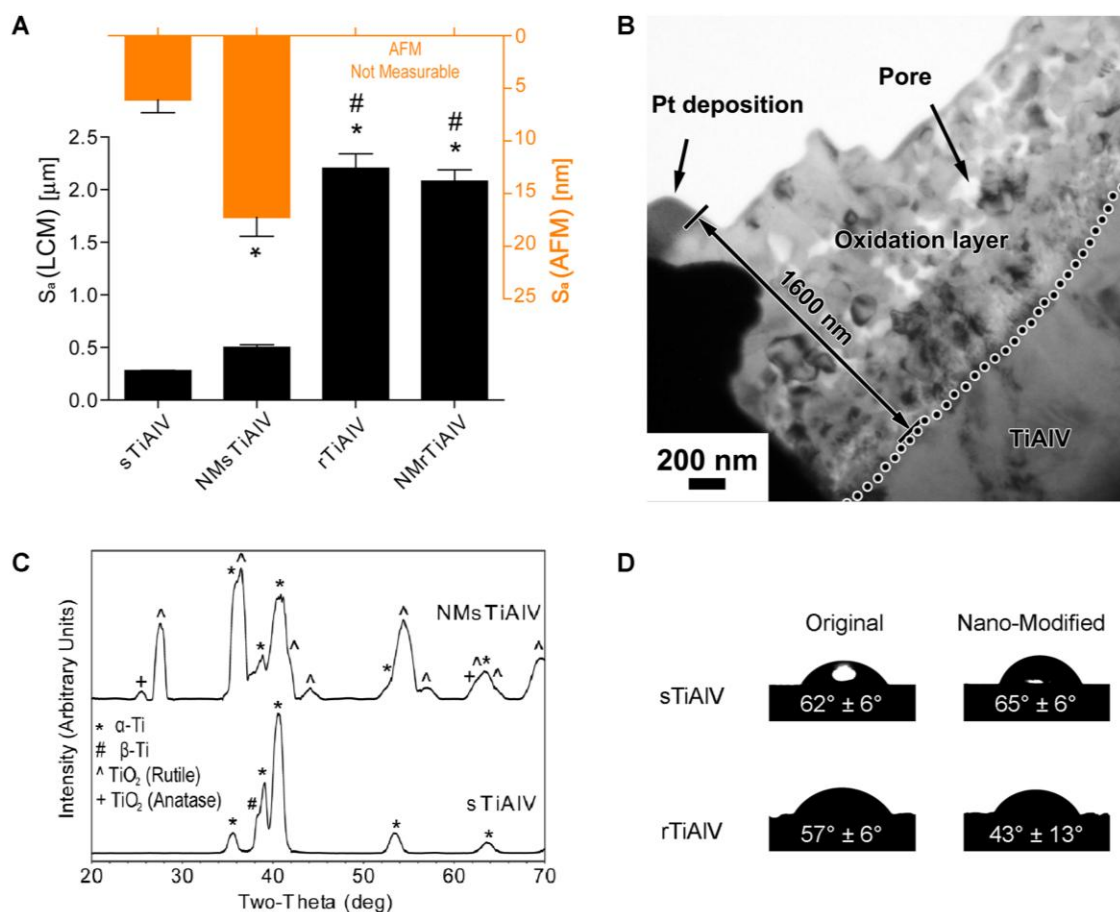


Figure 5.4. Surface characterization of nanomodified Ti alloy specimens. (A) Surface roughness average (S_a) of sTiAlV and NMSTiAlV surfaces measured by laser confocal microscopy (LCM, black bars) and atomic force microscopy (AFM, orange bars). AFM scans were not possible on microrough specimens, rTiAlV and NMSTiAlV, due to z-height tool limitations. * refers to a statistically-significant p value below 0.05 vs. sTiAlV; # refers to a statistically-significant p value below 0.05 vs. NMSTiAlV. (B) TEM evaluation of a NMSTiAlV surface cross-section prepared by focused ion beam (FIB) milling. The cross-sectional TEM image of the NMSTiAlV specimen reveals a conformal oxide layer that possesses pores and has a thickness of up to 1600 nm. (C) X-ray diffraction (XRD) patterns obtained from sTiAlV and NMSTiAlV specimens. The original sTiAlV specimen only exhibited peaks for α - and β -titanium, while the nanomodified NMSTiAlV specimen exhibited peaks for α -titanium, rutile and anatase TiO_2 . (D) Sessile-drop water contact angles on the surfaces of sTiAlV, NMSTiAlV, rTiAlV and NMSTiAlV specimens.

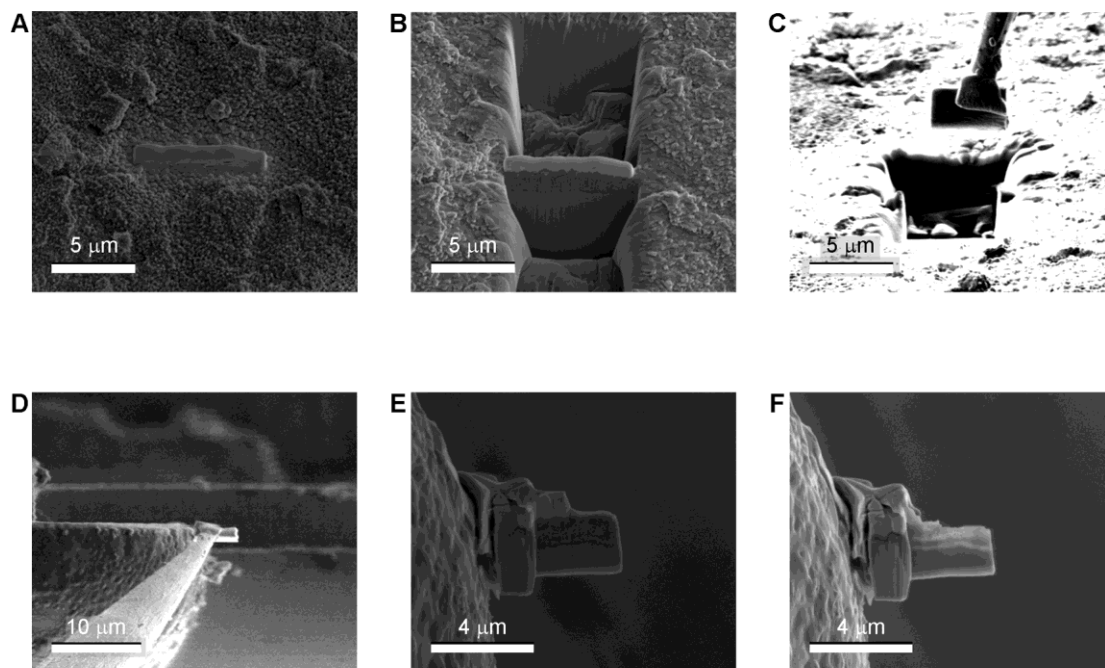


Figure 5.5. Focused ion beam (FIB) milling preparation of a TEM foil from a NM5TiAlV surface. Initially, the section of interest was (A) coated with platinum (Pt) to avoid damage from the ion beam. Subsequently, (B) slanted trenches were cut on both sides of the section to then (C) pull it out and (D) attach it to the copper (Cu) grid. The last steps of the TEM foil preparation involve (E) thinning of the sample to an electron-transparent thickness, followed by (F) careful cleaning to remove any debris from the surface of interest.

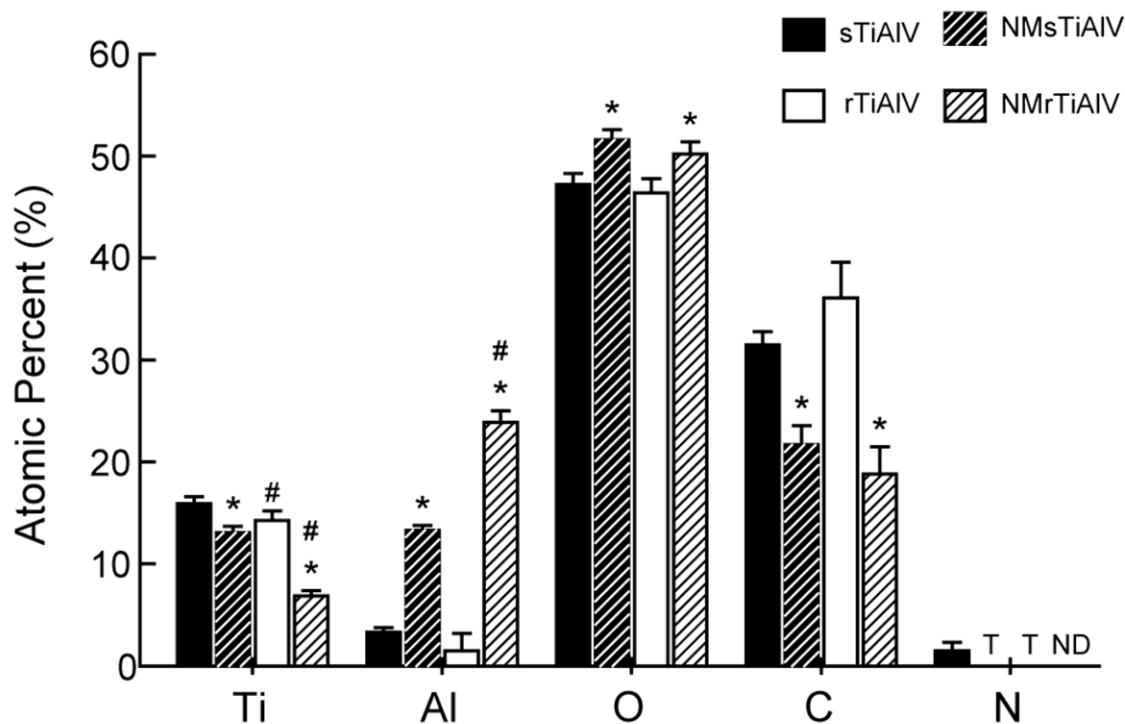


Figure 5.6. Elemental compositions of the sTiAlV, NMSTiAlV, rTiAlV and NMrTiAlV specimens measured by XPS. All samples were mainly composed of Ti, Al, and O, with C also highly present on the surface. N was also present at low levels on the sTiAlV surfaces, while NMSTiAlV and rTiAlV surfaces only had traces (T) and on the NMrTiAlV surfaces it was not detectable (ND). * refers to a statistically-significant p value below 0.05 vs. unmodified control; # refers to a statistically-significant p value below 0.05 vs. microsmooth control.

5.3.2. Osteoblast Lineage Cell Response to Nanomodified Surfaces

5.3.2.1. *Osteoblast Response*

Osteoblastic maturation of HOBs was highly sensitive to the generated nanostructures superimposed onto microrough Ti alloy surfaces in the absence of any exogenous soluble factors. Osteoblast cell number (Figure 5.7A), which decreases in differentiated cells due to a transcriptionally-restricted transition between proliferation and differentiation, was lower on the microrough surfaces, with the lowest levels on the combined microrough and nanostructured NMrTiAlV surfaces. At the same time, alkaline phosphatase specific activity (Figure 5.7B) and osteocalcin production (Figure 5.7C) were higher on the microrough alloy surfaces when compared to the microsmooth alloy surfaces. Additionally, alkaline phosphatase specific activity had a 2.5-fold increase, while osteocalcin production had a synergistic 8.5-fold increase on the NMrTiAlV specimens when compared to the rTiAlV specimens. The increase in differentiation markers on microrough surfaces was also coupled with higher levels of the anti-osteoclastogenesis factor osteoprotegerin (Figure 5.7D) and the angiogenic factor VEGF (Figure 5.7E). In the case of osteoprotegerin levels, no appreciable difference between rTiAlV and NMrTiAlV specimens was observed, while a 5-fold synergistic increase in VEGF production was observed for the NMrTiAlV surfaces relative to rTiAlV surfaces.

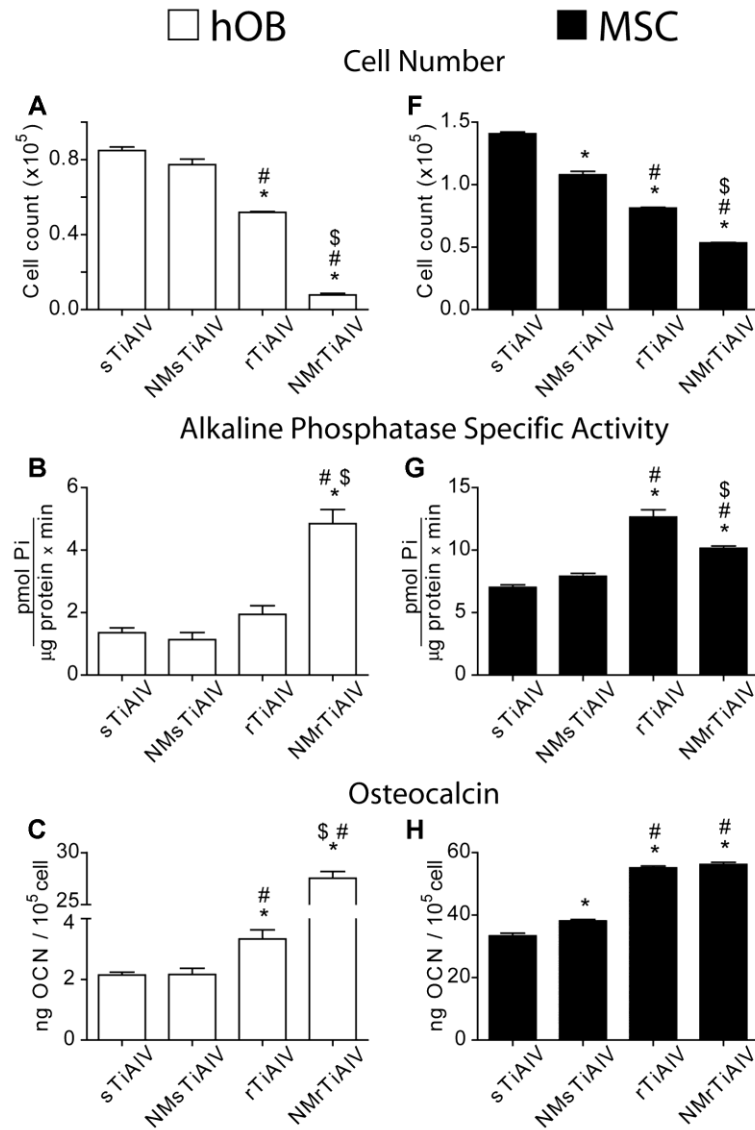


Figure 5.7. Effects of micro- and nanoscale surface modifications on human primary osteoblasts (A-E) and human MSCs (F-J). Osteoblasts and MSCs were plated on sTiAlV, NMSTiAlV, rTiAlV and NMrTiAlV surfaces and grown to confluence. The nanomodification involves surface oxidation in flowing synthetic air for 45 minutes at 740 °C. At confluence, (A, F) cell number, (B, G) alkaline phosphatase specific activity, (C, H) OCN, (D, I) OPG, and (E, J) VEGF levels were measured. Data represented are the mean \pm standard error of six independent samples. * refers to a statistically-significant p value below 0.05 vs. sTiAlV; # refers to a statistically-significant p value below 0.05 vs. NMSTiAlV; \$ refers to a statistically-significant p value below 0.05 vs. rTiAlV.

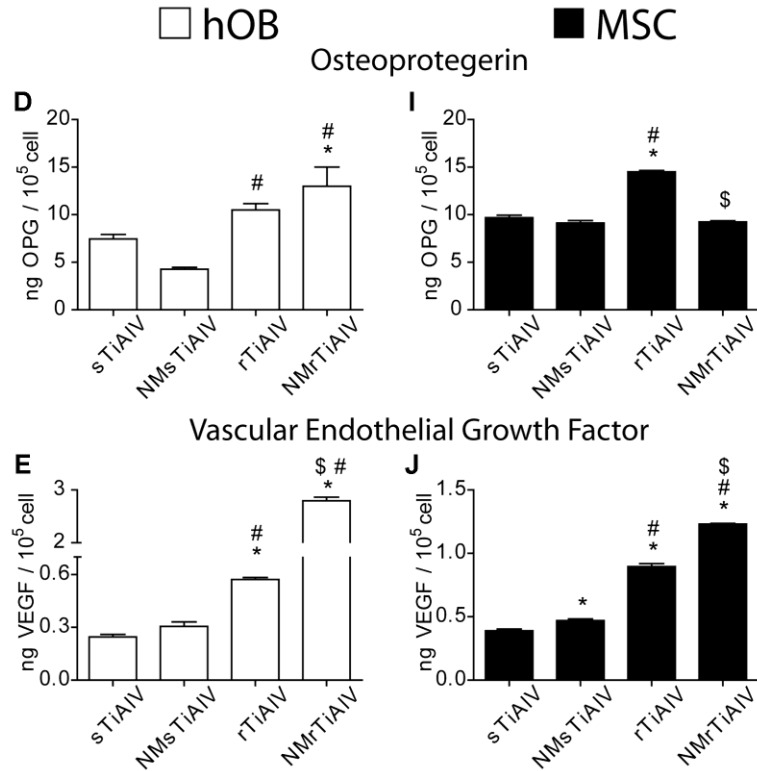


Figure 5.7. Continued

5.3.2.2. MSC Response

MSC numbers (Figure 5.7F) were 0.7-fold lower on the nanomodified NMsTiAlV specimens than for the starting sTiAlV specimens, and the cell number decreased further for the microrough rTiAlV specimens, with the lowest levels observed for the nanomodified NMrTiAlV specimens (0.7-fold vs. rTiAlV). However, although osteoblastic differentiation of MSCs was affected by microstructure, it was not responsive to culture on nanomodified surfaces. Alkaline phosphatase specific activity (Figure 5.7G) was 1.9-fold higher in cells cultured on microrough rTiAlV specimens compared to microsmooth sTiAlV specimens, as well as 1.3-fold higher than for the micro/nanostructured NMrTiAlV

specimens. Osteocalcin levels (Figure 5.7H) were also higher on the rTiAlV specimens than on the sTiAlV specimens, with no further significant enhancement for the NMrTiAlV surfaces. Osteoprotegerin levels (Figure 5.7I) on the microrough rTiAlV specimens were 1.5-fold higher when compared to the rest of the specimens, which all had similar levels (even when comparing the microsmooth specimens to the combined microrough and nanostructured NMrTiAlV specimens). In contrast, VEGF production was sensitive to the nanomodification (Figure 5.7J). VEGF levels were 1.2-fold higher on the NM sTiAlV surfaces when compared to sTiAlV surfaces, but the highest levels were found on the microrough specimens, with NMrTiAlV surfaces yielding 1.3-fold higher levels than rTiAlV surfaces.

5.4. Discussion

Surface nanomodification of dental and orthopaedic implants is becoming a common approach to enhance osseointegration [5]. Although several scientific reasons have been postulated for beneficial effects of nanostructures on the surfaces of osseous implants [7], fundamental questions remain to be answered regarding the initial cellular responses to these nanostructural features *in vitro* and *in vivo*. In addition, variations in various parameters of published *in vitro* reports (e.g., the size and nature of the nanostructures evaluated, as well as the phenotype, differentiation stage, and exogenous factors used to culture the cells) provide motivation for direct comparisons of some of these variables [31-33].

In this study, the cellular responses of progenitor and differentiated human osteoblast-lineage cells on the nanomodified surfaces of microsmooth and microrough Ti alloy specimens have been compared to evaluate the cells' abilities to respond to such nanostructures as revealed by the production of osteoblast differentiation markers and

release of proteins associated with osteogenesis and vasculogenesis. Our results show that nanostructures can be superimposed on TiAlV surfaces using a simple and effective oxidation-based treatment, which had been previously applied to commercially-pure (cp) Ti substrates [11]. However, unlike the TiO₂ surface chemistry generated on the cpTi surface, the nanostructured surface on the alloy had a higher Al content than was present on the unmodified surfaces. As reported previously using the immature MG63 osteoblastic cell line on nanomodified cpTi, HOB cells exhibited a synergistic enhancement in maturation on the nanomodified microrough surfaces, suggesting a greater role for nanotopography over surface chemistry for the maturation of differentiated osteoblast-lineage cells. MSCs on the alloy surfaces responded to microstructure with a less robust osteoblastic response than seen for HOBs on TiAlV and MG63s on the cpTi substrates, and they did not show evidence of further osteoblastic differentiation on the micro/nanostructured alloy surfaces. Instead, the MSCs generated increased VEGF production, indicating sensitivity to the micro/nanostructured surfaces, and suggesting that the surface chemistry could also play a role in determining cell response. These observations are discussed in detail below.

High temperature oxidation in an air atmosphere was used successfully to generate well-defined nanostructures with an average diameter (when viewed from above by SEM analyses) of 60 to 75 nm, as noted previously for cpTi [11], supporting the general utility of this method for a variety of metal materials. Relatively high and uniform concentrations of such oxidation-induced nanostructures covered the internal and external surfaces of implants with complex shapes (as well as the surfaces of microsmooth and microrough disk-shaped specimens used for *in vitro* studies), proving the clinical and industrial applicability of this treatment. The oxidation-induced

nanostructuring of TiAlV alloy surfaces yielded a relatively high density of fine nanostructural features even after just 45 minutes, and the features remained on the surfaces with low nanostructure coalescence or spallation after longer modification times of 90 and 180 minutes. This differed from our prior experience with cpTi, which required the longer treatment times to produce a nanostructured surface with comparable morphology [11].

A surface modification process that alters the nanoscale surface roughness while retaining other surface characteristics, allows for reduced ambiguity in assessing the role(s) of such nanoroughness on cell response. With the present oxidation-based process, the surface nanoroughness of Ti alloy specimens was significantly increased, as revealed by AFM and SEM analyses, without significantly degrading the surface microroughness, as measured by LCM analyses. Cross-sectional evaluation of the oxidized alloy surface by TEM analysis revealed that, although the oxide layer was up to 1.6 μm in thickness, the oxide layer conformed with, and remained attached to, the metal surface. The water contact angles of the starting and nanomodified surfaces were also similar, indicating that the surface wettability of the specimens was not greatly affected by the oxidation treatment.

The oxidation-based treatment did result in a chemical alteration of the specimen surfaces, as revealed by XPS analyses. The Al concentration increased, while Ti and C concentrations decreased after the oxidation treatment. The small change in oxygen content detected after oxidation indicated that a thin, native Ti-O-rich scale was present on the starting alloy surfaces, which apparently allowed for similar wetting by water as for the oxidized specimens. No peaks for V were detected in the XPS spectra of the oxidized specimens, as was the case for a previous study evaluating the oxidation of TiAlV samples at lower temperatures and for longer durations [34]. Naturally-passivated

Ti-Al alloy specimens tend to form an oxide layer composed almost exclusively of titania [35], whereas high temperature oxidation promotes the formation of an oxide scale with a higher alumina content [36]. Our results were in agreement with the aforementioned studies [35, 36]. Furthermore, the temperature of 740 °C used during our heat treatment promoted the formation of an oxide layer containing anatase and rutile titania, as well as an enrichment of aluminum as confirmed by XPS. However, distinct diffraction peaks for crystalline alumina were not detected.

Osteoblast maturation and local factor production were synergistically sensitive to the combined micro/nanostructured TiAlV surfaces, in agreement with our previous study evaluating osteoblast-like MG63 cell response to oxidation-modified, nanostructured Ti grade 2 specimens [11]. Lower osteoblast cell numbers were found on the microrough surfaces, with the lowest levels found on the combined microrough and nanostructured surfaces. Low cell number *in vitro* has commonly been perceived as a negative result with regards to osseointegration [37, 38] and has become the problem to be solved in some studies [39, 40]. However, the clinical successes of microrough surfaces relative to smoother surfaces that tend to promote proliferation *in vitro* [41], together with reports that have found a transcriptionally-restricted transition between proliferation and differentiation that forces osteoblasts to stop dividing once they start maturing [42], suggest otherwise. Our cell number results, coupled with a synergistically higher production of differentiation markers (especially of the late marker osteocalcin) on the micro- and nanostructured specimens, confirmed that the osteoblasts were maturing and producing the proteins necessary for bone formation. In addition, roughness at the microscale appeared to be more important than nanoscale roughness with regards to controlling the production of the local factor osteoprotegerin, which serves as a decoy receptor for RANKL to inhibit osteoclastogenesis and favor net bone formation.

Furthermore, the potent angiogenic factor VEGF, important for neovascularization of the implantation site [43], was strongly influenced by the hierarchically (micro/nano) structured surfaces. These results are also supported by the findings that oxidized TiAlV specimens can increase surface adsorption of key extracellular matrix components such as fibronectin, which could enhance cell response on these combined micro- and nanomodified surfaces [34]. Comparable synergistic maturation responses to nano/microstructured surfaces from HOBs on TiAlV substrates and from immature osteoblast-like MG63 cells on cpTi in our previous study [11], suggests that addition of nanostructures to the underlying microroughness of a substrate plays a more relevant role in the process of osteogenic maturation of differentiated osteoblast-lineage cells than surface chemistry.

MSC osteoblastic differentiation was sensitive to microroughness, as seen previously [27], but not sensitive to the nanostructures generated on our Ti alloys. Cell number was lower on the microrough surfaces than on the microsmooth surfaces, as was the case for the osteoblasts. Moreover, the production of differentiation markers was also enhanced on the microrough Ti alloy surfaces relative to microsmooth surfaces, which confirmed the influence of microroughness on the enhanced differentiation of MSCs [27, 44]. The lowest MSC numbers were found on the micro/nanostructured surfaces, which suggested that osteogenic differentiation was induced. However, MSCs growing on the combined microrough and nanostructured surfaces had lower alkaline phosphatase specific activity and produced similar osteocalcin levels than those growing on only microrough surfaces. The lower levels in alkaline phosphatase specific activity and equal levels of osteocalcin on the combined micro/nanostructured surfaces compared to the microrough-only surfaces suggest that these cells were not responding to the nanostructures via osteoblastic differentiation. An

alternative explanation is that MSC differentiation was accelerated and the peak in osteocalcin production had been reached on both the microrough and combined micro/nanorough surfaces. However, contrary to the latter conclusion is the fact that most of the studies evaluating micro/nanostructured surfaces have used osteogenic media with soluble factors, such as dexamethasone and β -glycerophosphate, to force the osteogenic differentiation of the stem cells, and these studies still found a higher expression of differentiation markers compared to microrough control surfaces [5, 32, 45]. In such cases, the exogenous factors used can effectively turn the MSCs into osteoblasts, which we have shown here do respond synergistically to the nanostructures on the Ti alloy. It is clear that MSCs and HOBs were differentially regulated by the surface, not only with respect to robustness of the response but also with respect to osteoprotegerin production. One other study compared human MSC and HOB response to nanostructured TiAlV substrates, without adding osteogenic media, using grooved, relatively microsmooth surfaces [46]. The authors found that MSCs were more sensitive to the nanogrooves than HOBs in terms of cell proliferation and cell viability, in agreement with the results reported in the present study. No other study, to our knowledge, has evaluated the response of MSCs to physiologically- and clinically-relevant, micro/nanostructured TiAlV surfaces without the addition of osteogenic soluble factors, which could explain the lack of understanding of the genuine *in vitro* response of these cells.

A comparison of the results obtained in this study between osteoblast-lineage cells at distinct differentiation stages revealed that primary osteoblasts were able to recognize the surface nanostructures and respond to them with a synergistic production of factors related to osteogenic maturation. Conversely, MSC osteoblastic differentiation was not as sensitive to the nanostructures, as evidenced by the lower-to-similar

production of osteogenic markers on the combined micro/nanostructured surfaces compared to the microrough surfaces. Our results show that MSCs were indeed responsive to the nanostructures formed on the Ti alloy or to the surface chemistry, as seen in cell number and VEGF production assays. The relatively low sensitivity of MSC osteoblastic differentiation towards these oxidation-induced nanostructures, coupled with reports showing the beneficial role of nanomodified implants *in vivo* [12, 47, 48], may indirectly suggest that, even if these stem cells were the first to approach the implant *in vivo*, they might already be committed to a specific lineage by the time they reach the surface.

5.5. Conclusions

The present paper demonstrates that the differentiation state of osteoblast-lineage cells can determine their response to oxidation-induced surface nanostructures on a titanium alloy in terms of the production of osteoblast differentiation markers, which has implications for clinical evaluation of new implant surface nanomodifications. The osteoblastic differentiation of primary human osteoblasts but not osteoblastic differentiation of MSCs was highly sensitive to nanostructures superimposed by oxidation onto microrough Ti alloy surfaces in the absence of any exogenous soluble factors. In contrast, MSCs responded to the nanostructured microrough surfaces with increased production of angiogenic factors. These findings support the conclusion that the successful osseointegration of an implant depends on contributions from osteoblast lineage cells at different stages of osteoblast commitment and indicates the importance of examining cell response in multiple *in vitro* models.

5.6. References

1. Jacobs JJ, Andersson GBJ, Bell JE, Weinstein SL, Dormans JP, Gnat SM, et al. United States bone and joint decade: the burden of musculoskeletal diseases in the United States. 1st ed. Rosemont: AAOS; 2008.
2. Fransson C, Wennstrom J, Berglundh T. Clinical characteristics at implants with a history of progressive bone loss. *Clin Oral Implants Res* 2008;19(2):142-147.
3. Granstrom G. Osseointegration in irradiated cancer patients: An analysis with respect to implant failures. *J Oral Maxillofac Surg* 2005;63(5):579-585.
4. Rho JY, Kuhn-Spearing L, Zioupos P. Mechanical properties and the hierarchical structure of bone. *Med Eng Phys* 1998;20(2):92-102.
5. Kubo K, Tsukimura N, Iwasa F, Ueno T, Saruwatari L, Aita H, et al. Cellular behavior on TiO₂ nanonodular structures in a micro-to-nanoscale hierarchy model. *Biomaterials* 2009;30(29):5319-5329.
6. Geblinger D, Addadi L, Geiger B. Nano-topography sensing by osteoclasts. *J Cell Sci* 2010;123(9):1503-1510.
7. Mulari MTK, Qu Q, Harkonen PL, Vaananen HK. Osteoblast-like cells complete osteoclastic bone resorption and form new mineralized bone matrix in vitro. *Calcif Tissue Int* 2004;75(3):253-261.
8. Boyan BD, Schwartz Z, Lohmann CH, Sylvia VL, Cochran DL, Dean DD, et al. Pretreatment of bone with osteoclasts affects phenotypic expression of osteoblast-like cells. *J Orthop Res* 2003;21(4):638-647.
9. Parfitt AM. The vascular contribution to bone remodeling. *J Bone Miner Res* 2000;15(4):823-823.
10. Wennerberg A, Albrektsson T. Effects of titanium surface topography on bone integration: a systematic review. *Clin Oral Implants Res* 2009;20:172-184.
11. Gittens RA, McLachlan T, Olivares-Navarrete R, Cai Y, Berner S, Tannenbaum R, et al. The effects of combined micron-/submicron-scale surface roughness and nanoscale features on cell proliferation and differentiation. *Biomaterials* 2011;32(13):3395-3403.
12. Tsukimura N, Ueno T, Iwasa F, Minamikawa H, Sugita Y, Ishizaki K, et al. Bone integration capability of alkali- and heat-treated nanobimorphic Ti-15Mo-5Zr-3Al. *Acta Biomater* 2011;7(12):4267-4277.
13. Orsini G, Piattelli M, Scarano A, Petrone G, Kenealy J, Piattelli A, et al. Randomized, controlled histologic and histomorphometric evaluation of implants with nanometer-scale calcium phosphate added to the dual acid-etched surface in the human posterior maxilla. *J Periodontol* 2007;78(2):209-218.
14. Collaert B, Wijnen L, De Bruyn H. A 2-year prospective study on immediate loading with fluoride-modified implants in the edentulous mandible. *Clin Oral Implants Res* 2011;22(10):1111-1116.
15. Isa ZM, Schneider GB, Zaharias R, Seabold D, Stanford CM. Effects of fluoride-modified titanium surfaces on osteoblast proliferation and gene expression. *Int J Oral Maxillofac Implants* 2006;21(2):203-211.
16. Giavaresi G, Fini M, Chiesa R, Giordano C, Sandrini E, Bianchi AE, et al. A novel multiphase anodic spark deposition coating for the improvement of orthopedic implant osseointegration: an experimental study in cortical bone of sheep. *J Biomed Mater Res A* 2008;85(4):1022-1031.

17. Jimbo R, Xue Y, Hayashi M, Schwartz HO, Andersson M, Mustafa K, et al. Genetic responses to nanostructured calcium-phosphate-coated implants. *J Dent Res* 2011;90(12):1422-1427.
18. Kokubo T, Kim HM, Kawashita M, Nakamura T. Bioactive metals: preparation and properties. *J Mater Sci Mater Med* 2004;15(2):99-107.
19. Crawford GA, Chawla N, Das K, Bose S, Bandyopadhyay A. Microstructure and deformation behavior of biocompatible TiO₂ nanotubes on titanium substrate. *Acta Biomater* 2007;3(3):359-367.
20. MacDonald DE, Rapuano BE, Schniepp HC. Surface oxide net charge of a titanium alloy: comparison between effects of treatment with heat or radiofrequency plasma glow discharge. *Colloids Surf B Biointerfaces* 2011;82(1):173-181.
21. Richert L, Variola F, Rosei F, Wuest JD, Nanci A. Adsorption of proteins on nanoporous Ti surfaces. *Surf Sci* 2010;604(17-18):1445-1451.
22. Davies JE. In vitro modeling of the bone/implant interface. *Anat Rec* 1996;245(2):426-445.
23. Dalby MJ, Gadegaard N, Tare R, Andar A, Riehle MO, Herzyk P, et al. The control of human mesenchymal cell differentiation using nanoscale symmetry and disorder. *Nat Mater* 2007;6(12):997-1003.
24. Mendonca DBS, Miguez PA, Mendonca G, Yamauchi M, Aragao FJL, Cooper LF. Titanium surface topography affects collagen biosynthesis of adherent cells. *Bone* 2011;49(3):463-472.
25. You MH, Kwak MK, Kim DH, Kim K, Levchenko A, Kim DY, et al. Synergistically enhanced osteogenic differentiation of human mesenchymal stem cells by culture on nanostructured surfaces with induction media. *Biomacromolecules* 2010;11(7):1856-1862.
26. Boyan BD, Bonewald LF, Paschalis EP, Lohmann CH, Rosser J, Cochran DL, et al. Osteoblast-mediated mineral deposition in culture is dependent on surface microtopography. *Calcif Tissue Int* 2002;71(6):519-529.
27. Olivares-Navarrete R, Hyzy SL, Hutton DL, Erdman CP, Wieland M, Boyan BD, et al. Direct and indirect effects of microstructured titanium substrates on the induction of mesenchymal stem cell differentiation towards the osteoblast lineage. *Biomaterials* 2010;31(10):2728-2735.
28. Olivares-Navarrete R, Hyzy SL, Chaudhri RA, Zhao G, Boyan BD, Schwartz Z. Sex dependent regulation of osteoblast response to implant surface properties by systemic hormones. *Biol Sex Differ* 2010;1(1):4.
29. Bretauiere JP, and Spillman, T. Alkaline phosphatases. Weinheim, Germany: Verlag Chemica; 1984.
30. Boyan BD, Batzer R, Kieswetter K, Liu Y, Cochran DL, Szmuckler-Moncler S, et al. Titanium surface roughness alters responsiveness of MG63 osteoblast-like cells to 1 alpha,25-(OH)₂D-3. *J Biomed Mater Res* 1998;39(1):77-85.
31. Zhao L, Mei S, Chu PK, Zhang Y, Wu Z. The influence of hierarchical hybrid micro/nano-textured titanium surface with titania nanotubes on osteoblast functions. *Biomaterials* 2010;31(19):5072-5082.
32. Mendonca G, Mendonca DBS, Aragao FJL, Cooper LF. The combination of micron and nanotopography by H₂SO₄/H₂O₂ treatment and its effects on osteoblast-specific gene expression of hMSCs. *J Biomed Mater Res A* 2010;94A(1):169-179.
33. Wilkinson A, Hewitt RN, McNamara LE, McCloy D, Dominic Meek RM, Dalby MJ. Biomimetic microtopography to enhance osteogenesis in vitro. *Acta Biomater* 2011;7(7):2919-2925.

34. MacDonald DE, Rapuano BE, Deo N, Stranick M, Somasundaran P, Boskey AL. Thermal and chemical modification of titanium-aluminum-vanadium implant materials: effects on surface properties, glycoprotein adsorption, and MG63 cell attachment. *Biomaterials* 2004;25(16):3135-3146.
35. Luthra KL. Stability of protective oxide-films on ti-base alloys. *Oxid Met* 1991;36(5-6):475-490.
36. Du HL, Datta PK, Lewis DB, Burnellgray JS. Air oxidation behavior of Ti-6Al-4V alloy between 650-degrees-C and 850-degrees-C. *Corros Sci* 1994;36(4):631-642.
37. Aita H, Hori N, Takeuchi M, Suzuki T, Yamada M, Anpo M, et al. The effect of ultraviolet functionalization of titanium on integration with bone. *Biomaterials* 2009;30(6):1015-1025.
38. Saito T, Hayashi H, Kameyama T, Hishida M, Nagai K, Teraoka K, et al. Suppressed proliferation of mouse osteoblast-like cells by a rough-surfaced substrate leads to low differentiation and mineralization. *Mater Sci Eng C Mater Biol Appl* 2010;30(1):1-7.
39. Pittrof A, Park J, Bauer S, Schmuki P. ECM spreading behaviour on micropatterned TiO(2) nanotube surfaces. *Acta Biomater* 2012;8(7):2639-2647.
40. Webster TJ, Ejirofor JU. Increased osteoblast adhesion on nanophase metals: Ti, Ti6Al4V, and CoCrMo. *Biomaterials* 2004;25(19):4731-4739.
41. Cochran DL. A comparison of endosseous dental implant surfaces. *J Periodontol* 1999;70(12):1523-1539.
42. Stein GS, Lian JB, Stein JL, VanWijnen AJ, Montecino M. Transcriptional control of osteoblast growth and differentiation. *Physiol Rev* 1996;76(2):593-629.
43. Raines AL, Olivares-Navarrete R, Wieland M, Cochran DL, Schwartz Z, Boyan BD. Regulation of angiogenesis during osseointegration by titanium surface microstructure and energy. *Biomaterials* 2010;31(18):4909-4917.
44. Wall I, Donos N, Carlqvist K, Jones F, Brett P. Modified titanium surfaces promote accelerated osteogenic differentiation of mesenchymal stromal cells in vitro. *Bone* 2009;45(1):17-26.
45. Khang D, Choi J, Im YM, Kim YJ, Jang JH, Kang SS, et al. Role of subnano-, nano- and submicron-surface features on osteoblast differentiation of bone marrow mesenchymal stem cells. *Biomaterials* 2012;33(26):5997-6007.
46. Calzado-Martin A, Mendez-Vilas A, Multigner M, Saldana L, Gonzalez-Carrasco JL, Gonzalez-Martin ML, et al. On the role of RhoA/ROCK signaling in contact guidance of bone-forming cells on anisotropic Ti6Al4V surfaces. *Acta Biomater* 2011;7(4):1890-1901.
47. Bjursten LM, Rasmusson L, Oh S, Smith GC, Brammer KS, Jin S. Titanium dioxide nanotubes enhance bone bonding in vivo. *J Biomed Mater Res A* 2010;92(3):1218-1224.
48. Mendonca G, Mendonca DBS, Simoes LGP, Araujo AL, Leite ER, Golin AL, et al. Nanostructured implant surface effect on osteoblast gene expression and bone-to-implant contact in vivo. *Mater Sci Eng C Mater Biol Appl* 2011;31(8):1809-1818.

CHAPTER 6. EFFECTS OF STRUCTURAL PROPERTIES OF ELECTROSPUN TiO₂ NANOFIBER MESHES ON THEIR OSTEOGENIC POTENTIAL

In [Wang X, Gittens RA, Song R, Tannenbaum R, Olivares-Navarrete R, Schwartz Z, Chen H, Boyan BD. Effects of structural properties of electrospun TiO₂ nanofiber meshes on their osteogenic potential. Acta Biomater 2012;8(2):878-885.]

6.1. Introduction

The decade from 2001 to 2011 has been termed the “bone and joint decade”, because it has been recognized that musculoskeletal injuries are the most reported health condition in the United States (US), with an associated cost close to 8% of the US gross domestic product in lost wages and healthcare related costs [1]. More than 25% of musculoskeletal injuries involve bone fractures, with many of these fractures not being able to heal by themselves, thus requiring some type of bone void filler that can promote bone regeneration and reduce healing time for the patient. With an aging population in developed countries and statistics showing, for example, that 1 in every 2 women over 50 years old will suffer an osteoporotic bone fracture [2], there is a pressing need to find reliable bone repair materials.

Tissue engineering offers a promising approach for repair and regeneration of damaged human tissue by mimicking the extracellular environment and taking advantage of the natural cues cells use to perform their role. A common methodology for bone tissue engineering is the fabrication of three-dimensional (3-D) porous scaffolds, which allow cells to invade the construct *in vitro* or *in vivo* and more closely mimic the native environment [3, 4]. There are several methods to prepare porous scaffolds, such as freeze-drying and salt-leaching methods for polymer scaffolds [5], and replica methods used in ceramics [3, 6]. Although discovered over 100 years ago [7], electrospinning has gained popularity recently as a simple and versatile method to

produce fibrous structures from synthetic and natural polymers with nano- to microscale dimensions [7, 8].

The electrospinning process has been extensively applied to create nanofiber scaffolds for cardiovascular [9], urologic [10] and bone tissue engineering applications [11], among others, using synthetic organic polymers such as poly(epsilon-caprolactone) (PCL) [12] and poly(lactide-co-glycolide) (PLGA) [13]. Natural polymers such as collagen [14] and silk fibroin [15] have also been used in the electrospinning setup. Electrospun scaffolds have also been made using a composite of synthetic and natural polymers to take advantage of the mechanical properties of the former and the biological performance of the latter [16, 17]. An attractive property of organic polymers is that they can be resorbed by the body and fully replaced by the native tissue [18]. These organic polymers can also provide surfaces for cell attachment and growth, but it is often necessary to functionalize them, specifically for bone applications, with osteogenic molecules, such as hydroxyapatite [11] and growth factors like bone morphogenic proteins (BMP) [19] to promote cell differentiation.

Ceramic scaffolds have also been considered as bone graft substitutes for bone repair, with calcium-based chemistries such as hydroxyapatite [20] and β -tricalcium phosphate (β TCP) [21] commonly used because of their bioactivity and, in some cases, tunable resorbability [3]. Studies using solid substrate surfaces show that cell differentiation is sensitive to micro- and nanoscale topography [22-26]. When osteoblasts or mesenchymal stem cells (MSCs) are cultured on titanium substrates, which have an inherent TiO_2 ceramic layer on the surface, they exhibit enhanced osteoblastic differentiation, particularly if the surface has both micro- and nanoscale features [27-29]. Although not bioresorbable, TiO_2 could serve as an attractive substrate for bone tissue engineering due to its good biological performance. Whether surface

structure also plays a role when cells are growing on TiO₂ nanofiber meshes is not known. The purpose of this study was to assess the contributions of nanofiber dimensions and microscale pattern on cell response. To do this, pure TiO₂ nanofiber meshes were fabricated using electrospinning to have different surface microroughness and nanofiber diameters.

6.2. Materials and Methods

6.2.1. Preparation and Characterization of TiO₂ Scaffolds

Titania nanofiber meshes were prepared from a TiO₂ gel solution prepared by hydrolysis of titanium(IV) isopropoxide (TiP) in poly(vinyl pyrrolidone) (PVP, $M_w \approx 300\,000$) and acetic acid. Initially, 0.5 mL of TiP was mixed with 0.5 mL ethanol, with 0.5 mL acetic acid used as catalyst. After stirring for 10 minutes, the solution was added to 1.5 mL of 6 % PVP or 10 % PVP in ethanol solution, and magnetically stirred for 30 minutes. To produce electrospun nanofiber meshes, 1 mL of such hybrid solution was loaded into a plastic syringe with a blunt-ended stainless steel needle. The nanofibers were spun using a feeding rate of 0.5 mL/h, a collection distance of 10 cm, and an applied voltage of 8 kV. To create a microscale pattern, the electrospun fibers were collected on a cross-hatched bronze net to imprint a pattern on the side of the mesh in contact with the collector. The PVP was removed from the fibers by heating in air at 700 °C for 3 hours on top of Si wafers, and all samples were sterilized under UV irradiation for at least 12 hours before characterization or cell experiments.

Sample topography and cell morphology were examined by scanning electron microscopy (Ultra 60 FEG-SEM; Carl Zeiss SMT Ltd., Cambridge, UK) using a 5 kV accelerating voltage and 30 μm aperture. Fiber dimensions and pore sizes were evaluated using image analysis software (ImageJ; NIH software) from three images of two different samples. Fiber diameter was evaluated at 20k X magnification and pore

size at 5k X, with at least 100 fibers and 200 pores per mesh determined manually and analyzed by the software.

The chemical composition of the scaffolds was examined by energy dispersive X-ray spectroscopy (INCA EDX; Thermo Fisher Scientific, West Palm Beach, FL), with two different scaffolds per group analyzed in at least three different sites. Additionally, surface atomic concentrations were obtained from two specimens per group, two spots per specimen by X-ray photoelectron spectroscopy (Thermo K-Alpha XPS; Thermo Fisher Scientific, West Palm Beach, FL). The instrument was equipped with a monochromatic Al-K α X-ray source ($h\nu = 1468.6$ eV) and spectra were collected using an X-ray spot size of 400 μm and pass energy of 200 eV, with 1 eV increments, at a 55 ° takeoff angle.

Surface roughness of the porous TiO₂ meshes was evaluated using a laser confocal microscope (Lext LCM; Olympus, Center Valley, PA). LCM analyses were performed over a 644 μm x 644 μm area using a scan height step of 50 nm, a 20 X objective, and a cutoff wavelength of 100 μm . Three scans each of at least two different samples per group were analyzed. The roughness parameters determined were mean surface roughness (S_a) and peak-to-valley height (S_z), and topographical images were also collected at the 20 X magnification.

Finally, crystal structure X-ray diffraction (XRD) was investigated using 1.8 kW Cu K α radiation, a 1 ° parallel plate collimator, a ¼ divergence slit, and a 0.04 rad soller slit (X'Pert PRO Alpha-1 diffractometer; PANalytical, Almelo, The Netherlands). Two samples per group were analyzed.

6.2.2. Cell Culture

MG63 cells (American Type Culture Collection, Rockville, MD) were cultured in Dulbecco's Modification of Eagle's Medium (DMEM Cellgro®; Mediatech, Inc., Manassas, VA), containing 10 % fetal bovine serum (Gibco, Carlsbad, CA) and 1 % penicillin–streptomycin (Gibco), at 37 °C in 5 % CO₂ and 100 % humidity. The MG63 cell line was originally derived from human osteosarcoma and has been shown to exhibit many characteristics of pre-mature osteoblasts, making it an attractive model for *in vitro* studies [30-32]. Cells were grown on 24-well plate tissue culture polystyrene (TCPS) using a seeding density of 20,000 cells/well. Alternatively, cells were seeded onto two different formulations of the TiO₂ meshes (6 % and 10 % PVP), both on their flat and patterned sides after UV sterilization overnight. The meshes were slightly large to fit in a 24-well plate, so plates with larger wells had to be used to avoid damage. Meshes were initially seeded in an untreated 6-well plate using a volume of 150 µL containing 20,000 cells to cover just the surface of the sample, and incubated for 4 hours to allow for initial cell attachment. Next, each well was brought up to a final volume of 2 mL and incubated for an additional 20 hours. After the first 24 hours, TiO₂ meshes were transferred to an untreated 12-well plate containing 1 mL of medium in each well. MG63 cells were fed every 48 hours until confluent on TCPS. Cells in all wells were then incubated with fresh media for 24 hours and harvested. Conditioned media were collected as described below. Cell layers were washed twice with DMEM, followed by two sequential incubations in 500 µL of 0.25% trypsin-EDTA (Gibco) for 10 minutes at 37 °C to ensure all cells were released from their substrate. Cells were then centrifuged at 2000 rpm for 15 minutes, resuspended in 10 mL of saline solution and counted with a Z1 Coulter particle counter (Beckman Coulter, Brea, CA). Cells were centrifuged again at 2000 rpm

for 15 minutes, the supernatant was decanted, and the cell pellets were resuspended in 500 μ L of 0.05 % Triton-X-100. Cells were lysed by sonication.

6.2.3. Biochemical Assays

Cell differentiation was evaluated as a function of alkaline phosphatase specific activity as an early differentiation marker, and osteocalcin content in the conditioned media as a late differentiation marker, as previously described [29]. Alkaline phosphatase specific activity was assayed as the release of *p*-nitrophenol from *p*-nitrophenylphosphate at pH 10.2 [33, 34] and values were normalized to the protein content, which was detected as colorimetric cuprous cations in a bicinchoninic reaction (BCA Protein Assay Kit; Pierce Biotechnology Inc., Rockford, IL, USA) at 570 nm (Microplate Reader; BioRad Laboratories Inc., Hercules, CA, USA) [35]. Osteocalcin levels in the conditioned media were measured with a commercially available radioimmunoassay kit (Human Osteocalcin RIA Kit; Biomedical Technologies, Stoughton, MA) using a LS1500 gamma counter (Perkin Elmer, Waltham, CA) as described previously [36].

The conditioned media were also assayed for protein levels of growth factors and cytokines, as described previously [37, 38]. Osteoprotegerin (OPG), a cytokine that works as a decoy receptor for receptor activator for nuclear factor κ B ligand (RANKL) to inhibit osteoclastogenesis, was measured using an enzyme-linked immunosorbent assay (ELISA) kit (DY805 Osteoprotegerin DuoSet; R&D Systems, Minneapolis, MN). Vascular endothelial growth factor (VEGF), a growth factor involved in vasculogenesis and angiogenesis, was also measured using an ELISA kit (DY293B VEGF DuoSet; R&D Systems).

6.2.4. Statistical Analysis

Data from characterization of the TiO₂ meshes are presented as the mean \pm one standard deviation (SD) of all the measurements performed on different samples. Data from cell experiments are presented as mean \pm standard error for six independent cultures. All experiments were repeated at least twice to ensure validity of the observations and results from individual experiments are shown. Data were evaluated by analysis of variance, and significant differences between groups were determined using Bonferroni's modification of Student's t-test. A p value below 0.05 was considered to indicate a statistically-significant difference.

6.3. Results

The process of electrospinning using the Ti(IV) isopropoxide and PVP mixture produced flexible, roughly-circular white meshes with an average diameter of 17 mm and less than 1 mm in thickness. After calcination at 700 °C for 3 hours, the meshes shrunk to an average diameter of 15 mm and became brittle. LCM images showed topographical differences between the two sides of the 6 % PVP (Figures 6.1A, B) and 10 % PVP (Figures 6.1C, D) TiO₂ meshes. The surface of the meshes that was exposed to the electrospinning setup was relatively flat, with fibers aligned randomly throughout the surface. In contrast, the surface of the mesh that was in contact with the cross-hatched bronze net used to collect the fibers retained the pattern stamped by the net, with bunches of aligned fibers forming ridges ranging from 13 to 26 μ m in height. SEM images (Figures 6.2A-D) and image analysis (Figures 6.2E, F) revealed that the meshes were porous, with a similar average pore size of 1.44 ± 0.89 μ m for 6 % PVP scaffolds and 1.76 ± 1.00 μ m for 10 % PVP scaffolds. However, the higher magnification SEM images (Figures 6.2B, D) showed that changing the preparation from 6 % to 10 % PVP

had an effect on the fiber diameter size, with the former having an average diameter of 184 ± 39 nm, and the latter a significantly larger average diameter of 343 ± 98 nm.

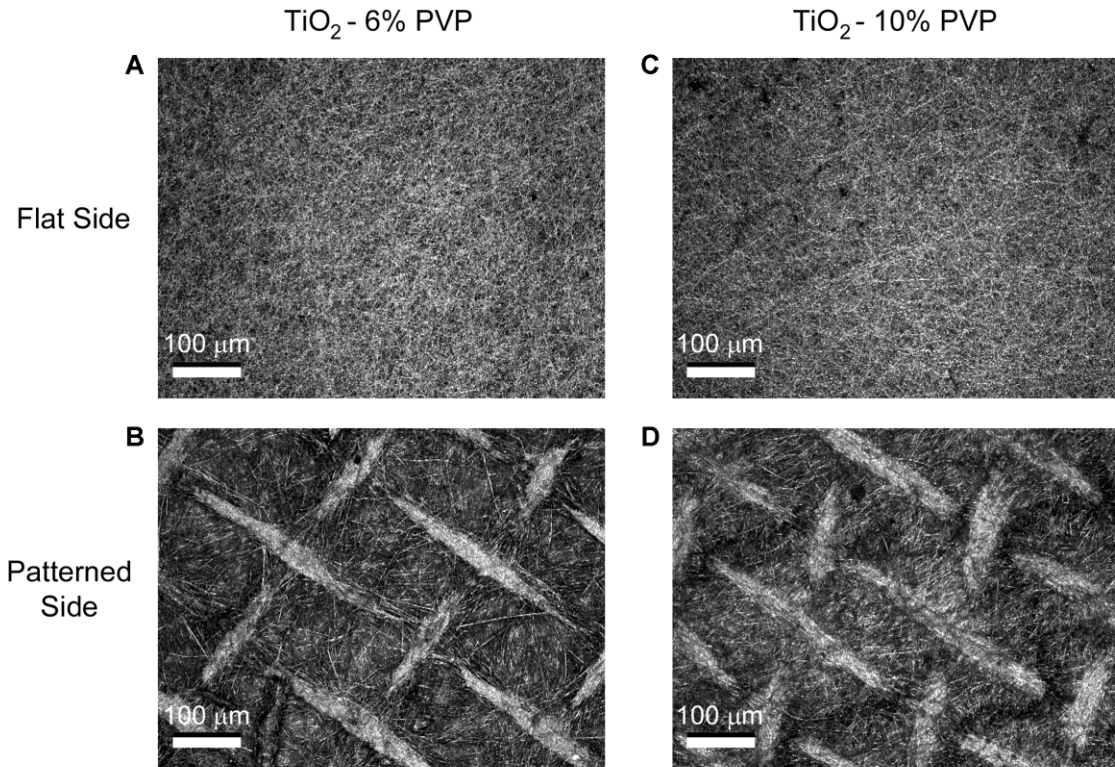


Figure 6.1. LCM images of TiO₂ meshes, made with (A, B) 6 % and (C, D) 10 % PVP showing their flat and patterned surfaces. The nanofibers on the flat side of the meshes are randomly aligned, whereas the patterned side of the meshes has a clear cross-hatch pattern with ridges of aligned nanofibers.

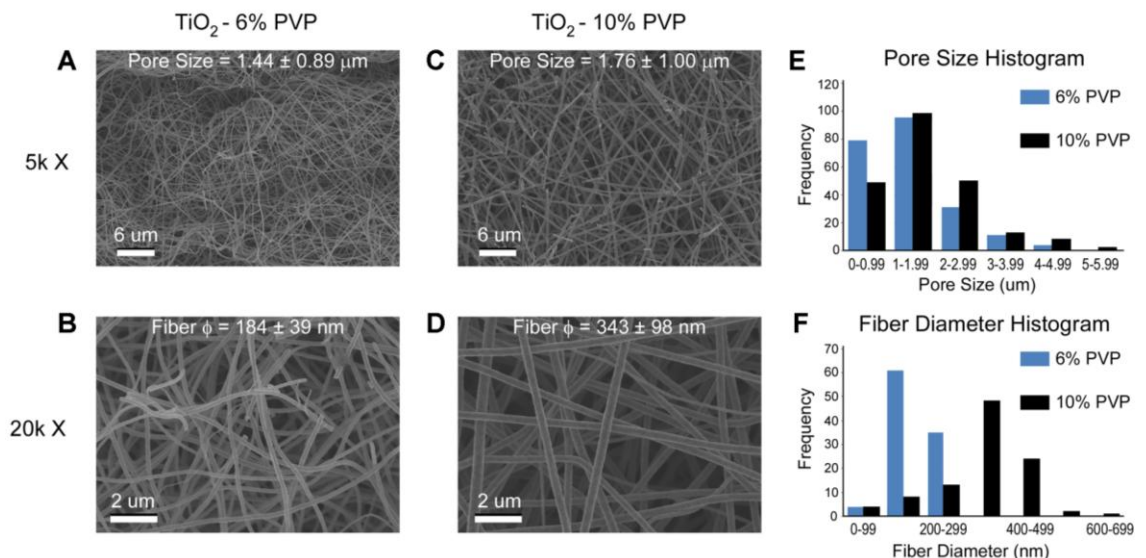


Figure 6.2. SEM images and analysis of the morphology of the electrospun nanofiber TiO₂ meshes produced with (A, B) 6 % or (C, D) 10 % PVP. (E) Histogram at low magnifications shows similar pore sizes for both mesh formulations. However, (F) histogram at higher magnifications reveals thinner nanofibers on the 6 % PVP meshes compared to the 10 % PVP.

Table 6.1. Surface roughness \pm standard deviation (SD) of TiO₂ meshes measured by LCM.

Sample	Roughness Average (S _a \pm SD) [μm]	Peak-to-Peak Height (S _z \pm SD) [μm]
TiO ₂ 6% PVP (flat)	0.57 ± 0.02	12.06 ± 3.33
TiO ₂ -6% PVP (patterned)	2.68 ± 0.35	53.00 ± 14.44
TiO ₂ -10% PVP (flat)	0.61 ± 0.05	25.11 ± 7.33
TiO ₂ -10% PVP (patterned)	2.15 ± 0.57	62.71 ± 8.79

LCM measurements (Table 6.1) revealed that the roughness of both 6 % and 10 % scaffolds was similar with their patterned side significantly rougher compared to the flat side. The XRD spectrum (Figure 6.3) of the nanofiber TiO₂ meshes after calcination presented main peaks for rutile and anatase crystal structures in both PVP concentrations, with small differences in the intensity of the peaks. Chemical analysis by EDX (Table 6.2) showed that the initial PVP concentrations did not affect the final chemical composition after calcination, which included Ti and O as the major components with a molar ratio close to 1:2 consistent with the TiO₂ molecular formula. Small traces of Si and Ca were detected and no C was found in the EDX spectra of all the samples. The surface-sensitive XPS analysis (Table 6.3) also showed O and Ti as the main chemical species in both mesh groups, as well as the presence of C and Si in the spectra.

Table 6.2. Elemental composition \pm standard deviation (SD) of TiO₂ meshes analyzed by EDX.

Sample	Concentration [Atomic % \pm SD]			
	O	Ti	Si	Ca
TiO ₂ - 6% PVP	72.5 \pm 2.0	27.4 \pm 2.1	0.3 \pm 0.0	-
TiO ₂ - 10% PVP	73.9 \pm 1.0	25.7 \pm 1.1	0.3 \pm 0.0	0.2 \pm 0.0

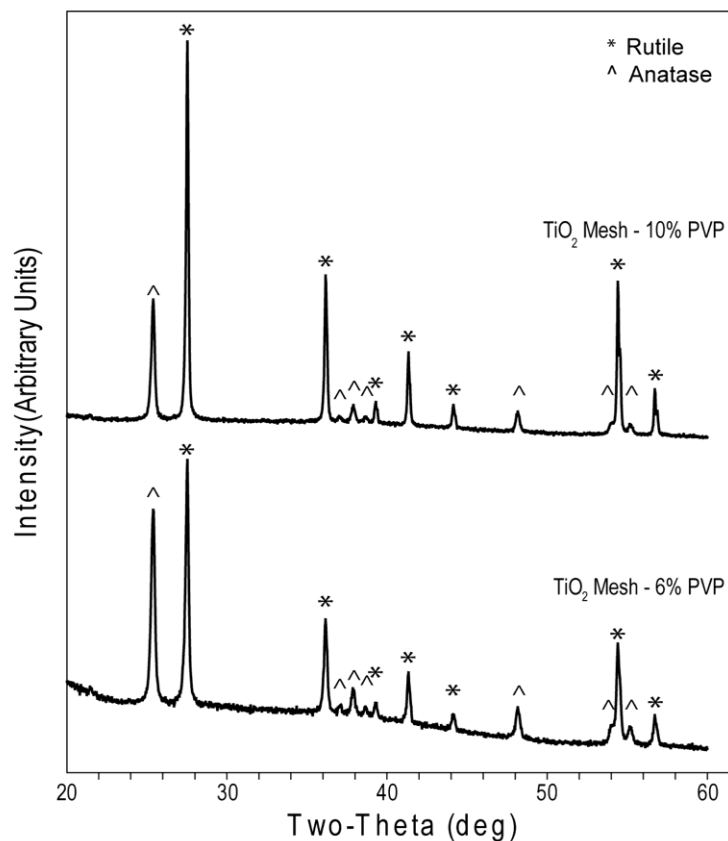


Figure 6.3. XRD spectra of 6 % and 10 % TiO₂ nanofiber meshes. All measured peaks were compared to their respective reference peaks (ICDD spectra database).

Table 6.3. Surface elemental composition \pm standard deviation (SD) of TiO₂ meshes analyzed by XPS.

Sample	Concentration [Atomic % \pm S.D.]			
	O	Ti	C	Si
TiO ₂ 6%PVP	61.1 \pm 1.5	22.2 \pm 2.0	11.8 \pm 0.6	2.7 \pm 1.2
TiO ₂ 10%PVP	63.7 \pm 0.8	23.8 \pm 0.8	8.94 \pm 2.8	2.99 \pm 2.2

Cell morphology was similar on flat (Figure 6.4) and patterned (Figure 6.5) sides of the TiO₂ meshes, regardless of the percent of PVP used during processing. The cells grew throughout the surface with elongated morphology and in some cases seemed to grow along some of the ridges of the patterned side and into the largest pores of both of the mesh. The number of cells on the patterned P6% and P10% groups were similar, but lower than the cell number of flat groups (Figure 6.6A). Cell number of all TiO₂ groups were lower than TCPS. Alkaline phosphatase was affected in a similar manner, with cells on the patterned side of the meshes having lower levels of enzyme activity than cells on the flat side, regardless of the PVP preparation (Figure 6.6B). Osteocalcin levels were higher on the P10% group when compared to the F10% and P6% groups (Figure 6.6C). Osteocalcin levels were also higher on all TiO₂ meshes compared to TCPS. Osteoprotegerin production was sensitive to both the microscale pattern of the surface and the size of the nanofibers, as the levels were higher on the F10% group compared to F6%, and on both P6% and P10% groups compared to their flat sides (Figure 6.6D). VEGF production was higher on P6% and P10% groups compared to TCPS, with P10% being significantly higher than its flat counterpart F10% (Figure 6.6E).

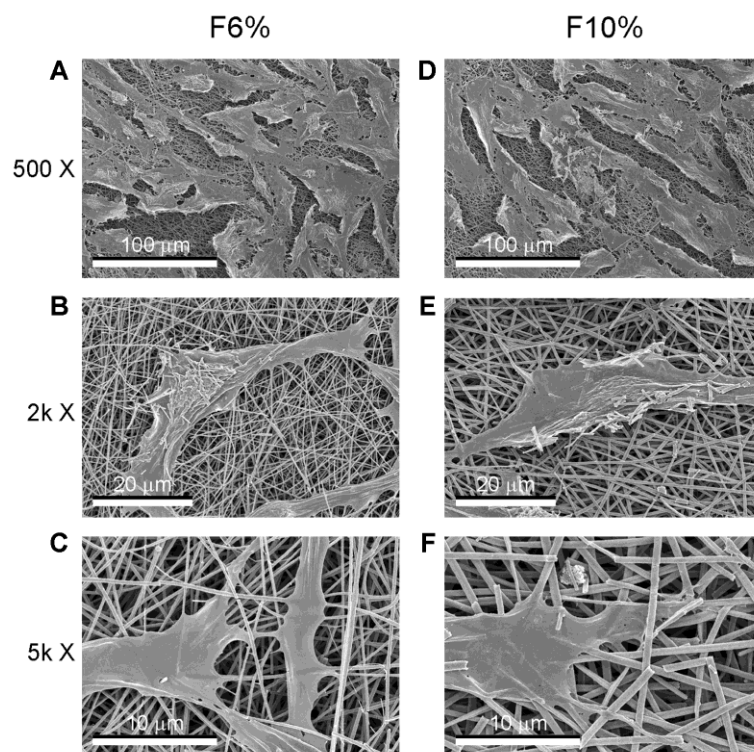


Figure 6.4. SEM images at different magnifications of the morphology of MG63 osteoblast-like cells cultured on the flat side of the nanofiber TiO₂ meshes.

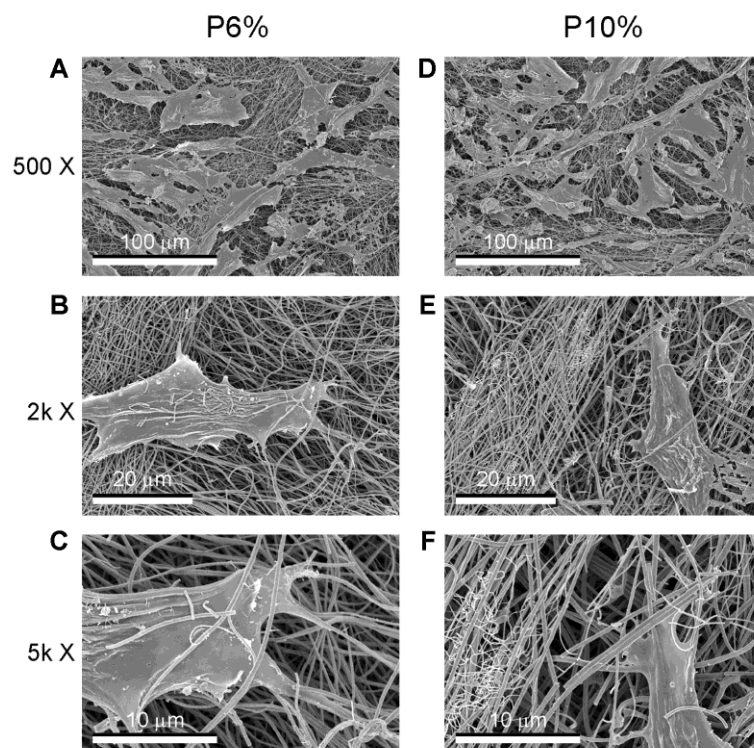


Figure 6.5. SEM images at different magnifications of the morphology of MG63 osteoblast-like cells cultured on the patterned side of the nanofiber TiO_2 meshes.

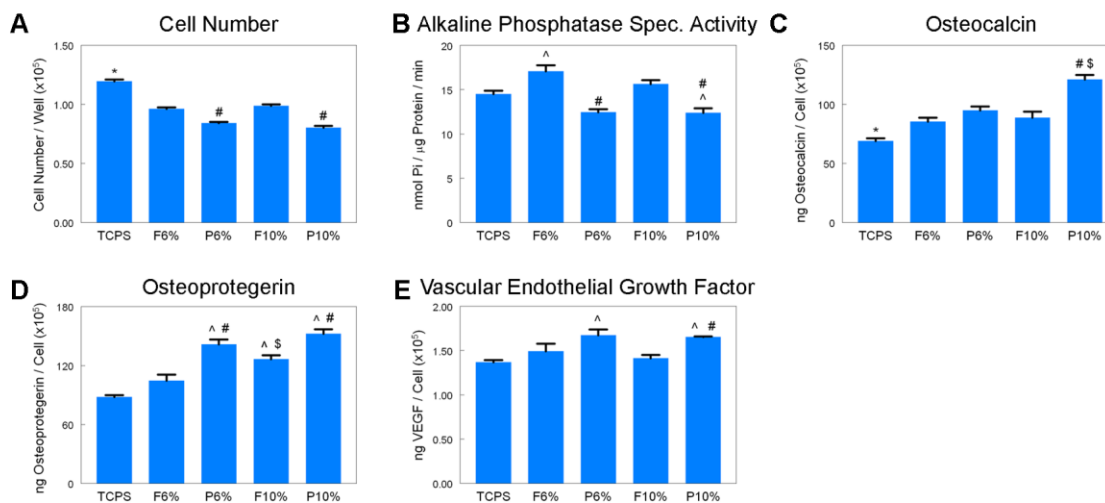


Figure 6.6. Effects of structural properties of electrospun nanofiber TiO₂ meshes on osteoblast maturation. MG63 cells were plated on flat or patterned sides of both 6 % and 10 % PVP TiO₂ meshes and grown to confluence. At confluence, (A) cell number, (B) alkaline phosphatase specific activity, (C) osteocalcin, (D) osteoprotegerin, and (F) VEGF levels were measured. Data represented are the mean \pm standard error of six independent samples. * refers to a statistically-significant *p* value below 0.05 vs. all TiO₂ groups; ^ refers to a statistically-significant *p* value below 0.05 vs. TCPS; # refers to a statistically-significant *p* value below 0.05 vs. flat side of the same formulation; \$ refers to a statistically-significant *p* value below 0.05 vs. 6 % PVP of the same side.

6.4. Discussion

In this study the electrospinning process was used to create pure TiO₂ meshes that had the same chemical composition and crystal structure, but different surface roughness and nanofiber diameter. Differences in surface roughness were achieved by contrasting the side of each mesh that was exposed to the injection needle with the side that was in contact with the patterned bronze collector resulting in a cross-hatch pattern.

LCM measurements confirmed the difference in roughness between the two sides of the meshes, and showed that the patterned side was comparatively rougher than the flat side. These results using inorganic fiber meshes support previous observations showing that different collector patterns affect the topography and fiber alignment of polymeric electrospun meshes [39, 40].

By changing the PVP concentration of the starting solution from 6 % to 10 % PVP, the samples ended up with different average nanofiber diameters. These results are consistent with previous studies on electrospun titania meshes [41], which showed that properties such as fiber diameter and pore size are dependent on electrospinning parameters such as PVP and titanium precursor concentrations, electric field strength, and solution feeding rate. Interestingly, these changes in surface roughness and fiber diameter were achieved without affecting the chemistry or the crystal structure of the substrates, thus emphasizing the effect of the structural variables of interest on cell response. In addition, the EDX results in combination with the lack of N in the XPS spectra supports the point that PVP was removed during calcination and the substrates are, indeed, mainly composed of TiO₂. However, the meshes became brittle after calcination, limiting their use for clinical applications. Our results are in agreement with other studies on similar meshes made with 7 % PVP after calcination at 700 °C for 2 hours that have found no additional weight loss measured by thermogravimetric analysis

[42]. The presence of C in the XPS spectra can be attributed to hydrocarbon and organic contamination, which has been well documented on studies of Ti/TiO₂ surfaces for implant applications when exposed to air [43, 44]. The traces of Si in both the EDX and XPS spectra possibly come from contamination during calcination of the meshes on top of the Si wafers.

Cell morphology was not sensitive to differences in microscale structure or nanofiber diameter. However, cultures grew throughout the entire surface and interacted very closely with the nanofibers. Even on the samples imprinted with the cross-hatch pattern, no major effects on cell morphology were observed, although a few cells did align with some of the ridges. Previous studies on electrospun polymeric scaffolds reported preferential attachment of cells along patterned and aligned nanofibers during early culture time points, but not after cells reach a larger percentage of confluence [45-47]. It is possible that during earlier time points in our study, cells alignment with the ridges of the cross-hatch pattern might have been more evident, although this was not evaluated in this study.

In the present study, the average pore size of the meshes was smaller than the size of the cells, so it was not possible for them to be incorporated into the mesh. However, cells still tried to migrate within the largest pores, as evidenced by single nanofibers covering parts of their cell extensions. Previously, non-woven electrospun scaffolds seeded with human mesenchymal stem cells (MSCs) have been shown to support cell growth with even distribution inside the scaffolds after culture in a dynamic flow bioreactor, and to promote neo-vascularization within the scaffolds in a nude mouse subcutaneous model [48]. Conversely, it has been recently reported that most conventional electrospinning collecting systems result in tightly packed layers of nanofibers that hinder cell infiltration [49]. The same group developed a new “focused,

low-density, uncompressed nanofiber” (FLUF) collection system that results in loosely packed scaffolds with large pores that allow improved infiltration of cells.

Cell number on the TiO₂ meshes was affected by the surface roughness of the samples and not necessarily by the size of the nanofibers. The rough side of both 6 % and 10 % PVP meshes had lower cell numbers than their smooth side. The effect of surface roughness on cell number has been previously reported by our lab and others for Ti/TiO₂ surfaces that promote osteoblast differentiation [29, 50-52]. The concept of decreased cell number on rougher surfaces that enhance osteoblast maturation has been explained as a transcriptionally regulated transition between cell proliferation and differentiation [53, 54]. In contrast, other groups have found higher cell numbers with an increase in nanoroughness [55], microroughness [56, 57] or a combination of both [28]. Our results are also in agreement with other studies on electrospun polymeric scaffolds, which have found no effects on osteoblast proliferation due to nanofiber alignment [40, 45] or nanofiber diameter [58].

Maturation of osteoblasts was controlled by a combination of surface roughness and fiber diameter on the TiO₂ meshes, or in other words a combination of microroughness and nanotopography created by the nanofibers. Alkaline phosphatase specific activity, which is a marker of osteoblast differentiation expressed during early stages, was lower on the rough side of the 6 % and 10 % TiO₂ meshes and higher on the flat side of the 6 % PVP meshes compared to TCPS. Osteocalcin, a late differentiation marker, was significantly higher on the rough side of 10 % PVP meshes compared to all other groups, suggesting that osteoblast were able to sense the combination of micro- and nanotopography and, thus, differentiation was enhanced on these samples. Osteocalcin production was also dependent on the chemistry of the substrate, as levels on all TiO₂ meshes were higher than on TCPS. Many studies

evaluating rough Ti/TiO₂ surfaces have reported enhanced differentiation as evidenced by higher levels of alkaline phosphatase specific activity and osteocalcin compared to smooth surfaces using MG63s [59] and MSCs [22]. Our results are in agreement with other studies that have also found lower levels of alkaline phosphatase specific activity with associated higher production of osteocalcin on microrough surfaces [59, 60] or combined micro/nanostructured surfaces that mimic bone structural hierarchy [29], suggesting a more mature osteoblastic phenotype. These results are attributed to the biphasic profile of alkaline phosphatase specific activity, with an earlier peak and subsequent downregulation in production that precedes the step-like upregulation of osteocalcin once the osteoblasts reach a certain stage of maturity [54]. Only few studies have looked at these differentiation markers on polymeric electrospun meshes, with no clear effect from nanofiber alignment [45] or diameter [58].

In addition, local factors OPG and VEGF were also sensitive to the combination of surface roughness and nanofiber diameter. OPG production was higher on the smooth side of the 10 % PVP meshes compared to the 6 % ones, favoring the larger nanofiber diameter on flat substrates. However, the highest levels of OPG were found on the rough side of the 6 % and 10 % PVP meshes compared to their smooth side. VEGF production had the highest levels on the rough side of both meshes compared to TCPS, with the 10% PVP mesh also having higher levels compared to its smooth counterpart. Overall, our results show enhanced osteoblast maturation and local factor production on rougher TiO₂ porous meshes with larger nanofiber diameter of around 340 nm (*i.e.*, 10 % PVP TiO₂ meshes). These results together with the cell number, ALP and OCN data suggest that surface roughness of porous TiO₂ substrates in combination with the nanotopography created by the fibers can drive the maturation process of osteoblasts on these surfaces.

6.5. Conclusion

In this study, we have evaluated the effect of porous and nanofiber TiO₂ meshes on the cell number, differentiation, and local factor production of osteoblasts. The surface roughness and fiber diameter of the meshes could be varied without affecting their chemistry or crystal structure, emphasizing the effect of the structural parameters on cell response. The different TiO₂ mesh groups supported osteoblast viability, as the cells grew throughout the entire surfaces. The TiO₂ chemistry seemed to enhance osteoblast maturation, as all experimental groups had lower cell number and higher levels of differentiation markers compared to TCPS. Although cell morphology was similar on all TiO₂ mesh groups, cell response was sensitive to the substrate. Moreover, cell number, differentiation and local factor production were regulated by different structural aspects of the meshes. Osteoblast final cell number was controlled by surface microroughness, whereas differentiation and local factor production were affected by both surface microscale pattern and nanofiber diameter, indicating that osteoblasts are sensitive to both the microroughness and nanotopography created by the TiO₂ nanofibers. Finally, the combination of micro/nanotopography created by the larger nanofibers enhanced osteoblast differentiation and local factor production, indicating that there might be a lower-limit threshold in the size of the nanofibers that could be sensed by the osteoblasts to differentiate and generate an osteogenic environment. In conclusion, inorganic scaffold structural cues alone can be used to drive cell differentiation and create an osteogenic environment without the use of exogenous factors and, thus, structural parameters should be carefully considered when designing a scaffold for tissue engineering applications.

6.6. References

1. Jacobs JJ, Andersson GBJ, Bell JE, Weinstein SL, Dormans JP, Gnat SM, et al. The burden of musculoskeletal diseases in the United States: AAOS; 2008.
2. Agrawal CM, Attawia M, Borden MD, Boyan BD, Bruder SP, Bucholz RW, et al. Bone graft substitutes: ASTM - AAOS; 2003.
3. Hing KA. Bioceramic bone graft substitutes: Influence of porosity and chemistry. *Int J Appl Ceram Technol* 2005;2:184-199.
4. Lutolf MP, Hubbell JA. Synthetic biomaterials as instructive extracellular microenvironments for morphogenesis in tissue engineering. *Nat Biotechnol* 2005;23:47-55.
5. Heijkants RGJC, Van Tienen TG, De Groot JH, Pennings AJ, Buma P, Veth RPH, et al. Preparation of a polyurethane scaffold for tissue engineering made by a combination of salt leaching and freeze-drying of dioxane. *J Mater Sci* 2006;41:2423-2428.
6. Miao XG, Tan DM, Li J, Xiao Y, Crawford R. Mechanical and biological properties of hydroxyapatite/tricalcium phosphate scaffolds coated with poly(lactic-co-glycolic acid). *Acta Biomater* 2008;4:638-645.
7. Sill TJ, von Recum HA. Electro spinning: Applications in drug delivery and tissue engineering. *Biomaterials* 2008;29:1989-2006.
8. Huang ZM, Zhang YZ, Kotaki M, Ramakrishna S. A review on polymer nanofibers by electrospinning and their applications in nanocomposites. *Compos Sci Technol* 2003;63:2223-2253.
9. Yoo JJ, Liu J, Soker S, Komura M, Lim G, Atala A, et al. Electrospinning fabrication of collagen-based scaffolds for vascular tissue engineering. *FASEB J* 2006;20:A1101-A1101.
10. McManus M, Boland E, Sell S, Bowen W, Koo H, Simpson D, et al. Electrospun nanofibre fibrinogen for urinary tract tissue reconstruction. *Biomed Mater* 2007;2:257-262.
11. Venugopal JR, Low S, Choon AT, Kumar AB, Ramakrishna S. Nanobioengineered electrospun composite nanofibers and osteoblasts for bone regeneration. *Artif Organs* 2008;32:388-397.
12. Yoshimoto H, Shin YM, Terai H, Vacanti JP. A biodegradable nanofiber scaffold by electrospinning and its potential for bone tissue engineering. *Biomaterials* 2003;24:2077-2082.
13. Li WJ, Laurencin CT, Caterson EJ, Tuan RS, Ko FK. Electrospun nanofibrous structure: A novel scaffold for tissue engineering. *J Biomed Mater Res* 2002;60:613-621.
14. Matthews JA, Wnek GE, Simpson DG, Bowlin GL. Electrospinning of collagen nanofibers. *Biomacromolecules* 2002;3:232-238.
15. Jin HJ, Chen JS, Karageorgiou V, Altman GH, Kaplan DL. Human bone marrow stromal cell responses on electrospun silk fibroin mats. *Biomaterials* 2004;25:1039-1047.
16. Bhattarai N, Edmondson D, Veiseh O, Matsen FA, Zhang MQ. Electrospun chitosan-based nanofibers and their cellular compatibility. *Biomaterials* 2005;26:6176-6184.
17. Zhang YZ, Ouyang HW, Lim CT, Ramakrishna S, Huang ZM. Electrospinning of gelatin fibers and gelatin/PCL composite fibrous scaffolds. *J Biomed Mater Res B Appl Biomater* 2005;72B:156-165.
18. Wagner WR, Hong Y, Huber A, Takanari K, Amoroso NJ, Hashizume R, et al. Mechanical properties and in vivo behavior of a biodegradable synthetic polymer

microfiber-extracellular matrix hydrogel biohybrid scaffold. *Biomaterials* 2011;32:3387-3394.

19. Li CM, Vepari C, Jin HJ, Kim HJ, Kaplan DL. Electrospun silk-BMP-2 scaffolds for bone tissue engineering. *Biomaterials* 2006;27:3115-3124.

20. Gao Y, Cao WL, Wang XY, Gong YD, Tian JM, Zhao NM, et al. Characterization and osteoblast-like cell compatibility of porous scaffolds: bovine hydroxyapatite and novel hydroxyapatite artificial bone. *J Mater Sci Mater Med* 2006;17:815-823.

21. Stein GS, Zhang Y, Hassan MQ, Li ZY, Stein JL, Lian JB, et al. Intricate gene regulatory networks of helix-loop-helix (HLH) proteins support regulation of bone-tissue related genes during osteoblast differentiation. *J Cell Biochem* 2008;105:487-496.

22. Olivares-Navarrete R, Hyzy SL, Hutton DL, Erdman CP, Wieland M, Boyan BD, et al. Direct and indirect effects of microstructured titanium substrates on the induction of mesenchymal stem cell differentiation towards the osteoblast lineage. *Biomaterials* 2010;31:2728-2735.

23. Mendonca G, Mendonca DBS, Aragao FJL, Cooper LF. Advancing dental implant surface technology - From micron- to nanotopography. *Biomaterials* 2008;29:3822-3835.

24. Mendonca G, Mendonca DBS, Simoes LGP, Araujo AL, Leite ER, Duarte WR, et al. The effects of implant surface nanoscale features on osteoblast-specific gene expression. *Biomaterials* 2009;30:4053-4062.

25. Biggs MJP, Richards RG, Dalby MJ. Nanotopographical modification: a regulator of cellular function through focal adhesions. *Nanomedicine* 2010;6:619-633.

26. Curtis ASG, Gadegaard N, Dalby MJ, Riehle MO, Wilkinson CDW, Aitchison G. Cells react to nanoscale order and symmetry in their surroundings. *IEEE Trans NanoBiosci* 2004;3:61-65.

27. Mendonca G, Mendonca DBS, Aragao FJL, Cooper LF. The combination of micron and nanotopography by H₂SO₄/H₂O₂ treatment and its effects on osteoblast-specific gene expression of hMSCs. *J Biomed Mater Res A* 2010;94A:169-179.

28. Kubo K, Tsukimura N, Iwasa F, Ueno T, Saruwatari L, Aita H, et al. Cellular behavior on TiO₂ nanonodular structures in a micro-to-nanoscale hierarchy model. *Biomaterials* 2009;30:5319-5329.

29. Gittens RA, McLachlan T, Olivares-Navarrete R, Cai Y, Berner S, Tannenbaum R, et al. The effects of combined micron-/submicron-scale surface roughness and nanoscale features on cell proliferation and differentiation. *Biomaterials* 2011;32:3395-3403.

30. Franceschi RT, James WM, Zerlauth G. 1-alpha,25-dihydroxyvitamin-D₃ specific regulation of growth, morphology, and fibronectin in a human osteo-sarcoma cell-line. *J Cell Physiol* 1985;123:401-409.

31. Lajeunesse D, Kiebzak GM, Frondoza C, Sacktor B. Regulation of Osteocalcin Secretion by Human Primary Bone-Cells and by the Human Osteosarcoma Cell-Line Mg-63. *Bone Miner* 1991;14:237-250.

32. Kieswetter K, Schwartz Z, Hummert TW, Cochran DL, Simpson J, Dean DD, et al. Surface roughness modulates the local production of growth factors and cytokines by osteoblast-like MG-63 cells. *J Biomed Mater Res* 1996;32:55-63.

33. Bretauiere JP, and Spillman, T. Alkaline phosphatases. Weinheim, Germany: Verlag Chemica; 1984.

34. Martin JY, Schwartz Z, Hummert TW, Schraub DM, Simpson J, Lankford J, et al. Effect of titanium surface-roughness on proliferation, differentiation, and protein-synthesis of human osteoblast-like cells (mg63). *J Biomed Mater Res* 1995;29:389-401.

35. Smith PK, Krohn RI, Hermanson GT, Mallia AK, Gartner FH, Provenzano MD, et al. Measurement of Protein Using Bicinchoninic Acid. *Anal Biochem* 1985;150:76-85.
36. Gundberg CM, Hauschka PV, Lian JB, Gallop PM. Osteocalcin - Isolation, Characterization, and Detection. *Methods Enzymol* 1984;107:516-544.
37. Simonet WS, Lacey DL, Dunstan CR, Kelley M, Chang MS, Luthy R, et al. Osteoprotegerin: A novel secreted protein involved in the regulation of bone density. *Cell* 1997;89:309-319.
38. Raines AL, Olivares-Navarrete R, Wieland M, Cochran DL, Schwartz Z, Boyan BD. Regulation of angiogenesis during osseointegration by titanium surface microstructure and energy. *Biomaterials* 2010;31:4909-4917.
39. Li D, Ouyang G, McCann JT, Xia YN. Collecting electrospun nanofibers with patterned electrodes. *Nano Lett* 2005;5:913-916.
40. Wang YZ, Wang GX, Chen L, Li H, Yin TY, Wang BC, et al. Electrospun nanofiber meshes with tailored architectures and patterns as potential tissue-engineering scaffolds. *Biofabrication* 2009;1.
41. Li D, Xia YN. Fabrication of titania nanofibers by electrospinning. *Nano Lett* 2003;3:555-560.
42. Park S-J, Chase GG, Jeong K-U, Kim HY. Mechanical properties of titania nanofiber mats fabricated by electrospinning of sol-gel precursor. *J Sol-Gel Sci Technol* 2010;54:188-194.
43. Rupp F, Scheideler L, Olshanska N, deWild M, Wieland M, Geis-Gerstorfer J. Enhancing surface free energy and hydrophilicity through chemical modification of microstructured titanium implant surfaces. *J Biomed Mater Res A* 2006;76A:323-334.
44. Massaro C, Rotolo P, De Riccardis F, Milella E, Napoli A, Wieland M, et al. Comparative investigation of the surface properties of commercial titanium dental implants. Part I: chemical composition. *J Mater Sci Mater Med* 2002;13:535-548.
45. Ma J, He X, Jabbari E. Osteogenic Differentiation of Marrow Stromal Cells on Random and Aligned Electrospun Poly(l-lactide) Nanofibers. *Ann Biomed Eng* 2010;39:14-25.
46. Meinel AJ, Kubow KE, Klotzsch E, Garcia-Fuentes M, Smith ML, Vogel V, et al. Optimization strategies for electrospun silk fibroin tissue engineering scaffolds. *Biomaterials* 2009;30:3058-3067.
47. Murugan R, Ramakrishna S. Design Strategies of Tissue Engineering Scaffolds with Controlled Fiber Orientation. *Tissue Eng* 2007;13:1845-1866.
48. Srouji S, Kizhner T, Suss-Tobi E, Livne E, Zussman E. 3-D Nanofibrous electrospun multilayered construct is an alternative ECM mimicking scaffold. *J Mater Sci - Mater Med* 2008;19:1249-1255.
49. Blakeney BA, Tambralli A, Anderson JM, Andukuri A, Lim D-J, Dean DR, et al. Cell infiltration and growth in a low density, uncompressed three-dimensional electrospun nanofibrous scaffold. *Biomaterials* 2011;32:1583-1590.
50. Wall I, Donos N, Carlqvist K, Jones F, Brett P. Modified titanium surfaces promote accelerated osteogenic differentiation of mesenchymal stromal cells in vitro. *Bone* 2009;45:17-26.
51. Zhao G, Zinger O, Schwartz Z, Wieland M, Landolt D, Boyan BD. Osteoblast-like cells are sensitive to submicron-scale surface structure. *Clin Oral Implants Res* 2006;17:258-264.
52. Kim MJ, Kim CW, Lim YJ, Heo SJ. Microrough titanium surface affects biologic response in MG63 osteoblast-like cells. *J Biomed Mater Res A* 2006;79:1023-1032.
53. Stein GS, Lian JB, Stein JL, VanWijnen AJ, Montecino M. Transcriptional control of osteoblast growth and differentiation. *Physiol Rev* 1996;76:593-629.

54. Lian JB, Stein GS. Concepts of osteoblast growth and differentiation - Basis for modulation of bone cell-development and tissue formation. *Crit Rev Oral Biol Medicine* 1992;3:269-305.
55. Han P, Ji WP, Zhao CL, Zhang XN, Jiang Y. Improved osteoblast proliferation, differentiation and mineralization on nanophase Ti6Al4V. *Chin Med J (Engl)* 2011;124:273-279.
56. Kubies D, Himmlova L, Riedel T, Chanova E, Balik K, Douderova M, et al. The interaction of osteoblasts with bone-implant materials: 1. The effect of physicochemical surface properties of implant materials. *Physiol Res* 2011;60:95-111.
57. Brett PM, Harle J, Salih V, Mihoc R, Olsen I, Jones FH, et al. Roughness response genes in osteoblasts. *Bone* 2004;35:124-133.
58. Badami A, Kreke M, Thompson M, Riffle J, Goldstein A. Effect of fiber diameter on spreading, proliferation, and differentiation of osteoblastic cells on electrospun poly(lactic acid) substrates. *Biomaterials* 2006;27:596-606.
59. Zinger O, Zhao G, Schwartz Z, Simpson J, Wieland M, Landolt D, et al. Differential regulation of osteoblasts by substrate microstructural features. *Biomaterials* 2005;26:1837-1847.
60. Zhao G, Raines AL, Wieland M, Schwartz Z, Boyan BD. Requirement for both micron- and submicron scale structure for synergistic responses of osteoblasts to substrate surface energy and topography. *Biomaterials* 2007;28:2821-2829.

**PART II: EVALUATION OF ELECTRICAL STIMULATION OF TITANIUM SURFACES
ON OSTEOLAST LINEAGE CELL RESPONSES**

CHAPTER 7. REVIEW OF BONE ELECTRICAL PROPERTIES AND THE ELECTRICAL IMPLICATIONS OF CORROSION ON OSTEOINTEGRATION OF TITANIUM IMPLANTS

In [Gittens RA, Olivares-Navarrete R, Tannenbaum R, Boyan BD, Schwartz Z. Electrical implications of corrosion for osseointegration of titanium implants. J Dent Res 2011;90(12):1389-1397.]

7.1. Biopotentials

Exogenous electrical control of cell and tissue physiology has been studied since the late 1700s with the work of scientists such as Luigi Galvani, Alessandro Volta, Carlo Matteucci, and Emil Du-Bois Reymond, leading to the discovery of biopotentials and injury potentials [1, 2]. Biopotentials are natural electrical properties that control normal growth and development of different types of cells and tissues [3, 4] (Figures 7.1A, C). Injury potentials are alterations to the normal potential patterns of intact tissue [5, 6], characterized by stable, long-lasting direct current (DC) voltage potentials induced between injured and intact tissues that persist until the wound has healed. These potentials can span hundreds of micrometers and are generated by currents of ions flowing through the injured tissue [7, 8] (Figures 7.1B, D). Currents of $1\text{-}100\mu\text{A}/\text{cm}^2$ have been measured in injured tissues [7, 9] and, assuming the resistivity of soft tissues to be $100\Omega\cdot\text{cm}$ [8, 10], these currents create voltage differences of $10\text{-}100\text{ mV}/\text{cm}$ across hundreds of micrometers.

Recent findings underscore the importance of endogenous electrical potentials in cell signaling and gene expression. Endogenous electrical potentials, and specifically injury potentials, have been associated with epithelial cell migration and advancement of the wound-healing front through activation of Src and inositol-phospholipid signaling pathways in a rat corneal model [11]. Disruption of endogenous electric potentials affected the migration speed and direction of the wound-healing front. The same group

also found that corneal epithelial cells from bovine eyes were sensitive to directional cues such as nanogrooves (*i.e.*, contact guidance) and electric fields (*i.e.*, electrotaxis) through the activation of small GTPases Rho and Cdc42, respectively [12]. The study showed that electrotaxis seemed to be more potent than, but not completely dominant over, contact guidance by setting the electric fields orthogonally to the nanogrooves and measuring the distance traveled by the cells. Furthermore, a cell-membrane voltage sensor, *Ciona intestinalis* voltage-sensor-containing phosphatase (Ci-VSP), has been identified, which is activated by changes in membrane potential and can initiate signaling cascades [13, 14].

7.2. Electrical Signals in Bone

Both biopotentials and injury potentials are found in bone. Electrical properties and electrical stimulation of bone have been investigated since the 1950s, beginning with the piezoelectric nature of osseous tissue [15]. When forces were applied to sections of previously dried human and ox femurs, directly proportional voltages could be measured that were dependent on the collagen fiber alignment. This led to the idea that electrical signals could be related to the process of bone formation. Additional endogenous electrical properties of bone have been discovered since and are suggested to play a role in the feedback mechanism of bone remodeling and development [16, 17].

Biopotentials in bone are classified into two sub-groups, due in part to the complexity of bone structure: strain-related potentials (SRP) and biopotentials. SRPs include the piezoelectric behavior (*i.e.*, electric potential in response to applied forces) of bone due to the structure and dipolar charge of collagen, and streaming potentials associated with the flow of fluid and ions through porous bone. The sub-group of

biopotentials in bone results from contribution of biological processes such as osteoblast membrane potential, extracellular matrix acidification and ion release caused by osteoclast bone resorption, and cell junctions of osteocytes. *In vivo*, these electrical signals work in concert to provide the correct environment for normal bone growth and development, but can be disrupted or altered by injury potentials after trauma and during healing.

Mechanical forces have been shown to direct the process of bone remodeling [18, 19]. Accordingly, areas of bone under stress tend to grow and those areas under no mechanical load tend to be resorbed [20]. This is believed to be a result of the physical stress alteration and biochemical activation of particular bone cells [20]. As a parallel event, however, areas of bone that are under mechanical load generate a more negative polarity than areas under smaller or no loads [15, 21] (Figure 7.2A). Thus, bone growth could also be attributed to negative polarity and bone resorption to positive polarity, suggesting that electrical signals work as a feedback mechanism for bone remodeling [2, 6].

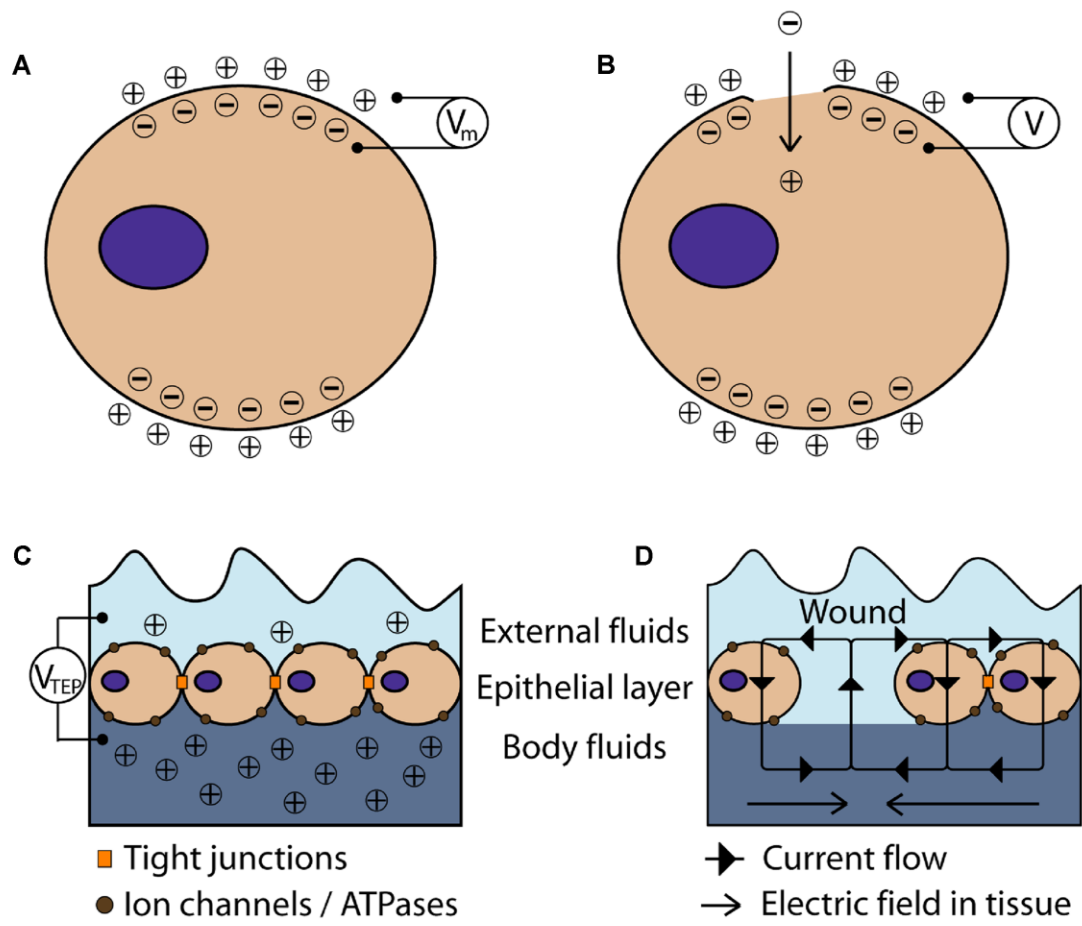


Figure 7.1. Schematics of injury potentials. (A) Electrical potential of a cell across an intact plasma membrane (V_m). (B) Inward current flow, and associated potential (V), after localized injury to the cell plasma membrane. (C) Transepithelial electrical potential (V_{TEP}) across an intact cell layer of the skin. (D) Short-circuit caused by a wound across the skin. Adapted from [8].

The relationship between negative potentials and bone growth is seen during long bone fracture healing [6, 22, 23]. In children, fractured long bones tend to overgrow with respect to their counterparts [24, 25], and there is an increase in apoptosis in the growth plate [26]. Interestingly, both the healing site and growth plate tend to have a more negative potential compared to the nearby intact tissue [2, 27] (Figure 7.2B). During development, the growth plate has a negative potential, while the growth plate of mature subjects tends to have a neutral voltage [28]. Consequently, negative potentials in the growth plate after fracture may be related to bone overgrowth since cortical bone healing and repair should not increase bone length. However, the negative potential found at the fracture site may coordinate bone healing and may directly influence the polarity of the growth plate.

The relationship between mechanical stimuli, electrical potentials, and bone remodeling can also be seen in orthodontic treatment of patients with malocclusion. Tipping and translational mechanical forces applied during orthodontic treatment deform and remodel alveolar bone and periodontal tissue, resulting in tooth movement [29, 30]. Quantitative techniques such as finite element analysis have been used to assess forces affecting tooth movement [31, 32]. Although the experimental design and parameters measured varied between studies, the results indicate a direct relationship between the magnitude of the applied stress and the level of bone and periodontal ligament remodeling. Some studies have correlated excessive forces to orthodontically-induced inflammatory root resorption [33].

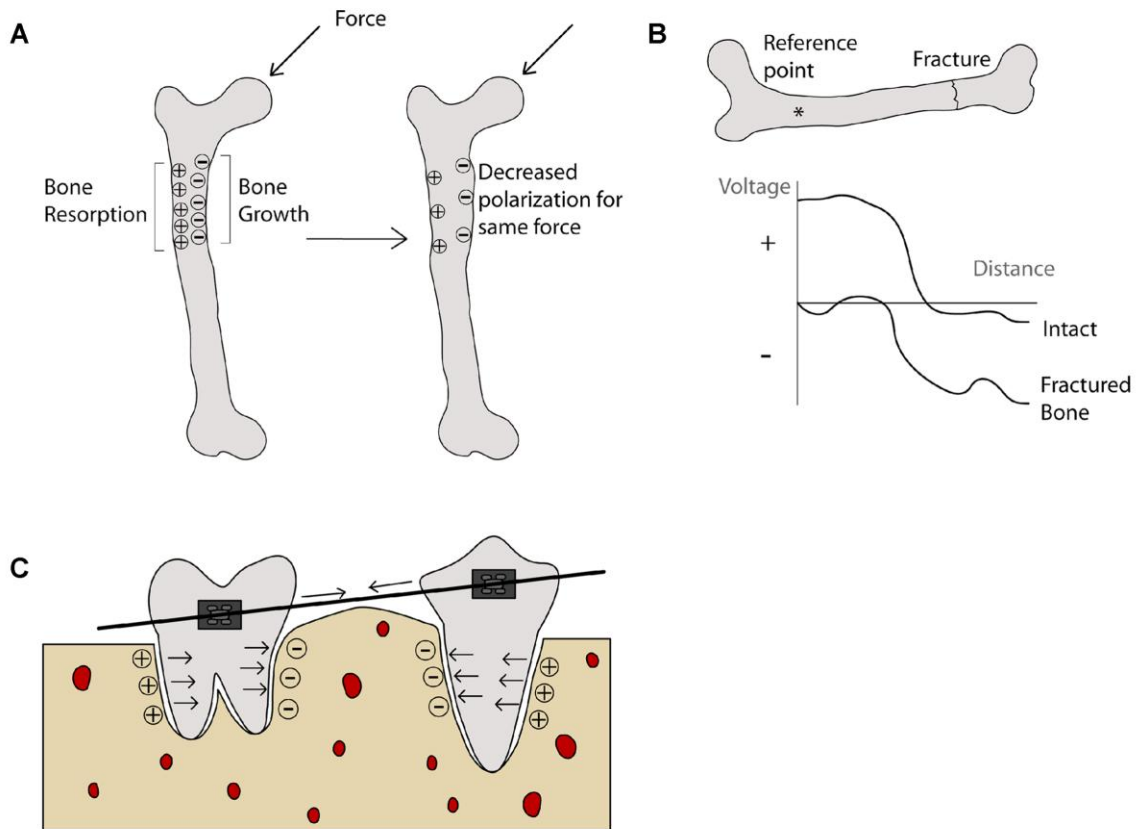


Figure 7.2. Schematics of the relationship between mechanical forces and electrical signals in bone. (A) Polarization of bone under applied mechanical forces; (B) voltage versus distance comparison between intact and 1-hour post-fracture bones; (C) simplified mechanical forces and respective polarization of bone and periodontal ligament under orthodontic treatment. Adapted from [2].

Despite innate differences between the origin of long bones and maxillofacial bone, forces applied on teeth and surrounding alveolar bone generate similar electrical potentials [34, 35]. The electrical polarization of these tissues has also been correlated to bone remodeling. Areas with high osteoblast activity and bone growth show negative polarization, while areas under resorption due to higher osteoclast levels show a positive or neutral polarization [36] (Figure 7.2C). One suggested hypothesis states that these electrical potentials may provide a more direct measurement of the mechanical forces delivered by orthodontic devices and help provide a more personalized treatment [37].

7.3. Electrical Stimulation of Bone

The role of these electrical signals in bone growth and development have prompted several research groups to study bone repair using methods to electrically stimulate cells and tissues *in vitro* [38, 39] and *in vivo* [40, 41] with very successful outcomes. Some have associated bone growth enhancement after electrical stimulation to the production of osteoinductive factors such as bone morphogenetic proteins (BMPs) 2, 4, 5 and 6 [39, 42], as well as with levels of intracellular and extracellular calcium [38, 43]. However, differences in experimental design and the electrical parameters used, and the over-simplification of *in vitro* models that do not account for many aspects of *in vivo* conditions has hindered the systematic investigation of the molecular pathways involved with cell responses. Additionally, it is not well understood if electrical stimulation affects every type of bone (e.g., cortical, trabecular, membranous) in a similar manner. Fundamental understanding of the molecular pathways involved in electrical stimulation are necessary to elucidate the role of electrical signals in the bone-implant interface and thus, allow better system designs for personalized treatment.

Electrical stimulation systems can be classified into three main groups depending on the nature of the electrical signals being supplied: direct current stimulation, capacitive stimulation, and inductive stimulation.

7.3.1. Direct Current (DC) Stimulation

DC stimulation, or faradic stimulation, is an invasive method that applies a DC electric field to growing cells either directly through the surface on which they are growing, or indirectly through the medium in which they are growing (Figure 7.3A). Common parameters applied include fixed currents of 1-50 $\mu\text{A}/\text{cm}^2$, which can affect osteoblast proliferation and expression of differentiation markers [39, 44]. The majority of published studies using *in vitro* DC stimulation use electrodes submerged in the tissue culture medium, establishing a DC electric field and inducing electrochemical currents between the anode and the cathode [45, 46]. However, the products generated at the cathode and the anode can have enhancing or detrimental effects on cell response, respectively [23, 44], obscuring the results of DC electrical stimulation.

Titanium (Ti) implants can be used as cathodes for DC electrical stimulation [47]. One such device was developed to fit inside a dental implant healing abutment and supply electrical stimulation to canine mandibular bone [48]. Biphasic electric stimulation increased bone formation and bone-to-implant contact when compared to control implants. Ti substrates used in a typical configuration with submerged electrodes in the media showed increased osteoblast density by DAPI staining [46, 49]. Although Ti is one of the most used materials for bone implants, *in vitro* osteoblast response to electrical stimulation supplied directly through Ti substrates serving as electrodes remains unexplored.

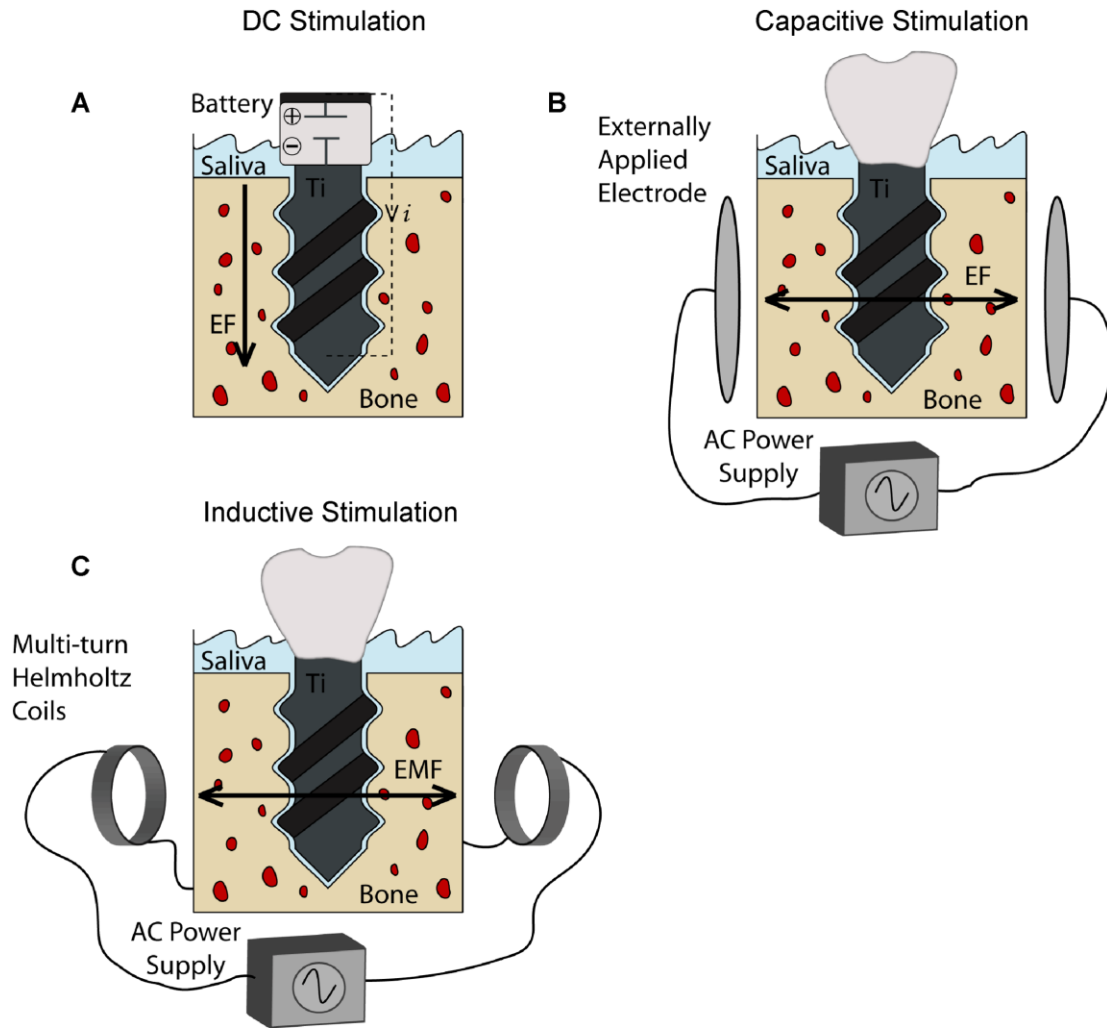


Figure 7.3. Schematics of different electrical stimulation systems. (A) DC electrical stimulation setup consisting of a battery that generates an electric field (EF) directly through the implant device. The implant becomes the cathode, the anode is exposed to the oral cavity, and the surrounding tissue serves as a path to close the circuit and allow flow of current. (B) Capacitive stimulation setup, consisting of two externally-applied electrodes that generate an electric field (EF). (C) Inductive stimulation setup, consisting of a pair of multi-turn Helmholtz coils connected in series to generate an electromagnetic field (EMF).

7.3.2. Capacitive Stimulation

In capacitive stimulation, electrodes are applied externally to the skin above the area to be stimulated, inducing an electric field that can influence cell response (Figure 7.3B). Common external stimulation systems use alternating current (AC) parameters that vary between 1-50 V at frequencies of 60-200,000 Hz, and effective electric field strengths from 0.1 to 5 V/m [50, 51]. Cells grown *in vitro* on tissue culture substrates are either stimulated through the media using an AC power supply or sandwiched between electrodes without media contact. Capacitive stimulation is advantageous because it is non-invasive, and it has been shown to have an effect both *in vitro* [42, 52] and *in vivo* [53, 54]. However, the therapeutic results depend on patient compliance, and high voltages and frequencies applied may cause irritation [2, 55]. Since capacitive stimulation cannot be applied directly to the affected osseous tissue, and because of the complexities of measuring local current densities in the site of interest, it is difficult to predict the subsequent effects.

7.3.3. Inductive Stimulation

Inductive stimulation is a non-invasive method that uses a coil or pair of coils connected in series, with their axis perpendicular to the long bone, to generate pulsed electromagnetic fields (PEMFs) and small secondary electric fields [2] (Figure 7.3C). These magnetic fields and the induced electric fields have been shown to influence cell response and gene expression [52, 56, 57].

In a series of studies performed in our lab, the effects of PEMFs on MG63 osteoblast-like cells were shown to reduce cell number, and increase osteoblast maturation, collagen synthesis, and local factor production, including transforming growth factor- β 1 (TGF- β 1) [58]. Cells from human hypertrophic and atrophic nonunion tissues have been used to evaluate the effect of PEMFs on nonunion fractures,

commonly treated with electrical stimulation [59]. Cells exposed to PEMFs increased TGF- β 1, with no effect on cell proliferation or differentiation, suggesting that improvements in nonunions after PEMFs result from changes in local factor production near the affected area. Finally, mesenchymal stem cells (MSCs) were used to evaluate the effect of PEMFs on progenitor cell differentiation, one of the first types of cells to arrive after implant placement [56, 60]. PEMF synergistically increased MSC osteogenesis when cells were cultured on calcium phosphate disks in the presence of the osteoinductive factor bone morphogenetic protein-2 (BMP-2), as determined by increased alkaline phosphatase, osteocalcin, and TGF- β 1. These results suggest that electrical stimulation may also improve bone healing and osseointegration by increasing osteogenic differentiation of MSCs.

Like capacitive stimulation, inductive stimulation has no electrochemical effect on the tissue because it is non-invasive. Clinically, one disadvantage is that therapy success depends on patient compliance [55]. Additionally, the non-localized application of inductive stimulation may affect multiple types of tissues surrounding the injury site.

Taking in consideration what is known about mechanical stimulation and the different electrical stimulation systems, improvements in bone growth and repair can be achieved through different molecular pathways, including integrin- and IP3-mediated pathways [61, 62] (Figure 7.4).

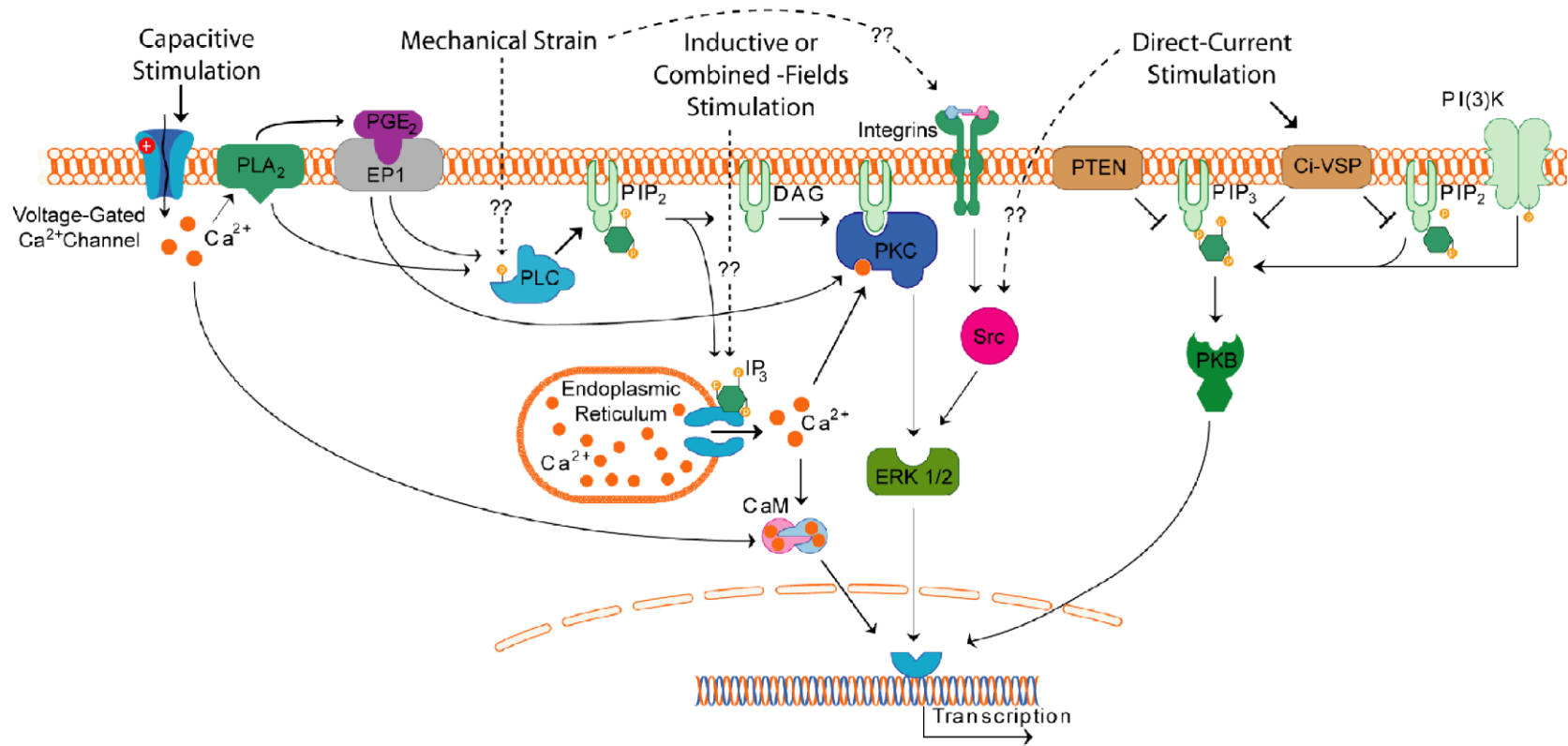


Figure 7.4. Schematic of possible cell signaling pathways activated by mechanical and electrical stimulation systems.

7.4. Electrical Implications of Corrosion

Metals are used for dental and orthopaedic implants because of their mechanical properties such as weight-to-strength ratio and good biological performance. However, metallic devices are prone to corrosion, particularly in aqueous environments under extreme conditions. Corrosion resistance depends on temperature, pH, ion concentration, substrate size, and chemistry, but it is not inherent to the material itself as implied in many studies [63]. Ti is corrosion resistant under controlled environments in the absence of load. In the human body, the physiological environment in combination with constant, cyclic implant loading can significantly enhance corrosion rates [64-67]. Extreme acidic conditions found during inflammation [68], fretting between implant and bone [69], and galvanic corrosion between Ti implants and other metallic alloys used for common dental procedures [70] could greatly affect the mechanical stability and outcome of dental implants.

7.4.1. Basic Electrochemistry

The basic unit of electrochemistry is the electrochemical cell, which is composed of two electrodes (anode and cathode) and an aqueous electrolyte serving as a connecting path. Electrochemical reactions on the surface of an electrode can be oxidative (anodic), generating electrons and ions, or reductive (cathodic), consuming electrons and generating metal atoms or other molecules (Figure 7.5). An electrode is defined by how reactive it is compared to the opposite electrode to which it is connected. In some situations, a single metal device can serve as both the anode and the cathode, and so a second electrode is not required to complete the circuit.

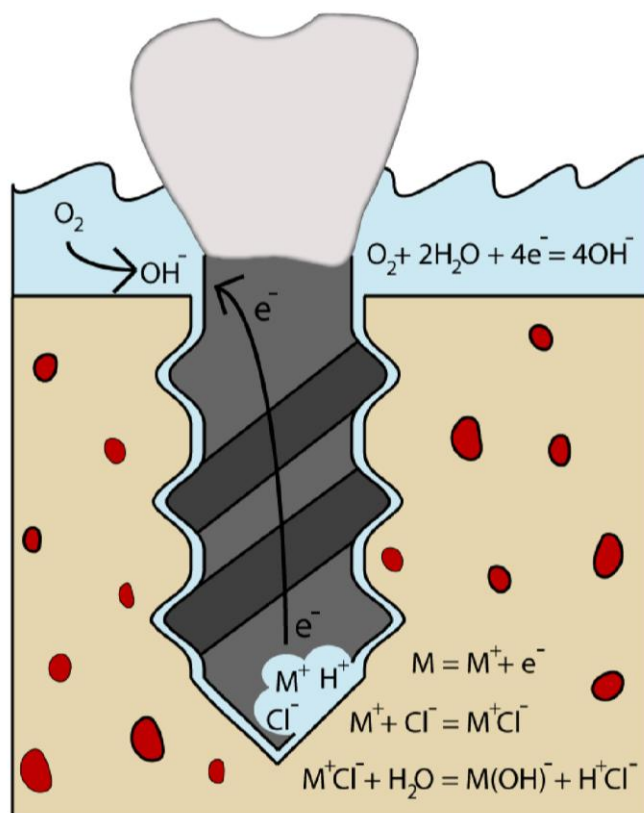


Figure 7.5. Schematic of the initiation and mechanism of corrosion of a dental implant.

Metallic implants for bone applications submerged in ion-rich electrolytes in the body constitute a basic corrosion cell. Large currents can be induced by the flow of ions and electrons generated during electrochemical reactions occurring between the corroding metallic surface and the electrolyte. These currents are generally used to measure the corrosion rate of a metal because they are directly related to the release of metal ions or, in other words, the material degradation. Consequently, corrosion events result in the formation of small pits on the surface of the device that can amplify the corrosive environment around the implant and compromise its mechanical stability. This can lead to shortening of the implant's lifetime and sudden failure [67, 71, 72] (Figure

7.5). Products of the electrochemical reactions may have cytotoxic, or even neoplastic effects on the tissue surrounding the implant, serving as an additional cause of rejection or aseptic loosening [73-75]. However, the electrical implications of corrosion on the surrounding tissue have not been extensively investigated [76].

7.4.2. Passivity of Titanium

Certain metals like Ti oxidize easily, forming a very thin, stable passive layer that is self-limiting and protects the surface of the metal from further oxidation. This behavior, passivity, gives Ti its high corrosion resistance under certain controlled conditions where, otherwise, it would undergo strong active corrosion. Metals can have stable passivity, where the oxide layer self-heals immediately after being ruptured, or unstable passivity, where the oxide layer is unable to heal after disruption and the bare metal is exposed to active corrosion. Both of these events depend on the oxidizing or reducing potential of the environment. The passive oxide layer formed on the surface of Ti may be responsible for its good biological performance, since it is less reactive than bare Ti. Additionally, it may mimic the ceramic nature of bone and allow biochemical bonding with the newly formed bone [77].

Most materials chosen for implant applications exhibit passivity properties and, thus, relatively low corrosion rates compared to other more reactive metals, such as zinc, magnesium or vanadium, which undergo active corrosion even in relatively neutral pH. However, certain environmental conditions can breach the protective oxide layer formed on the surface of these passive materials and cause corrosion, affecting the mechanical integrity of the implant and the health of the surrounding tissue.

Work by our group and many others, has shown that implant surface properties such as roughness, chemistry, and energy directly influence tissue response by affecting protein adsorption and modulating cell proliferation and differentiation [78, 79].

Additionally, innovations in surface modification techniques have improved the biological performance of metallic implants [80, 81]. However, some modifications may diminish mechanical properties of the bulk material, resulting in surface microcracks, increased corrosion rates [67, 71, 82] and, thus, increased corrosion currents and potentials that may affect surrounding cells and tissues.

7.4.3. Types of Corrosion

The most common types of corrosion found in metallic materials used for implant applications are galvanic, fretting and pitting/crevice corrosion, as well as environmentally induced cracking (EIC).

Galvanic corrosion occurs with direct contact of two dissimilar metals in an electrolytic solution [83]. The difference in electrochemical potential of the two metals promotes oxidation of the more reactive metal. This becomes the anode, which generates a flow of electrons and ions to the cathode. In one study, spine implant constructs consisting of pedicle screws, connectors and rods that had mixed components made of stainless steel (SS) and titanium were investigated for signs of galvanic corrosion under dynamic loads [84]. The results showed no evidence of corrosion on surfaces of the implant that had not been in contact with other components, and only minor signs of corrosion at the interfaces between SS-Ti, Ti-Ti and SS-SS, with the latter actually having the greatest amount of corrosion. Galvanic corrosion is not common in dental implant applications because of the presence of only one component, the dental screw, and the insulating nature of the protective passive layer that forms on the surface. Nevertheless, in some patients the surrounding tissue could serve as a medium for electrical flow between metallic implants and other types of alloys used in dentistry for amalgams or orthodontic devices. Galvanic corrosion could also amplify the rates of corrosion initiated by other mechanisms described below [70, 85].

Fretting corrosion is caused by the repeated micromotion or friction of a metal component against another material that causes mechanical wear and breaks up the passivating layer on the contact surface of the metallic device [86]. Fretting between dental implants and bone during implantation and due to cyclic loads imparted from chewing has been suggested as a cause of Ti corrosion and metal ion release [69, 73]. Fretting could also be an issue in total hip replacements, where it could generate wear-debris and ions from friction between joint and socket [65, 87]. The release of metal debris and ions has been linked to inhibition of cell differentiation, cytotoxicity, phagocytosis of Ti particles by macrophages and other cells, inflammation and neoplasia [75, 88-90]. Recent studies have shown that fretting and oxide disruption at the surface of load-bearing implants can cause corrosion current densities to increase and generate open-circuit potentials in excess of -500 mV [69, 91]. Abnormal electrical signals may affect the response and stability of the adjacent tissue and fretting corrosion may amplify other types of corrosion by rupturing the passivating film and exposing bare Ti.

Pitting corrosion occurs as a result of the spontaneous breakdown of the passive film on a flat and evenly exposed area [86, 92]. Crevice corrosion is a localized corrosion due to a geometrical confinement in the design of the device or from a previously corroded region on the surface. The common mechanism of propagation for both usually involves a differential aeration cell (Figure 7.5). In this, the region undergoing active corrosion has restricted solution flow due to geometric confinement and initially depletes local oxygen concentration, generating high levels of metal ions and electrons that are consequently consumed by the surface exposed to high levels of oxygen. While pitting corrosion is not likely to occur on Ti surfaces, crevice corrosion has been found [73, 93]. In one study, corrosion currents from Ti alloy lumbar interbody fusions were directly related to lumbar pain and periprosthetic bone loss in patients [73].

EIC is the brittle mechanical failure of metallic devices under stress levels significantly lower than their ultimate tensile strength. This occurs in susceptible materials in corrosive environments and under continuous loading. The magnitudes of the forces that can cause EIC vary over a wide range and include forces that, under non-corrosive conditions, would be considered negligible. EIC is the most common cause of corrosion in implants for bone applications [66, 94] and because of its localized nature may go unnoticed until catastrophic failure.

7.5. Clinical Relevance of Corrosion

Corrosion of metallic implants, a topic extensively discussed in orthopaedic literature, may jeopardize the mechanical stability of the implant and the integrity of the surrounding tissue [69, 95]. Implant failure in the form of aseptic loosening, or osteolysis, may result from metal release in the form of wear debris or electrochemical products generated during corrosion events [96-98]. Metal ions such as Ti^{4+} , Co^{2+} and Al^{3+} have been shown to decrease DNA synthesis, mitochondrial dehydrogenase activity, mineralization, and mRNA expression of alkaline phosphatase and osteocalcin in ROS 17/2.8 cells [89]. Similarly, phagocytosis of Ti particles caused cytotoxicity in a concentration-dependent manner in neonatal rat calvarial osteoblasts [99] and MG63 cells [90].

While implant loosening is less prominent in the dental literature, metal traces originating from dental implants have been found in blood, liver, lungs, and lymph nodes [100-102]. These metal ions and wear debris may also contribute to aseptic loosening by promoting inflammatory complications that may result in macrophage activation, bone resorption and, rarely, in the potential development of neoplasia [74, 103]. Recently, titanium dioxide (TiO_2) was classified as possibly carcinogenic to human beings (*i.e.*,

group 2B) at the International Agency for Research on Cancer (IARC) [104]. Animal studies in rodents provided sufficient evidence of the carcinogenic effects of TiO₂, although epidemiological cohort studies in humans were inconclusive. Furthermore, the immediate and systemic cytotoxic and neoplastic effects of corrosion remain controversial because of conflicting studies that have found no effects of Ti ions or Ti particles on cells [75]. Moreover, the nanograms of metal per gram of tissue found *in vivo* [105, 106] are difficult to compare to the micrograms and milligrams of metal per milliliters of solution used to create an effect in *in vitro* studies [90, 99].

The electrical implications of corrosion and its effect on the surrounding tissue may be an important key to this puzzle, but such effects still remain unclear. Corrosion events generate electrical currents due to electron transfer from ions in the solution to the metallic surface where reactions are occurring. These abnormal currents, and coupled electrical potentials, are directly related to the cyclic loads applied to the implant [69, 91]. In dental and orthopaedic applications, cyclic loads are to be expected from the forces exerted after every bite or every step, respectively. Consequently, it is fair to suggest that cells and tissues in patients with implants are exposed to abnormal electrical signals for extended periods of time. As described previously, bone cells are sensitive to electrical signals and, thus, could be strongly affected by these corrosion currents. Moreover, these abnormal electrical signals may provide an alternate explanation to the unresolved causes of inflammatory complications and eventual aseptic loosening.

With the growing popularity of treatments like early implant loading, it is imperative to consider the effects of electrical signals on the early stages of osseointegration as well as on long-term outcome. The concern of reducing implant corrosion might be addressed and is being addressed by different methods such as new

formulations of metallic alloys that improve the mechanical and corrosion properties of the implant [107-109]; surface modifications that stabilize the reactivity of the surface [67]; or electrical protection (*i.e.*, stimulation) of implants. However, a fundamental understanding of the consequences of abnormal electrical signals on the growth and development of cells and tissues is required to design appropriate solutions and provide patients adequate treatment.

7.6. References

1. Piccolino M. Luigi Galvani and animal electricity: two centuries after the foundation of electrophysiology. *Trends Neurosci* 1997;20(10):443-448.
2. Black J. *Electrical Stimulation: Its Role in Growth, Repair, and Remodeling of the Musculoskeletal System*. New York: Praeger Publishers; 1987.
3. Levin M, Thorlin T, Robinson KR, Nogi T, Mercola M. Asymmetries in H⁺/K⁺-ATPase and cell membrane potentials comprise a very early step in left-right patterning. *Cell* 2002;111(1):77-89.
4. Ferrier J, Ross SM, Kanehisa J, Aubin JE. Osteoclasts and osteoblasts migrate in opposite directions in response to a constant electrical-field. *J Cell Physiol* 1986;129(3):283-288.
5. Levin M. Large-scale biophysics: ion flows and regeneration. *Trends Cell Biol* 2007;17(6):261-270.
6. Becker RO, Spadaro JA, Marino AA. Clinical experiences with low intensity direct-current stimulation of bone-growth. *Clin Orthop* 1977;124:75-83.
7. Lokietek W, Pawluk RJ, Bassett CAL. Muscle injury potentials - source of voltage in undeformed rabbit tibia. *J Bone Jt Surg (Br)* 1974;B 56(2):361-369.
8. McCaig CD, Rajniecek AM, Song B, Zhao M. Controlling cell behavior electrically: Current views and future potential. *Physiol Rev* 2005;85(3):943-978.
9. Borgens RB, Jaffe LF, Cohen MJ. Large and persistent electrical currents enter the transected lamprey spinal-cord. *Proc Natl Acad Sci U S A* 1980;77(2):1209-1213.
10. Faes TJC, van der Meij HA, de Munck JC, Heethaar RM. The electric resistivity of human tissues (100 Hz-10 MHz): a meta-analysis of review studies. *Physiol Meas* 1999;20(4):R1-R10.
11. Zhao M, Song B, Pu J, Wada T, Reid B, Tai GP, et al. Electrical signals control wound healing through phosphatidylinositol-3-OH kinase-gamma and PTEN. *Nature* 2006;442(7101):457-460.
12. Rajniecek AM, Foubister LE, McCaig CD. Prioritising guidance cues: Directional migration induced by substratum contours and electrical gradients is controlled by a rho/cdc42 switch. *Dev Biol* 2007;312(1):448-460.
13. Iwasaki H, Murata Y, Kim YJ, Hossain MI, Worby CA, Dixon JE, et al. A voltage-sensing phosphatase, Ci-VSP, which shares sequence identity with PTEN, dephosphorylates phosphatidylinositol 4,5-bisphosphate. *Proc Natl Acad Sci U S A* 2008;105(23):7970-7975.

14. Murata Y, Iwasaki H, Sasaki M, Inaba K, Okamura Y. Phosphoinositide phosphatase activity coupled to an intrinsic voltage sensor. *Nature* 2005;435(7046):1239-1243.
15. Fukada E, Yasuda I. On the piezoelectric effect of bone. *J Phys Soc Jpn* 1957;12(10):1158-1162.
16. Rubinacci A, Black J, Brighton CT, Friedenberg ZB. Changes in bioelectric potentials on bone associated with direct-current stimulation of osteogenesis. *J Orthop Res* 1988;6(3):335-345.
17. Guzelsu N, Demiray H. Electro-mechanical properties and related models of bone tissues - review. *Int J Eng Sci* 1979;17(7):813-851.
18. Burr DB, Robling AG, Turner CH. Effects of biomechanical stress on bones in animals. *Bone* 2002;30(5):781-786.
19. Hou B, Fukai N, Olsen BR. Mechanical force-induced midpalatal suture remodeling in mice. *Bone* 2007;40(6):1483-1493.
20. Duncan RL, Turner CH. Mechanotransduction and the functional-response of bone to mechanical strain. *Calcif Tissue Int* 1995;57(5):344-358.
21. Bassett CAL, Becker RO. Generation of electric potentials by bone in response to mechanical stress. *Science* 1962;137(3535):1063-1064.
22. Bassett CA, Pawluk RJ, Becker RO. Effects of electric currents on bone in vivo. *Nature* 1964;204(495):652-654.
23. Black J, Baranowski TJ, Brighton CT. Electrochemical aspects of dc stimulation of osteogenesis. *Bioelectrochem Bioenerg* 1984;12(3-4):323-327.
24. Wray JB, Goodman HO. Post-fracture vascular phenomena and long-bone overgrowth in the immature skeleton of the rat. *Journal of Bone and Joint Surgery-American Volume* 1961;43(7):1047-1055.
25. Aitken AP, Blackett CW, Cincioth JJ. Overgrowth of the femoral shaft following fracture in childhood. *J Bone Joint Surg Am* 1939;21:334-338.
26. Gaber S, Fischerauer EE, Frohlich E, Janezic G, Amerstorfer F, Weinberg AM. Chondrocyte apoptosis enhanced at the growth plate: a physeal response to a diaphyseal fracture. *Cell Tissue Res* 2009;335(3):539-549.
27. Friedenberg ZB, Brighton CT. Bioelectric potentials in bone. *J Bone Jt Surg (Am)* 1966;A 48(5):915-923.
28. Lai WM, Mow VC, Sun DD, Ateshian GA. On the electric potentials inside a charged soft hydrated biological tissue: Streaming potential versus diffusion potential. *Journal of Biomechanical Engineering-Transactions of the Asme* 2000;122(4):336-346.
29. Meikle MC. The tissue, cellular, and molecular regulation of orthodontic tooth movement: 100 years after Carl Sandstedt. *Eur J Orthod* 2006;28(3):221-240.
30. Isaacson RJ, Lindauer SJ, Davidovitch M. On tooth movement. *Angle Orthod* 1993;63(4):305-309.
31. McGuinness NJP, Wilson AN, Jones ML, Middleton J. A stress-analysis of the periodontal-ligament under various orthodontic loadings. *Eur J Orthod* 1991;13(3):231-242.
32. Cobo J, Sicilia A, Arguelles J, Suarez D, Vijande M. Initial stress-induced in periodontal tissue with diverse degrees of bone loss by an orthodontic force - tridimensional analysis by means of the finite-element method. *Am J Orthod Dentofacial Orthop* 1993;104(5):448-454.
33. Brezniak N, Wasserstein A. Orthodontically induced inflammatory root resorption. Part II: The clinical aspects. *Angle Orthod* 2002;72(2):180-184.
34. Zengo AN, Pawluk RJ, Bassett CAL. Stress-induced bioelectric potentials in dentoalveolar complex. *Am J Orthod Dentofacial Orthop* 1973;64(1):17-27.

35. Cochran GVB, Pawluk RJ, Bassett CAL. Stress generated electric potentials in mandible and teeth. *Arch Oral Biol* 1967;12(7):917-920.
36. Norton LA, Hanley KJ, Turkewicz J. Bioelectric perturbations of bone - research directions and clinical-applications. *Angle Orthod* 1984;54(1):73-87.
37. Norton LA. Implications of bioelectric growth-control in orthodontics and dentistry. *Angle Orthod* 1975;45(1):34-42.
38. Wang Q, Zhong SZ, Jun OY, Jiang LX, Zhang ZK, Xie Y, et al. Osteogenesis of electrically stimulated bone cells mediated in part by calcium ions. *Clin Orthop* 1998(348):259-268.
39. Kim IS, Song JK, Zhang YL, Lee TH, Cho TH, Song YM, et al. Biphasic electric current stimulates proliferation and induces VEGF production in osteoblasts. *Biochim Biophys Acta* 2006;1763(9):907-916.
40. Brighton CT, Hunt RM. Ultrastructure of electrically induced osteogenesis in the rabbit medullary canal. *J Orthop Res* 1986;4(1):27-36.
41. Shafer DM, Rogerson K, Norton L, Bennett J. The effect of electrical perturbation on osseointegration of titanium dental implants - a preliminary-study. *J Oral Maxillofac Surg* 1995;53(9):1063-1068.
42. Wang ZY, Clark CC, Brighton CT. Up-regulation of bone morphogenetic proteins in cultured murine bone cells with use of specific electric fields. *Journal of Bone and Joint Surgery-American Volume* 2006;88A(5):1053-1065.
43. Aaron RK, Boyan BD, Ciombor DM, Schwartz Z, Simon BJ. Stimulation of growth factor synthesis by electric and electromagnetic fields. *Clin Orthop* 2004;419:30-37.
44. Bodamyali T, Kanczler JM, Simon B, Blake DR, Stevens CR. Effect of Faradic products on direct current-stimulated calvarial organ culture calcium levels. *Biochem Biophys Res Commun* 1999;264(3):657-661.
45. Curtze S, Dembo M, Miron M, Jones DB. Dynamic changes in traction forces with DC electric field in osteoblast-like cells. *J Cell Sci* 2004;117(13):2721-2729.
46. Ercan B, Webster TJ. Greater osteoblast proliferation on anodized nanotubular titanium upon electrical stimulation. *Int J Nanomedicine* 2008;3(4):477-485.
47. Dodge GR, Bowen JR, Oh CW, Tokmakova K, Simon BJ, Aroojis A, et al. Electrical stimulation of the growth plate: A potential approach to an epiphysiodesis. *Bioelectromagnetics* 2007;28(6):463-470.
48. Song JK, Cho TH, Pan H, Song YM, Kim IS, Lee TH, et al. An Electronic Device for Accelerating Bone Formation in Tissues Surrounding a Dental Implant. *Bioelectromagnetics* 2009;30(5):374-384.
49. Ercan B, Webster TJ. The effect of biphasic electrical stimulation on osteoblast function at anodized nanotubular titanium surfaces. *Biomaterials* 2010;31(13):3684-3693.
50. Lorch DG, Brighton CT, Gupta R, Corsetti JR, Levine SE, Gelb ID, et al. Biochemical pathway mediating the response of bone cells to capacitive coupling. *Clin Orthop* 1998(350):246-256.
51. Shigino T, Ochi M, Hirose Y, Hirayama H, Sakaguchi K. Enhancing osseointegration by capacitively coupled electric field: A pilot study on early occlusal loading in the dog mandible. *Int J Oral Maxillofac Implants* 2001;16(6):841-850.
52. Brighton CT, Wang W, Seldes R, Zhang GH, Pollack SR. Signal transduction in electrically stimulated bone cells. *J Bone Jt Surg (Am)* 2001;83A(10):1514-1523.
53. Brighton CT, Tadduni GT, Pollack SR. Treatment of sciatic denervation disuse osteoporosis in the rat tibia with capacitively coupled electrical-stimulation - dose-response and duty cycle. *Journal of Bone and Joint Surgery-American Volume* 1985;67A(7):1022-1028.

54. Lirani-Galvao APR, Chavassieux P, Portero-Muzy N, Bergamaschi CT, Silva OL, Carvalho AB, et al. Low-Intensity Electrical Stimulation Counteracts the Effects of Ovariectomy on Bone Tissue of Rats: Effects on Bone Microarchitecture, Viability of Osteocytes, and Nitric Oxide Expression. *Calcif Tissue Int* 2009;84(6):502-509.
55. Gan JC, Glazer PA. Electrical stimulation therapies for spinal fusions: current concepts. *Eur Spine J* 2006;15(9):1301-1311.
56. Schwartz Z, Simon BJ, Duran MA, Barabino G, Chaudhri R, Boyan BD. Pulsed electromagnetic fields enhance BMP-2 dependent osteoblastic differentiation of human mesenchymal stem cells. *J Orthop Res* 2008;26(9):1250-1255.
57. Bodamyali T, Bhatt B, Hughes FJ, Winrow VR, Kanczler JM, Simon B, et al. Pulsed electromagnetic fields simultaneously induce osteogenesis and upregulate transcription of bone morphogenetic proteins 2 and 4 in rat osteoblasts in vitro. *Biochem Biophys Res Commun* 1998;250(2):458-461.
58. Lohmann CH, Schwartz Z, Liu Y, Guerkov H, Dean DD, Simon B, et al. Pulsed electromagnetic field stimulation of MG63 osteoblast-like cells affects differentiation and local factor production. *J Orthop Res* 2000;18(4):637-646.
59. Guerkov HH, Lohmann CH, Liu Y, Dean DD, Simon BJ, Heckman JD, et al. Pulsed electromagnetic fields increase growth factor release by nonunion cells. *Clin Orthop* 2001(384):265-279.
60. Schwartz Z, Fisher M, Lohmann CH, Simon BJ, Boyan BD. Osteoprotegerin (OPG) production by cells in the osteoblast lineage is regulated by pulsed electromagnetic fields in cultures grown on calcium phosphate substrates. *Ann Biomed Eng* 2009;37(3):437-444.
61. Brighton CT, Fisher JRS, Levine SE, Corsetti JR, Reilly T, Landsman AS, et al. The biochemical pathway mediating the proliferative response of bone cells to a mechanical stimulus. *Journal of Bone and Joint Surgery-American Volume* 1996;78A(9):1337-1347.
62. Wang N, Butler JP, Ingber DE. Mechanotransduction across the cell-surface and through the cytoskeleton. *Science* 1993;260(5111):1124-1127.
63. Bhattarai SR, Khalil KA-R, Dewidar M, Hwang PH, Yi HK, Kim HY. Novel production method and in-vitro cell compatibility of porous Ti-6Al-4V alloy disk for hard tissue engineering. *Journal of Biomedical Materials Research Part A* 2008;86A(2):289-299.
64. Brunette D, Tengvall P, Textor M, Thomsen P. *Titanium in Medicine: Material Science, Surface Science, Engineering, Biological Responses and Medical Applications*. First ed. Berlin: Springer; 2001.
65. Long M, Rack HJ. Titanium alloys in total joint replacement - a materials science perspective. *Biomaterials* 1998;19(18):1621-1639.
66. Lewis AC, Kilburn MR, Papageorgiou I, Allen GC, Case CP. Effect of synovial fluid, phosphate-buffered saline solution, and water on the dissolution and corrosion properties of CoCrMo alloys as used in orthopedic implants. *J Biomed Mater Res A* 2005;73A(4):456-467.
67. Papakyriacou M, Mayer H, Pypen C, Plenk H, Stanzl-Tschegg S. Effects of surface treatments on high cycle corrosion fatigue of metallic implant materials. *Int J Fatigue* 2000;22(10):873-886.
68. Lassus J, Salo J, Jiranek WA, Santavirta S, Nevalainen J, Matucci-Cerinic M, et al. Macrophage activation results in bone resorption. *Clin Orthop Relat Res* 1998(352):7-15.
69. Gilbert JL, Mehta M, Pinder B. Fretting Crevice Corrosion of Stainless Steel Stem-CoCr Femoral Head Connections: Comparisons of Materials, Initial Moisture, and

Offset Length. Journal of Biomedical Materials Research Part B-Applied Biomaterials 2009;88B(1):162-173.

70. Grosogeat B, Reclaru L, Lissac M, Dalard F. Measurement and evaluation of galvanic corrosion between titanium/Ti6Al4V implants and dental alloys by electrochemical techniques and auger spectrometry. Biomaterials 1999;20(10):933-941.

71. Teoh SH. Fatigue of biomaterials: a review. Int J Fatigue 2000;22(10):825-837.

72. Mudali UK, Sridhar TM, Raj B. Corrosion of bio implants. Sadhana-Academy Proceedings in Engineering Sciences 2003;28:601-637.

73. Denaro V, Papapietro N, Sgambato A, Barnaba SA, Ruzzini L, De Paola B, et al. Periprosthetic electrochemical corrosion of titanium and titanium-based alloys as a cause of spinal fusion failure. Spine 2008;33(1):8-13.

74. McGuff HS, Heim-Hall J, Holsinger FC, Jones AA, O'Dell DS, Hafemeister AC. Maxillary osteosarcoma associated with a dental implant: report of a case and review of the literature regarding implant-related sarcomas. J Am Dent Assoc 2008;139(8):1052-1059.

75. Doran A, Law FC, Allen MJ, Rushton N. Neoplastic transformation of cells by soluble but not particulate forms of metals used in orthopaedic implants. Biomaterials 1998;19(7-9):751-759.

76. Denaro V, Cittadini A, Barnaba SA, Ruzzini L, Denaro L, Rettino A, et al. Static electromagnetic fields generated by corrosion currents inhibit human osteoblast differentiation. Spine 2008;33(9):955-959.

77. Sul YT, Johansson C, Byon E, Albrektsson T. The bone response of oxidized bioactive and non-bioactive titanium implants. Biomaterials 2005;26(33):6720-6730.

78. Kieswetter K, Schwartz Z, Dean DD, Boyan BD. The role of implant surface characteristics in the healing of bone. Crit Rev Oral Biol Medicine 1996;7(4):329-345.

79. Schwartz Z, Boyan BD. Underlying Mechanisms at the Bone-Biomaterial Interface. J Cell Biochem 1994;56:340-347.

80. Buser D, Broggini N, Wieland M, Schenk RK, Denzer AJ, Cochran DL, et al. Enhanced bone apposition to a chemically modified SLA titanium surface. J Dent Res 2004;83(7):529-533.

81. Wang XX, Yan W, Hayakawa S, Tsuru K, Osaka A. Apatite deposition on thermally and anodically oxidized titanium surfaces in a simulated body fluid. Biomaterials 2003;24(25):4631-4637.

82. Hazar Yoruc AB, Kelesoglu E. Fatigue behaviour of the chemically treated titanium grade 4 implant material. Journal of Optoelectronics and Biomedical Materials 2009;1(2):200-208.

83. Kaesche H. Corrosion of Metals: Physicochemical Principles and Current Problems. First ed. Berlin: Springer; 2003.

84. Serhan H, Slivka M, Albert T, Kwak SD. Is galvanic corrosion between titanium alloy and stainless steel spinal implants a clinical concern? Spine J 2004;4(4):379-387.

85. Reclaru L, Meyer JM. Study of corrosion between a titanium implant and dental alloys. J Dent 1994;22(3):159-168.

86. Landolt D. Corrosion and Surface Chemistry of Metals. First ed. Lausanne, Switzerland: EPFL Press; 2007.

87. Ingham E, Fisher J. Biological reactions to wear debris in total joint replacement. Proceedings of the Institution of Mechanical Engineers Part H-Journal of Engineering in Medicine 2000;214(H1):21-37.

88. Rahal MD, Delorme D, Branemark PI, Osmond DG. Myelointegration of titanium implants: B lymphopoiesis and hemopoietic cell proliferation in mouse bone marrow exposed to titanium implants. Int J Oral Maxillofac Implants 2000;15(2):175-184.

89. Sun ZL, Wataha JC, Hanks CT. Effects of metal ions on osteoblast-like cell metabolism and differentiation. *J Biomed Mater Res* 1997;34(1):29-37.
90. Lohmann CH, Schwartz Z, Koster G, Jahn U, Buchhorn GH, MacDougall MJ, et al. Phagocytosis of wear debris by osteoblasts affects differentiation and local factor production in a manner dependent on particle composition. *Biomaterials* 2000;21(6):551-561.
91. Goldberg JR, Gilbert JL. Electrochemical response of CoCrMo to high-speed fracture of its metal oxide using an electrochemical scratch test method. *J Biomed Mater Res* 1997;37(3):421-431.
92. Evans U. *The Corrosion and Oxidation of Metals: Scientific Principles and Practical Applications*. First ed. London: Edward Arnold; 1960.
93. Charles AE, Ness MG. Crevice corrosion of implants recovered after tibial plateau leveling osteotomy in dogs. *Vet Surg* 2006;35(5):438-444.
94. Bundy KJ, Marek M, Hochman RF. In vivo and in vitro studies of the stress-corrosion cracking behavior of surgical implant alloys. *J Biomed Mater Res* 1983;17(3):467-487.
95. Jacobs JJ, Gilbert JL, Urban RM. Corrosion of metal orthopaedic implants. *Journal of Bone and Joint Surgery-American Volume* 1998;80A(2):268-282.
96. Dorr LD, Bloebaum R, Emmanual J, Meldrum R. Histologic, biochemical, and ion analysis of tissue and fluids retrieved during total hip-arthroplasty. *Clin Orthop* 1990(261):82-95.
97. Jacobs JJ, Roebuck KA, Archibeck M, Hallab NJ, Glant TT. Osteolysis: Basic science. *Clin Orthop* 2001(393):71-77.
98. Jacobs JJ, Urban RM, Hallab NJ, Skipor AK, Fischer A, Wimmer MA. Metal-on-metal Bearing Surfaces. *J Am Acad Orthop Surg* 2009;17(2):69-76.
99. Pioletti DP, Takei H, Kwon SY, Wood D, Sung KLP. The cytotoxic effect of titanium particles phagocytosed by osteoblasts. *J Biomed Mater Res* 1999;46(3):399-407.
100. Lugowski SJ, Smith DC, McHugh AD, Vanloon JC. Release of metal-ions from dental implant materials in vivo - determination of Al, Co, Cr, Mo, Ni, V, and Ti in organ tissue. *J Biomed Mater Res* 1991;25(12):1443-1458.
101. Smith DC, Lugowski S, McHugh A, Deporter D, Watson PA, Chipman M. Systemic metal ion levels in dental implant patients. *Int J Oral Maxillofac Implants* 1997;12(6):828-834.
102. Finet B, Weber G, Cloots R. Titanium release from dental implants: an in vivo study on sheep. *Mater Lett* 2000;43(4):159-165.
103. Poggio CE. Plasmacytoma of the mandible associated with a dental implant failure: a clinical report. *Clin Oral Implants Res* 2007;18(4):540-543.
104. Baan R, Straif K, Grosse Y, Secretan W, El Ghissassi F, Coglian V, et al. Carcinogenicity of carbon black, titanium dioxide, and talc. *Lancet Oncology* 2006;7(4):295-296.
105. Frisken KW, Dandie GW, Lugowski S, Jordan G. A study of titanium release into body organs following the insertion of single threaded screw implants into the mandibles of sheep. *Aust Dent J* 2002;47(3):214-217.
106. Hanawa T. Metal ion release from metal implants. *Materials Science & Engineering C-Biomimetic and Supramolecular Systems* 2004;24(6-8):745-752.
107. Mareci D, Chelariu R, Gordin DM, Ungureanu G, Gloriant T. Comparative corrosion study of Ti-Ta alloys for dental applications. *Acta Biomater* 2009;5(9):3625-3639.

108. Oliveira NTC, Guastaldi AC. Electrochemical stability and corrosion resistance of Ti-Mo alloys for biomedical applications. *Acta Biomater* 2009;5(1):399-405.
109. Yamazoe J, Nakagawa M, Matono Y, Takeuchi A, Ishikawa K. The development of Ti alloys for dental implant with high corrosion resistance and mechanical strength. *Dent Mater J* 2007;26(2):260-267.

CHAPTER 8. DELIVERY OF FIXED DC POTENTIALS TO TITANIUM SURFACES FOR THE ENHANCEMENT OF OSTEOBLAST DIFFERENTIATION

In [Gittens RA, Olivares-Navarrete R, Rettew R, Butera R, Alamgir F, Boyan BD, Schwartz Z. Delivery of fixed DC potentials to titanium surfaces for the enhancement of osteoblast differentiation. Bioelectromagnetics 2012;(Submitted).]

8.1. Introduction

The role of endogenous electrical signals in normal bone growth and development has prompted the study of bone repair using external electrical stimulation of cells and tissues *in vitro* [1, 2] and *in vivo* [3, 4]. Electrical stimulation can be supplied using different setups such as direct current (DC), capacitive or inductive stimulation, of which DC stimulation offers great promise because it can be incorporated to implantable devices in order to minimize issues related to patient compliance with treatment. Most commonly, DC stimulation, also known as faradic stimulation, uses an electrode close to the injury site to apply a DC current and associated electric field to nearby cells and tissues [5]. Electrical stimulation has been used clinically to promote bone regeneration in cases of fractures with delayed union or nonunion, but its widespread application has been hindered by inconclusive effectiveness results due to small sample size in a few randomized trials and differences in the electrical signals selected from limited *in vitro* results [6, 7].

Another application that could potentially benefit from the use of electrical stimulation is in the field of implantology and osseointegration of metallic implants. Titanium and its alloys are widely used in dental and orthopaedic applications due to their favorable mechanical properties and good biological performance. The modification of Ti surface properties, such as surface roughness and chemistry, has been used to enhance the interactions between bone and the implant [8, 9]. However, success rates are still not satisfactory for certain populations of compromised patients [10]. The idea of

enhanced osseointegration through electrically-stimulated Ti implants has recently started to be explored [3, 4], but is not well understood in part because of the lack of *in vitro* models that represent the *in vivo* conditions of supplying the electrical signals directly through the surface in contact with the cells and tissue.

In vitro DC stimulation models usually use electrodes submerged in the tissue culture medium to establish fixed DC currents between the anode and the cathode in order to influence the growing cells [11, 12]. DC currents are treated as a drug, with electrons representing an actual physical entity that can be measured and administered [13]. Several reports confirm the beneficial effects that supplying these electrical signals has on bone formation [1, 2, 5]. However, the role of fixed DC currents on osteoblast maturation remains controversial. The flow of faradic current in culture medium is highly difficult to model and it is unclear if these currents directly interact with the cells growing on the substrates or act on them indirectly through the resulting electric fields. Finally, the electrochemical products generated on the surface of both negative and positive electrodes differ widely, with hydrogen peroxide and hydroxyl ions forming around the cathode and metallic and hydrogen ions forming around the anode [14, 15], possibly obscuring the results of DC electrical stimulation. Fixed potentials have been less studied, but they mimic the endogenous injury potentials more effectively and can also control bone growth and regeneration successfully [16].

In this study we present an *in vitro* system that allows electrical stimulation of osteoblasts directly through their Ti substrates, and our results show that fixed DC potentials in the absence of electrochemical currents can enhance osteoblast differentiation and local factor production. Our hypothesis is that electrical stimulation supplied directly through cathodically polarized surfaces can promote osteoblast differentiation at lower potentials and inhibit differentiation at higher potentials.

8.2. Materials and Methods

8.2.1. Titanium Specimens

Ti disks with a diameter of 15 mm and thickness of 1 mm (ASTM F67 unalloyed Ti grade 2 for surgical implant applications, sheet stock) were supplied by Institut Straumann AG (Basel, Switzerland), and treated as described previously [17]. Briefly, after being punched from metal sheets, the specimens were degreased in acetone and later exposed to an aqueous solution consisting of 2 % ammonium fluoride, 2 % hydrofluoric acid and 10 % nitric acid at 55 °C for 30 seconds to generate “pre-treatment” (PT, $S_a = 0.43 \pm 0.02 \mu\text{m}$) Ti disks. Clinically-relevant, microrough Ti specimens were used as positive controls and were generated by sandblasting PT specimens with corundum grit (0.25-0.50 mm) at 5 bar, followed by etching in a solution of hydrochloric and sulfuric acids heated above 100 °C for several minutes (proprietary process of Institut Straumann AG) to produce “sandblasted-large-grit-acid-etched” (SLA, $S_a = 3.29 \pm 0.18 \mu\text{m}$) disks. For surface characterization studies, some of the PT disks were laser etched with distinct geometric figures (*i.e.*, triangle, square, pentagon and hexagon) to be used as coordinates for specific locations on the surface. The samples were then rinsed with water and sterilized by gamma irradiation at 25 kGy overnight ($\geq 12 \text{ h}$).

8.2.2. Electrical Stimulation System

An electrical stimulation system was designed to resemble a standard 24-well tissue culture polystyrene (TCPS) plate to deliver fixed DC potentials to cells growing on Ti substrates (Figures 8.1A-C). Custom-made polycarbonate (PC) screw-caps, which tightly fit a 15 mm Ti disk on the top, sealed the threaded wells of the PC plates. The PC caps had a threaded hole through the middle for a small spring and a metal screw to establish a secure electrical connection with the bottom side of Ti substrates. Leaks in

the system were prevented by using O-rings (McMaster-Carr, Atlanta, GA) for the PC caps and pipe thread sealant tape (McMaster-Carr) for the metal screws. Electrical stimulation was provided with a dual-source DC power supply (6302D; Topward, Taipei Hsien, Taiwan) in fixed potential mode. A stainless steel bar was used to short-circuit all the wells in one row to ensure all the samples in the group were being stimulated with the same potential. The anode was connected to one row of the plate and the cathode to the following row, in order to establish positive and negative polarities, respectively (Figure 8.1D). All the wells in the plate were maintained electrically insulated to isolate the effects of the fixed DC potentials. The flow of current between two rows was negligible, as confirmed with a source meter (SMU 2400; Keithley, Cleveland, OH). For voltage-dependent experiments, additional dual-source (MPS 620M; Kepco, Inc., Flushing, NY) and single-source (ZUP 10-20; TDK-Lambda, Tokyo, Japan) DC power supplies were used. For one of the experiments, a potentiostat (WaveNow potentiostat; Pine, Durham, NC) was used in open circuit potential (OCP) configuration and connected in parallel to a custom-made PC plate to record the voltage supplied during electrical stimulation experiments. For all experiments, the supplied signals were monitored every 30 minutes with a multimeter (80 series V; Fluke, Everett, WA) connected in parallel to measure voltage.

8.2.3. Electrochemical Measurements

PT disks were characterized electrochemically by cyclic voltammetry (CV) using a WaveNow potentiostat (Pine). A three-electrode electrochemical cell with a Pt wire as a counter electrode and a Ag/AgCl reference electrode was used to evaluate the charging currents associated with each type of disk in an acidic environment, and to check the susceptibility of the culture medium to break down with respect to voltage. For these types of cyclic voltammetry tests, regions where the curve is flat represent the

capacitive charging of the electrode-electrolyte interface where the constant-current value should be proportional to surface area; whereas regions where the curve rises correspond to oxidation or reduction reactions occurring in the electrolyte. CV experiments were performed at a scan rate of 50 mV/s in either 1 M sulfuric acid solution or full cell culture medium consisting of Dulbecco's modified Eagle medium (DMEM; cellgro®, Mediatech, Inc, VA, USA) containing 10 % fetal bovine serum (FBS; Gibco, CA, USA) and 1 % penicillin-streptomycin (P/S).

8.2.4. Surface Analysis of Ti Specimens

The Ti specimen surface topography was qualitatively evaluated using a cold field-emission scanning electron microscope (S-4700 FE-SEM; Hitachi, Ltd., Tokyo, Japan) before and after electrical stimulation. PT specimens were imaged at specific locations using laser-etched coordination markings. The same specimens were then placed in the custom PC plates and electrically stimulated for 2 hours inside an incubator at 37 °C with 5 % CO₂ and 100 % humidity. Immediately after stimulation, samples were rinsed in ultra-pure water and dried overnight. Finally, electrically stimulated specimens were imaged in the same locations to check for changes at the micro- and nanoscale. Images were recorded using a 5 kV accelerating voltage and 30 µm aperture.

8.2.5. Cell Culture Model and Assays

MG63 cells were obtained from the American Type Culture Collection (Rockville, MD) and were cultured in DMEM 10 % FBS and 1 % P/S at 37 °C in an atmosphere of 5 % CO₂ and 100 % humidity. Cells were grown at a density of 10,000 cells/cm² on TCPS to check for confluence; on PT and SLA controls that were not electrically stimulated; or on the experimental PT surfaces that were stimulated with the anode (positive lead) or cathode (negative lead) of the different fixed DC potentials depending on the particular study design, described as follows.

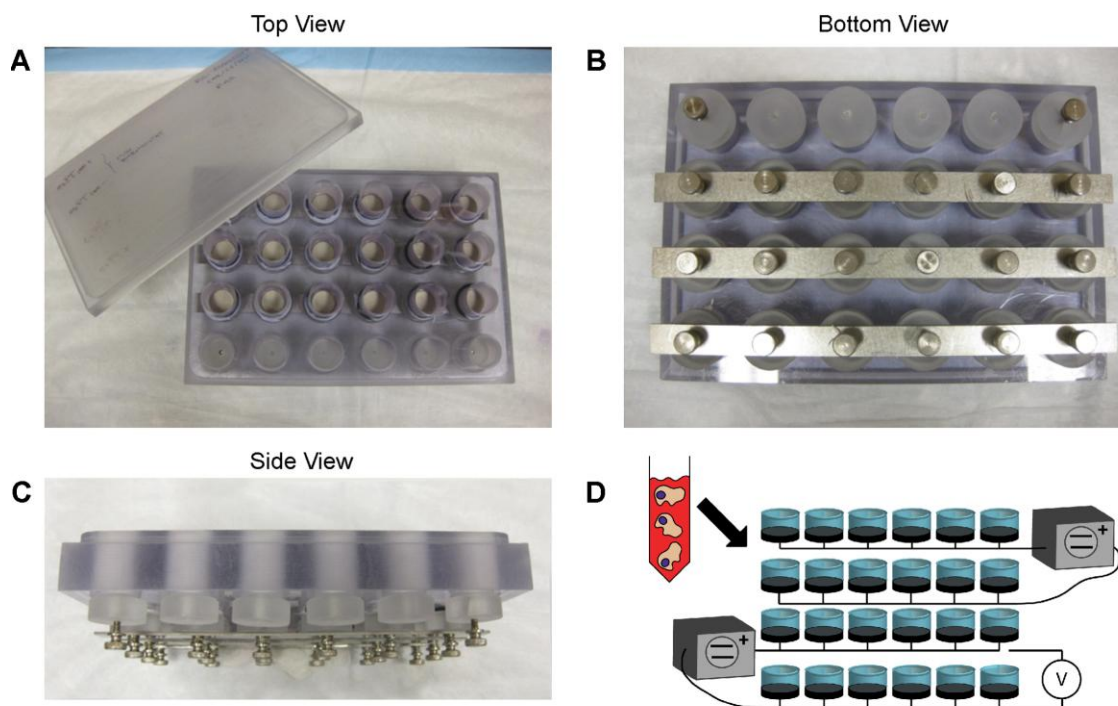


Figure 8.1. Optical images and schematic of a custom-made electrical stimulation system used to deliver fixed DC potentials to cells growing on Ti substrates. (A-C) Polycarbonate (PC) plates were designed to resemble a standard tissue culture polystyrene (TCPS) plate with 24 threaded wells that were sealed with PC caps carrying the Ti specimens. Direct electrical connections were established directly underneath the Ti specimens using metal screws and a series of springs to provide anodic or cathodic polarization to the surface. (D) Schematic of the electrical stimulation setup for cell experiments. (A) All the disks in one row were connected to the anode of the power supply and the subsequent row was connected to the cathode. MG63s were plated on these anodically or cathodically polarized surfaces. For monitoring purposes, a set of experimental groups were connected to a potentiostat to measure the voltage being supplied.

To compare the effect of anodically and cathodically polarized surfaces on MG63 response, cells were plated in standard tissue culture plates using electrically-isolated PT surfaces as a negative control and SLA surfaces as a positive control, considering that osteoblasts are known to differentiate on rougher surfaces. In addition, cells were stimulated with 100 mV using anodically (PT100+) or cathodically (PT100-) polarized PT surfaces. Another set of electrically stimulated groups were connected to a potentiostat to monitor the potential that was being supplied (PT100+, PT100- w/potentiostat).

Electrically-isolated surfaces on TCPS plates provide a good negative control for electrical stimulations experiments, but the possibility exists that establishing electrical connections with the bottom of PT specimens, even without electrical stimulation, could still affect the surface polarization and cause an effect on MG63 cell response. To evaluate this phenomenon, additional experiments were performed on electrically-isolated PT control surfaces on tissue culture polystyrene (PT) or on non-stimulated PT control surfaces on PC custom-made plates (PT0) compared to cathodically (PT100-) polarized PT surfaces.

Finally, voltage-dependent effects on osteoblast maturation were also evaluated on PT surfaces. MG63 cells were plated on non-stimulated PT control surfaces (PT0) or on surfaces that were anodically and cathodically stimulated with 100, 200, 300, 400 or 500 mV in the custom-made PC plate. Only the cells on the cathodically polarized surfaces were harvested after treatment for cell assays.

MG63 cells were fed 24 hours after they were plated on the different surfaces and every 48 hours until confluent, as evaluated on the TCPS substrate. At confluence, cells were treated with fresh medium and experimental groups were electrically stimulated with their respective DC potentials for 2 hours. After stimulation, cells were incubated for an additional 22 hours and harvested for assays. Conditioned media were

collected, and cell layers were washed twice with serum-free medium, released from their substrate by two sequential incubations in 500 μ L 0.25 % trypsin for 10 minutes at 37 °C, and counted with a Z1 Coulter particle counter (Beckman Coulter, Brea, CA). Subsequently, cells were resuspended in 500 μ L 0.05 % Triton-X-100 and lysed by sonication for further analyses.

Osteocalcin content in the conditioned media, used as a late differentiation marker, was measured using a commercially available radioimmunoassay kit (Human Osteocalcin RIA Kit; Biomedical Technologies, Stoughton, MA), as described previously [29], using a LS1500 gamma counter (Perkin Elmer, Waltham, CA).

The conditioned media were also assayed for protein levels of local factors important for bone development. Osteoprotegerin (OPG), a cytokine that works as a decoy receptor for “receptor activator for nuclear factor κ B ligand” (RANKL) to inhibit osteoclastogenesis, was measured using enzyme-linked immunosorbent assay (ELISA) kits (DY805 Osteoprotegerin DuoSet; R&D Systems, Minneapolis, MN). Vascular endothelial growth factor (VEGF), a potent growth factor involved in vasculogenesis and angiogenesis, was also measured using enzyme-linked immunosorbent assay (ELISA) kits (DY293B VEGF DuoSet; R&D Systems).

8.2.6. Statistical Analysis

Data from experiments examining cell response are presented as mean \pm standard error for six independent cultures per variable, or as treatment over electrically-isolated PT controls for three different experiments. All experiments were repeated at least twice to ensure validity of the observations and results from individual representative experiments are shown. Data for each experiment were evaluated by analysis of variance, and significant differences between groups were determined using Tukey’s modification of Student’s t-test for independent studies,

and regular Student's t-test for treatment over control analyses. A p-value below 0.05 was considered to indicate a statistically-significant difference.

8.3. Results

8.3.1. Characterization of Electrical Stimulation System

Routine validation measurements on the custom-made electrical stimulation plates confirmed that the potential supplied by the power supplies was stable over the 2-hour period used for cell experiments (Figure 8.2A), and that the current between electrodes/wells in different rows was negligible (below 100 pA, shown in Figure 8.2B). Electrochemical characterization of the PT specimens showed that in 1 M sulfuric acid, the PT surface had constant current values close to 1 μ A with stable hysteresis maintained throughout the test (Figure 8.3A). When using cell culture media as the electrolyte (Figure 8.3B), the current rose sharply at around 0.8 V. The curve also showed small peaks between 0.1 and 0.2 V that were transient and only present in the first cycle. No media breakdown was evident at the potentials used for cell experiments. Additionally, qualitative evaluation of PT surfaces by SEM showed that there were no topographical changes due to the applied potentials (Figure 8.4). Some surface charging distortion was evident on the SEM images of PT surfaces after electrical stimulation (Figure 8.4D), probably due to adsorbed proteins from the media during treatment.

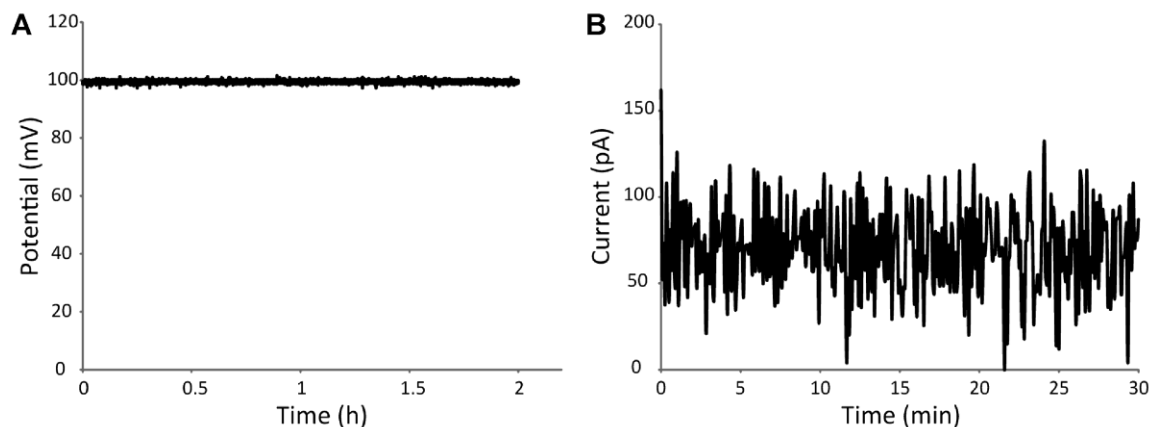


Figure 8.2. Routine characterization of voltage and currents in the electrical stimulation system. (A) Voltage supplied by power supply during the 2-hour window used for cell experiments showed good stability. (B) Current measurements between two adjacent electrodes/wells were below the 100 pA detection limit of the measuring device.

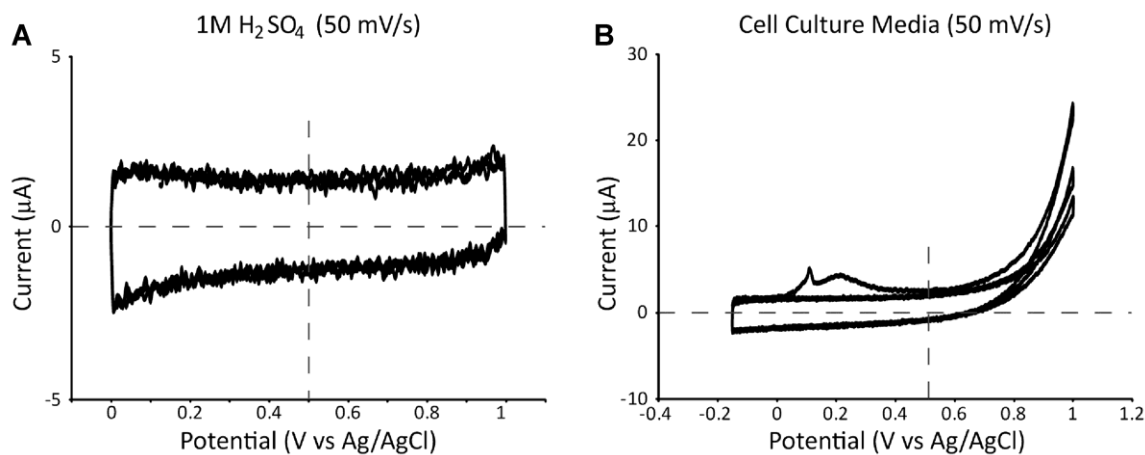


Figure 8.3. Cyclic voltammetry curves for PT surfaces in (A) 1 M sulfuric acid or (B) cell culture media. In the acidic environment, the PT surfaces showed relatively-low current values with constant hysteresis, suggesting low susceptible to oxidation (or oxygen gas evolution). In cell culture media, the curve revealed a sharp increase at higher voltages that corresponded to breakdown of the media. None of the samples exhibited any media breakdown at the potentials used for cell experiments.

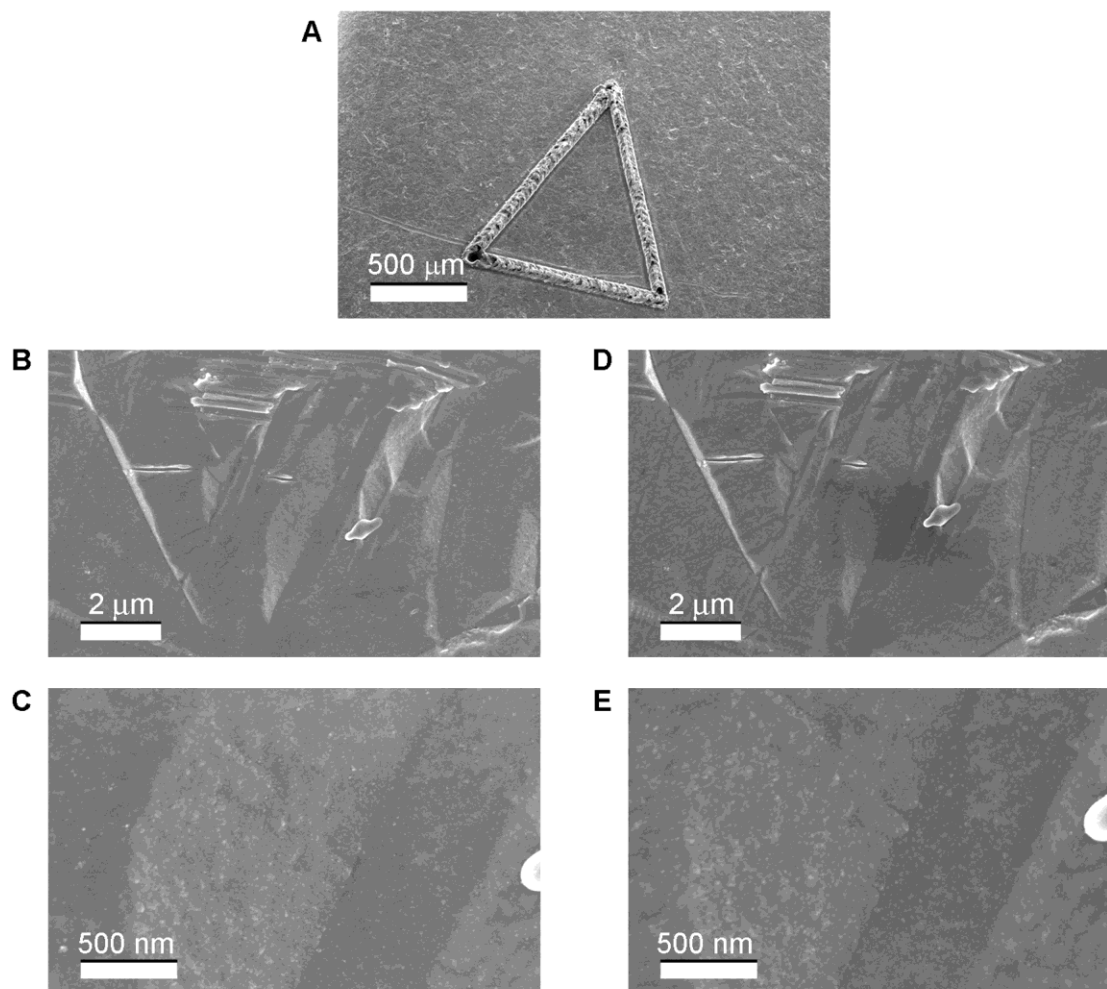


Figure 8.4. SEM images of laser-etched PT surface before and after electrical stimulation. Laser-etched markings were used to find the same location on the surface as received and after 2 hours of electrical stimulation in the custom-made PC plates with culture media. No visible differences were found after stimulation, except for some electron charging on the surface after stimulation, probably due to protein adsorption from the media.

8.3.2. Cell Assays: Cathodic vs. Anodic Effect

Osteoblast-like MG63s were sensitive to fixed DC potentials supplied directly through their Ti substrates. MG63 cell number (Figure 8.5A) was lower in the electrically stimulated groups when compared to both electrically-isolated PT and SLA controls, with the lowest levels found on the PT100- group. The effect of the electrical stimulation on cell number was diminished when connected to the potentiostat, but still had lower levels than PT controls. Production of osteocalcin was sensitive to the electrical stimulation and had the highest levels on the PT100- group (Figure 8.5B). The increase in osteocalcin levels by the electrical stimulation was completely lost when connecting the potentiostat to measure the voltage. Production of the anti-osteoclastogenic factor osteoprotegerin was greatly enhanced by the electrical stimulation, especially on the cathodically stimulated surfaces, and this effect was again diminished when monitoring with the potentiostat (Figure 8.5C). In addition, VEGF levels increased on the PT100- group, when compared to control groups and the cathodic group monitored by the potentiostat (Figure 8.5D).

8.3.3. Electrically-Isolated Versus Non-Stimulated Controls

Significant differences were found on the cathodically polarized PT surfaces stimulated with 100 mV when compared to the control PT surfaces on the electrically-isolated TCPS plates, but not to control PT surfaces on the non-stimulated custom-made plates. Cell number decreased on both PT0 and PT100- groups when compared to the electrically isolated PT controls, with the lowest levels found on the PT100- group (Figure 8.6A). However, the difference between PT0 and PT100- was not significant. At the same time, the highest levels of the late differentiation marker osteocalcin were found on the PT100- group, which were significantly different compared to PT controls but not to PT0 controls (Figure 8.6B). A similar response was found for osteoprotegerin,

with the levels found on PT100- being significantly higher than PT controls but not statistically different than PT0 (Figure 8.6C). In addition, comparable levels of VEGF were found on PT0 and PT100- groups, which were slightly lower than PT controls (Figure 8.6D).

8.3.4. Voltage-Dependent Effect of Stimulated PT Surfaces on MG63 Response

The enhancement of osteogenic differentiation by electrical stimulation through cathodically polarized PT surfaces was voltage dependent. Initial studies, described above, confirmed that PT surfaces connected to the 100 mV cathode elicited the strongest maturation response from MG63s, compared to the anode. Thus, subsequent voltage-dependent studies focused on cathodically polarized surfaces. When additional potentials of 200, 300, 400 and 500 mV were evaluated, cell number decreased with an increase in the supplied potential, with the PT500- group having 40 % lower numbers than non-stimulated PT0 surfaces (Figure 8.7A). Osteocalcin production was the highest on the PT500- group, which had levels 70 % higher than PT0 and PT100- groups (Figure 8.7B). Production of osteoprotegerin (Figure 8.7C) and VEGF (Figure 8.7D) also responded to the higher DC potentials. Osteoprotegerin production was 100 % higher on PT400- and 70 % higher on PT500- groups when compared to PT0, whereas VEGF had 50 % higher levels on the PT300- and PT500- groups compared to the PT0 controls.

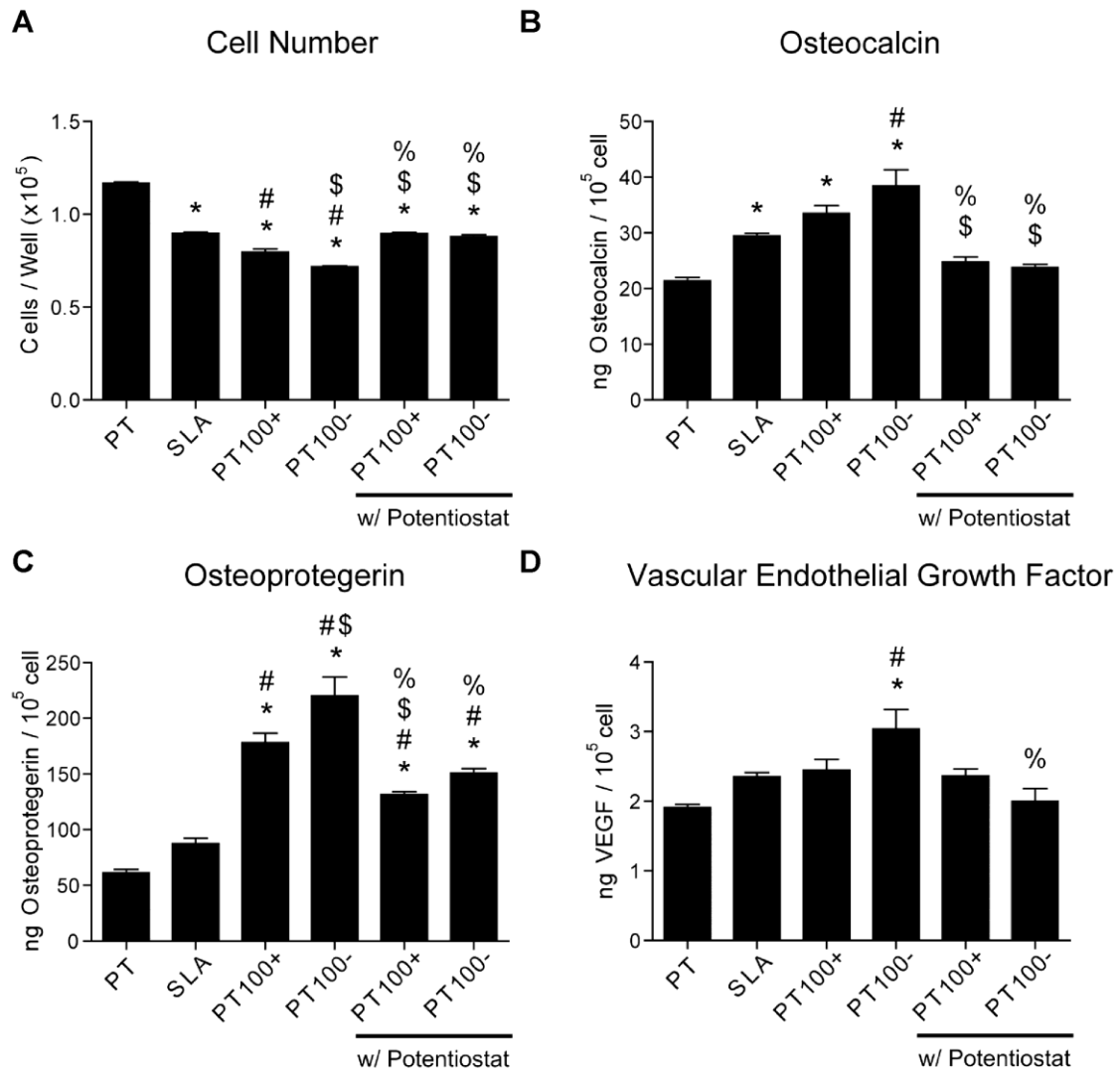


Figure 8.5. Effects of anodically and cathodically polarized surfaces using fixed DC potentials of 100 mV on osteoblast-like MG63 cells. Cells were plated on PT and SLA electrically-isolated controls, as well as surfaces connected to the anode (PT100+) and the cathode (PT100-) of a power supply. Two additional electrically-stimulated groups were also connected to a potentiostat to monitor the electrical signals supplied (PT100+, PT100- w/potentiostat). At confluence, checked on TCPS, (A) cell number, (B) osteocalcin, (C) osteoprotegerin, and (D) VEGF levels were measured. Data represented are the mean \pm standard error of six independent samples. * refers to a statistically-significant p value below 0.05 vs. PT; # refers to a statistically-significant p value below 0.05 vs. SLA; \$ refers to a statistically-significant p value below 0.05 vs. PT100+; % refers to a statistically-significant p value below 0.05 vs. PT100-.

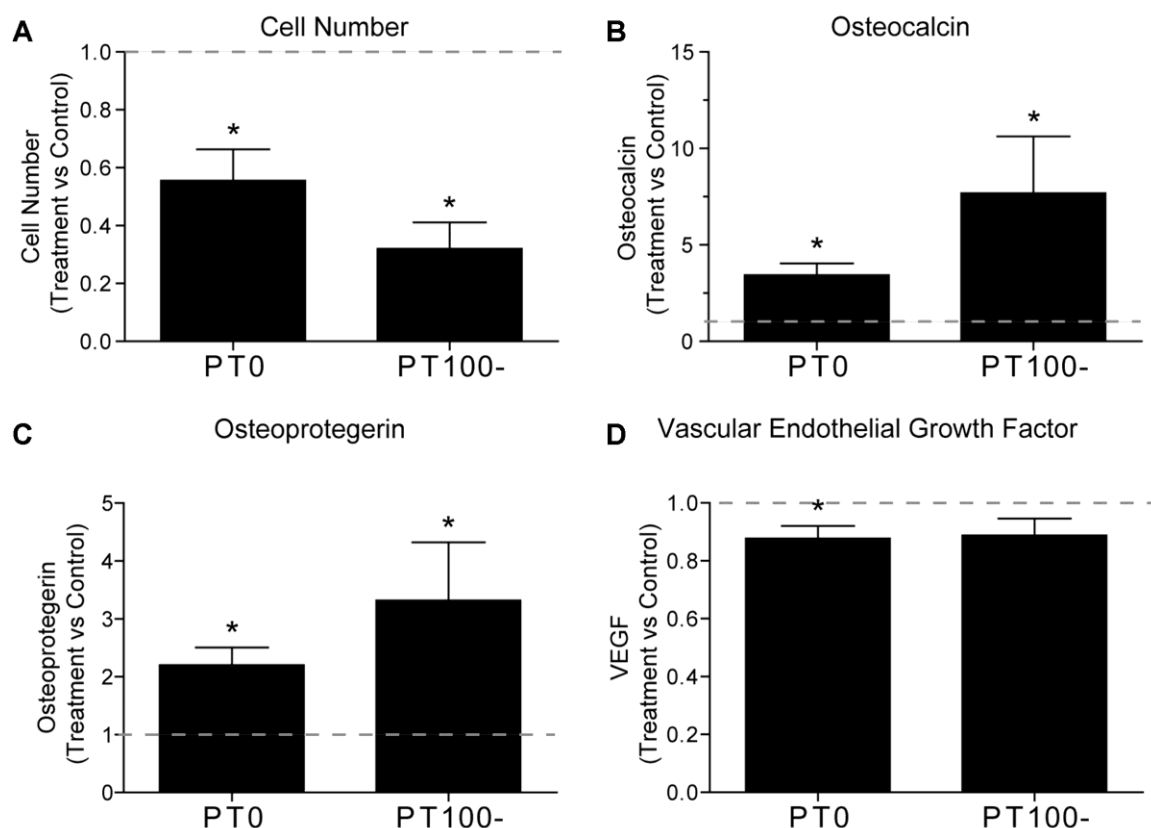


Figure 8.6. Evaluation of different control surfaces on the response of osteoblast-like MG63 cells. Cells were plated on electrically-isolated PT controls on TCPS plates (PT) and compared to non-stimulated PT controls on custom-made plates (PT0) and 100-mV cathodically polarized PT surfaces (PT100-). At confluence, checked on TCPS, (A) cell number, (B) osteocalcin, (C) osteoprotegerin, and (D) VEGF levels were measured. Data represented as treatment over control analyses \pm standard error of three different experiments with six independent samples each. * refers to a statistically-significant p value below 0.05 vs. PT; # refers to a statistically-significant p value below 0.05 vs. PT0.

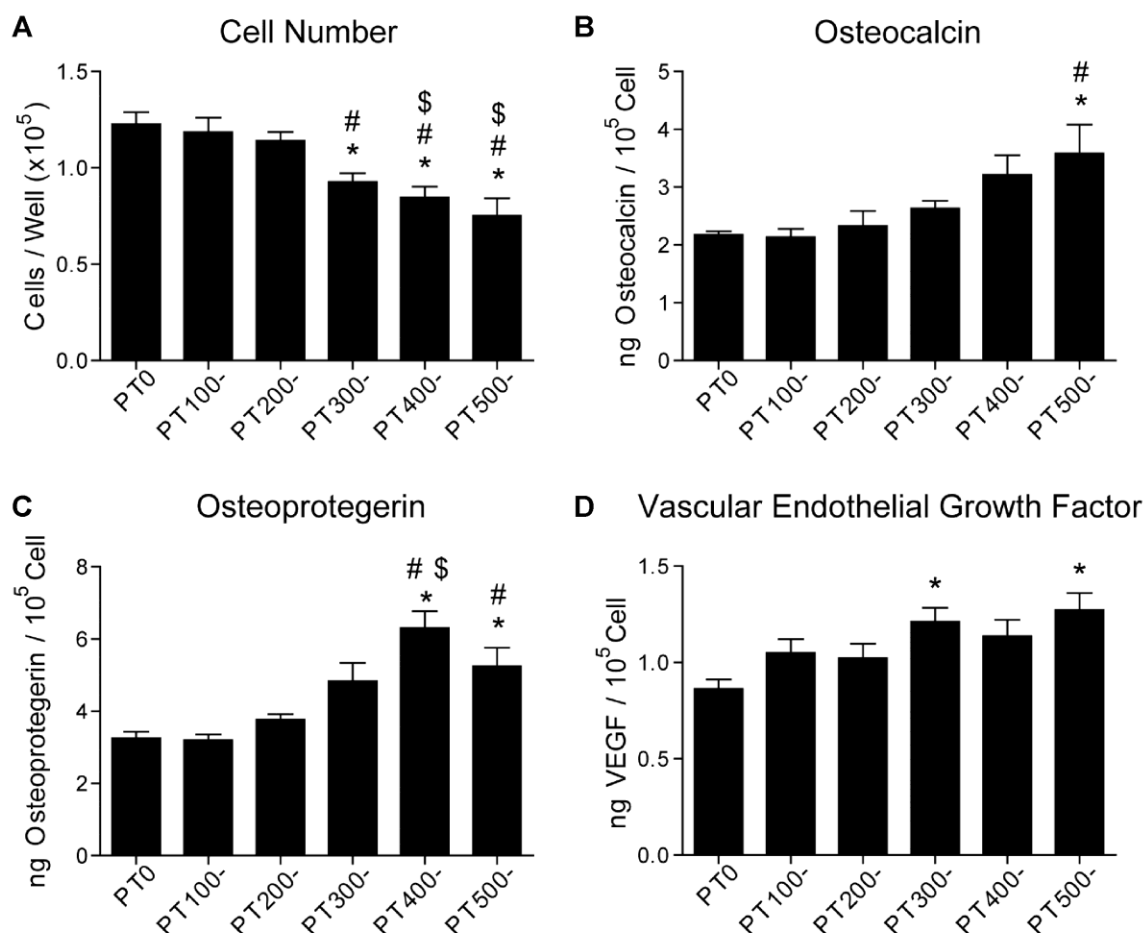


Figure 8.7. Voltage-dependent effects of cathodically polarized PT surfaces on osteoblast-like MG63 cells. Cells were plated on non-stimulated PT0 controls, as well as PT surfaces stimulated with fixed DC potentials of 100, 200, 300, 400 and 500 mV. At confluence, checked on TCPS, (A) cell number, (B) osteocalcin, (C) osteoprotegerin, and (D) VEGF levels were measured on the cathodically polarized surfaces. Data represented are the mean \pm standard error of six independent samples. * refers to a statistically-significant p value below 0.05 vs. PT; # refers to a statistically-significant p value below 0.05 vs. PT100-; \$ refers to a statistically-significant p value below 0.05 vs. PT200-; % refers to a statistically-significant p value below 0.05 vs. PT300-.

8.4. Discussion

Recently, implantable devices that supply DC stimulation directly through their surface to the surrounding tissue have been used to provide localized treatment and improve osseointegration [4, 18]. However, *in vitro* models that represent these conditions need to be developed, as most available systems provide electrical stimulation to cells indirectly through the tissue culture medium [11, 12]. In this study a new *in vitro* electrical stimulation system was designed to provide stimulation directly through Ti substrates used to culture cells. The results demonstrate that osteoblast maturation responds strongly to fixed DC potentials supplied through cathodically polarized Ti surfaces and the response is voltage-dependent.

We successfully designed and implemented an *in vitro* system that allowed direct electrical connections directly underneath the Ti substrates used to culture the cells. In this way, the surfaces where the cells are growing could be used as the electrodes that supply the electrical stimulation. Most *in vitro* systems for DC stimulation have been modeled after *in vivo* conditions to treat nonunions, where electrodes are placed nearby the healing ends of the injured bone [19]. Thus, *in vitro* setups commonly submerge electrodes in the culture media to supply fixed DC currents and associated potentials to cells growing on standard TCPS [20]. However, such a setup does not necessarily represent a situation where the actual osseointegrating implant is providing the electrical stimulation [4]. Additionally, the flow of current through the media/electrodes promotes electrochemical reactions on the anode and the cathode that could confound the results [14], and is not clear if both the currents and the potentials are needed for the beneficial effects of the electrical stimulation. The system designed in this study also attempted to isolate the effects of supplied DC potentials without the influence of flowing currents.

The electrochemical stability of the electrolyte is an important factor to consider when applying electrical stimulation. Although no currents were detected in the system, which minimizes the possibility of electrochemical reactions occurring around the electrodes, cyclic voltammetry tests were performed on PT surfaces using a standard three-electrode electrochemical cell to ensure that the voltages used would not elicit oxidation of the surface or breakdown of the media. In the acidic environment, specimens showed relatively-low current values with constant hysteresis throughout the test, indicating good electrochemical stability. Sudden rises in the current curve are indicative of the onset of oxidation, and it appears relatively-smooth PT surfaces were not susceptible to oxidation (or oxygen gas evolution) under these conditions. When the cyclic voltammetry tests were performed on the cell culture media, the current increased sharply at higher voltages. The sharp increase in the curve corresponds to breakdown of the media, and the PT surfaces seem to facilitate this breakdown at the higher potentials. However, media breakdown was not exhibited until at least 0.6 V, which was higher than the potentials used for the cell experiments. Small current peaks were found before 0.5 V during the first voltammetry cycle in media, possibly due to surface passivation reactions, but these were considered negligible because of their transient nature. In addition, no topographical changes were detected on the Ti surfaces after simulated runs in the *in vitro* electrical stimulation system, which is important to ensure that the responses obtained during cell experiments are strictly caused by the fixed DC potentials.

MG63s were sensitive to electrical stimulation with 100 mV, and this effect was more pronounced on the surfaces that were cathodically polarized. Cell number, which is directly related to proliferation and inversely related to differentiation, was lower in the electrically stimulated groups, with the lowest levels on the negatively charged surface.

Conversely, other studies evaluating the effects of electrical stimulation have found an increase in proliferation upon DC stimulation through the culture media [1, 12]. However, these studies have failed to correlate the increase in proliferation with a corresponding increase in cell differentiation.

Additionally, several studies on microrough surfaces, which are well documented to promote osteoblast differentiation, confirm that the transcriptionally regulated transition from a proliferative to a differentiated state leads to lower cell numbers on the rougher surfaces [21, 22]. This falls in agreement with our results showing lower cell numbers coupled to higher levels of the late differentiation marker osteocalcin on the electrically stimulated groups, even when compared to clinically-relevant, microrough control surfaces. The highest levels of osteocalcin were found on the negatively charged group, which is in accord with a number of other reports associating negative polarities with the natural process of bone healing [23] and the beneficial effects of electrical stimulation [3]. Interestingly, anodic polarization also seemed to promote osteoblast differentiation but to a lesser extent, which has not been commonly shown in the literature possibly due to the detrimental effects of electrochemical products produced around the anode in common *in vitro* setups [14]. Production of the local factors osteoprotegerin, an inhibitor of osteoclastogenesis, and VEGF, a potent angiogenic factor important for bone development, were also significantly higher on the cathodically polarized surfaces. Remarkably, the results differed when connecting a monitoring device to measure the potentials supplied to the experimental groups. The electrical stimulation effect was lost in all the cell assays performed on the groups connected to a potentiostat used as a voltmeter, underscoring the susceptibility of the system to instrumentation leak currents.

Our initial studies assessing the effects of electrical stimulation on osteoblast responses were performed using control surfaces that were electrically-isolated in standard TCPS plates. However, to rule out the possibility that the response of osteoblasts could be affected just by establishing electrical connections with the substrates, studies were carried out evaluating non-stimulated control surfaces on the custom-made plates. Osteoblast maturation and osteoprotegerin production were significantly enhanced on the cathodically polarized surfaces when compared to the electrically-isolated surfaces in TCPS plates, as seen in the initial studies. Interestingly, there was a trend of increased maturation and osteoprotegerin production on the stimulated surfaces compared to the non-stimulated controls in the custom-made plates, although this change was not statistically significant. VEGF levels were not greatly influenced by electrical stimulation with 100 mV. The non-stimulated specimens were not connected to the power supply, but still were short-circuited with the stainless steel bar, which could have affected their native distribution of surface charges. Another possibility is that the chemistry of the PC custom-made plates could be exerting an influence on the growth of the cells.

Cell experiments were also performed using different potentials on the cathodically polarized PT surfaces, and the response of osteoblast-like cells was voltage-dependent. Cell number was lower on the groups stimulated with the higher potentials, and these data in combination with higher production of differentiation markers suggests that the cells growing on the cathodically polarized PT surfaces exhibited a more mature phenotype with an increase in potentials. The effects of the higher potentials on osteoblast differentiation were also accompanied by higher production of local factors osteoprotegerin and VEGF, which have been shown to enhance osseointegration *in vivo* [1, 24]. Our results indicate that the maturation of

osteoblasts growing on relatively smooth surfaces can be accelerated by increasing the strength of the DC potential supplied. Our hypothesis when designing these experiments was that electrical stimulation at lower potentials would promote osteoblast differentiation but higher potentials would inhibit differentiation, as had been shown previously in the case of the extreme signals found during corrosion events [25]. The range of potentials evaluated in this study did not show any detrimental effect on the development and maturation of osteoblasts on relatively smooth surfaces even at the highest levels, which instead promoted osteoblast maturation. The possibility exists that even higher potentials than the ones provided could inhibit the maturation of osteoblasts, but this was not explored in this study.

During corrosion events, electric potentials are generated in association with extreme electrochemical currents that result in products injurious to the cells, such as metal and hydrogen ions [14, 26, 27]. Corrosion-related electrochemical products and wear debris have been implicated in complications surrounding orthopaedic implants, such as aseptic loosening [28, 29]. However, the electrical currents and potentials present during corrosion events could also have an effect on cell response. The *in vitro* system described in this study is connected in such a way as to avoid the flow of currents through the culture medium while supplying cathodic polarization to the surfaces where the cells are growing. Our results suggest electrochemical potentials by themselves may not contribute to the detrimental effects of corrosion events around implants, leaving currents and associated electrochemical products as possible causes for the negative impact of corrosion.

The success of dental and orthopedic implants is dependent upon the osseointegration of the implant with the surrounding bone and this, in turn, is greatly dependent on the surface properties of the device. Faster and better osseointegration

has become the driving force of many research efforts to satisfy the demands of an increasing aging population. Properties such as surface roughness [30, 31], surface chemistry [32] and surface energy [33] have been found to affect cell response, and if tailored appropriately, can enhance cell differentiation, local factor production and, consequently, bone growth and osseointegration [34]. In the same way, electrical stimulation of implants should be considered as an additional tool for the enhancement of bone growth and repair in patients with compromised or diseased bone, and new strategies should focus on the effective translation of successful *in vitro* models to clinical settings.

8.5. Conclusions

In this study we present an *in vitro* system that provides electrical stimulation of cells with fixed DC potentials, in the absence of electrochemical currents. DC stimulation was supplied directly through the Ti substrates used to culture cells, with the surfaces being either anodically or cathodically polarized. MG63 differentiation and local factor production was more pronounced on cathodically polarized surfaces when compared to the anode, and this effect was susceptible to leak currents introduced by monitoring instrumentation. The effect of fixed DC potentials also seemed to be voltage-dependent, with higher potentials promoting a greater enhancement of osteoblast differentiation. Our results suggest that electrochemical potentials may not be responsible for the detrimental effects of corrosion events around implants.

8.6. References

1. Kim IS, Song JK, Zhang YL, Lee TH, Cho TH, Song YM, et al. Biphasic electric current stimulates proliferation and induces VEGF production in osteoblasts. *Biochim Biophys Acta* 2006;1763(9):907-916.

2. Wang Q, Zhong SZ, Jun OY, Jiang LX, Zhang ZK, Xie Y, et al. Osteogenesis of electrically stimulated bone cells mediated in part by calcium ions. *Clin Orthop* 1998;348:259-268.
3. Cook SD, Patron LP, Christakis PM, Bailey KJ, Banta C, Glazer PA. Direct current stimulation of titanium interbody fusion devices in primates. *Spine J* 2004;4(3):300-311.
4. Song JK, Cho TH, Pan H, Song YM, Kim IS, Lee TH, et al. An Electronic Device for Accelerating Bone Formation in Tissues Surrounding a Dental Implant. *Bioelectromagnetics* 2009;30(5):374-384.
5. Becker RO, Spadaro JA, Marino AA. Clinical experiences with low intensity direct-current stimulation of bone-growth. *Clin Orthop* 1977;124:75-83.
6. Kooistra BW, Jain A, Hanson BP. Electrical stimulation: Nonunions. *Indian J Orthop* 2009;43(2):149-155.
7. Goldstein C, Sprague S, Petrisor BA. Electrical Stimulation for Fracture Healing: Current Evidence. *J Orthop Trauma* 2010;24:S62-S65.
8. Buser D, Broggini N, Wieland M, Schenk RK, Denzer AJ, Cochran DL, et al. Enhanced bone apposition to a chemically modified SLA titanium surface. *J Dent Res* 2004;83(7):529-533.
9. Giavaresi G, Fini M, Chiesa R, Giordano C, Sandrini E, Bianchi AE, et al. A novel multiphase anodic spark deposition coating for the improvement of orthopedic implant osseointegration: an experimental study in cortical bone of sheep. *J Biomed Mater Res A* 2008;85(4):1022-1031.
10. Granstrom G. Osseointegration in irradiated cancer patients: An analysis with respect to implant failures. *J Oral Maxillofac Surg* 2005;63(5):579-585.
11. Curtze S, Dembo M, Miron M, Jones DB. Dynamic changes in traction forces with DC electric field in osteoblast-like cells. *J Cell Sci* 2004;117(13):2721-2729.
12. Ercan B, Webster TJ. Greater osteoblast proliferation on anodized nanotubular titanium upon electrical stimulation. *Int J Nanomedicine* 2008;3(4):477-485.
13. Black J. *Electrical Stimulation: Its Role in Growth, Repair, and Remodeling of the Musculoskeletal System*. New York: Praeger Publishers; 1987.
14. Bodamyali T, Kanczler JM, Simon B, Blake DR, Stevens CR. Effect of Faradic products on direct current-stimulated calvarial organ culture calcium levels. *Biochem Biophys Res Commun* 1999;264(3):657-661.
15. Gittens RA, Olivares-Navarrete R, Tannenbaum R, Boyan BD, Schwartz Z. Electrical implications of corrosion for osseointegration of titanium implants. *J Dent Res* 2011;90(12):1389-1397.
16. Baranowski TJ, Black J, Brighton CT. Microenvironmental changes associated with electrical-stimulation of osteogenesis by direct-current. *J Electrochem Soc* 1983;130(3):C120-C120.
17. Zhao G, Schwartz Z, Wieland M, Rupp F, Geis-Gerstorfer J, Cochran DL, et al. High surface energy enhances cell response to titanium substrate microstructure. *J Biomed Mater Res* 2005;74A:49-58.
18. Yonemori K, Matsunaga S, Ishidou Y, Maeda S, Yoshida H. Early effects of electrical stimulation on osteogenesis. *Bone* 1996;19(2):173-180.
19. Hagiwara T, Bell WH. Effect of electrical stimulation on mandibular distraction osteogenesis. *J Craniomaxillofac Surg* 2000;28(1):12-19.
20. Hammerick KE, James AW, Huang ZB, Prinz FB, Longaker MT. Pulsed Direct Current Electric Fields Enhance Osteogenesis in Adipose-Derived Stromal Cells. *Tissue Engineering Part A* 2010;16(3):917-931.

21. Olivares-Navarrete R, Raz P, Zhao G, Chen J, Wieland M, Cochran DL, et al. Integrin alpha 2 beta 1 plays a critical role in osteoblast response to micron-scale surface structure and surface energy of titanium substrates. *Proc Natl Acad Sci U S A* 2008;105(41):15767-15772.
22. Stein GS, Lian JB, Stein JL, VanWijnen AJ, Montecino M. Transcriptional control of osteoblast growth and differentiation. *Physiol Rev* 1996;76(2):593-629.
23. Friedenber ZB, Brighton CT. Bioelectric potentials in bone. *J Bone Jt Surg (Am)* 1966;A 48(5):915-923.
24. Schwartz Z, Fisher M, Lohmann CH, Simon BJ, Boyan BD. Osteoprotegerin (OPG) production by cells in the osteoblast lineage is regulated by pulsed electromagnetic fields in cultures grown on calcium phosphate substrates. *Ann Biomed Eng* 2009;37(3):437-444.
25. Gilbert JL, Zarka L, Chang EB, Thomas CH. The reduction half cell in biomaterials corrosion: Oxygen diffusion profiles near and cell response to polarized titanium surfaces. *J Biomed Mater Res* 1998;42(2):321-330.
26. Ramp WK, Lenz LG, Kaysinger KK. Medium pH modulates matrix, mineral, and energy-metabolism in cultured chick bones and osteoblast-like cells. *Bone Miner* 1994;24(1):59-73.
27. Black J, Baranowski TJ, Brighton CT. Electrochemical aspects of dc stimulation of osteogenesis. *Bioelectrochem Bioenerg* 1984;12(3-4):323-327.
28. Jacobs JJ, Roebuck KA, Archibeck M, Hallab NJ, Glant TT. Osteolysis: Basic science. *Clin Orthop* 2001(393):71-77.
29. Lohmann CH, Dean DD, Koster G, Casasola D, Buchhorn GH, Fink U, et al. Ceramic and PMMA particles differentially affect osteoblast phenotype. *Biomaterials* 2002;23(8):1855-1863.
30. Olivares-Navarrete R, Hyzy SL, Hutton DL, Erdman CP, Wieland M, Boyan BD, et al. Direct and indirect effects of microstructured titanium substrates on the induction of mesenchymal stem cell differentiation towards the osteoblast lineage. *Biomaterials* 2010;31(10):2728-2735.
31. Gittens RA, McLachlan T, Olivares-Navarrete R, Cai Y, Berner S, Tannenbaum R, et al. The effects of combined micron-/submicron-scale surface roughness and nanoscale features on cell proliferation and differentiation. *Biomaterials* 2011;32(13):3395-3403.
32. Sul YT, Johansson C, Wennerberg P, Cho LR, Chang BS, Albrektsson P. Optimum surface properties of oxidized implants for reinforcement of osseointegration: Surface chemistry, oxide thickness, porosity, roughness, and crystal structure. *Int J Oral Maxillofac Implants* 2005;20(3):349-359.
33. Liu X, Lim JY, Donahue HJ, Dhurjati R, Mastro AM, Vogler EA. Influence of substratum surface chemistry/energy and topography on the human fetal osteoblastic cell line hFOB 1.19: Phenotypic and genotypic responses observed in vitro. *Biomaterials* 2007;28(31):4535-4550.
34. Schwartz Z, Boyan BD. Underlying Mechanisms at the Bone-Biomaterial Interface. *J Cell Biochem* 1994;56:340-347.

CHAPTER 9. CONCLUSIONS AND FUTURE PERSPECTIVES

The present work has established the development of a simple and clinically-relevant nanomodification for titanium (Ti) and Ti alloy implants that superimposes high and homogeneous coverage of nanostructures on the surface of microsmooth and microrough specimens. In addition, a new *in vitro* system has been developed to allow electrical stimulation of cells through Ti substrates used to culture the cells.

The presentation of nanostructures on microsmooth surfaces had a moderate effect on osteoblast maturation and local factor production. However, combined micro/nanostructured surfaces synergistically promoted the maturation and local factor production of osteoblasts on these surfaces when compared to microsmooth or microrough-only surfaces. These responses were consistent even when using different osteoblast cell types (MG63s vs hOBs) and different substrate chemistries (Ti vs TiAlV). Conversely, MSC responses to nanostructures were different than those found on osteoblasts and were dependent on substrate chemistry. On one hand, MSC differentiation and local factor production on Ti substrates was suppressed when cultured on micro/nanostructured surfaces compared to microrough surfaces. Superposition of nanostructures on microrough surfaces reduced MSC production of differentiation markers and local factors to the levels of microsmooth surfaces. On the other hand, MSC differentiation was similar between microrough and micro/nanostructured surfaces but local factor production was differentially regulated, with angiogenic factors being highly expressed on the micro/nanostructured surfaces. These findings support the conclusion that the successful osseointegration of an implant depends on contributions from osteoblast lineage cells at different stages of osteoblast

commitment and indicates the importance of examining cell response in multiple *in vitro* models.

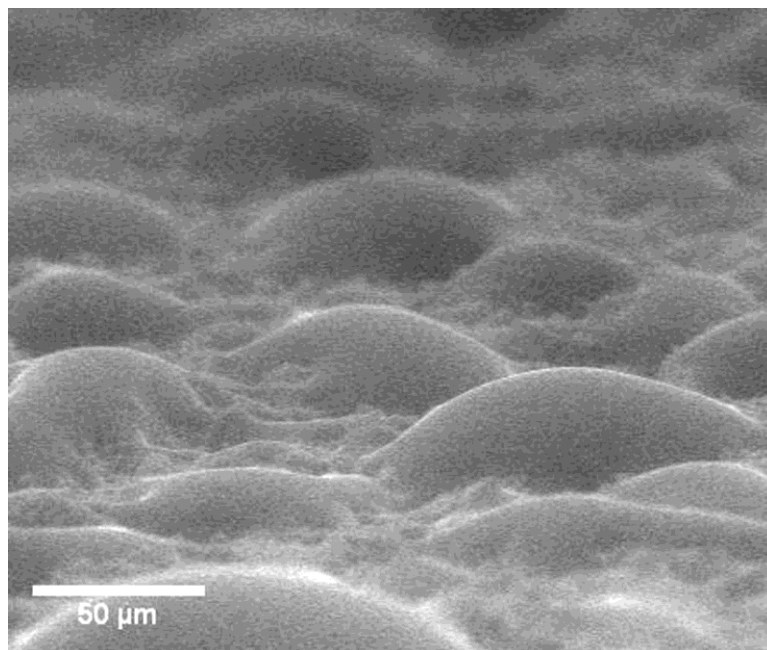
Electrical stimulation using fixed DC potentials promoted osteoblast maturation and local factor production, and this effect was more pronounced on cathodically polarized surfaces when compared to the anode. The beneficial effects of electrical stimulation were susceptible to leak currents introduced by monitoring instrumentation. The effect of fixed DC potentials also seemed to be voltage-dependent, with higher potentials promoting a greater enhancement of osteoblast differentiation. Our results suggest that electrochemical potentials may not be responsible for the detrimental effects of corrosion events around implants.

These studies provided exciting results that contribute to the fundamental understanding of the interactions between cells and surfaces. However, as any good research project, it also opened the door for many other interesting questions that remain to be answered. Our experiments were instrumental in establishing the phenomena of osteoblast lineage cell response to nanostructures and electrical potentials, but mechanistic evaluations of the molecular pathways at play are mandatory to have a better understanding that can lead to intelligent design of surfaces for bone implant applications.

In the case of the nanomodification project, it is not clear if the response exhibited by osteoblast lineage cells is specific to the oxidation-based nanostructures generated by our process, or if this is a general response to different nanostructures. Comparisons between the effects of differently-produced nanostructures on the protein production and gene expression of osteoblast lineage cells would be helpful to elucidate these uncertainties. In the case of the electrical stimulation system, voltage-dependent effects on osteoblast lineage cells must be assessed using microrough and

micro/nanostructured surfaces to investigate if these beneficial effects of electrical stimulation are additive or synergistic to those effects elicited by topography. The possibility remains that the effects of electrical potentials are dependent on the differentiation state of osteoblast lineage cells. Also, oxidized specimens that have thick, insulating oxide layers might be ideal substrates for stimulation with fixed DC potentials if the effects are mediated through surface charges.

APPENDIX A



Video A.1. Representative video of the condensation dynamics of water droplets on microrough Ti (SLA) surfaces, showing how droplets nucleate and the contact angle evolves. (gittens_rolando_a_201212_phd_videoa1_esem, 1.9MB)

VITA

ROLANDO A. GITTENS IBACACHE

Rolando A. Gittens Ibacache was born in Panama, Republic of Panama, where he attended the school Instituto Italiano Enrico Fermi and received a B.S. in Electrical & Electronics Engineering from the Universidad Tecnológica de Panamá (EE, 2006) before coming to Georgia Tech to pursue a doctorate in Bioengineering. During his time at Tech he also received a M.Sc. in Material Science and Engineering (MSE, 2011), submitted two patent applications for surface nano-modifications of titanium implants, and had the opportunity to travel to several national and international prestigious conferences where he earned various awards, such as the Young Investigator Award at the International Association for Dental Research (IADR) conference two years in a row (2012, 2011).

